Steady and unsteady body-force modeling of propeller aerodynamics

Hugues Pantel

RÉPUBLIQUE FRANÇAISE
Liberté Égalité Fraternité

Doctorat de l'Université de Toulouse

délivré par l'ISAE-SUPAERO

Steady and unsteady body-force modeling of propeller aerodynamics

---

Thèse présentée et soutenue, le 4 décembre 2024 par

Hugues PANTEL

École doctorale
MEGEP - Mécanique, Energétique, Génie civil, Procédés

Spécialité
Dynamique des fluides

Unité de recherche
ISAE-ONERA EDyF Energétique et Dynamique des Fluides

Thèse dirigée par
Xavier CARBONNEAU et Fabrice FALISSARD

Composition du jury
M. Marcello MANNA, Président, University of Naples Federico II
M. Jens Nørkær SØRENSEN, Rapporteur, Technical University of Denmark
M. Leo VELDHUIS, Rapporteur, Delft University of Technology
M. William THOLLET, Examinateur, Airbus
M. Xavier CARBONNEAU, Directeur de thèse, ISAE-SUPAERO
M. Fabrice FALISSARD, Co-directeur de thèse, ONERA

Membres invités
M. Guillaume Dufour, Co-encadrant, ISAE-SUPAERO

A mon grand-père.

Acknowledgements

The work conducted throughout these three years of research was made possible thanks to the involvement of many people that I would like to thank.

I would first like to thank Professors Veldhuis and Sørensen for taking the time to review my thesis and for their valuable reports. In particular, I want to thank Professor Sørensen for taking the time to come to Paris in person to attend the defense. I would also like to thank Professor Manna and Mr. Thollet who agreed to be examiners of this work, and for their valuable comments and questions during the thesis defense.

Je souhaite aussi remercier Xavier de m'avoir fait confiance pour mener à bien ces recherches. Un immense merci à mes deux encadrants, Guillaume et Fabrice, sans qui ce travail n'aurait jamais vu le jour. Merci Guillaume pour le temps que tu m'as accordé chaque semaine, pour ta rigueur, tes connaissances sur le body-force, et pour ta capacité à me faire prendre du recul à chacun de nos points. Tu as vraiment eu le rôle d'un directeur de thèse, et pour cela je te remercie. Un grand merci également à Fabrice pour ta disponibilité, pour ton exigence, et pour ton soutien au quotidien. Pendant ces trois ans tu as su me remotiver quand tous mes résultats de première année étaient à jeter à cause d'un bug, quand notre stagiaire nous a fait faux bond, ou quand je me suis rendu compte qu'écrire le manuscrit c'était pas super fun. Merci également de m'avoir appris au cours de la thèse à ne pas être toujours d'accord avec toi, c'est une bonne leçon de vie pour la suite. Mais surtout, tu as su me communiquer ton amour profond pour les tourbillons. Je ne sais pas si ça me servira beaucoup dans mon avenir professionnel, mais grâce à toi j'ai changé mon pseudo des forums d'escalade en Tourbiceps, et ça je ne suis pas près de l'oublier.

Un grand merci à Biel et à tous les membres de l'équipe H2T qui m'ont aidé, de près ou de loin, pendant mes travaux. En particulier, merci à Ronan d'avoir pris du temps que tu n'avais pas pour tester tes modèles sur mon hélice. Merci à Luis et Thomas pour votre immense travail sur MOLA. En particulier merci Luis pour tout ce que tu as fait sur le body-force stationnaire et sur le chimère instationnaire. Sans toi je pense que je serais toujours en train de galérer sur elsA v4 et sur des vieux scripts Python2. Merci à Danny pour tes précieux conseils sur mes maillages, le chimère, et j'en passe. Merci également pour ta bonne humeur au quotidien, et pour être le gars sûr qui va attaquer le buffet lorsqu'il y a un pot.

Merci à toute l'équipe de doctorants, vous n'êtes peut-être pas encore tous docteurs en mécanique des fluides, mais sachez que dans mon cœur, vous êtes au moins tous docteurs en « écouter Hugues se plaindre ». Merci pour les pauses, les restos, les verres, et les séances d'escalade. Merci à mes collègues de bureau successifs : Ilyès pour ne pas m'avoir suffisamment dégouté de faire une thèse à l'époque de mon stage, Victor et Johan avant que le bureau stagiaire se transforme en bureau MSAE, Antoine pour m'avoir encouragé à finir ma thèse en trois ans, et Alessandro pour toutes tes expertises turbomachines et toutes ces fois ou on discutait de tout et de rien dans notre bureau. Merci également à Cyril et Chiara, avec qui on a formé une super équipe de choc du body-force. Merci pour votre motivation inébranlable. Les termes sources inspiraient toujours une folle joie de vivre, et en plus nos calculs marchaient toujours à chaque fois du premier

coup, trop facile. Merci Cyril d'avoir fait l'ancien en me filant tes templates. Merci Chiara d'avoir toujours été partante pour faire une pause. Merci à la one-man-army du « body-fausse », incarnée par Masa. Hâte de demander à ta soutenance pourquoi il n'y a que deux pales dans tes simus, dont une qui ne tourne même pas.

Merci à tous les copains de Centrale et du lycée qui m'ont soutenu d'un peu plus loin. Merci pour les bars, les bars, encore les bars, et parfois les pique-niques. Un grand merci à Vincent pour ces presque 2 ans passés en coloc à kiffer, comme on en rêvait au lycée, à faire des soirées jusqu'à pas d'heure, à manger du poulet frit, et à refaire le monde sur notre canap' face à la super déco du proprio. Un grand merci à Jules pour cette solidarité dans les galères de doctorants. Un grand merci à Narindo pour tes sages conseils sur ma vie après la thèse.

Un immense merci à toute ma famille pour m'avoir appris à vulgariser mon sujet encore et encore, jusqu'à ce que je finisse moi-même par comprendre ce que je faisais. Merci Papa d'avoir toujours essayé de me ramener sur terre pendant mes moments de doute, à coups de « non mais tu sais pas la chance que t'as que ça se passe aussi bien nia nia nia ». C'était pas facile à entendre, mais avec le recul, je pense que t'avais raison. Merci Maman pour ton soutien inconditionnel, même quand j'ai loupé mon avion en rentrant de conf. Merci à tous les deux d'avoir su créer à la maison un cadre propice à la curiosité et à l'intérêt pour les sciences. Merci Louis pour ces sorties escalade lorsqu'on rédigeait nos manuscrits. In fine le tien ressemble plus à un rapport de stage, mais chacun se plie aux exigences de son domaine. Si j'avais su j'aurais peut-être fait médecine aussi, ça aurait été plus facile. Merci Blanche pour tes playlists, tes livraisons de raviolis, et tes supers schémas. T'es vraiment la super petite sœur que tu crois être. N'hésite pas à nous inviter plus au resto par contre.

Enfin, merci à Carla d'avoir été mon réservoir d'air frais pendant ces trois années un peu folles. Merci de m'avoir accompagné dans les termes sources, et pour tes questions qui montraient parfois que tu avais tout compris bien mieux que moi. Maintenant promis j'arrête les diplômes qui ne servent à rien et je me concentre sur des choses un peu plus utiles, à commencer par mon permis de conduire.

Summary

More and more aircraft prototypes are based on propeller propulsion (eVTOL, distributed electric propulsion, regional aircraft). Unlike turbojet engines, which are shrouded, propellers interact significantly with the airframe. One of the major challenges in developing these aircraft is to quantify the interaction effects on aerodynamic performance, i.e. to assess the impact of propeller and/or rotor positioning on the flight envelope. To achieve this, numerical simulation methods are used, with more or less detailed modeling of the propulsion system depending on the purpose of the simulation. Today, two types of methods are favored:

- Unsteady simulations which model the flow around the rotating blades by solving the unsteady Navier-Stokes equations. This method provides an accurate description of the wake, but its computation cost can be prohibitive during the design phase.
- Steady simulations that model propellers using source terms in the Navier-Stokes equations. This method significantly saves computation time compared to a full simulation, since it is steady and avoids meshing the propeller blades. However, because it is steady, it cannot account for certain unsteady phenomena that can be critical.

The aim of this thesis is to gain a better understanding of how the steady source term models work, and to develop a method for unsteady propeller modeling using source terms. The latter is based on the "Actuator Line" method, which provides a realistic representation of the wake, and in particular of the blade tip vortex structures. This method, which is widely used in wind turbine sector (incompressible flows, few blades), needs to be extended and validated for propellers (compressible flows, high number of blades, high loading). The final objective is to use these two models to capture the mutual aerodynamic interactions between propeller wake and wing, when the engine is placed in front of a lifting surface. The study of the steady model, called RANS/BET, has led us to general conclusions about propeller modeling using source terms. These relate to the computation of the propeller loads using the blade element theory, the distribution of source terms in the computational domain, and the importance of the source term in the energy equation. Several tip-loss corrections were also compared. The final model was evaluated for several blade pitch angles in axial flight, and for incidence angles from 3° to 9°. For each flight point, thrust is predicted within 2% of the blade-resolved reference, and power within 1%. Blade loads are analyzed in detail. The model reproduces the velocity fields with a fidelity of the same order of magnitude as for the propeller loads. The unsteady model has been implemented in an original manner, and evaluated on the same flight points as the steady model. It systematically overestimates loads by around 5%, especially at the blade tip. This discrepancy was found to be relatively independent of model parameterization and mesh size, whereas the models described in the literature are very sensitive to all these parameters. The model also reproduces the propeller wake very well, and a study of blade tip vortices has been carried out. Both models are evaluated for a propeller placed in front of a wing. The load distribution along the wing is very well predicted, both time-averaged and time-accurate for the actuator line model. The effect of the wing disturbance on propeller performance is also well captured, with deviations of the same order of magnitude as in the isolated configuration.

Résumé

De plus en plus de prototypes d'aéronefs se basent sur une propulsion à hélices (eVTOL, propulsion électrique distribuée, avions régionaux). Contrairement aux turboréacteurs qui sont carénés, les hélices interagissent fortement avec la cellule avion. Un des enjeux majeurs du développement de ces appareils est de quantifier les effets d'intégration sur les performances aérodynamique, c'est-à-dire d'évaluer l'impact du positionnement des hélices et/ou rotors sur l'enveloppe de vol. On utilise pour cela des méthodes de simulations numériques des écoulements avec des modélisations plus ou moins fines du système propulsif en fonction de la finalité de la simulation. De nos jours deux types de méthodes sont privilégiées :

- Une simulation instationnaire qui modélise l'écoulement autour des pales en rotation en résolvant les équations de Navier-Stokes instationnaires. Cette méthode décrit le sillage de façon précise mais a un coût de calcul et un temps de restitution qui peuvent être prohibitifs lors des phases de conception.
- Une simulation stationnaire qui modélise les hélices par des termes sources dans les équations de Navier-Stokes. Cette méthode permet de significativement gagner en temps de calcul par rapport à une simulation complète car elle est stationnaire et permet d'éviter de mailler les pales de l'hélice. Toutefois, du fait de son aspect stationnaire, elle ne permet pas de rendre compte de certains phénomènes instationnaires pouvant être dimensionnants.

L'objectif de la thèse est d'une part de mieux comprendre comment fonctionnent ces modélisations par termes sources stationnaires, et d'autre part de développer une modélisation instationnaire d'hélices par termes sources. Celle-ci s'appuie sur la méthode dite "Actuator Line" et permet de représenter de façon réaliste le sillage tourbillonnaire des pales. Cette méthode, répandue dans le domaine éolien (écoulements incompressibles, faible nombre de pales), doit être étendue et validée pour la problématique des hélices (écoulements compressibles, nombre de pales élevé, fort chargement). Le but final est d'utiliser ces deux modèles pour capturer les interactions aérodynamiques réciproques entre le système propulsif et la cellule de l'appareil. L'étude du modèle stationnaire, appelé RANS/BET, a permis de tirer des conclusions générales sur la modélisation d'hélices par termes sources. Celles-ci portent notamment sur le calcul des efforts par la théorie de l'élément de pale, la distribution des termes sources dans le domaine de calcul et sur l'importance du terme source dans l'équation de l'énergie. Plusieurs corrections de bout de pale ont aussi été comparées. Le modèle final a été évalué sur une hélice pour plusieurs angles de calage en vol axial et pour des incidences de 3° à 9°. Pour chaque point de vol, la traction est prévue à 2% de la référence pale maillée, et la puissance à moins de 1%. Les efforts sur pale sont analysés en détail. Le modèle reproduit les champs de vitesse aussi fidèlement que les efforts. Le modèle instationnaire, implémenté de manière innovante, a été évalué sur les mêmes cas d'application. Il surestime systématiquement les charges de 5% environ, surtout en tête. Cet écart est peu sensible au paramétrage du modèle et au maillage, là où les modèles décrits dans la littérature sont très sensibles à ces paramètres. Le modèle restitue également très bien le sillage tourbillonnaire de l'hélice. Les deux modèles sont aussi évalués dans le cas d'une hélice en interaction avec une aile. La distribution des charges sur l'aile est très bien prévue, à la fois en moyenne temporelle et en instantanée. La perturbation de l'aile sur la performance hélice est également bien capturée, avec des écarts du même ordre de grandeur qu'en configuration isolée.

Table of contents

Nomenclature

Acronyms

AD	Actuator Disk
AL	Actuator Line
BEMT	Blade Element Momentum Theory
BET	Blade Element Theory
BR	Blade-Resolved
BR-C	Blade-Resolved Chimera
BR-FM	Blade-Resolved Full-Matched
CFD	Computational Fluid Dynamics
CPU	Central Processing Unit
FFT	Fast Fourier Transform
GMT	General Momentum Theory
LES	Large Eddy Simulation
LL	Lifting-Line
RANS	Reynolds Averaged Navier Stokes
RPM	Rotation Per Minute
URANS	Unsteady Reynolds Averaged Navier Stokes
1P	In-Plane

Variables

a	induction factor
$\overline{a}$	average induction factor
a_b	induction factor along the blade
A	control surface, m^2; or amplitude of an FFT mode
A_l	lateral surface of the control volume, m^2
b	wing span, m
c	chord length, m
$\overline{c}$	average chord length, m
c_{tip}	chord length at blade tip, m
C_d	drag coefficient of a blade section
C_l	lift coefficient of a blade section
C_n	normal force coefficient of a blade section
C_p	pressure coefficient along a wing section

C_t	tangential force coefficient of a blade section
C_D	drag coefficient of the wing
C_L	lift coefficient of the wing
C_P	$P/(\rho_0 n^3 D^5)$ power coefficient
C_T	$T/(\rho_0 n^2 D^4)$ thrust coefficient
dl	average length of mesh cell, m
D	propeller diameter, m; or drag, N
e	specific internal energy, J.kg^{-1}
$\boldsymbol{e}_.$	unit vector
E	specific total energy, J.kg^{-1}
$\boldsymbol{f}$	scaled blade load, N
f_a	blade section load in the axial direction, N
f_t	blade section load in the tangential direction, N
$\boldsymbol{F_{1P}}$	propeller in-plane force averaged over a revolution, N
F_{cal}	calibrated tip-loss correction of the blade loads
F_G	Glauert's tip-loss factor
F_P	Prandtl's tip-loss factor
F_S	Shen et al.'s tip-loss factor
F_x	axial blade load, N
F_t	tangential blade load, N
g	generic volumic distribution function, m^{-3}
g_{1D}	one-dimensional Gaussian distribution function, m^{-1}
g_{2D}	two-dimensional Gaussian distribution function at iso-radius, m^{-2}
g_{3D}	three-dimensional Gaussian distribution function, m^{-3}
g_{tr}	truncated three-dimensional Gaussian distribution function, m^{-3}
h	specific enthalpy, J.kg^{-1}
H	stagnation pressure, Pa
J	$V_0/(nD)$ advance ratio
$l_.$	cell length in a given direction, m
l_{BF}	length of the steady body-force volume, m
L	lift, N
$\dot{m}$	mass flow rate, kg.s^{-1}
M	Mach number
n	angular velocity of propeller, rev.s^{-1}
$\boldsymbol{n}$	outward pointing normal
n_a	number of points in the axial direction
n_r	number of points in the radial direction
n_θ	number of points in the azimuthal direction
N_b	number of blades
p	pressure, Pa
P	propeller power, W
$\boldsymbol{q}$	heat flux vector, J.s^{-1}.m^{-2}
Q	propeller torque, N.m
r	radial coordinate, m
R	propeller radius, m
R_h	hub radius, m
Re	Reynold's number

s_E	energy source term, W.m^{-3}
$s_{E,v}$	energy source term relative to viscous losses, W.m^{-3}
$\boldsymbol{s_M}$	momentum source term, N.m^{-3}
S	specific entropy, J.kg^{-1}.K^{-1}
t	time, s
T	propeller thrust, N; or temperature, K
$\boldsymbol{u}$	velocity vector in the absolute frame, m.s^{-1}
v	fluid velocity, m.s^{-1}
$\boldsymbol{v_{rel}}$	fluid velocity in the rotating frame, m.s^{-1}
V_0	freeflow velocity, m.s^{-1}
$\mathcal{V}$	computational volume, m^3
$\mathcal{V}_c$	control volume for analytic studies, m^3; or mesh cell volume, m^3
$\partial\mathcal{V}_c$	boundary of the control volume, m^2
w	axial distribution function for the RANS/BET model
$\boldsymbol{w_i}$	induced velocity, m/s
x	coordinate along the X-axis, m
y	coordinate along the Y-axis, m
z	coordinate along the Z-axis, m
Z	normalization factor of g_{tr}
α	effective angle of attack of a blade section, °
β	pitch angle of a blade section, °
Γ	blade circulation, m^2.s^{-1}
Γ_∞	blade circulation for an infinite number of blades, m^2.s^{-1}
Γ_b	blade circulation for a finite number of blades, m^2.s^{-1}
δ	Dirac function, m^{-3}
δ_s	distance between wake sheets, m
Δt	time-step, s
$\Delta\phi$	angle rotated in a time-step, °
ϵ	Gaussian smearing parameter, m
η	TV_0/P propeller propulsive efficiency
θ	azimuthal coordinate, °
Θ	incidence angle, °
λ	$\Omega R/V_0$ tip-speed ratio
Π	pressure force on the control volume, N
ρ	density, kg.m^{-3}
ρ_0	freeflow density, kg.m^{-3}
$\boldsymbol{\tau}$	viscous stress tensor, N.m^{-2}
σ	$(N_b c)/(2\pi r)$ local solidity
$\boldsymbol{\sigma}$	$-p\mathbb{I}+\boldsymbol{\tau}$ total stress tensor, N.m^{-2}
ϕ	local flow angle, °; or phase angle of an FFT mode, °
Ψ	phase of in-plane force relative to the Z-axis, °
ω	fluid angular velocity around blade, rad.s^{-1}
Ω	angular velocity of propeller, rad.s^{-1}

Subscripts

$\bullet_0$	inlet or reference flow quantity
$\bullet_1$	outlet quantity
$\bullet_a$	axial component
$\bullet_r$	radial component
$\bullet_R$	quantity in the rotor plane
$\bullet_t$	tangential component
$\bullet_x$	x component
$\bullet_y$	y component
$\bullet_z$	z component

Superscripts

$\bullet^+$	immediately downstream of the rotor disk
$\bullet^-$	immediately upstream of the rotor disk
$\bullet^{cor}$	corrected quantity with a tip-loss correction
$\bullet^{CFD}$	sampled form the CFD computation
$\bullet^i$	induced
$\bullet^{p-o}$	power-off

Introduction

As the consequences of global warming become more pressing, the debate is polarizing around the future of the aviation industry. In 2018, it was responsible for 2.6% of the global CO_2 emissions. By accounting for the non-CO_2 effects (condensation trails, NO_x emissions...), the contribution of commercial aviation to the global effective radiative forcing between 2000 and 2018 rises to around 5.1% [44]. The industry has committed to reaching the ambitious goal of net zero emissions by 2050 [32]. This objective is all the more challenging that the air traffic is rapidly growing. It was multiplied by 13 between 1973 and 2018, and despite a temporary setback during the global 2020 pandemic, it is planned to grow between 3% and 5% each year until 2050 [19]. Even though reducing traffic is the most effective way of significantly lowering the impact of commercial aviation on the environment, the industry itself has realistically no grasp on the magnitude of the traffic. Such a regulation can only be made by public institutions, on a regional if not global scale. As a result, the aviation industry must use its own levers to cut down on its emissions as much as possible. One of these levers is to reduce aircraft fuel consumption by improving propulsive efficiency. To do so, manufacturers increase the by-pass ratio of current turbofans and are investigating returning to non-shrouded architectures. These designs include propellers which were mostly abandoned in the 1960s with the rise of turbojets to increase flight speed, during an era of abundant and affordable oil. New propulsive configurations have also been under study during the last 20 years, such as the Counter Rotating Open Rotor. Its development has however been mostly abandoned in the last few years in favor of the Open Fan, which is composed of a rotor and a stator. Open fans are advertised to offer efficiency gains of up to 20% [76].

Yet the absence of nacelle creates significant interactions between the rotors and the aircraft's airframe. This can lead to substantial aerodynamic, aeroelastic, and aeroacoustic challenges:

- These interactions can have a few aerodynamic consequences, the risk being the degradation of the aircraft's lift-to-drag ratio and of the propeller performance. First, the propeller, by its slipstream, interacts with the airframe. For instance, a propeller in tractor configuration creates an up-wash on one side of the wing and a down-wash on the other. This can substantially alter the wing's operating conditions compared to isolated conditions. Second, the airframe conversely modifies the propeller in-flow. The distortion in the rotor plane is most often non-uniform, leading to unsteady blade loads throughout a rotation. This significantly changes the propeller's operating point, which can modify propulsive efficiency. Yet if the aircraft architecture accounts correctly for these interactions, the plane can be overall more efficient than the isolated modules put together. For instance, Deere et al. showed that mounting propellers on wing tips could lead to a reduction of wing induced drag during cruise by 7.5% [17].

- These aerodynamic interactions lead to aeroelasticity challenges, for both the wing and the

rotor. First, in tractor configuration, the propeller slipstream can cause periodic twisting stress in the wing downstream. Furthermore, the unsteady blade loads mentioned previously often lead to loads in the propeller plane. These loads, which can be of the same order of magnitude as the propeller thrust, are also unsteady and can in particular cause wing deformations. They can also induce structural instabilities of the supporting pylon, known as whirl flutter. Second, the blade loads can also distort the blade shape itself, which in turn modifies propeller performance.

- The propeller vortex system induces periodic pressure fluctuations on the aircraft, especially where the tip vortices and the viscous wakes hit the airframe. In pusher configuration the propellers ingest the pylon wake, leading to pressure fluctuations as well. In both cases, strong noise radiations are created, which add to the already significant emissions of the propellers due to the lack of shielding by the nacelle. This consideration is all the more important for Open Fans that include fast-rotating (and sometimes transonic) blades, and a stator that can get hit by the rotor tip vortices.

On top of the ones previously mentioned, interaction effects also create difficulties related to aircraft stability, control, and passenger safety, just to name a few. These issues are particularly complex and difficult to predict when many propellers are concerned, where rotors not only interact with the airframe, but with one another as well. This is for instance the case for distributed electric propulsion concepts, where multiple propellers must be optimally integrated into the airframe to achieve the desired performance.

These challenges, associated to propeller and airframe interactions, are especially difficult to tackle for several reasons. First, they are multidisciplinary, and trade-offs are necessary between disciplines. For example, whereas it may be beneficial to place propellers at wing tips for aerodynamic gains, it can prove to be impossible in some cases for structural considerations. These compromises require discussions between several teams, and are particularly frequent during the pre-design steps. Second, these challenges need to be investigated by both aircraft and engine manufacturers. Indeed, as explained previously the performance of the airframe and the propulsive system are deeply coupled, and the aircraft performance needs to be addressed as a whole. However, a collaboration between actors from different private companies is often complicated due to confidentiality and intellectual property. Third, as mentioned previously, these challenges are relatively new because the interactions are more limited for turbojets. As a result, depending on the method of propulsion chosen (propellers, open fan, distributed), the optimal aircraft architecture may differ significantly from the conventional tube-and-wing configuration. Such an aircraft requires extensive validation to be certified to fly, which is a lengthy process. Finally, these challenges and difficulties need to be overcome as soon as possible to meet the climate objectives of the sector while remaining competitive for operators, thus highlighting the need for methods that can accelerate development cycles. In this context, the global objective of the present work is to develop efficient modeling approaches to tackle propeller-aircraft interactions.

From these challenges can be deduced a list of criteria to assess the performance of a modeling tool to predict propeller-airframe and propeller-propeller interactions. Such a model should:

1. account for the coupled effect of the propellers on the airframe and the retro-action of the airframe on the propellers.
2. be easily compatible with aeroelasticity and aeroacoustic studies.
3. simplify confidentiality issues between aircraft and engine manufacturers.

4. be able to explore off-design points.

5. be fast enough to allow quick design loops for pre-design studies.

Classically, aerodynamic interactions are evaluated using fully resolved unsteady Computational Fluid Dynamics (CFD) simulations, which solve the Reynolds Averaged Navier Stokes (RANS) equations. This method computes the flow around the rotating propeller blades and thus gives a good prediction of the wake, and of the unsteady blade and airframe loads. It can furthermore be coupled with aeroelasticity or aeroacoutic solvers, and is often able to correctly model off-design points with appropriate numerical parameters. However, fully resolved unsteady CFD is computationally too complex and expensive during pre-design studies. Furthermore, these computations require the transfer of confidential geometries between companies. This reveals the need for another model, better fitted for quick design loops.

The main cost of the fully resolved unsteady CFD RANS simulations comes from the modeling of the rotating blades. This is done using unsteady techniques, such as moving overlapping meshes or sliding meshes. As a result, a promising lead to significantly reduce computational cost while maintaining the fidelity of CFD on the airframe is to model the propeller's effect on the flow instead of fully solving it. This can be done by using boundary conditions in the computational domain, or by adding source terms in the Navier-Stokes equations, which are also known as body forces. The modeling of the blades in CFD was initially done using actuator disk-like models. These models average the propeller effect over a full revolution, thus making it possible to study interaction effects by conducting steady simulations. However these simulations only solve the mean flow and do not include unsteady effects, such as the blade tip vortices. Sørensen and Shen [94] thus developed an unsteady actuator disk model, called the actuator line. This model uses local CFD velocities to compute the blade loads with the Blade Element Theory, and distributes these loads as source terms in the close proximity of each blade positions. These source terms rotate at each time-step to create a helical wake behind the rotor. Both steady and unsteady models are of interest while studying propeller-airframe interaction effects, depending on the purpose of the study and on the computational resources available. Furthermore, these types of models can satisfy the five criteria presented, as will be detailed in the rest of the dissertation.

These body-force methods were mostly developed for the wind turbine sector, because of its long-lasting need to predict wind-farm interactions. For such applications, full blade-resolved CFD computations are evidently not practical. As a result, body-force modeling of wind turbines is already quite mature in this field, for both steady and unsteady methods. For instance, extensive research has been made to determine the best practices to conduct actuator line computations for LES simulations of wind turbines [48, 84, 98]. These studies pointed out in particular that the turbine power prediction strongly depends on mesh refinement and on the way the source terms are distributed into the CFD computation. Stevens et al. [87] compared actuator disk and actuator line Large Eddy Simulations (LES) to wind tunnel results of a model-sized wind farm of five rows of three turbines, including atmospheric boundary layer effects. The actuator disk model agrees very well with the experimental data, whereas the actuator line model yields mixed results due to the relatively coarse mesh used. However, the wide majority of wind turbine applications of the body-force models were made with LES simulations, which would be prohibitively expensive for propeller studies in a pre-design context. The proven dependency of the actuator line model's results to the grid refinement could could prove challenging for the RANS meshes used for aeronautical applications. Furthermore, wind turbines operate at different Mach and

Reynolds numbers than propellers, and the interaction lengths are far greater than for aeronautical applications. Thus the direct application of the body-force models from the wind turbine sector to propellers may not be straightforward.

Actuator disk-CFD models made for propeller applications do exist in literature, but by analogy with Glauert's Blade Element Momentum Theory (BEMT) [28], they are most often implemented as boundary conditions rather than body-forces. These boundary conditions rely on pressure jumps to model propeller thrust and impose a flow deflection to account for the torque [23, 60]. A few steady fully-coupled body-force models exist, such as the one developed by Ortun [62], which injects the source terms in the volume swept by the blades and with a density function that unevenly distributes the loads in the chordwise directions. This contrasts with wind turbine models that most often use 1D, 2D or 3D Gaussian distribution functions. The different methods have however never been thoroughly compared and analyzed on a unique test-case.

They are still very few propeller applications of the actuator line model as used in the wind turbine sector. Stokkermans [89] successfully used the actuator disk and actuator line models to replicate the interaction effects of a wing tip-mounted propeller. However this was done with prescribed propeller loads from the reference blade-resolved computation, i.e. only with a one-way coupling. Schollenberger et al. [79] were recently able to achieve a full coupling, but they used 3D airfoil polars from blade-resolved simulations and not the classical 2D airfoil polars.

This motivates the present study, which aims to develop and validate steady and unsteady fully coupled body-force models for propeller aerodynamics modeling, that are compatible with pre-design studies. These models are based on the ones developed for wind turbine computations, but adapted for aeronautical applications. The approach consisted in developing the two models and validating them on a three-bladed light propeller by comparing the results to reference BEMT, lifting line, and full blade-resolved URANS computations. This was conducted on an isolated propeller configuration, and on an installed configuration composed of a propeller in front of a straight wing. The thesis is organized as follows.

In the first chapter, a literature review of aerodynamic modeling of rotors is presented. It focuses on blade-based models, i.e. models based on the Blade Element Theory (BET), because only those methods are investigated in the thesis. The chapter includes a presentation of the basics of propeller aerodynamics, an overview of actuator disk methods, and in-depth description of steady and unsteady CFD-BET body-force couplings.

The second chapter describes the studied configurations, the solvers, numerical methods, and meshes used to run the CFD and lifting line computations. This section also presents the 2D airfoil polars used for all BET analyses in the BEMT, lifting line and body-force models.

The third chapter focuses on the development of a physically consistent steady body-force model, called the RANS/BET model, which relies on a full coupling between the blade element theory and CFD-RANS. First, the solved equations and the implementation are presented, highlighting the strong point of this model, which is to be flexible regarding source term distribution in the CFD computation. An in-depth study of source term distribution methods is then conducted, and very general conclusions are drawn by comparing the results to fundamental actuator disk theory results. Because the RANS/BET model time-averages the propeller effect on the flow, it does not model the blade tip vortices and and their effect should be accounted for during the BET computations. As a result, tip-loss corrections are required, and these are investigated in this chapter as well. Finally, different formulations of the energy source terms are investigated. This is a research problem that is specific to aeronautical applications, as CFD equations are solved in the incompressible regime for wind turbine cases, so the energy equation is omitted.

The fourth chapter presents an unsteady body-force model, which also relies on a full coupling between the blade element theory and CFD-RANS. It is an actuator line model that was slightly modified to be optimized for propeller applications. The model and its implementation are first described, and then the effect of source term distribution and velocity sampling are presented. Finally the model robustness is evaluated by investigating mesh and time-step sensitivity.

The two body-force models are then compared to lifting line with free wake computations, and to full blade-resolved CFD computations. The fifth chapter assesses the models on an isolated propeller configuration: first on the nominal axial operating point, then for varying blade pitch angles, and finally under incidences of 3°, 6°, and 9°. In the sixth chapter, the models are applied to an installed configuration which includes a propeller in front of a wing. Time-averaged and unsteady results are analyzed, for both propeller and wing loads.

Finally, conclusions are drawn and recommendations for future work are given.

The research conducted throughout the PhD has lead to two journal articles and two conference papers:

- [66]: H. Pantel, F. Falissard, and G. Dufour, *Assessment of Reynolds-Averaged Navier-Stokes/Blade Element Theory Body Force Method for Propeller Modeling*, AIAA Journal, 62 (2024), pp. 758-775.

  DOI: 10.2514/1.J063302

- [22]: F. Falissard and H. Pantel, *On the Use of Lifting Line Approaches for Propellers with Large Chord Variations*, AIAA Journal, 62 (2024), pp. 2377-2380.

  DOI: 10.2514/1.J063937

- [65]: H. Pantel, F. Falissard, and G. Dufour, *Assessment of a RANS/BET Body Force Method for Propeller Modeling*, in AIAA AVIATION 2023 Forum, San Diego, United States of America, June 2023, American Institute of Aeronautics and Astronautics.

  DOI: 10.2514/6.2023-3668

- [67]: H. Pantel, F. Falissard, and G. Dufour, *Simulation of an Installed Propeller by means of Steady and Unsteady Body-Force Modeling*, in ICAS 2024: 34th Congress of the International Council of the Aeronautical Sciences, Florence, Italy, Sept. 2024.

Chapter 1

Literature review of rotor modeling

Before getting into the developments made throughout the thesis, this chapter presents a literature review of aerodynamic modeling of rotors. Diagrams and equations are derived for propellers, but the literature review addresses all rotor modeling applications. The chapter focuses on blade-based models, i.e. models based on the Blade Element Theory (BET), because only those methods are investigated in the thesis. The objective here is not to be exhaustive, but rather to explain the theoretical concepts needed in the following chapters.

First, the basics of propellers are presented, including important definitions and an insight into how a propeller operates in non axial flow. Second, the major actuator disk theories are described: the main results of the momentum theories are recalled, the blade element theory is presented, and the tip-loss corrections are introduced. In the third section, a review of steady CFD-actuator disk models is conducted, focusing on those relying on the use of source terms. The models are categorized depending on the way they compute the blade loads, and how they distribute the loads in the CFD computation. A review of the tip-loss corrections is also made, because these models are steady and cannot model the tip vortices. This is one of the advantages of the actuator line, an unsteady body-force model, which is presented next. This last section presents the original model, and recalls in particular the different methods used in the literature to distribute the source terms and to sample the velocities used for the BET. Tip corrections, which are sometimes used with coarser grids, are briefly mentioned to complete the chapter.

Contents

1.1 Basics of propeller flows

1.1.1 Definitions

A propeller is a propulsive device which consists of a set of N_b blades that rotate at an angular velocity Ω around a nacelle. In this work, the X axis is chosen to be the rotation axis. The propeller advances in the air at a velocity V_0. The forward speed of the aircraft and the rotational speed of the propeller can be compared in a dimensionless parameter, the advance ratio J:

$$J = \frac{V_0}{nD}, \tag{1.1}$$

where n is the rotational speed of the propeller in revolutions per second and D is the propeller diameter.

The blade geometry can be seen as a stack of airfoils between the hub's radius R_h and the blade's tip radius R. The blade's specificity comes from the shape of the airfoils, and the way they are stacked on top of each other. These parameters are detailed hereafter, and a diagram of a slice of a blade section is shown in figure 1.1.

- The chord length, $c(r)$, refers to the length of the airfoil located at radius r.
- The pitch angle of each blade section, $\beta(r)$, refers to the angle between the airfoil's chord line and the rotation plane. It can also be written as the sum of the section's twist angle and the blade pitch angle, which usually corresponds to the pitch angle of the blade section located at $0.75R$.
- The sweep angle refers to the axial curvature of a blade section relative to its radial direction. Instead of extending straight outward from the hub, the blade may be swept backward in the direction of the freeflow velocity.
- The dihedral angle refers to the azimuthal curvature of the blade line in the rotation plane.

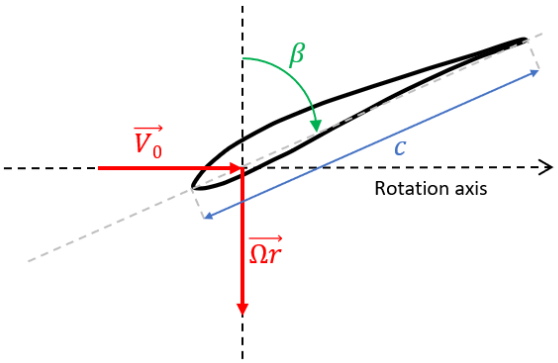

Figure 1.1: Diagram of a blade section.

In its rotation, the propeller creates a force T, the thrust, normal to the rotation plane. To achieve the rotation, the engine must compensate a resisting torque Q. The power P delivered in the shaft must then be

$$P = \Omega Q. \tag{1.2}$$

To compare thrust and power from one propeller to the other, dimensionless parameters are used. These are the thrust and power coefficients, defined as:

$$C_T = \frac{T}{\rho_0 n^2 D^4}, \tag{1.3}$$

$$C_P = \frac{P}{\rho_0 n^3 D^5}, \tag{1.4}$$

where ρ_0 is the density of the freestream flow. The propulsive efficiency, η, is computed as

$$\eta = \frac{V_0 T}{P} = \frac{J C_T}{C_P}. \tag{1.5}$$

During the flight, propeller thrust can be regulated in two main ways, depending on the design of the propeller and the type of engine. For high speed flight, the most common method involves adjusting the blade pitch angle, which requires a complex mechanism within the nacelle that allows the blades to rotate around their axis. This system allows for a more precise control of the thrust while maintaining efficient engine performance across different flight conditions. An alternative method, which is becoming more popular with the growing use of electric engines, is to control thrust by varying the angular velocity of the propeller. Electric engines are particularly well-suited for this approach due to their ability to quickly and efficiently adjust rotational speed without the need for complex mechanical systems. For turboprops however, this method requires to modify the rotation velocity of the internal engine components, and this is most often done at the cost of efficiency. In this dissertation the studies are conducted at the same rotation velocity and by varying the blade pitch angle.

1.1.2 Flow physics of an isolated propeller in axial flow

In axial flow, any point on the propeller blade has a helical trajectory. The vortices shed from the blades thus have a helical motion. This includes the tip vortices as well as the vortex sheet, as shown in figure 1.2. The flow is unsteady in the absolute frame, but is steady in the relative frame bound to a blade.

1.1.3 Flow physics of a propeller under incidence or in interaction

When the propeller inflow is not fully axial, when the rotor is under an incidence angle Θ for instance, the flow is no longer steady in the relative frame because the blade inflow varies with its azimuthal position. When the incidence angle is positive, the downward moving blade (advancing side) sees a greater velocity and an increased angle of attack than the upward moving one (retreating side), leading to a non-axisymmetric disk load (Figure 1.3). The same is true for a propeller in axial flow that is not isolated. For example, a wing placed behind a propeller creates an up-wash in the rotor plane, which also induces non-axisymmetric blade loads.

The blade load variation throughout a propeller revolution leads to the appearance of a non-zero average in-plane (1P) force $\boldsymbol{F_{1P}}$ when adding the contribution of each blade. These loads are limiting for aircraft structures and must be well predicted during the design phase. In this dissertation the 1P loads are studied as a modulus and a phase angle Ψ (defined by the conventions of figure 1.3). The modulus corresponds to the norm of the in-plane force, and the phase corresponds to the angle between the upward axis and the 1P force vector.

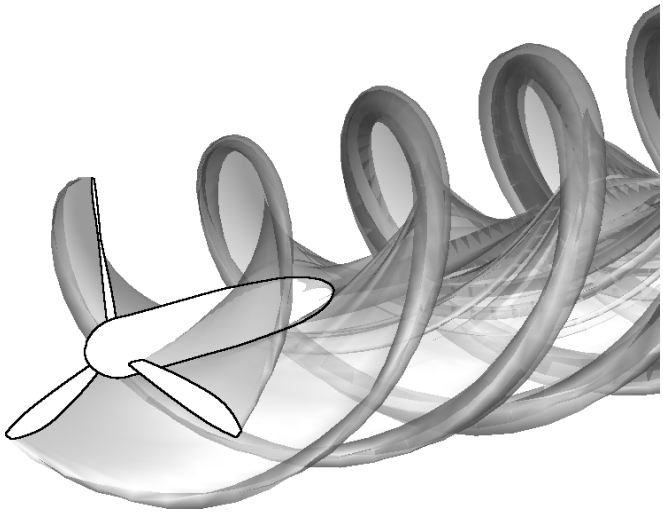

Figure 1.2: Vortex system of a propeller in axial flow.

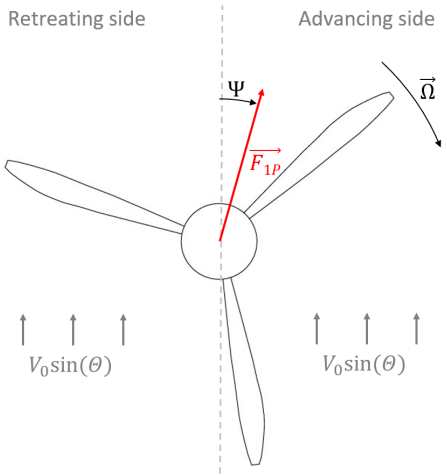

Figure 1.3: Diagram of a propeller under an incidence Θ.

1.2 Actuator disk theories

The most convenient way to model a propeller is to average its effect on the flow over a whole revolution. This removes blade to blade interactions and the complex modeling of the tip vortices. Furthermore, under uniform axial inflow, this leads to a steady axisymmetric solution. Considering the axial dimensions of the rotor compared to the wake characteristic length, it is also possible to further assume that the propeller is infinitely thin, its effect on the flow being accounted for as a discontinuity of pressure. The models that rely on these assumptions are known as actuator disk (AD) models, and their basic description and equations are presented in this section.

1.2.1 The axial momentum theory

The axial momentum theory, also known as the axial actuator disk, dates back to the second half of the 19th century in the work of Rankine [74] and Froude [25]. The objective of their work was to maximize propeller efficiency for the marine industry. They proposed to model the rotor as a disk that induces a pressure discontinuity in an ideal incompressible flow, while maintaining the continuity of axial velocity. In this section, the swirl induced by the propeller is neglected. The inflow is purely axial and uniform. A diagram of the control volume $\mathcal{V}_c$ that is studied is represented in figure 1.4. First, it is assumed that the velocity fields are constant by axial section, i.e. that they do not vary with the radius.

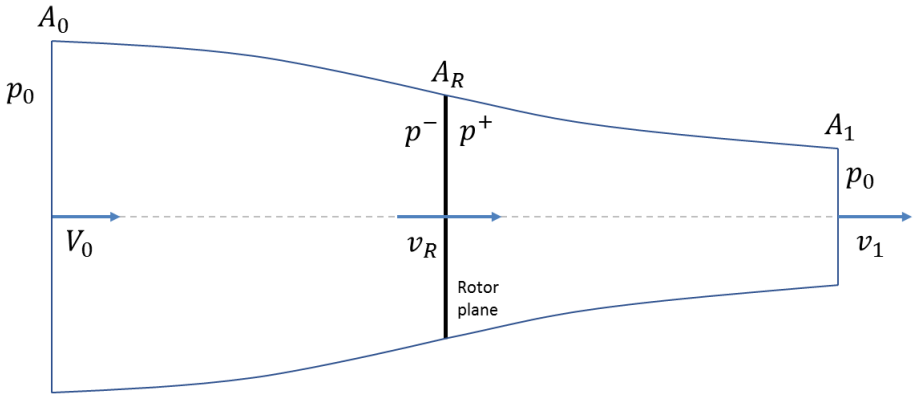

Figure 1.4: Control volume studied in the axial momentum theory.

The conservation of mass yields the following expression for the mass flow rate:

$$\dot{m} = \int \rho v \mathrm{d}A = \rho V_0 A_0 = \rho v_R A_R = \rho v_1 A_1. \tag{1.6}$$

The conservation of momentum over the control volume gives

$$\int_{\partial \mathcal{V}_c} \rho \boldsymbol{v}(\boldsymbol{v} \cdot \boldsymbol{n}) \mathrm{d}A = \boldsymbol{T} - \int_{\partial \mathcal{V}_c} p \boldsymbol{n} \mathrm{d}A, \tag{1.7}$$

where $\partial \mathcal{V}_c$ is the boundary surface of the control volume, $\boldsymbol{n}$ is the outward pointing normal, and $\boldsymbol{T}$ is the thrust of the propeller. By considering a cylinder with a very large radius centered around the propeller, it can be shown that the pressure contribution to the control volume is equal to zero [28]. Projecting equation (1.7) in the axial direction yields:

$$T = \int_{A_1} \rho v_1^2 \mathrm{d}A - \int_{A_0} \rho V_0^2 \mathrm{d}A. \tag{1.8}$$

Since the velocity fields are assumed constant by section, and using the mass conservation from equation (1.6), the previous expression can be further simplified to

$$T = \rho v_R A_R (v_1 - V_0). \tag{1.9}$$

Applying Bernoulli's equation on both sides of the propeller leads to the expression of the pressure increase across the disk

$$\Delta p = \frac{1}{2} \rho (v_1^2 - V_0^2). \tag{1.10}$$

Then by writing the thrust as the resultant of the pressure forces on the disk and by equalizing with the expression from equation (1.9), the fundamental result of the axial momentum theory is obtained:

$$v_R = \frac{1}{2}(v_1 + V_0). \tag{1.11}$$

This equation shows that the velocity in the rotor plane is the average between the upstream and downstream velocities, or, equivalently, that the velocity induced in the propeller plane is half the one induced in the ultimate wake.

In most cases however, the velocity fields vary with the radius, so it is interesting to rather study an annular control volume located between r and $r + dr$, shown in figure 1.5.

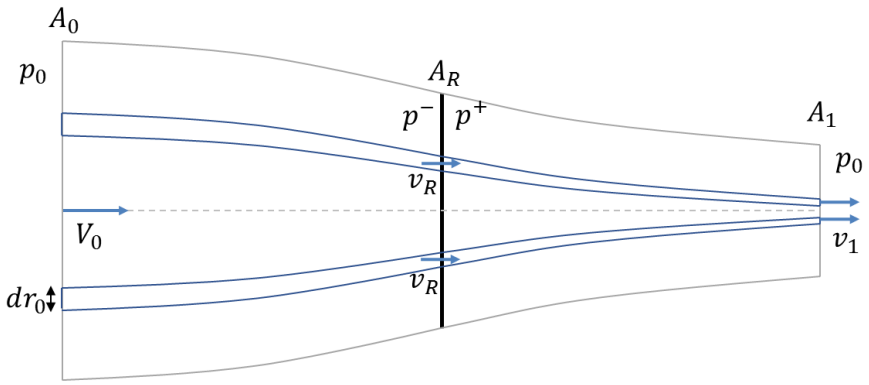

Figure 1.5: Annular control volume studied in the axial momentum theory.

On this annular control volume, the momentum equation (1.7) projected in the axial direction gives:

$$\rho v_1^2 \mathrm{d}A_1 - \rho V_0^2 \mathrm{d}A_0 = \mathrm{d}T - \overbrace{\left[-p_0 A_0 + p_0 A_1 + \int_{A_l} p\boldsymbol{n}\cdot\boldsymbol{e_x}\mathrm{d}A\right]}^{\Pi}, \tag{1.12}$$

where A_l is the lateral surface of the annular control volume. However in this case, contrary to the study of the whole stream tube, it has not been established that the pressure contribution Π is equal to zero. According to Glauert [28], neglecting this term comes down to neglecting the mutual interference between the annular elements, and he assumes that it is in general very small. Verifying this hypothesis requires a fully resolved pressure field, which can only be obtained by CFD. Sørensen and Mikkelsen [92] analyzed this by running CFD-actuator disk computations on a wind turbine under constant radial load. They found that $\Pi/\mathrm{d}T$ is indeed very small on the majority of the blade, but reaches up to 15% at the blade tip. They also show that the value of $\Pi/\mathrm{d}T$ rises with rotor load. The approximation $\Pi = 0$ is nevertheless always used due to the impossibility of computing Π with a simple momentum model. With this approximation, equations (1.9) and (1.10) can be derived in the same way for the annular volume, leading to equation (1.11) that is this time valid for velocities that vary with the radius, and to the infinitesimal expression of the thrust:

$$\mathrm{d}T = \rho v_R \mathrm{d}A_R (v_1 - V_0). \tag{1.13}$$

This model was initially used to maximize efficiency for propeller design or power for turbines. However it does not model the rotational flow, so it ignores the energy lost in the swirl. The general momentum theory, which adds on to the axial momentum theory to include rotational flow, is presented hereafter.

1.2.2 The general momentum theory

This section presents the General Momentum Theory (GMT) as described by Glauert [28]. Other variations exist which make slightly different approximations. For more information, the reader is invited to refer to Sørensen's textbook in which he first derives the general equations with no approximation, and then details the different simplifications by also analyzing their validity [90].

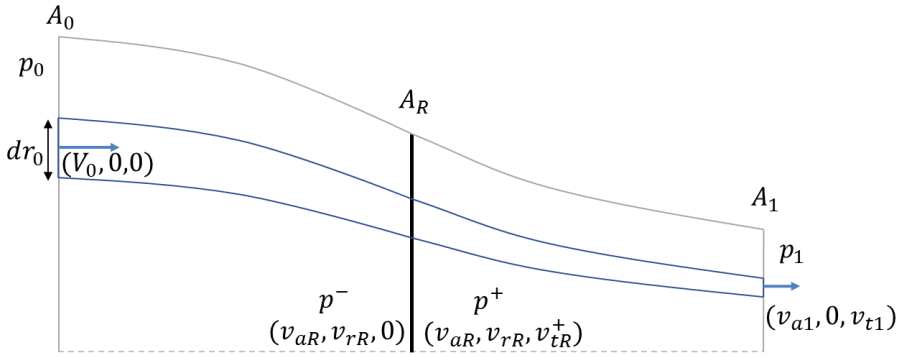

Figure 1.6: Section of the annular control volume studied in the general momentum theory.

A diagram of the studied control volume is shown in figure 1.6. Continuity of axial velocity v_{aR} and radial velocity v_{rR} is assumed across the disk. However, tangential velocity is assumed to jump from 0 just before the disk to v_{tR}^+ just after the disk. The value of the tangential velocity at the disk, v_{tR}, will be investigated at the end of the section. In the ultimate wake, the contraction is stabilized so the radial velocity is zero. Furthermore, contrary to the axial momentum theory, p_1 is a priori not strictly equal to p_0 because of the swirl in the slipstream. Indeed, it can be shown that in the wake the radial pressure gradient compensates the centrifugal force, such that

$$\frac{\partial p_1}{\partial r_1} = \rho \frac{v_{t1}^2}{r_1}. \tag{1.14}$$

Applying Bernoulli's equation before and after the propeller gives the two following expressions of the stagnation pressure:

$$H_0 = p_0 + \frac{1}{2}\rho V_0^2 = p^- + \frac{1}{2}\rho(v_{aR}^2 + v_{rR}^2), \tag{1.15}$$

$$H_1 = p^+ + \frac{1}{2}\rho(v_{aR}^2 + v_{rR}^2 + v_{tR}^{+2}) = p_1 + \frac{1}{2}\rho(v_{a1}^2 + v_{t1}^2). \tag{1.16}$$

Subtracting the two expressions gives

$$H_1 - H_0 = (p^+ - p^-) + \frac{1}{2}\rho v_{tR}^{+2} \tag{1.17}$$

and

$$p_0 - p_1 = \frac{1}{2}\rho(v_{a1}^2 - V_0^2) + \frac{1}{2}\rho(v_{t1}^2 - v_{tR}^{+2}). \tag{1.18}$$

Expressions of the thrust and torque can be deducted from the momentum equations. For the thrust, the same approximation is made as for the axial momentum theory by neglecting the contribution of the pressure forces on the lateral boundaries of the control volume:

$$\mathrm{d}T = \rho v_{a1}(v_{a1} - V_0)\mathrm{d}A_1 - (p_0 - p_1)\mathrm{d}A_1. \tag{1.19}$$

The torque is equal to the angular momentum imparted to the fluid:

$$\mathrm{d}Q = \rho r v_{a1} v_{tR}^{+}\mathrm{d}A_R. \tag{1.20}$$

Glauert then proceeds to manipulate these equations to obtain a system of 5 equations for 6 variables: v_{a1}, v_{aR}, v_{t1}, v_t^+, $\frac{\mathrm{d}T}{\mathrm{d}r}$, and $\frac{\mathrm{d}Q}{\mathrm{d}r}$. This system will not be detailed as it is still relatively complex and Glauert proceeds to make some simplifications. These rely on the fact that at a given radius, the swirl in the wake is small relative to the blade's rotation velocity. The two approximations are

$$p_0 \approx p_1 \tag{1.21}$$

and

$$p^+ - p^- \approx H_1 - H_0. \tag{1.22}$$

This further simplifies the expression of the thrust to recover the one of the annular axial momentum theory from equation (1.13). Under these assumptions, equation (1.11), which links the axial velocities from the rotor plane and the wake is also still valid. By defining the axial and tangential induction factors as

$$a_a = \frac{v_{aR} - V_0}{V_0} \tag{1.23}$$

and

$$a_t = \frac{v_{tR}^{+}}{2\Omega r}, \tag{1.24}$$

the final expressions for thrust and torque can then be written:

$$\frac{\mathrm{d}T}{\mathrm{d}r} = 4\pi r \rho V_0^2 a_a(1 + a_a) \tag{1.25}$$

$$\frac{\mathrm{d}Q}{\mathrm{d}r} = 4\pi r^3 \rho V_0 \Omega a_t(1 + a_a). \tag{1.26}$$

Furthermore, writing the Bernoulli equation in the relative frame across the propeller gives another formulation of the pressure jump across the disk:

$$\begin{aligned}(p^+ - p^-) &= \frac{1}{2}\rho(2v_{tR}^{+}\Omega r - v_{tR}^{+2}) \\ &= 2\rho\Omega^2(1 - a_t)a_t r^2\end{aligned} \tag{1.27}$$

By writing the thrust as equal to the pressure forces across the disk, and writing the equality with equation (1.25), a simple equation linking a and a' is obtained:

$$(1+a_a)a_a = \frac{\Omega^2 r^2}{V_0^2}(1-a_t)a_t. \tag{1.28}$$

Equations (1.25), (1.26), and (1.28) thus form a system such that if the radial distribution of a or a' is given, $\frac{\mathrm{d}T}{\mathrm{d}r}$ and $\frac{\mathrm{d}Q}{\mathrm{d}r}$ can be deduced immediately. This system can for example be used to draw general conclusions on propeller efficiency and energy loss.

However this simplified system eliminates v_{a1} and v_{t1}, the velocities in the wake, and doesn't involve v_{tR}, the tangential velocity in the rotor plane. v_{a1} can be obtained using equation (1.11) which is still valid in this case, as discussed previously. Rewritten with the general notations, it gives:

$$v_{aR} = \frac{1}{2}(v_{a1} + V_0). \tag{1.29}$$

In his textbook, Glauert proposes an elegant demonstration based on vortex theory to simply link v_{tR}, v_{tR}^+, and v_{t1}. His proof is detailed hereafter, as this important result will be used in the rest of the dissertation.

Glauert's starting point is that to compute the induced velocities, it is too complex to consider the full system of helical vortex sheets which constitute the propeller slipstream. He thus makes the assumption that the propeller has an infinite number of blades and that the vorticity is distributed on the whole fluid and not only located on a few vortex sheets.

For a blade with constant circulation, the vortex system is then a cylindrical vortex sheet located at the boundary of the slipstream. As illustrated in figure 1.7, instead of stacked helical vortex lines, the vorticity of the sheet can be seen as:

1. an infinite number of vortex rings that contribute only to the axial acceleration of the flow, noted R

2. an infinite number of vortex lines that contribute to the tangential acceleration of the flow, noted LL

3. an axial vortex AA

In the general case where the circulation varies along the blade, the trailing vortex system is composed of an infinite number of the previous one located at each radius. The full vortex system is made up of this trailing vortex system and of bound vortices located in the propeller plane on an infinite number of radial lines at every azimuth.

Because the fluid upstream of the propeller is irrotational, the tangential velocity immediately in front of the propeller must be zero by conservation of circulation. The bound vortices created by the lift of each blade section creates a rotational motion, causing an angular velocity $-\omega$ immediately in front and $+\omega$ immediately behind the propeller. The trailing vortex system must cancel out the component $-\omega$ upstream of the propeller, so it can be concluded that it generates an angular velocity of $+\omega$. Adding the contributions of the bound and trailing vortices leads to an angular velocity of $+\omega$ in the propeller plane, and $+2\omega$ immediately behind the propeller. Furthermore by conservation of circulation, $v_{tR}^+ r^+$ remains constant in the wake. Thus by neglecting

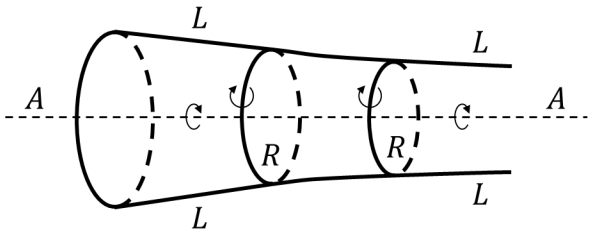

Figure 1.7: Simplified vortex system, adapted from [28].

the contraction of the slipstream, the tangential velocity remains constant in the wake, leading to a simple link between v_{tR}, v_{tR}^+, and v_{t1}:

$$v_{tR} = \frac{1}{2} v_{tR}^+ = \frac{1}{2} v_{t1}. \tag{1.30}$$

This expression explains in particular the $\frac{1}{2}$ factor in the definition of a_t in equation (1.24).

1.2.3 The blade element theory

The general momentum theory presented previously can compute propeller loads distributions if given a radial velocity profile in the wake, but it cannot estimate any propeller performance from scratch, nor can it account for specific propeller geometry. As a result, this tool is not fitted for propeller design. This can only be achieved with an approach that relies on the specifics of blade aerodynamics. This was first proposed by Froude [26] and Drzewiecki [21] at the end of the 19$^{\text{th}}$ century. The idea behind this theory is to consider a propeller blade as a stack of n_r independent elements of length dr. Each element is characterized by its airfoil shape, chord length c, and local pitch angle β. When the blade rotates, each element sees a relative inflow vector $\boldsymbol{v_{rel}} = (v_a, v_t)$. This vector makes an angle ϕ with the propeller plane such that:

$$\tan\phi = \frac{v_a}{v_t} \tag{1.31}$$

The effective angle of attack α on the section thus is:

$$\alpha = \beta - \phi \tag{1.32}$$

A diagram of the blade section is represented on figure 1.8.

The aerodynamic forces of each section can be expressed by introducing its lift and drag coefficients C_l and C_d:

$$\mathrm{d}L = \frac{1}{2} \rho c v_{rel}^2 C_l \mathrm{d}r \tag{1.33}$$

$$\mathrm{d}D = \frac{1}{2} \rho c v_{rel}^2 C_d \mathrm{d}r \tag{1.34}$$

These forces can then be projected to obtain the thrust and torque distributions along the blades:

$$\frac{\mathrm{d}T}{\mathrm{d}r} = \frac{1}{2} \rho c v_{rel}^2 C_n \tag{1.35}$$

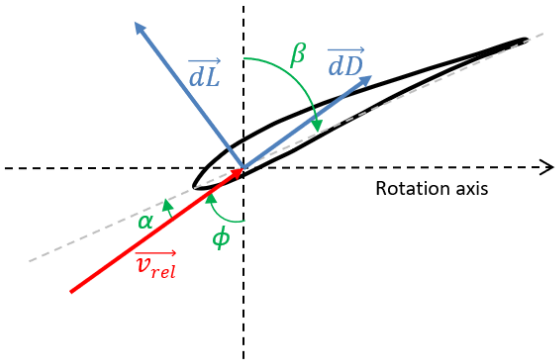

Figure 1.8: Diagram of a blade section in the Blade Element Theory.

$$\frac{\mathrm{d}Q}{\mathrm{d}r} = \frac{1}{2}\rho r c v_{rel}^2 C_t \tag{1.36}$$

$$\text{where} \quad C_n = C_l\cos\phi - C_d\sin\phi \quad \text{and} \quad C_t = C_l\sin\phi + C_d\cos\phi \tag{1.37}$$

The blade element theory (BET) relies on the assumption that the loads on a given blade element are the same as the ones on a portion of length $\mathrm{d}r$ of an infinite wing of the same airfoil and same chord length as the blade element, translating in the air at a velocity v_{rel} and angle of incidence α. The lift and drag coefficients of infinite wings have the advantage of being much more convenient to obtain than for rotating blade sections. Furthermore these coefficients can be stored in databases as functions of airfoil shape, incidence angle α, Mach number M, and Reynolds number Re. The blade element theory implies that all blade elements are independent from one another and neglects radial flow, as $\boldsymbol{v_{rel}}$ only accounts for axial and tangential velocities.

In summary, the blade element theory is able to compute individual blade loads if given the velocity field seen by each section. This differs from the momentum theory, which only predicts the propeller loading averaged over a revolution. As a results, this method can predict blade loads under any conditions, even non-axisymmetric flow, if provided with the correct velocity fields in the propeller plane. The accuracy of the model comes from the velocities used to compute the angle of attack. In his original model, Drzewiecki [21] uses the blade's kinematic velocities, $\boldsymbol{v_{rel}} = (V_0, \Omega r)$. However, this neglects the velocities induced by the circulation created on the blade, which leads to overestimated angles of attack, especially near blade tips. In 1935, Glauert proposed to rather use the general momentum theory to obtain the induced velocities in the propeller plane [28].

1.2.4 The blade element momentum theory

The method relies on both the general momentum theory and the blade element approach. The theories are compatible in the sense that they both consider independent radial subdivisions of the propeller disk, but since the momentum theory considers an axysymmetric averaged flow, the results of the BEMT can therefore only give averaged loads. It is thus assumed that all blades have the same loading, and that the propeller radial thrust and torque distributions can be obtained by multiplying equations (1.35) and (1.36) by the number of blades N_b:

$$\frac{\mathrm{d}T}{\mathrm{d}r} = \frac{1}{2}N_b\rho c v_{rel}^2 C_n \tag{1.38}$$

$$\frac{\mathrm{d}Q}{\mathrm{d}r} = \frac{1}{2} N_b \rho r c v_{rel}^2 C_t. \tag{1.39}$$

In this case, the velocities considered account for the induced velocities computed using the GMT. $\boldsymbol{v_{rel}}$ can be thus be written as the sum of the kinematic velocity $(V_0, \Omega r)$ and the induced velocity vector $\boldsymbol{w_i}$, or in an equivalent manner, $\boldsymbol{v_{rel}} = (V_0(1+a_a), \Omega r(1-a_t))$ by considering the definitions of a_a and a_t. A diagram of the blade section is represented in figure 1.9.

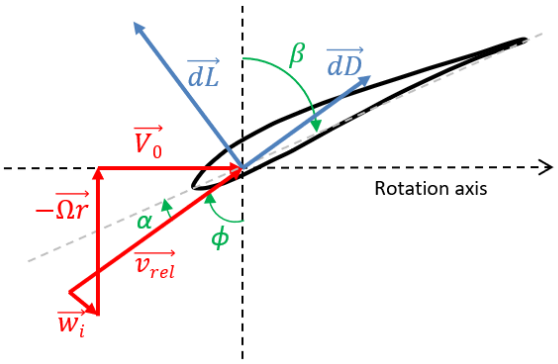

Figure 1.9: Diagram of a blade section in the Blade Element Momentum Theory.

The flow angle ϕ is computed using equation (1.31), which in this case gives:

$$\phi = \tan^{-1}\left(\frac{V_0(1+a_a)}{\Omega r\,(1-a_t)}\right). \tag{1.40}$$

By equalizing the propeller thrust and torque using the BET (equations (1.38) and (1.39)) and the GMT (equations (1.25) and (1.26)) and simplifying, two fundamental relations are obtained:

$$a_a = \frac{1}{\frac{4\sin^2\phi}{\sigma C_n} - 1} \tag{1.41}$$

$$a_t = \frac{1}{\frac{4\sin\phi\cos\phi}{\sigma C_t} + 1} \tag{1.42}$$

where $\sigma = \dfrac{N_b c}{2\pi r}$ is the local solidity.

These equations can be used to estimate propeller performance using the following procedure:

1. Divide the propeller into radial elements so that the propeller geometry is correctly discretized. Steps 2 through 6 must be conducted for all elements.
2. Initialize a_a and a_t
3. Compute ϕ using equation (1.40) and α with equation (1.32).
4. Compute the local Mach number M, Reynolds number Re, and use α and v_{rel} to interpolate in tabulated 2D polars of the airfoils of the blade to obtain C_l and C_d.

5. Compute C_n and C_t using equation (1.37).
6. Compute a_a and a_t with equations (1.41) and (1.42)
7. Loop back to step 3 until convergence.
8. Compute $\frac{\mathrm{d}T}{\mathrm{d}r}$ and $\frac{\mathrm{d}Q}{\mathrm{d}r}$ using equations (1.38) and (1.39).
9. Integrate $\frac{\mathrm{d}T}{\mathrm{d}r}$ and $\frac{\mathrm{d}Q}{\mathrm{d}r}$ to obtain the propeller thrust T and power P.

The BEMT relies on the real blade geometry, and is thus the first low-order model capable of propeller design. It is still widely used today, especially in pre-design steps. However it does rely on some restrictive assumptions, including the fact that the rotor should be lightly loaded or that the rotors are assumed to have an infinite number of blades, because it relies on the momentum theory. Some corrections have been developed since then to broaden the range of application of this tool.

1.2.5 Tip-loss corrections

The equations that form the momentum theory are derived under the assumption of azimuthally independent stream tubes, thus making them applicable only to rotors with an infinite number of blades. As explained previously, such a rotor has a cylindrical slip stream and no individual blade tip vortices are formed. In practice however, the finite number of blades does create a system of tip vortices which modify the induced velocities seen by the blades, especially in the tip area.

Another way to interpret this is to view the velocities computed by the momentum theory as the time-averaged flow field of a rotor with a finite number of blades. The effect of the individual blades on the flow is smeared across the whole disk which, in particular, hides the effect of the tip vortices. This is illustrated in Figure 1.10 which shows the axial and tangential velocity fields in the propeller plane computed by BEMT and by a lifting line simulation. The lifting line method models the blades individually, and thus also represents the tip vortices through a free wake model. The blade positions in the lifting line computation are shown in black lines. It is clear that the velocities on these lines differ from the ones on a radial line in the BEMT computation. As a result, the blade loads computed by each method also differ. The BEMT equations must therefore be modified to account for the effect of the tip vortices.

In his dissertation [3], Betz showed that a lightly loaded rotor with a finite number of blades is of ideal efficiency if the circulation along the blades is such that the vortex sheets have a rigid helical motion. This implies in particular that there is no wake contraction. With these assumptions, Prandtl derived an analytic expression of the circulation along the propeller blades [3, 68]. The idea behind his reasoning is that in a rigid wake, the vortex sheets are impermeable and the flow must go around them. Outside of the wake, the velocity is constant and equal to the free flow velocity. A slice of this wake is shown on Figure 1.11a, where the straight lines represent the helical vortex sheets and the other lines represent the streamlines of the flow. By neglecting the swirl, the wake can be further approximated to vertical lines, as shown in Figure 1.11b. For rotors with an infinite number of blades, the rigid sheets are infinitely close to one another so the flow is not distorted, as illustrated in Figure 1.11c. It thus becomes clear that reducing the number of blades modifies the circulation around the blades, especially near the tip.

Prandtl focused on the geometry from figure 1.11b and solved the flow around the segments using a Joukowski conformal mapping. He then computed the circulation distribution Γ_b along

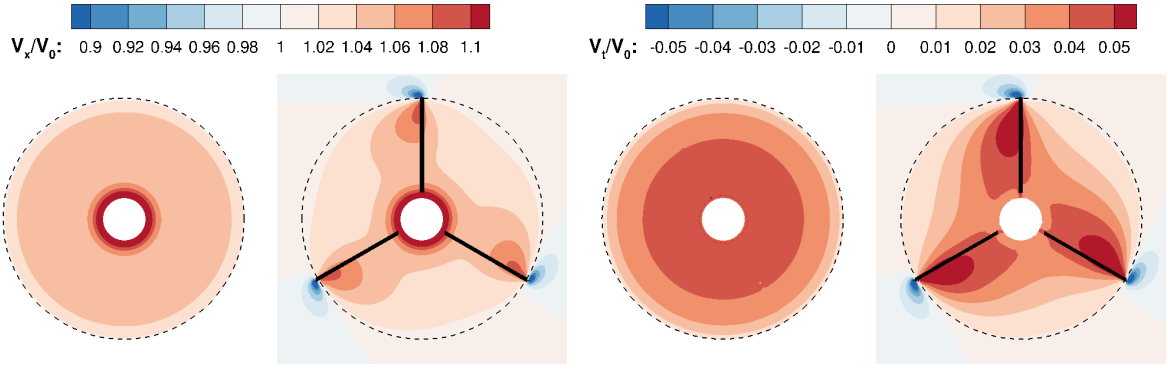

(a) v_x/V_0 - BEMT (b) v_x/V_0 - Lifting line (c) v_t/V_0 - BEMT (d) v_t/V_0 - Lifting line

Figure 1.10: Velocity fields in rotor plane from BEMT and lifting-line computations.

each segment from the velocity potential. The final expression depends in particular on δ_s, the spacing between the vortex sheets. δ_s can tend to 0 to obtain the circulation Γ_∞ along the blades for a rotor with an infinite number of blades. The well-known tip-loss correction from Prandtl, F, corresponds to the ratio of the circulation distribution along the blade of a rotor with a finite number of blades and infinite number of blades:

$$F = \frac{N_b \Gamma_b}{\Gamma_\infty} = \frac{2}{\pi} \arccos\left[\exp\left(-\frac{\pi(R-r)}{\delta_s}\right)\right] \tag{1.43}$$

With a few approximations to estimate δ_s, the final expression is:

$$F_P = \frac{2}{\pi} \arccos\left[\exp\left(-\frac{N_b}{2}\sqrt{1+\lambda^2}\left(1-\frac{r}{R}\right)\right)\right] \tag{1.44}$$

where $\lambda = \dfrac{\Omega R}{V_0}$ is the tip-speed ratio.The full demonstration is presented in recent literature [7, 73, 90] with more detail than in Prandtl's original work.

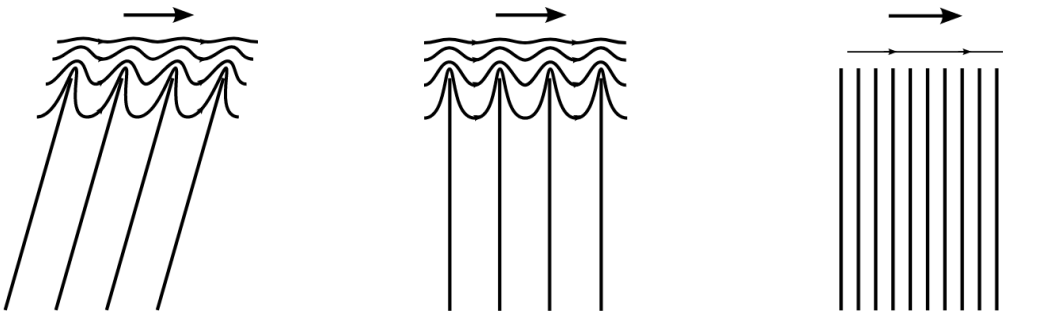

(a) Real wake, finite number of blades (b) Approximate wake, finite number of blades (c) Approximate wake, infinite number of blades

Figure 1.11: Prandtl's interpretation of a propeller wake, from [7].

With the same assumptions as Prandtl, Glauert [28] also looks into a correction factor but by focusing on induced velocities rather than on circulation. Indeed, he defines the correction factor

as the ratio of $\overline{a}$ the average induction factor between two vortex sheets, and a_B the induction factor along the vortex sheet:

$$F = \frac{\overline{a}}{a_B} \tag{1.45}$$

This reasoning leads to an expression that is identical to Prandtl's factor from equation (1.43). This shows the equivalence between the two perceptions of the correction factors that was mentioned at the beginning of this subsection: either as a correction for rotors with a finite number of blades, or as a way to recover non-averaged velocities from an azimuthaly-averaged computation. Glauert then proceeds to make a few approximations to make the correction compatible with BEMT. The final expression, F_G, is still widely used in BEMT codes today:

$$F_G = \frac{2}{\pi}\arccos\left[\exp\left(-\frac{N_b(R-r)}{2r\sin\phi}\right)\right] \tag{1.46}$$

where ϕ is the local flow angle defined in equation (1.31).

From here, a challenge still remains to correctly implement this correction in the BEMT equations. Glauert argues that equations (1.38) and (1.39) should be multiplied by F_G, which is compatible with the interpretation of F as a ratio of circulation in which case equations (1.35) and (1.36) should be divided by F_G.

$$\frac{\mathrm{d}T}{\mathrm{d}r} = 4\pi r\rho U_0^2 F_G a_a(1+a_a) \tag{1.47}$$

$$\frac{\mathrm{d}Q}{\mathrm{d}r} = 4\pi r^3\rho U_0\Omega F_G a_t(1+a_a) \tag{1.48}$$

Similarly to what was done in section 1.2.4, the corrected axial and tangential induction factors can be derived:

$$a_a = \frac{1}{\frac{4F_G\sin^2\phi}{\sigma C_n} - 1} \tag{1.49}$$

$$a_t = \frac{1}{\frac{4F_G\sin\phi\cos\phi}{\sigma C_t} + 1} \tag{1.50}$$

Yet this implementation of the tip-correction in BEMT is not without criticism. The resulting equations (1.47) and (1.48) show that the mass flow, which corresponds to the $(1+a_a)$ factor, is not corrected. Some researchers argue that it should be, as modifying the induced velocities should in theory also modify the mass flow. Wilson and Lissaman [103] propose to multiply all induction factors from equation (1.38) by F, thus also correcting the mass flow, but they do not modify the mass flow in the torque equation. This leads to an induced velocity that is not orthogonal with the kinematic blade velocity, which is a condition that is implied by equation (1.28). De Vries attempts to fix this by also correcting the mass flow in the torque equation [16].

Shen et al. [82] show that these formulations still lead to inconsistencies at the blade tips because they lead to non-zero loads at $r = R$. They argue that this is non-physical, as in reality the pressure equalization between the pressure and suction sides of the tip of the blade should lead to a

loading equal to zero. They propose to use the work of De Vries [16] and to add another correction implemented by multiplying the coefficients C_n and C_t with the factor F_S in equations (1.38) and (1.39),

$$F_S = \frac{2}{\pi}\arccos\left[\exp\left(-g_S\frac{N_b(R-r)}{2r\sin\phi}\right)\right] \tag{1.51}$$

where

$$g_S = \exp\left(-0.125\left(\frac{N_b\Omega R}{U_\infty} - 21\right)\right) + 0.1 \tag{1.52}$$

and the constants were calibrated on experimental results of wind turbine cases at different tip speed ratios. This factor F_S is approximately equal to 1 on the whole blade, except at the very tip where it rapidly drops to 0 to model the pressure equalization.

To sum up on tip-loss corrections, because the actuator-disk like methods only model rotors with an infinite number of blades, they must be corrected to accurately predict the performance of real rotors. It is important to understand the complexity of what is asked of a tip-loss correction, which is basically to analytically recover the flow along the blade from a time-averaged solution. Under some precise and restrictive assumptions, it is possible to link the circulation along the blades of a rotor with an infinite number of blades to the one of a rotor with a finite number of blades. However, even if given such a link, the correct way to integrate a correction in a BEMT model is not straightforward and still debated today. On top of that, inconsistencies due to the nature of the assumptions made in BEMT models ask for complementary corrections, such as the one by Shen et al. [82].

1.3 Steady CFD-actuator disk models

The actuator-disk models presented previously are able to predict rotor performance and wake velocities for a very low cost, which makes them efficient design tools. However, they were derived under specific assumptions that are not necessarily met in modern aeronautics applications. For instance, open fans and regional propellers are highly loaded, making the contraction of the wake non-negligible. Furthermore, the models were initially made for uniform axial inflow, and even if corrections exist to account for incidence, they are generally unfit to study interaction effects.

CFD-RANS is a great tool to evaluate interaction effects because it can solve a wide variety of geometries with accuracy and limited assumptions. Yet the cost of full blade-resolved CFD can quickly become prohibitive, especially during the design phase. A solution is to replace the rotors with steady actuator disks in CFD computations. This idea originated in the 1970s to limit computational costs and mesh complexity. Many CFD-Actuator Disks (CFD-AD) models exist in literature and each has its specific features. The models studied in this thesis rely on blade-based approaches, i.e. models that compute blade loads using the blade-element theory. In this section, the most common practices are classified depending on how the propeller loads are computed and how they are accounted for in the CFD computation. Furthermore, depending on how the propeller loads are computed, they sometimes necessitate tip-loss corrections for the same reasons as the analytical actuator disk models. Finally, the end of the section presents an overview of body-force models that are commonly used in turbomachinery applications, which do not use the blade element theory, to put the other models into perspective.

1.3.1 Rotor loading computation

This section focuses on the computation of the rotor loads. The way the loads can be accounted for in the CFD computation will be detailed in the next section. The first CFD-actuator disk computations were run using prescribed disk loading. In 1977, Schetz and Favin [77] used an axisymmetric CFD-AD method to model a propeller pushing a submarine. In their computation the disk load is prescribed, the total thrust being obtained from tests in isolated configuration and its radial distribution estimated to maximize the loading at 70% of the blade radius. Initially their model only included axial acceleration. The modeling of the swirl was added in 1979, but still using prescribed loads [78]. Their study was able to evaluate the effect of the propeller on the submarine boundary layer, but it was limited by the restrictive one-way coupling. In 1992, Sørensen and Myken proposed a similar model to simulate a wind turbine with a prescribed elliptic loading [93].

Most fully-coupled blade-based models rely on the blade element theory to compute the loads. Rajagopalan and Lim were the first to implement such a coupling between CFD and BET [71] in a 2D simulation. They propose to model the rotor as a line discretized in the radial direction like in the BET. They extract local velocities from the CFD computation on each point of this line and to use them to fuel the BET analyses, using

$$\boldsymbol{v_{rel}} = (v_a^{CFD}, v_t^{CFD} - \Omega r). \tag{1.53}$$

A diagram of a blade section for a CFD-BET model is shown figure in 1.12.

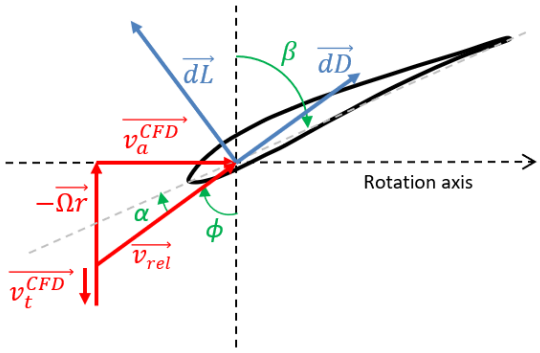

Figure 1.12: Diagram of a blade section in a CFD-BET computation.

The strength of this approach comes from the fact that the induced velocities are solved, and not modeled as for the BEMT. In particular, this makes it possible to overcome a number of constraints, such as neglecting wake contraction. Using the same equations from section 1.2.3, Rajagopalan and Lim compute an angle of attack for each section and use tabulated 2D airfoil data to compute the axial and tangential disk loadings. Their study focuses on a helicopter rotor in hover, so the computation is axisymmetric. In 1995 Sørensen and Kock develop a similar 2D model for wind turbine simulations [91].

In 1993, Rajagopalan and Mathur [72] modeled a helicopter rotor in forward flight and were thus required to make adjustments to their original model to allow non-axisymmetric loading. This was done by discretizing the rotor disk in a number n_θ of azimuthal lines, each one split in a few elements like in the 2D approach. A BET analysis is then conducted at every point of this

discretized disk using the local velocity at each of these points. This yields the axial and tangential forces exerted on each blade element

$$\begin{cases} f_a(r,\theta) = \frac{1}{2}\rho c(r) v_{rel}(r,\theta)^2 C_n(r,\theta) dr \\ f_t(r,\theta) = \frac{1}{2}\rho c(r) v_{rel}(r,\theta)^2 C_t(r,\theta) dr, \end{cases} , \tag{1.54}$$

where the radial and tangential dependencies have been added for the sake of clarity. In this equation, C_n and C_t are computed using equation (1.37) from lift and drag coefficients interpolated from tabulated airfoil polars. It is important to note that as for the BET, no radial velocity is considered in this model and radial loads are neglected. The loads of each element can then be projected into the Cartesian frame, and a scaling factor is applied to recover the correct time-averaged local rotor loads:

$$\boldsymbol{f}(x,y,z) = \frac{N_b}{n_\theta}(f_x, f_y, f_z). \tag{1.55}$$

The model is time averaged because the rotor load is distributed on a whole disk, but not azimuthally averaged, in the sense that the disk loading does account for local perturbations. As a result this 3D approach is well suited to study interaction effects, and in 1995 Zori and Rajagopalan [107] use it to estimate rotor-airframe interactions in forward flight. Since then many 3D applications of similar CFD-BET models where made in different domains.

For the methods that rely on the blade element theory and 2D airfoil polars, a tip-loss correction is necessary for the same reasons detailed in section 1.2.5 for BEMT. The implementation of these corrections for CFD-BET computations are detailed in section 1.3.3. Furthermore, in many aeronautical applications, the radial flow on the blades is non-negligible and the blade sections can hardly be considered as independent from one another, thus challenging the BET assumptions. As a result, some authors developed variants of the classical CFD-BET models that are more suited for these types of applications.

Schollenberger and Lutz [80] compare the use of 2D, 2.5D and 3D airfoil polars in an actuator disk model to simulate a two-blade propeller. The 2D airfoil polars correspond to the classical approach, where the airfoil polars are obtained by means of 2D RANS simulations of the different airfoils that constitute the blade. The database is made for each airfoil by varying the incidence angle and the free-flow Mach number (or often the Reynolds number in wind turbine applications). The 3D polars are made by using 3D RANS to solve the flow around an isolated fully resolved blade in the relative frame with periodic side boundary conditions, and are thus much more expensive that the 2D approach. However they include the radial flow, blade-to-blade effects, and the tip vortices. Computations are made by varying the blade advance ratio to modify the angle of attack of the different sections. The 2.5D airfoil polars correspond to an approach in between the 2D and 3D methods. The idea is to divide the blade into a few blade portions of radial length $\Delta r = 0.02R$. The blade portions are simulated in 3D RANS in the relative frame, using periodic boundary conditions on the lateral sides of the domain, and symmetry boundary conditions above and below the blade portion. The three different approaches to compute the airfoil polars are summarized in figure 1.13.

The benefits of the 2.5D approach are that the inertia effects are included in the polar because of the rotation of the section. Radial flow is also somewhat allowed even if very limited compared to the full 3D approach because of the symmetry boundary conditions. Furthermore

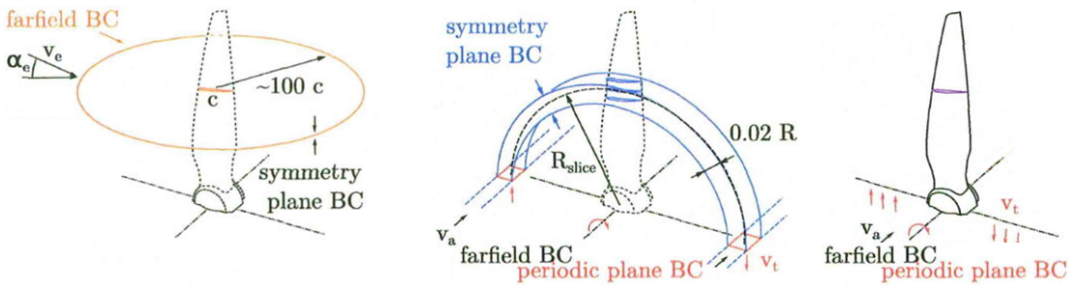

(a) 2D (b) 2.5D (c) 3D

Figure 1.13: Airfoil polar extraction methods, adapted from [80].

due to the periodic side conditions, this data base includes the blade-to-blade effects between the airfoils, which is neglected in the 2D approach. While negligible for propellers with few blades, blade-to-blade effects are expected to have major effects on the section loads for propellers with a large number of blades. For the same reason as for the 2D airfoil polars, the 2.5D method still requires a tip-loss correction.

Because the 2.5D and 3D polars include more physical phenomena than those in 2D, they therefore require less additional empirical corrections (for rotational blade-to-blade and tip effects). However, the major drawback of the 2.5D and 3D methods is that they require the estimation of the angle of attack on the blade sections. Schollenberger and Lutz use a technique by Johansen and Sørensen [37] which consist in averaging the flow in an annular slice upstream and downstream the blade section, and assuming that the velocity needed to compute the angle of attack on the blade is the linear interpolation between the two averages. However the solution depends on the size of the annular sections and on their distance to the blade. This last part was studied by Schollenberger et al. [79] who concluded that the slices should be placed $0.5c$ from the rotor plane in order for their CFD-AD model to give the best blade loading predictions, but this conclusion could depend on rotor geometry and inflow conditions. Other methods exist to estimate the angle of attack on blade sections, and some do not rely on calibrations. Shen et al. propose a method based on the estimation of the blade's bound circulation [81]. Valentin and Bernardos compare the stagnation point location of blade sections to tabulated 2D airfoil polars to recover the local angle of attack [100]. However to the author's knowledge these methods have yet to be applied to compute 2.5D or 3D airfoil databases to be used for BET computations.

Yet, the gains in fidelity offered by 2.5D or 3D airfoil databases are obtained at the cost of flexibility. The computed database is specific to a blade geometry, a blade count, and a blade pitch angle. If any propeller changes are to be made, the databases need to be computed again. As a result, using 2.5D or 3D airfoil databases may be particularly useful for highly loaded propellers once the rotor geometry is set, but may be unsuitable for pre-design studies.

1.3.2 Loading distribution in CFD

Once the loads have been calculated, they can be accounted for in the CFD computation in one of two ways. By analogy with the infinitely thin analytical actuator disk theory, the rotor load can be implemented using an in-fluid boundary condition. Fejtek and Roberts [23] used BET as in the previous

section to obtain the axial and tangential load distributions on a tilt-rotor modeled by and actuator disk. The thrust is then used to compute a local pressure jump across the disk, and the torque to obtain the discontinuity in tangential velocity with equation (1.20). Details on the conversion of these two quantities into fluxes between the cells on both sides of the boundary conditions can be found in the work of Yu [104] with the assumption of subsonic and incompressible flow across the disk. Since then, implementations compatible with compressible flow have also been developed [70].

The rotor loads can also be included in the CFD computations using volumic source terms, also called body forces, in the momentum and energy equations of the Navier-Stokes equations. They are accounted for on the right hand side of the equations, as shown below:

$$\frac{\partial \rho \mathbf{u}}{\partial t} + \nabla \cdot \left(\rho \mathbf{u}\mathbf{u}\right) = -\nabla p + \nabla \cdot \boldsymbol{\tau} + \mathbf{s_M} \tag{1.56}$$

$$\frac{\partial \rho E}{\partial t} + \nabla \cdot \left(\rho h_t \mathbf{u}\right) = \nabla \cdot (\boldsymbol{\tau} \cdot \mathbf{u}) - \nabla \cdot \mathbf{q} + s_E \tag{1.57}$$

where $\boldsymbol{\tau}$ is the viscous stress tensor, E the specific total energy, h_t the specific total enthalpy, and $\mathbf{q}$ is the heat flux vector. $\mathbf{s_M}$ and s_E are the source terms that model the effect of the rotor on the flow. $\mathbf{s_M}$ accelerates the flow in the momentum equations. It is expressed in N.m^{-3} and it is computed from the local rotor force $\boldsymbol{f}(x, y, z)$ in N and a volumic distribution function. s_E, expressed in W.m^{-3}, adds the associated work in the energy equation. It is rarely detailed in literature, and the most common formulations are studied in sections 3.4 and 4.1.4.

Using body forces was for example the approach taken by Whitfield and Jameson [102] to model the effect of a propeller on a transonic wing. However they do not explicitly show how the propeller loads $\boldsymbol{f}$ are converted into the bod-force field $\boldsymbol{s_M}$. Sørensen and Myken [93] use a dirac function to apply the rotor loads on a single layer of grid cells in the rotor disk. This is the source term approach that comes the closest to the analytical infinitely thin actuator disk. Their expression of the momentum source term is

$$\boldsymbol{s_M} = \boldsymbol{f}\, \delta(r \leq R, x = x_R), \tag{1.58}$$

where δ is the Dirac function and x_R the axial coordinate of the rotor plane.

In 2004, Le Chuiton compared different implementations of CFD-AD models using boundary conditions and source terms [43]. The models were tested on an interaction case between a helicopter rotor and fuselage. Le Chuiton found that the models implemented as boundary conditions had robustness and stability issues, especially in forward flight. His source term model consistently led to converged computations despite slight oscillations on the side of the disk in some cases, which are most likely due to the numerical schemes. To avoid these oscillations, Sørensen et al. [95] used a 3D gaussian kernel g_{3D} to distribute the loads

$$g_{3D}(x, y, z) = \frac{1}{\epsilon^3 \pi^{3/2}} \exp\left(-\frac{x^2 + y^2 + z^2}{\epsilon^2}\right), \tag{1.59}$$

leading to the expression of the body force field:

$$\boldsymbol{s_M} = \boldsymbol{f} * g_{3D}. \tag{1.60}$$

In this expression, $*$ is the convolution product. Since $\boldsymbol{f}$ is discrete because only defined on the $n_r.n_\theta$ points that discretize the rotor disk, $\boldsymbol{s_M}$ can be re-written as a double sum:

$$\boldsymbol{s_M}(x,y,z) = \sum_{j=1}^{n_\theta}\sum_{i=1}^{n_r} \boldsymbol{f_{ij}}\, g_{3D}\left(x-x_{ij}, y-y_{ij}, z-z_{ij}\right). \tag{1.61}$$

This formulation illustrates that each rotor disk element located at (x_{ij}, y_{ij}, z_{ij}) induces a load $\boldsymbol{f_{ij}}$ distributed around it using and isotropic 3D Gaussian function. The body-force field at a given mesh point is the sum of the contribution of each rotor disk element distributed by the means of its own Gaussian kernel. This projection method thus smears the rotor load in the proximity of the disk, which avoids sudden discontinuities, especially at the tip.

Since then, there has been significant progress in numerical methods and more stable boundary condition actuator disks have been developed. These models are still used currently [60, 80], but the source term approach is nowadays more popular because of the flexibility if offers. Whereas the rotor plane must coincide with the grid points to define the boundary conditions, the source terms can be defined in the cells located in the general area of the propeller, thus smoothing the discontinuities and putting less constraints on the mesh. In particular the 3D Gaussian kernel is still widely used today because it is the simplest to implement. Indeed, it can be used on any meshes with any type of coordinate systems, and for rotors that don't necessarily match the mesh structure such as coned rotors [57]. Furthermore, it is also convenient to use for comparison with the actuator line model, which classically distributes the source terms using the same 3D Gaussian kernel [48, 94].

However this kernel distributes sources above the physical radius of the blade. It also distorts the radial loading, as a section located at a given radius will have an influence not only at its own radius, but also slightly lower and higher due to the smearing. As a result, a 1D Gaussian is also used to smear the source terms in the axial direction and not the others in order to limit distortion [89, 106]:

$$g_{1D}(x) = \frac{1}{\epsilon\pi^{1/2}} \exp\left(-\frac{x^2}{\epsilon^2}\right). \tag{1.62}$$

By analogy with the turbomachinery methods that will be presented in section 1.3.4, which in essence compute source terms that vary with the axial coordinate, Ortun [62] used an axial distribution function to better model the physics of the flow on a real airfoil. He projected the loads in the CFD computation with a Weibull function to concentrate the sources at the quarter chord of the blade, instead of the middle, as when using a Gaussian distribution. Furthermore he only distributed the sources in the volume swept by the blade. This model was used to study the installation effects of a propeller on a wing. The same setup was used by Reboul et al. [75] for aeroacoustic predictions of an eVTOL rotor.

1.3.3 Tip-loss corrections

Since CFD solves a time-averaged flow, the sampled velocities used for the BET computations must be corrected to account for the effect of the tip vortices if using 2D (or 2.5D) airfoil polars. Section 1.2.5 showed that tip-loss corrections are complex and that even in BEMT, the way they should be applied is not clear. The same is true for CFD-AD computations, as will be shown in this section.

For aeronautical applications the interaction effects are often studied for a given thrust. Depending on the engine technology, this is achieved by adapting the rotation speed or the blade

pitch angle. The use of a tip-loss correction can thus be circumvented by trimming the propeller slightly more than if a correction was applied [62]. However this lowers the loads on the whole blade and not only the tip, leading to a distortion of the radial distribution compared to blade-resolved computations.

Sørensen and Kock were the first to attempt to apply a tip correction to a CFD-AD computation [91]. They propose to introduce the tip-loss factor in the computation of the source term by dividing the lift coefficient by F_G. This comes down to replacing $\boldsymbol{s_M}$ by $\boldsymbol{s_M}/F_G$ in equation (1.56). Indeed, in their model only the lift is used to compute the source terms. However no correction is made on the sampled velocities, and the loads computed by the BET are directly used as the real propeller loads, only the source terms are affected by the correction. The idea behind this is that because the CFD computation is time averaged, the loads computed by BET should be corrected to become time averaged before they are included in the CFD computation. However it can be argued that since the velocities are time averaged, the BET loads are already time-averaged.

Mikkelsen et al. [57] and Mikkelsen [58] propose to correct the velocities sampled in CFD before the BET analysis. Indeed since the tip vortices modify the induced velocities and thus the angle of attack on the real blade, it makes sense to correct them before computing the propeller loads. The corrections of the induction factors they used are shown below, where the signs have been changed from turbine to propeller convention:

$$a_a^{cor} = \frac{a_a^{CFD}}{F_G(a_a^{CFD}+1) - a_a^{CFD}} \tag{1.63}$$

$$a_t^{cor} = \frac{a_t^{CFD}}{F_G(1-a_t^{CFD}) + a_t^{CFD}} \tag{1.64}$$

where

$$\begin{cases} a_a^{CFD} = \dfrac{\left(v_x^{CFD} - v_0\right)}{v_0} \\ a_t^{CFD} = \dfrac{v_t^{CFD}}{\Omega r} \end{cases} . \tag{1.65}$$

The corrected axial and tangential velocities can be computed from the corrected induction factors, leading to a corrected angle of attack which is used to compute the BET loads. These loads are then directly injected in the CFD computation as source terms. This approach is physically coherent as the CFD computation thus gives the time-averaged flow induced by the corrected loads, i.e. the loads the propeller would have seen if the flow had not been time-averaged. However equations (1.63) and (1.64) were derived under the assumption that

$$\frac{1+a_a^{CFD}}{a_a^{CFD}} = \frac{4\sin^2\phi}{\sigma C_n} = \frac{1+a_a^{cor}}{F_G a_a^{cor}} \quad \text{and} \quad \frac{1-a_t^{CFD}}{a_t^{CFD}} = \frac{4\sin\phi\cos\phi}{\sigma C_t} = \frac{1-a_t^{cor}}{F_G a_t^{cor}}, \tag{1.66}$$

which was not thoroughly proven.

Shen et al. [83] later corrected this by replacing equations (1.63) and (1.64) with Glauert's interpretation of the tip-loss factor, i.e. as a ratio of induction factors, leading to the simple relations:

$$\begin{cases} a_a^{cor} = \dfrac{a_a^{CFD}}{F_G} \\ a_t^{cor} = \dfrac{a_t^{CFD}}{F_G} \end{cases} . \tag{1.67}$$

Equation (1.65) can then be inverted to obtain the corrected axial and tangential velocity fields from the sampled velocities:

$$\begin{cases} v_x^{cor} = \dfrac{\left(v_x^{CFD} - v_0\right)}{F_G} + v_0 \\ v_t^{cor} = \dfrac{v_t^{CFD}}{F_G} \end{cases} . \tag{1.68}$$

The local flow angle ϕ can then be computed from equation (1.53) and (1.32). Shen et al. explain that because the correction factor F_G depends on ϕ, an iterative procedure must be used on equations (1.46) and (1.68) to reach convergence.

Zhong et al. [106] compared these three implementations of the Glauert tip-loss for CFD-BET computations. They found that on wind-turbine cases, it is the implementation of Shen et al. that best matched experimental results. They also observed that this implementation led to very similar results as BEMT computation using the Glauert correction. However all three implementations still overestimated the loads at the tip, leading them to use another correction they initially developed for BEMT [105], yielding better results.

In their publication, Shen et al. [83] also add their correction for BEMT, as presented at the end of section 1.2.5, which relies on the correction factor F_S. For CFD-BET simulations, this is done in the same way as for BEMT computations by multiplying the coefficients C_n and C_t by F_S in equation (1.54).

1.3.4 Differences with turbomachinery body-force models

For the body-force models presented in this section, the starting point was to compute the blade loads on isolated lines using the blade element theory, and then to distribute the loads in the azimuthal direction to model a time-averaged flow (blade-based models). Some body-force rotor modeling methods proceed the other way around, by first considering a blade row in interaction instead of isolated blades. It is then more natural to model the blade loads from the azimuthally averaged flow (averaged-based models). These models are most often used in turbomachinery applications, where there are many blades in a row and thus the blades are in strong interaction.

Marble [46] proposed the first axisymmetric representation of a blade row, where he demonstrated how the effects of the blades can be represented as forces, with the assumption of an infinite number of blades spread along the row. By analyzing the energy source term, he distinguished two components of the blade force, one normal to the relative flow direction responsible for the flow turning, and one parallel to the relative flow in the opposite direction to model the losses (and thus the entropy rise). Although this type of model is not based on 2D airfoil polars, it is interesting to note that the way the forces are decomposed in two components are similar to the lift and drag, but in the local sense, as the relative flow direction changes along the blade.

Just like for the blade-based models presented previously, the averaged-based branch also has a wide variety of models, depending on how the forces are modeled. Only a short summary is presented here to give a novel perspective compared to what is usually seen in external rotor modeling. Extensive reviews are proposed in Thollet's and Dosne's PhD theses [20, 96]. As the normal force can be viewed as a way to turn the flow, one approach is to incrementally adjust its magnitude until the flow matches a prescribed direction, which usually is the airfoil camber line corrected by an empirical deviation model. This is the approach adopted in most throughflow models [85] but also in recent body force models (Guo and Hu [29] for instance). Another approach is to model the local force acting on blade portions (i.e. the mesh cell discretizing the blade

zone), but without resorting to using airfoil polars. This can for instance be done using thin airfoil theory [31, 97] applied using a local relative angle of attack at each position in the blade domain. Many formulations also exist for the parallel force, from computing a source term from an imposed overall entropy variation, using empirical correlations, to modeling the drag force with a local empirical formula.

Since these models most often do not rely on any outside database (tabulated airfoil polars, or even blade geometry details), their accuracy relies either on empirical correlations or on coefficients that must be calibrated using blade-resolved computations. Each model has its own specific features and is more or less robust to a change of operating conditions compared to the calibration point.

In the previous subsections, it was explained that the blade-based models compute line loads using the blade element theory and then distribute them in the axial direction with a projection function. It is interesting to note that one class of the models discussed above is usually implemented in a comparable way: when the overall loss is imposed, the axial distribution of the parallel force is left to the choice of the user. Most of the time, a linear loss increase is imposed [29] but more elaborate streamwise distribution have proposed to mimic the actual flow distribution [64]. On the other hand, for models that are formulated locally [31, 97] the streamwise distribution is directly connected to the local geometry, with a possible additional impact of the calibration.

Finally, additional corrections also exist for these models, from corrections to better account for compressibility, to ones that account for the acceleration of the flow linked to the reduction of the cross-section because of the high number of blades. These developments have not yet been applied to blade-based models to compute highly loaded propellers. However, Kiffer et al. [38] did use an averaged-based model initially developed for turbomachinery to model an eight-bladed propeller. They also proposed a calibration method so that once calibrated, the model does not rely on any geometry parameter, which is very convenient in a context were sharing intellectual property between engine and aircraft manufacturers is increasingly difficult.

1.4 The actuator line model

The downside of actuator disk methods is that, even for CFD-AD simulations, it only models the time-averaged flow. It is still a very effective tool because it allows to conduct steady simulations where blade-resolved computations necessitate unsteady, and therefore expensive, simulations. When studying interaction effects, CFD-AD computations can give valuable information: the average flow, the average loads on the airframe, the blade loads for each azimuth, and other important data such as the propeller in-plane loads. However they cannot account for the unsteady phenomena, like the interactions between airframe and blade tip vortices.

The advantage of the blade-based models presented in sections 1.3.1 to 1.3.3 is that they are not necessarily linked to a time average. Indeed, the BET models individual blades and can be directly used in a CFD computation without averaging. This is the basis of the actuator line model presented in this section.

1.4.1 The original model

The original actuator line model was developed by Sørensen and Shen in 2002 [94]. It consists in computing the blade loads with the BET and distributing them in a CFD computation as source terms in the close proximity of each blade positions, rather that to smear them over a disk like for

actuator disk models. The position of these actuator lines rotate at each time-step, creating a helical wake behind the rotor.

There are as many actuator lines as rotor blades, and they are located along each blade's quarter chord line. Each line is split in n_r elements, as for the blade element theory. The CFD velocities are evaluated at each actuator line point and a local relative velocity $\boldsymbol{v_{rel}}$ is computed using equation (1.53). The axial and tangential loads exerted on each element is computed using tabulated 2D airfoil polars as in the CFD-BET approach using equation (1.54). These loads are then projected into the Cartesian frame, and this time no scaling factor is needed because $n_\theta = N_b$:

$$\boldsymbol{f}(x, y, z) = (f_x, f_y, f_z). \tag{1.69}$$

However by proceeding in this manner, the loads are concentrated on N_b lines which would lead to unstable computations if the loads were injected in CFD as is. In their publication, Sørensen and Shen thus distribute the loads using a 3D Gaussian kernel, just as for the steady CFD-BET computations. The source terms are computed using equation (1.60), which can be expressed with sums like in equation (1.61) by replacing n_θ with N_b:

$$\boldsymbol{s_M}(x, y, z) = \sum_{j=1}^{N_b} \sum_{i=1}^{n_r} \boldsymbol{f_{ij}}\, g_{3D}\left(x - x_{ij}, y - y_{ij}, z - z_{ij}\right). \tag{1.70}$$

A slice and an iso-surface of a source term field from an actuator line simulation of a three-bladed propeller is shown figure 1.14. In Sørensen and Shen's model, the source terms were accounted for in the Navier-Stokes equations formulated in vorticity-velocity variables. Mikkelsen was the first to use the actuator line model with the velocity-pressure formulation [58] as in equation (1.56) but for incompressible flow.

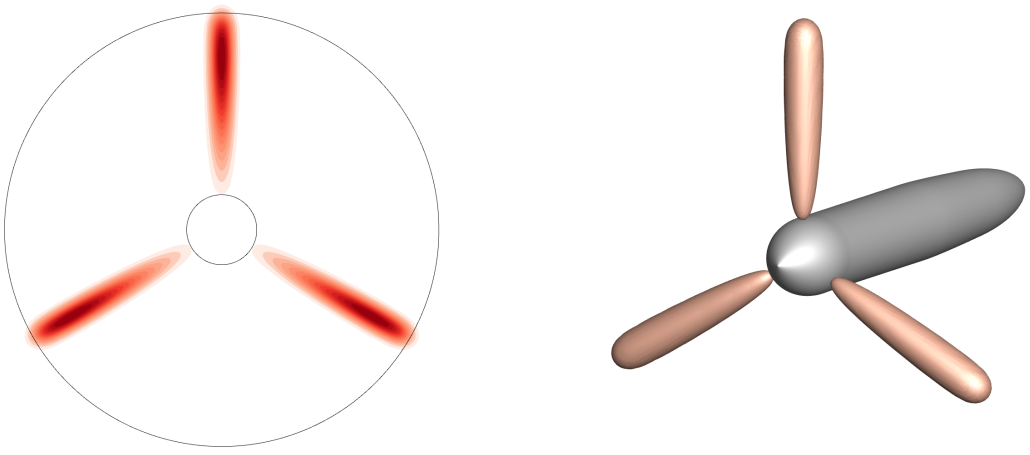

(a) Slice of source terms field

(b) Iso-surface of source terms field

Figure 1.14: Actuator line simulation of a three-bladed propeller.

At each time step, the actuator lines are rotated, so the sampled velocities change and so does the source term field. Sørensen and Shen show that their model is capable of accurately predicting the power of a wind turbine and give a good representation of the wake. They even show that their model is insensitive to mesh refinement. However no information is given in regards to the

best practices. The value of their Gaussian parameter ϵ is not disclosed, and no detail is given into how the velocities are sampled. As a result the effects of both these parameters were the focus of many of the studies that followed.

1.4.2 The Gaussian parameter ϵ

In the actuator line model, the Gaussian parameter ϵ is an adjustable parameter that must be chosen by the user. Sørensen and Shen give no specific detail into its effect and give no recommendations [94]. Studies around its optimal value were abundantly published in the years following the release of the original article. This section summarizes the implications of this choice and the answers provided by literature over the years.

1.4.2.1 Effect on model stability

The first impact of the choice of ϵ is on the stability of the computation. If the Gaussian distribution is too tight around the actuator line, i.e. if ϵ is too small, it makes sense for the computation to have difficulties converging. Indeed, concentrated source terms lead to strong gradients, which are not well accounted for by numerical schemes. This was first studied in 2003 by Mikkelsen [58], who found that too small an ϵ creates oscillations near the tip of the actuator lines. He observed that these oscillations could be partly avoided by using a value of ϵ between dl and $4dl$, where dl corresponds to the average mesh cell dimension. Troldborg [98, 99] also witnessed radial oscillations of the induction factors for $\epsilon = 1.5dl$, and recommended using at least

$$\epsilon \geq 2dl. \tag{1.71}$$

This lower limit for ϵ to avoid oscillations was also validated by Martinez-Tossas et al. [48, 49], and is nowadays a widely accepted criteria. Still, this value does seem to depend on the CFD solver and numerical schemes, as Shives and Crawford [84] find that oscillations can be avoided for $\epsilon \geq 4dl$ and Stokkermans et al. [89] for $\epsilon \geq dl$.

1.4.2.2 Effect on model accuracy

Apart from its effect on the stability of the computation, the Gaussian parameter ϵ plays a major role in the accuracy of the actuator line model, on both its capacities to predict the rotor loads and the flowfield. Ivanell et al. [33] show that to improve wake fidelity, ϵ should be chosen as small as possible. Indeed, Troldborg [99] explains that if ϵ is too large, the tip vortices are significantly smeared by the Gaussian function. This leads to smaller induced velocities at the tip of the actuator lines, and thus to overestimated tip loads. It is thus important to find a compromise between model stability and accuracy. In line with what was presented previously to ensure computation stability, Troldborg proposes

$$\epsilon \approx 2dl \tag{1.72}$$

as a good compromise.

To better represent the physics of the flow, Shives and Crawford [84] suggest to vary ϵ along the blade span by linking it to the local blade chord length c. By comparing the wake velocities from actuator line computations and analytical references on an infinite wing, a constantly loaded

wing, and an elliptical wing, they find that the best results are obtained for $\frac{1}{8} \leq \frac{\epsilon}{c} \leq \frac{1}{4}$. Since then, ϵ is widely linked to the chord length, and the general guideline

$$\frac{\epsilon}{c} \approx \frac{1}{4} \tag{1.73}$$

is the most often used, in particular for its physical interpretation: when using an isotropic 3D Gaussian projection kernel, 99.5% of the source terms are distributed in a ball of a diameter equal to the local airfoil chord. By combining the criteria from equations (1.71) and (1.73), a general criteria for cell size is obtained:

$$dl \leq \frac{c}{8}. \tag{1.74}$$

This is actually quite restrictive and shows that actuator line meshes should be significantly refined in the propeller area in order to obtain optimal results. This is discussed further in section 1.4.5 dedicated to tip corrections for the actuator line model.

Jha et al. [35] show that using a constant ϵ along the actuator line constantly overestimates the blade loads. They propose to use a constant value of ϵ/c^*, where c^* is a local equivalent chord length computed by reducing the blade to an elliptical wing. They find that such a radial distribution of ϵ yields better results than a direct variation with the local chord, and much better results than a constant value of ϵ.

1.4.3 Source term distribution

Similarly to the CFD-AD models, different types of projection kernels are used in the actuator line model. This section presents the most common practices found in literature.

1.4.3.1 3D Gaussian

The 3D Gaussian function initially used in 2002 by Sørensen and Shen [94] was the only one used until around 2015, and it is still widely used today. This can be explained by the simplicity of its implementation on all types of meshes and coordinate systems, and by its robustness. Indeed, it smears the loads in all directions so it limits discontinuities and thus instabilities. Furthermore, each mesh point is overlapped by different Gaussians, which also tends to stabilize the computation.

However this method is not without downsides. First, it distributes source terms above the geometrical limits of the blade, as can be seen at the blade tips in figure 1.14a. This smears the tip vortex above the blade radius, which leads to reduced induced velocities at the tip of the actuator line. This amplifies the overestimation of the loads, mentioned in section 1.4.2.2, which are inherent to actuator line modeling. Second, the Gaussian distribution kernel also induces a distortion of the blade radial loading. Indeed, because an actuator line element influences the flow above and below it, the integral of the sources at a given radius is not equal to the blade load at this exact radius. This is particularly true where the load gradients vary rapidly.

Merabet and Laurendeau [54] propose to fix the first issue by truncating the Gaussian function for $r \leq R_h$ and $r \geq R$ and then re-normalizing by integrating g_{tr} over the computational volume $\mathcal{V}$:

$$\boldsymbol{s_M}(x,y,z) = \sum_{j=1}^{N_b} \sum_{i=1}^{n_r} \boldsymbol{f_{ij}} \frac{1}{Z_{ij}} g_{tr}\left(x - x_{ij}, y - y_{ij}, z - z_{ij}\right), \tag{1.75}$$

where

$$g_{tr} = \begin{cases} g_{3D}, & \text{if } R_h \leq r \leq R \\ 0, & \text{otherwise} \end{cases} \quad \text{and } Z_{ij} = \int_{\mathcal{V}} g_{tr} d\mathcal{V}. \tag{1.76}$$

However this distorts the radial loads even more by increasing the quantity of sources terms at the actuator line tips. Yet this may have a beneficial side effect, as it increases the induced velocities at the tips and thus tends to limit the loading overestimation.

1.4.3.2 2D Gaussian

The two limitations of the 3D Gaussian kernel described above can fixed by using a 2D Gaussian kernel instead. This is initially suggested by Mikkelsen [58] who distributes the source terms on planes normal to the actuator line. The implementation is however more complicated than for a 3D Gaussian function and is likely more costly in computing resources. Furthermore the discontinuity in sources at $r = R$ leads to stronger oscillations than for a 3D Gaussian distribution. Ivanell et al. [33] use the same kind of model based on Mikkelsen's recommendations. Jha et Schmitz [36] develop and validate a similar model, named Actuator Curve Embedding (ACE).

Stokkermans et al. [89] also use a 2D Gaussian to distribute the sources around the actuator line, but in a plane that is curved with a constant radius instead of normal to the line:

$$g_{2D}(r,\theta,x) = \frac{1}{\epsilon^2 \pi} \exp\left(-\frac{x^2 + r^2\theta^2}{\epsilon^2}\right). \tag{1.77}$$

In particular, this method ensures a better continuity when the actuator line rotates between time steps. In this publication, which is one of the few that study a propeller, Stokkermans et al. show that with this setup, the actuator line model with prescribed loads is able to replicate the time accurate pressure distribution on a wing placed behind the rotor computed by a full blade-resolved CFD simulation. However, they only conducted a one-way coupled computation.

A diagram of the distribution methods presented so far is shown in figure 1.15.

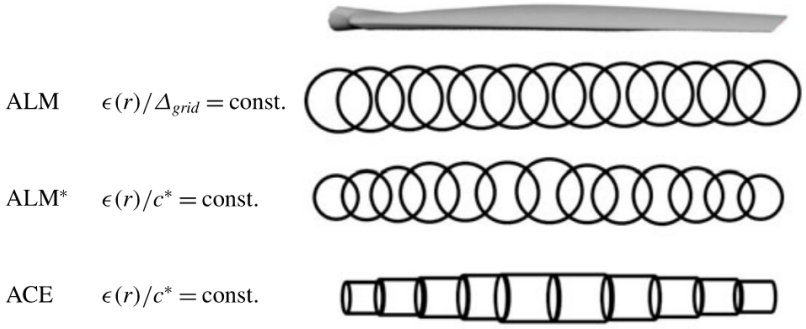

Figure 1.15: Summary of different source term distribution techniques for the actuator line model, from [36].

1.4.3.3 Non-isotropic distributions

Whether 2D or 3D, the Gaussians functions presented previously are isotropic, meaning that the ϵ parameter is the same in all the directions of distribution. In 2015 Mittal et al. [59] were the

first to implement a non-isotropic 3D Gaussian kernel by using a different parameter in the radial direction. In the actuator line model, the radial discretization needs to be chosen in accordance with local mesh size and ϵ. Indeed, there needs to be sufficient overlap between the Gaussians of two consecutive points in order to avoid drops in source term distribution along the blade, which would lead to oscillations in the flow. More detail can be found in the work of Mikkelsen [58] and Martinez-Tossas et al. [48]. This consideration leads to an additional constraint on ϵ, or on the actuator line discretization which can lead to a significant increase in computation time. Mittal et al. thus propose to use a different ϵ in the radial direction than in the other two. However they find that this leads to a model that is less robust than other practices. In any case, their work has paved the way for the use of non-isotropic Gaussian functions.

Since then, non-isotropic Gaussian functions are rather used to try to better model the flow physics. In 2009, Troldborg [98] explains that, ideally, the source terms should be distributed around each section's local chord and that they should model the pressure distribution on a real airfoil. However, at the time, this would have led to unreasonable computation times. In 2017, Martinez-Tossas et al. [50] show they obtain a better prediction of the flow field around a 2D airfoil if using an elliptical Gaussian kernel to distribute the source terms relative to the lift. Churchfield et al. [11] use three different Gaussian parameters in the chordwise, thicknesswise, and radial directions in order to shape the source terms like a real wind-turbine. Cormier et al. [12] and Schollenberger et al. [79] use a Gumbel function in the chordwise direction to concentrate the source terms near the front of the volume rather than at the middle with a Gaussian function, thus replicating the loading of a thin airfoil. The idea is similar to what was proposed by Ortun [62] with a Weibull function for his steady CFD-AD model.

In their publication, Cormier et al. [12] compare the effects of using an isotropic 3D Gaussian function, a non-isotropic 3D Gaussian function, and a combination of Gaussian and Gumbel functions. For each type of distribution the same blade loading is prescribed so the differences in velocity fields only come from the different distributions. They use a fine mesh, with a cell size of $dl = c/10$ at the blade tip, so it can be assumed that all distribution methods are correctly discretized. They find that the distributions lead to no significant differences in the tip vortex structures. They explain this by the fact that the different methods all lead to an approximately equal distribution width at the blade tip region. At first glance, this is in contradiction with Churchfield et al. [11] who showed that using a non-isotropic 3D Gaussian function did lead to a better flow prediction than when using an isotropic 3D Gaussian function. However, in their publication, Churchfield et al. [11] used a fully coupled approach and did not use a prescribed loading like Cormier et al. [12]. This shows that for the actuator line model, the source term distribution and the velocity sampling are deeply related, and that conclusions drawn on a simulation with prescribed loads can prove to be irrelevant when applying a full coupling. In any case, this shows the importance of the velocity sampling step, which is described in the following section.

1.4.4 Velocity sampling

1.4.4.1 Point sampling

In their original actuator-line publication, Sørensen and Shen [94] give no detail into the way they sample the velocities used for the BET computation. In his PhD thesis, Mikkelsen [58] explains that the velocities are sampled on the actuator line points. In practice, this is done by linear interpolation between the actuator line point and the closest grid points.

Because these velocities are then used to compute an angle of attack which is assumed equivalent to the pitch angle of an airfoil in a 2D simulation, the sampled velocities should not include the effects of the bound circulation induced by the source terms. However, it should include the velocities induced by the tip vortices or any other object of the computation that creates interactions. In 2017 Martinez-Tossas et al. [50] showed that if the airfoil drag is neglected, sampling the velocities at the actuator line points, i.e. at the center of the isotropic Gaussian function, does indeed remove the contribution of the bound circulation. However, the drag force leads to a deceleration of the flow at the sampling point that has an influence on the computed angle of attack. They thus propose a correction of the sampled velocities to account for this effect on the drag.

1.4.4.2 Local average sampling

Sampling the velocities on the actuator line points leads to a model that can be both very dependent on the choice of the Gaussian parameter and unstable. This leads Mittal et al. [59] to explore other velocity sampling methods. For instance, they try to give each actuator line point the velocities averaged between its 7 or 21 closest neighbors, thus making the model more robust. However, this model is still very dependent of the ϵ parameter that is used.

Forsythe et al. [24] and Churchfield et al. [11] propose to compute a local velocity average weighted by the kernel g for each actuator line element, g being the same kernel used for the distribution of the source terms:

$$\boldsymbol{v_{ij}} = \int_{\mathcal{V}} \boldsymbol{v}\, g_{ij}\, d\mathcal{V}. \tag{1.78}$$

These velocities are then used for the BET analyses. The authors give an analytic proof in their work that under the assumptions of 2D steady incompressible flow, and by neglecting viscosity and drag, this weighted average is equal to what is considered as V_0 in the definition of the lift and drag coefficients. Under these assumptions, the result of the velocity sampling technique is independent of the source term distribution method, and in particular of the Gaussian parameter ϵ. However the authors warn that the assumptions are less valid at the tip of the blade where the radial variation of the flow is strong, thus challenging the 2D hypothesis. It could also be argued that a correction to account for the drag in the sampling process is still necessary, as the one proposed by Martinez-Tossas et al. [50]. Churchfield et al. show that this integral velocity sampling reduces oscillations and make the point that it is necessary when using distribution functions that are not centered on the actuator line, such as the Gumble function used by Cormier et al. [12].

This integral velocity sampling method is commonly used today, especially in the helicopter industry where the rotors are highly disturbed by strong interaction effects [45, 54].

1.4.4.3 Offset sampling

To avoid the instabilities linked to sampling the velocities in close proximity to the lines, some authors have proposed alternative solutions that consist in evaluating the velocities at an offset from the actuator line elements.

Weihing et al. [101] sample the velocity on a monitor point at some distance upstream of the actuator line element and then correct it iteratively by subtracting the induced velocity of the bound vortex by applying Biot-Savart's law. This method was initially developed by Shen et al. [81] to compute the angle of attack distribution on a full blade-resolved simulation.

Bühler et al. [8] compare this method with another that consists in averaging the velocities extracted on a circle centered on the actuator line element. They find that both methods are very similar except at the tip where the circle-average technique is sightly better than the other.

The advantage of both these methods is that they can also be applied to bladed-simulations, and could thus be used for actuator line models with 3D airfoil polars that were made using the same sampling techniques, thus avoiding coherency problems. However both methods a priori depend on the position of the monitor points and on the distribution functions, which requires additional calibration.

1.4.4.4 Comparison

Each sampling technique presented previously requires a specific implementation which can take time to develop. As a result, the different methods are rarely compared thoroughly. Despite this, Merabet and Laurendeau [53] made a parametric study of 5 sampling techniques in 2D cases. They compared:

- using the velocity from the closest cell to the actuator element,
- averaging the velocities of the N closest cells,
- estimating the velocity by bi-linear interpolation of the closest cells,
- using the integral velocity sampling method,
- correcting the velocity from a monitor point by subtracting the influence of the bound vortex.

They find that the integral velocity sampling method yields the lowest errors and is more consistent from one test case to another. Furthermore, it does not depend on calibration, and was found to be insensitive to the position of the actuator element compared to cell centers. This method is also the only one that is truly adapted to non-isotropic distributions.

Merabet and Laurendeau warn that regardless of the velocity sampling methods, the results get worse if:

- the mesh is coarse compared to the source term distribution function,
- the drag is significant, thus causing a global velocity deficit,
- viscous or compressibility effects are important.

1.4.5 Tip corrections

This section briefly explains why tip corrections for actuator line models are in some cases necessary, and presents just a few results from this active area of research. First, it is important to understand that the physics behind the tip correction of the actuator line is drastically different from the tip-loss correction of actuator disk models. As explained in section 1.2.5 and 1.3.3, the tip-loss correction was developed to account for the tip vortices when using the BET to compute loads from averaged velocities. In the actuator line model, the flow is not averaged and includes in particular the tip vortices. As a result, Prandtl's factor should not be used in an actuator line simulation.

That being said, we have explained that because the actuator line model relies on smearing functions, the induced velocities at each element are too small and the loads are thus overestimated, especially at the tip. To limit this phenomenon, very fine meshes can be used to correctly discretize

very concentrated smearing functions, i.e. Gaussian kernels with a small value of ϵ compared to the local chord length c. However in most cases, this leads to unreasonably large meshes which defeats the point of the method.

As a result, researchers have tried to understand how to modify the method for coarser meshes. In 2020, Dağ and Sørensen [15] (initially Dağ in 2017 in his PhD thesis [14]) propose a correction known as a vortex-based smearing correction. They showed that the bound vortices created by the actuator line's 3D Gaussian kernel are Lamb-Oseen viscous vortices [42, 63] with a core radius of ϵ, which are centered on the actuator line elements. They argue that in classical lifting-line theory, the bound vortices are actually potential vortices with no viscous core. They thus explain that the smearing in the actuator line model creates a deficit of induced velocities in the bound vortex cores. This is illustrated in figure 1.16. Yet as explained in section 1.4.4, the velocity sampling method should not account for the bound vortices. However, Dağ and Sørensen conjecture that the trailing vortices have the same structure as the bound vortices. This was shown by Meyer Forsting et al. [55] for a rectangular wing. As a result the lack of induced velocities in the vortex core created by the smearing is also present in the wake, and these do have an influence on the actuator line velocities.

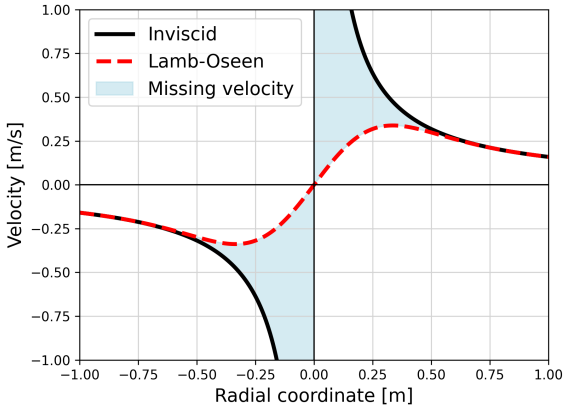

Figure 1.16: Velocity deficit in the vortex core due to smearing, adapted from [55].

Dağ and Sørensen propose to model the rotor wake with a prescribed geometry, and to use it to estimate the induced velocity that was removed by the smearing. This missing velocity is computed at each actuator line point, and is then added to the sampled velocity before computing the angle of attack. Because the velocity deficit is computed from the circulation on the actuator line, which itself depends on the corrected velocity, an iterative procedure is required. They show that with this correction, their actuator line model is capable of closely matching lifting line results on a straight wing and validated BEMT results on a rotor. Meyer Forsting et al. [55] use a similar model with a free wake approach. They show that their corrected actuator line model matches ideal lifting line results and that their non-corrected model matches lifting line with viscous core results, thus validating the model further. This model was recently linearized by Kleine et al. [39] to obtain a non-iterative correction.

Martinez-Tossas and Meneveau [51] developed a filtered lifting line theory with a Gaussian vorticity distribution, in a similar manner as Caprace et al. [10]. They use it to derive an analytical model to evaluate the velocity difference between the optimal Gaussian smearing parameter $\epsilon = c/4$

and bigger values. This model is then applied to actuator line computations of straight wings with various kernel sizes. The authors show that with this correction, the blade loads are independent of the Gaussian kernel, even for large values of ϵ.

However, these models only correct the induced velocities used during the BET computation. Evidently, they do not affect the resolution of the wake, the smearing of the vortices being inevitably linked to the size of the distribution kernel, as shown by Meyer Forsting et al. [56]. An accurate representation of the wake will always require tight kernels and fine meshes.

Conclusion

To summarize, this chapter first introduced basic definitions needed when studying propeller in axial and non-axial flow. Fundamental propeller modeling results were then recalled using actuator disk-like modeling. In particular, it was shown using the general momentum theory that the induced axial and tangential velocities in the far wake are twice those in the propeller plane. The blade element theory was introduced, which is used in both CFD-actuator disks and actuator line models to compute the propeller loads. It was shown that for CFD-actuator disks models, there is no clear consensus on how the source terms should be distributed in the computation. The correct way to implement tip-loss corrections in these computations is also not clear. For the actuator line model, the literature demonstrates that the model is very sensitive to the Gaussian smearing parameter ϵ. It should be chosen large enough to ensure computation stability, but as small as possible to maximize model accuracy. It was shown that the model often overestimates blade loads at the tip because of smeared tip vortices induced by the Gaussian projection function, and different source term distribution methods exist to limit the overshoot. Different velocity sampling techniques where also developed to try to reduce the dependency of the computation to ϵ.

This review was deemed to give sufficient background on the stakes surrounding each model to explain the choices made in chapters 3 and 4. These will focus on the development of models that best answer the issues presented previously.

Chapter 2

Test cases and numerical methods

This chapter first presents the configurations studied in the thesis. The propeller is the ONERA HAD-1 propeller, a three-bladed light propeller designed to operate at sea level. The geometry details of the propeller as well as the reasons behind its choice are explained. An installed configuration is also shown, which consists of a wing downstream of the propeller, to validate the ability of the body-force models to predict interaction effects. The setups for the finite volume computations are then described, including numerical methods and meshes used for the blade-resolved and body-force computations. The solver used for the lifting line computations is also presented. The methodology used to compute the tabulated 2D airfoils polars, on which rely both body-force methods and the lifting line model, is presented at the end of the chapter.

Contents

2.1 Geometries and operating points

2.1.1 Isolated propeller

2.1.1.1 Propeller description

The rotor studied throughout this dissertation is the ONERA HAD-1 propeller [62] shown in figure 2.1. It is a three-bladed light propeller created to be representative of a general aviation propeller. It was designed according to the minimum induced loss method of Adkins and Liebeck [1], for a tip Mach number equal to 0.5, a 1.6 meter diameter and a propeller thrust representative of the cruise condition of a general aviation aircraft with two propellers. In addition, the blade chord distribution obtained with the Adkins and Liebeck method was smoothed with the parameterization proposed by Borer et al. [6]. The blade's chord and twist distributions are shown in figure 2.2. Attention should be paid to the fact that the chord rapidly decreases near the tip of the blade. The blade's quarter chord line is straight, meaning that the sweep and dihedral angles are equal to zero. However, a sweep is induced at the leading edge because of the chord variation, especially at the tip.

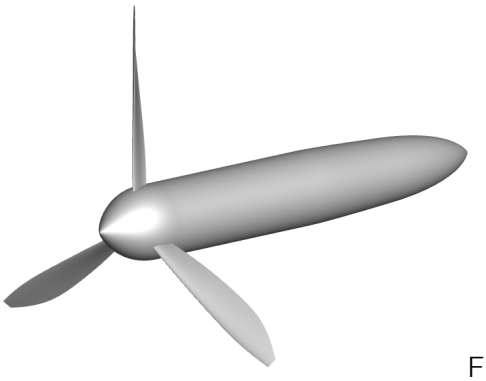

Figure 2.1: HAD-1 propeller.

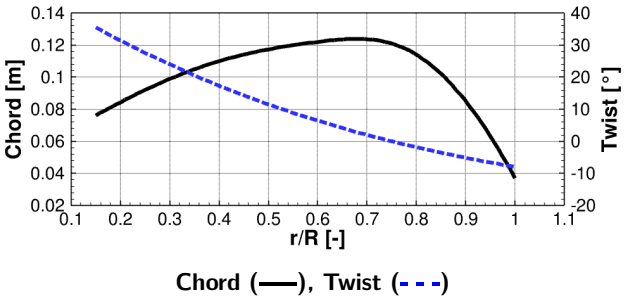

Figure 2.2: Chord and twist distributions of HAD-1 blade.

The blades are mounted on an axisymmetric hub. In the thesis two types of hub are used, either a closed nacelle or an infinitely long cylinder. Their shapes are shown in figure 2.3. The infinitely long cylinder is convenient for numerical reasons because it avoids flow separation at the back of the nacelle. However it is less realistic and cannot be used with a Chimera approach on a Cartesian background grid. The closed nacelle is sufficiently long to avoid differences on propeller performance between the two geometries, but the impact on the wake can be significant. For each study, the choice of the hub geometry will be given for the sake of clarity.

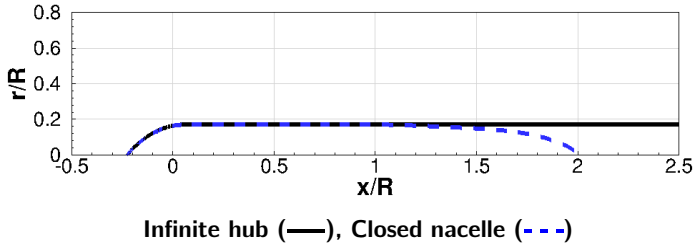

Figure 2.3: Hub geometries used in the study.

Table 2.1: Propeller geometry

Parameter	Value
Blade count N_b	3
Tip radius R, m	0.8
Hub-to-tip ratio	0.15

The propeller is designed to fly at sea-level altitude at an infinite Mach number M_0 of 0.3. The propeller's geometry and cruise operating point are summarized in tables 2.1 and 2.2. The reference radius for the blade pitch angle is chosen at 75% of the propeller's tip radius. The propeller's performance on the operating point is recapped in table 2.3. This data, shown here for reference, was computed by a CFD-RANS blade-resolved simulation, and will be detailed in the rest of the thesis.

Table 2.2: HAD-1 cruise operating point

Parameter	Value
Mach number M_0	0.3
Angle of incidence Θ, °	0
Air temperature T_0, K	288.15
Air density ρ_0, kg.m^{-3}	1.225
Rotation speed, rpm	2031
Advance ratio J	1.9
Blade pitch angle, °	45

Table 2.3: Performance at operating point

Parameter	Value
Thrust T, N	1390
Power P, kW	164.5
Thrust coefficient C_T	0.15
Power coefficient C_P	0.33
Efficiency η	0.862

2.1.1.2 Propeller characterization

The objective of the thesis is to develop and validate body-force models that rely on the blade element theory. The first step in the validation process is thus to study the models on a test case that satisfies the assumptions of the BET. It is essentially for this reason that the HAD-1 propeller was chosen as the validation case. With a helical tip Mach number of 0.58, the flow around the blades is fully subsonic and compressible, which distinguishes this propeller from most wind turbines. The compressibility can be accounted for in the computation of the airfoil polars, so it is a priori not an issue. However a restrictive assumption of the BET is that the blade sections are independent and that they can be represented by 2D airfoil polars. This is known not to be the case for highly loaded propellers and should be verified on the HAD-1 propeller.

Figure 2.4 shows the friction lines on a blade of the HAD-1 propeller, under the conditions from table 2.2. The images of the suction side have been mirrored for the inflow to always come from the left side. The friction lines are horizontal on the majority of the blade, comforting the assumption of 2D flow and the use of 2D airfoil polars computed from horizontal blade sections. Near the tip of the blade the lines get less horizontal, especially at the very tip where the pressure equalization between the two sides leads to as small separation of the flow. This phenomenon is quite localized but can still lead to a degradation of the models that rely on the BET.

This thesis will also evaluate the ability of the developed body-force models to compute a propeller characteristic by changing the blade pitch angle. The study is conducted within the optimal conditions where the flow is fully attached. Otherwise, the 2D airfoil polars need to be time-averaged and corrected for rotational effects, which tend to delay profile stall [86]. This was not investigated in the current work, so the body-force models will only focus on points that are fully attached. A full propeller characteristic computed by blade-resolved CFD RANS is shown in figure 2.5. The thrust curve is linear until a pitch angle of 51°, after which flow separation begins. Below 37°, the incidence on the blade sections starts being too negative and the lift changes direction. The body-force models will thus only be evaluated in chapter 5 for blade pitch angles between 37° degrees and 49°. A more detailed analysis of the propeller for varying pitch angles is presented in appendix A, where a focus is made for pitch angles of 33°, 37°, 45°, 51° and 55° to

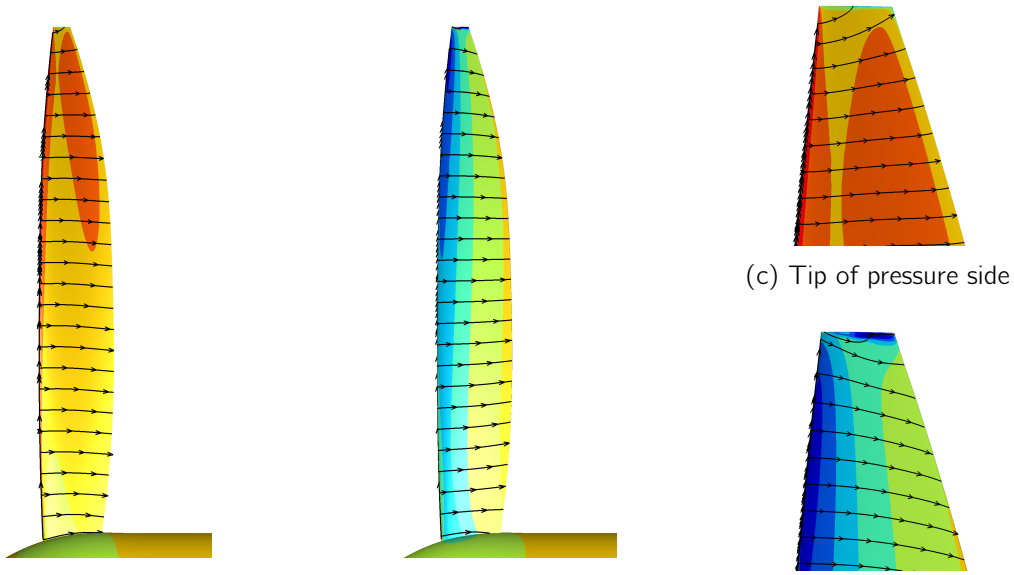

(a) Pressure side (b) Suction side (c) Tip of pressure side (d) Tip of suction side

Figure 2.4: Friction lines on HAD-1 blade, colored by pressure.

illustrate the different flow regimes at which the propeller can operate. In particular, it is shown that the flow is two dimensional on the blade between 37° and 51°, thus ensuring that the pitch angles investigated with the body-force models are compatible with BET assumptions.

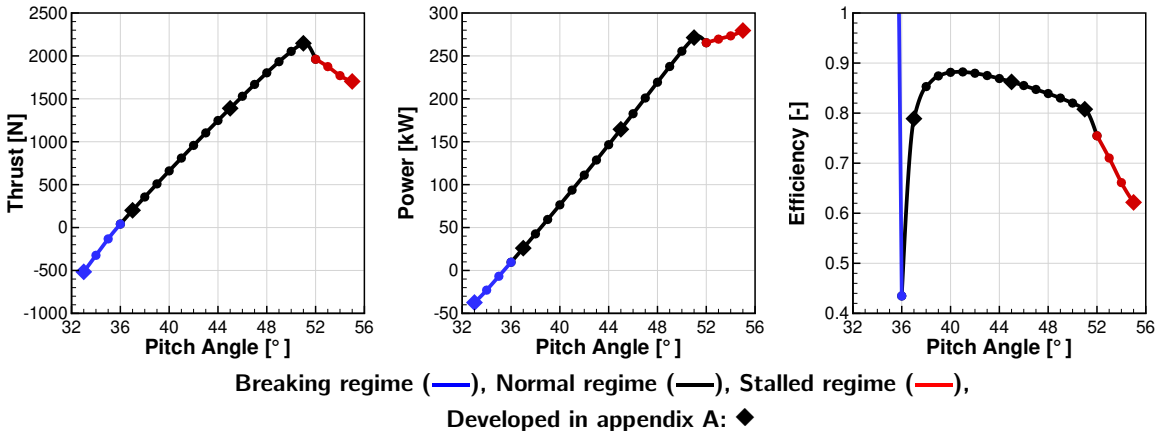

Figure 2.5: Propeller characteristics obtained by blade-resolved CFD RANS computations.

2.1.2 Installed configuration

The body-force methods are most valuable when the inflow is not axisymmetric, such as in cases where the propeller interacts with the airframe. The models must thus be able to correctly account for the mutual interaction of the rotor and the airframe. Their capacity to do so is thus evaluated on a simple configuration composed of the HAD-1 propeller placed upstream of a straight wing. The configuration is shown in figures 2.6, 2.7, and 2.8. The wing leading edge is located $\mathbf{0.75}R$ behind the rotation center in the X direction and $\mathbf{0.6}R$ above the rotation center in the Z direction. The wing geometry parameters are detailed in table 2.4. It was chosen sufficiently long to limit the effect of the wing tip vortices on the propeller wake, as this phenomenon is not the focus of the thesis. However, it is close enough to the propeller so it interacts significantly with the propeller slipstream, and creates an important perturbation in the propeller plane. When studying the wing loads, the analyses will only focus on a restricted portion of the wing that is the most affected by the interaction, shown between the black lines in figures 2.6 and 2.7. It is $4R$ long in the spanwise direction and centered on the propeller.

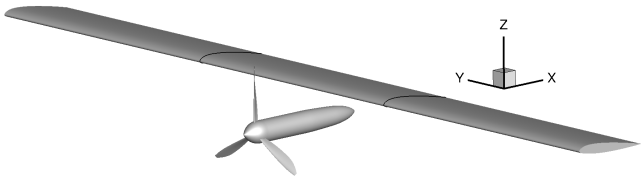

Figure 2.6: Installed configuration.

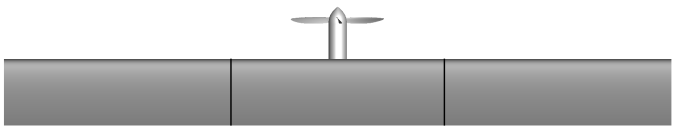

Figure 2.7: Installed configuration – top view.

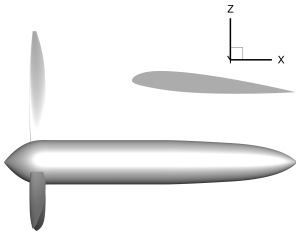

Figure 2.8: Installed configuration – side view.

Table 2.4: Wing geometry

Parameter	Value
Airfoil	NACA23012
Span b, m	10.0
Chord, m	1.0
Pitch angle, °	4.0

2.2 Finite volume computations

2.2.1 Solver and numerical methods

2.2.1.1 Solver presentation

All CFD simulations were carried out using the elsA [9] computational code developed at ONERA. This aerodynamic solver uses a finite volume method at the mesh cell centers. It includes both structured and unstructured solvers and solves the compressible Navier-Stokes equations. This multipurpose code is used for both internal flow configurations (turbomachinery) and external aerodynamic applications (propeller, helicopter, airplane).

The elsA solver offers different possibilities to compute blade-resolved rotors:

- For an isolated propeller under undisturbed axial inflow, the most efficient manner to proceed is to compute a single blade channel with lateral periodic boundary conditions. This reduces the mesh size by $1/N_b$. Furthermore in the relative frame the flow is steady, which allows solving the steady RANS equations to save computational time.
- For installed propellers, a Chimera method can be used [69]. In this approach, different independent meshes overlap a background mesh, which is often Cartesian. The flow is solved on each mesh, and information is transferred from one mesh's boundary to the other by interpolation. When all meshes are static, the data concerning which cell of a given mesh's boundary interpolates on which cell of the background mesh (and vice-versa) can be computed during the pre-process step. However, when the meshes move in the background grid (rotating blades for example), the interpolation coefficients must be recomputed at each time step which can be very costly compared to the time spent solving an iteration. Furthermore, for the interpolation to run smoothly and to avoid loss of information from one mesh to the other, the meshes should have similar cell sizes at the overlap. In practice this is often difficult to do, and the interpolation area is often associated with strong numerical diffusion. Even so, the Chimera approach is often used to study interaction effects because it offers great freedom in the geometries and mesh movements that can be explored. In this thesis, a Chimera approach was used as well to model the isolated propeller under incidence.

Other approaches are also supported by elsA, such as sliding meshes, but they were not investigated in this work.

The elsA solver also offers the possibility of using a coupling script. After each CFD iteration, the flow solution on the mesh can be accessed using a python script. This is known as the trigger method. This method offers great freedom in terms of coprocess, such as extractions or couplings with other software. However, any action taken in the python script is made outside of the optimized framework of the solver and is generally slow compared to implementations directly made in the solver. Regardless, this method is very useful for defining body forces, as new fields can be defined in the mesh cell-centers during the trigger step, and these will be used as source terms in the Navier-Stokes equations at the following iteration. As a result, this trigger method is convenient for BET-based body-force models because it allows velocity extraction, force computation, and source term distribution between iterations. However, a drawback of this approach is that the trigger only gives access to the time loop, and not to the sub-iterations of a second order time scheme. This aspect is a limiting factor in the actuator line framework, as will be explained in section 4.3.2.

2.2.1.2 Numerical methods

In this work, elsA solves the RANS equations in compressible regime (steady or unsteady depending on the case) on structured meshes. The convective fluxes are discretized using a second-order centered scheme with scalar artificial viscosity [34] and Martinelli's correction [47]. The coefficients of the second-order nonlinear, fourth-order linear dissipation and Martinelli's scaling exponent are set, respectively, to $k^{(2)} = 0.5$, $k^{(4)} = 0.016$, and $\alpha = 0.3$. The diffusive fluxes are discretized using a second-order centered scheme. For the steady simulations, the pseudo time-marching scheme used is the first-order backward Euler scheme. In the computations a linear CFL (Courant-Friedrichs-Lewy) number [13] ramp is used, from 1 to 10 in 1000 iterations. The unsteady simulations are carried out using the Gear scheme [27], a second-order three-time-level implicit backward-difference scheme, with 20 to 25 Newton sub-iterations between each time step depending on the configuration. For the blade-resolved simulations, the time-step was chosen so the propeller rotates 0.5° at each iteration. For the actuator line simulations, the propeller rotates 1° between each iteration, unless specified otherwise. The turbulence modeling relies on a $k-\omega$ Kok turbulence model [40] with shear-stress transport (SST) correction [52].

Characteristic relation-based flow boundary conditions are used at the computational domain inlet, outlet, and radial boundary with infinite flow values corresponding to the ones given in table 2.2. This boundary condition will be referred to as farfield in the rest of the dissertation. All solid surfaces are considered as adiabatic walls.

2.2.2 Meshes for blade-resolved simulations

2.2.2.1 Full-matched structured mesh

The full-match structured meshes were made using the NUMECA Autogrid mesh generation software. It provides multiblock grids of a single blade channel from a given geometry and desired mesh parameters. Initially, five grids were made with different levels of refinement. The number of cells in each grid is given in table 2.5. Each mesh was built so that the first cell in the boundary layer complies with the y^+ requirement of the turbulence model of $y^+ \leq 1$. Slices of mesh 4, which contains 10.1 million cells, are shown in figure 2.9.

Table 2.5: Grid-dependency study results

Grid	Number of cells	Thrust [N]	Power [kW]
1	3,363,296	1393.1	165.08
2	5,065,824	1390.6	164.90
3	6,958,816	1392.5	164.87
4	10,132,608	1389.7	164.39
5	12,452,352	1389.7	164.37
F	24,532,928	1389.7	164.51

A RANS simulation was conducted on each grid using the numerical setup detailed in section 2.2.1.2, solving a single blade channel in the relative frame with periodic boundary conditions. The operating point is the one from table 2.2. The propeller thrust and power are shown in table 2.5. Using the finest mesh as reference, it appears these two quantities of interest are converged well below 1%, even on the coarsest mesh. The radial distributions of blade axial and tangential loads were found to be nearly identical for each mesh. The same was noted for the azimuthal averages of velocity fields in the wake, which are of interest for comparison with

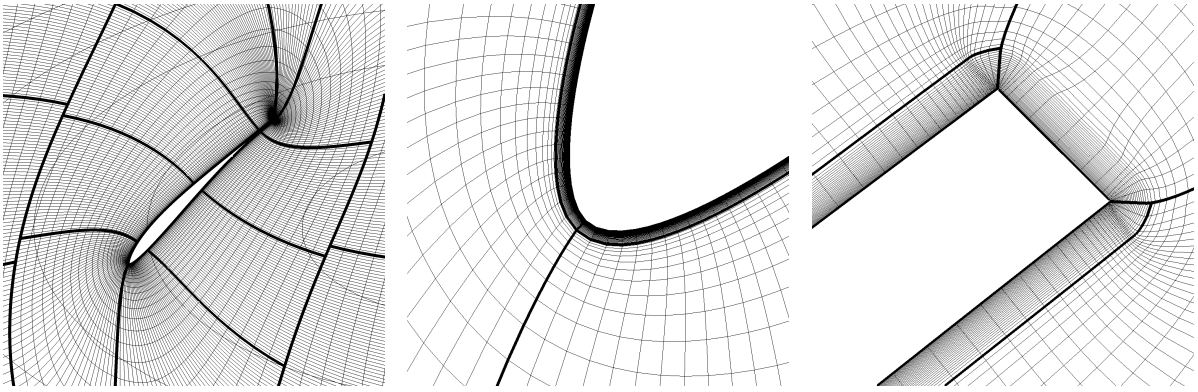

(a) Blade section (b) Leading edge section (c) Trailing edge section

Figure 2.9: Slices of a full-matched structured blade-resolved mesh – mesh 4.

the steady body-force model. As a result, grid convergence is assumed sufficient for the RANS blade-resolved computations to be used as references for propeller performance predictions.

Throughout the PhD, it was found that these meshes were not refined enough in the wake to allow an accurate comparison of the flow physics with the actuator line model, especially when looking at the blade wake and the tip vortices. It was therefore decided to create a final mesh with a different topology, more refined in the wake, as shown in figure 2.10. The propeller thrust and power are shown in table 2.5 for the grid labeled F, and they are very similar to the values from the other meshes. Slices of the wake velocity fields half a rotor radius behind the propeller are shown in figure 2.11 for mesh 4 and mesh F to illustrate the better wake resolution.

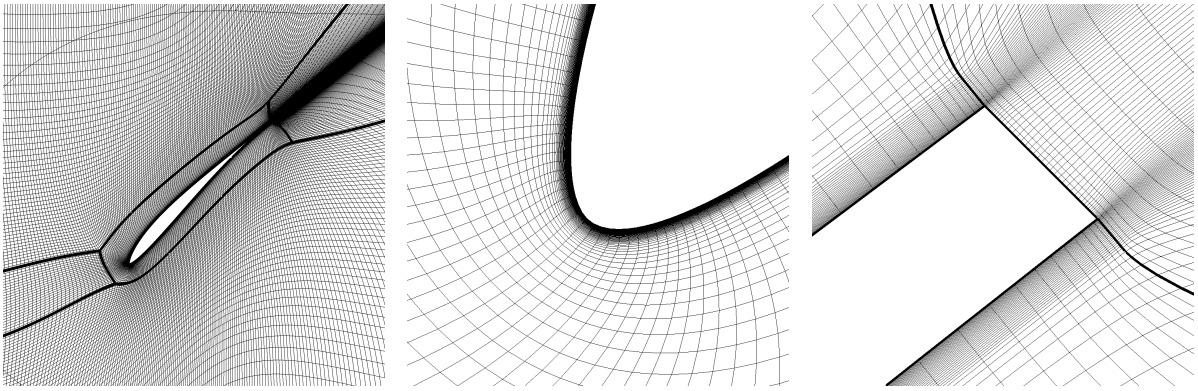

(a) Blade section (b) Leading edge section (c) Trailing edge section

Figure 2.10: Slices of a full-matched structured blade-resolved mesh – final mesh.

Grid F will be used in chapters 3 and 4 as a reference for studies of the isolated propeller under axial flow. Indeed, this mesh offers the best representation of the flow physics because its refinement was adapted to the shape of the vortex structure. It is thus an appropriate reference to understand what aspect of the flow physics the body-force models can and cannot model. For chapters 5 and 6, where the idea is rather to evaluate the performance of the body-force models, it makes more sense to compare the results to a blade-resolved Chimera computation because it is often the method that is used when studying installation effects. This Chimera mesh is presented in the following section.

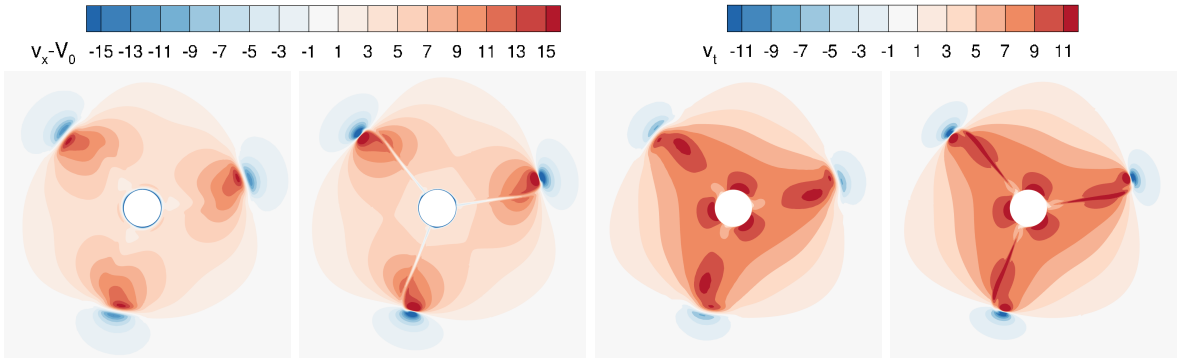

(a) Mesh 4 – v_x (b) Mesh F – v_x (c) Mesh 4 – v_t (d) Mesh F – v_t

Figure 2.11: Slices of axial and tangential velocity fields have a radius behind the propeller for mesh 4 and mesh F.

2.2.2.2 Chimera mesh

For the installed configuration, a Chimera approach is used for the reasons presented in section 2.2.1.1. The total mesh is composed of 5 body-fitted meshes and a background Cartesian grid. Each blade has its own mesh of 4 million cells and the hub mesh has 5 million cells. The blade meshes penetrate the hub mesh all the way to the hub surface, using a double-wall boundary condition. The wing mesh has 8 million cells that are mostly concentrated in the area in the propeller wake (i.e. in the area delimited by the two lines in figure 2.7). All body-fitted meshes solve the boundary layer down to $y^+ = 1$. At each time step, the blade and hub meshes rotate in the static background mesh. The latter contains 80 million cells to preserve the blade tip vortices accurately for at least 2.5 propeller radii, where the cell dimension is equal to $c_{max}/15$. Slices of the mesh are shown in figure 2.12. As mentioned at the end of the previous section, this Chimera mesh, but without the wing, will be used as reference in chapters 5 and 6. This choice will be explained at the beginning of section 5.1.1.

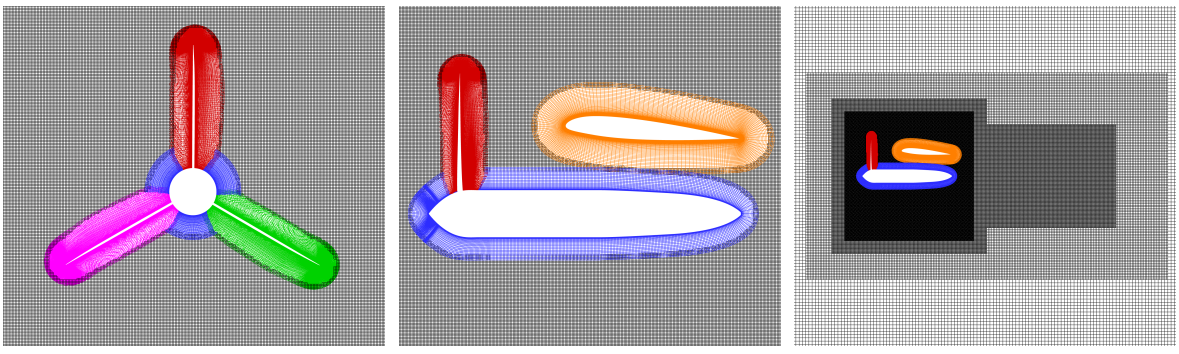

(a) Axial slice in propeller plane (b) Longitudinal slice (c) Wake refinement

Figure 2.12: Blade-resolved Chimera mesh for the installed configuration.

For the Chimera method to work optimally, the cell size of two overlapping meshes must be around the same size in the interpolation region. This is particularly difficult to achieve at the

boundary between the blade mesh and the background grid. A slice of a blade section at $r = 0.75R$ is shown in figure 2.13a, and a focus at the overlap boundary behind the trailing edge is made in figure 2.13b. The masked cells are blanked, only the computed and interpolated cells are shown. This mesh is satisfying because no orphans are detected during the computation, i.e. the cells that must be interpolated always find donor cells. This is mainly due to the fact that there is sufficient overlap between the two meshes and that the radial length of the blade cells are equal to the size of the background cells. However in the azimuthal direction, there are roughly two blade cells for one background cell. The interpolation thus acts as a filter that tends to smear the flow in the azimuthal direction. The background cells are still very small so most of the flow physics go through, but it was found that phenomenon that are very thin in the azimuthal direction, such as the blade viscous wake, are sometimes cut off. This is standard in this type of simulation, and unfortunately it is difficult to fix. A solution is to divide by 2 the cell length of the background grid in the propeller area, but because it is a Cartesian mesh, this would multiply by 8 number of cells, which is too expensive for the case considered. Furthermore, it would only push the issue to the boundary of the next level of Cartesian derefinement. Another solution is to divide by 2 the number of points on the airfoil, but this would potentially reduce the accuracy of the simulation, and the viscous wake might never fully develop in the first place. As a consequence the computations of the installed configuration were run with the mesh from figure 2.13, and the difference in cell size in the azimuthal direction will be recalled during the critical analyses of the flow in chapters 5 and 6.

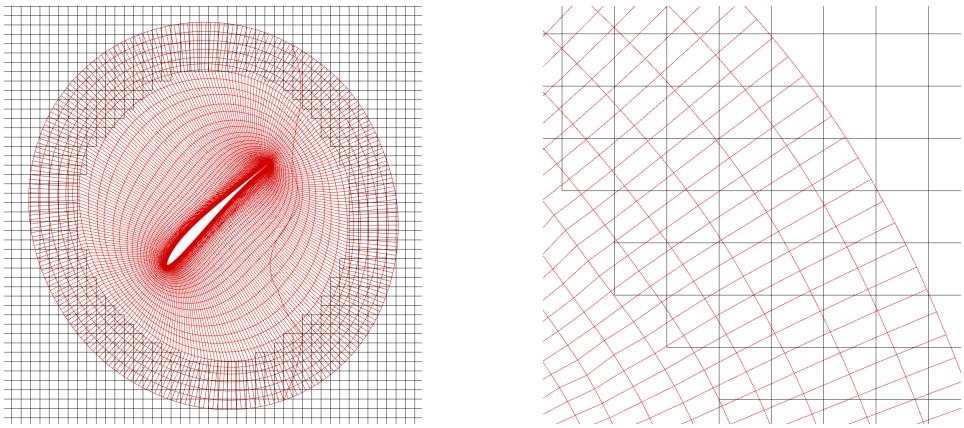

(a) Slice at $r = 0.75R$ (b) Zoom behind the trailing edge

Figure 2.13: Body-fitted blade mesh used in Chimera computations.

As mentioned previously, the blade-resolved results presented in chapter 5 were obtained with a Chimera mesh of the isolated configuration. The same blade and hub meshes as for the installed configuration were used. The background mesh is a Cartesian grid composed of 33 million cells, similar to the one used for the Chimera body-force computations in isolated configuration, presented in next section.

2.2.3 Meshes for body-force computations

Two types of meshes are used for the body-force computations. The first is a full-matched multi-block structured mesh of the infinitely long cylindrical hub composed of 10 million cells. It

does not include the blade mesh, since their effect is modeled by source terms. Slices of this mesh are shown in figure 2.14. This mesh is used for parametric studies of the steady body-force model, so it needs to be refined in the propeller area to be capable of testing different ways of distributing the source terms, as will be shown in section 3.2.1. This mesh is only used for the RANS/BET computations of chapter 3.

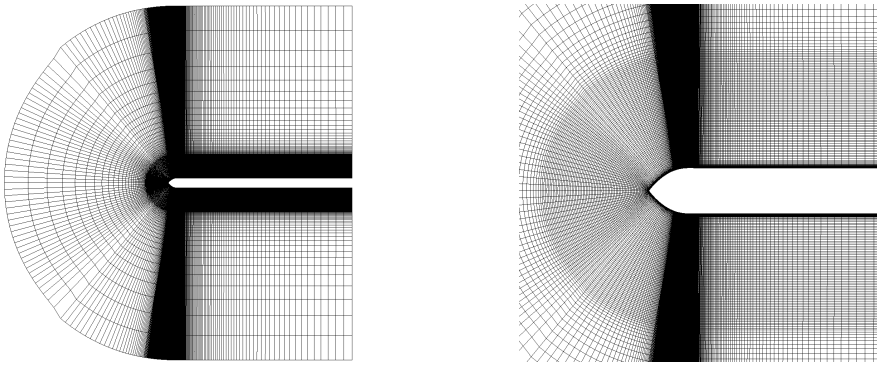

(a) Slice at Y=0 (b) Zoom in the propeller area

Figure 2.14: Steady body-force mesh with an infinite hub.

All other body-force computations are run using a Chimera approach. The same mesh is used for the actuator line and RANS/BET computations. For the isolated configuration, the Chimera mesh is composed of a body-fitted hub mesh (5 million cells), a cylindrical mesh in the propeller area (1.5 million cells), and a background Cartesian grid (33 million cells) which is the same as for the Chimera blade-resolved mesh in isolated configuration. Slices of this mesh are shown in figures 2.15a and 2.15b. The cylindrical mesh goes almost all the way down to hub wall in the radial direction, stopping just over the boundary layer. This choice was made to avoid the appearance of root vortices in the actuator line computations, and will be detailed in section 4.1.3. In this cylinder, the points are equally distributed in the azimuthal and axial directions, but they are set closer together in the radial direction around the blade tip radius. The background grid is refined in the propeller wake area over a distance of approximately 2 radii behind the propeller. In this zone, the cell length is equal to 8mm ($c_{max}/15$ or $c_{tip}/5$). During the study of the actuator line model, a mesh two times more refined in the propeller area will also be studied to validate the results. For the installed configuration, the same mesh as for the blade-resolved approach is used, except that the body-fitted blade meshes are replaced by the cylinder form the isolated configuration, as shown in figure 2.15c.

In both the isolated and installed configurations, all meshes are static, meaning that the interpolation coefficients do not have to be recomputed at each iteration. This can simply be done in the pre-process step, thus saving significant time during the computation. The rotation of the spinner is accounted for with a prescribed rotation velocity at the wall.

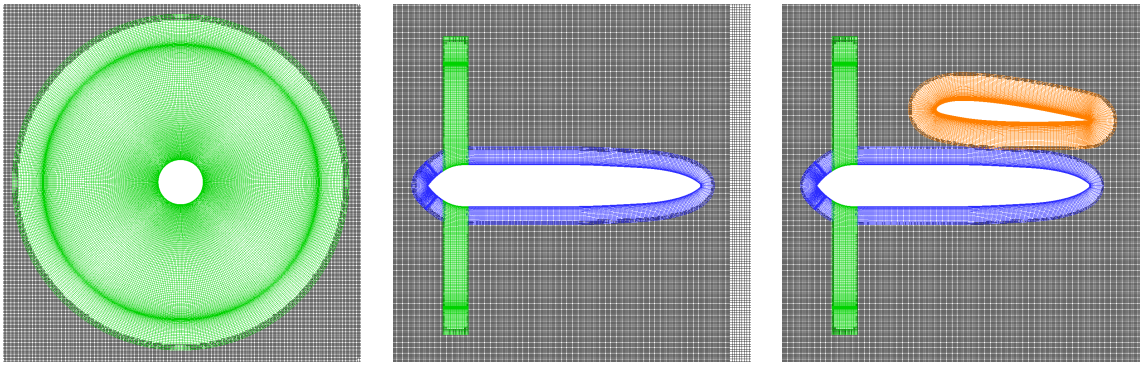

(a) Axial slice in propeller plane

(b) Longitudinal slice – isolated configuration

(c) Longitudinal slice – installed configuration

Figure 2.15: Body-force Chimera meshes.

2.3 Lifting line computations

Throughout the dissertation, the body-force results are compared to results from lifting-line with free-wake computations. The benefit of this method is that it uses the same BET approach as the body-force models, using the same 2D airfoil polars. Furthermore, the free wake includes the modeling and roll-up of the tip vortices, which makes it interesting to evaluate the tip correction of the RANS/BET model, and the smearing effect of the actuator line.

The lifting-line calculations are performed with the PUMA solver (Potential Unsteady Methods for Aerodynamics), developed by ONERA. It relies on a coupling between a kinematic module and an aerodynamic module based on a free-wake model combined with a lifting-line approach. The lifting-line method relies on 2D airfoil polars to compute the airloads on the blade sections. The free-wake model implements Mudry's theory [61], which rigorously describes the unsteady evolution of a wake modeled by a potential discontinuity surface. The PUMA code is parallelized using OpenMP and the multilevel Fast Multipole Method has been implemented for the computation of the velocities induced by each wake panel on any element. In recent years, it has been successfully applied and validated on fixed and rotating wings applications such as propellers [2], conventional and compound helicopters [5], as well as wind turbines [4]. A free wake computed by PUMA of the HAD-1 propeller is shown if figure 2.16. The blades and hub were added in the picture for reference. The wake panels are colored by circulation.

When the rotor is not fully isolated, PUMA is also able to consider the non-lifting potential field of solid surfaces with arbitrary geometries using a panels method. The solver can also be given a perturbation field during the computation of the propeller loads and the convection of the free wake. This second method was preferred in this work as it was found to be more robust than the first. Regardless, PUMA was only used for the isolated configuration, so the perturbation field only accounts for the acceleration of the flow close to the hub.

The lifting line method can evaluate the propeller performance in isolated conditions, but it can only account for a one-way coupling when studying installation effects, as the variation of propeller loads have no retro-action on the perturbation fields. This tool is thus effective to have a first order approximation of installation effects on propeller performance.

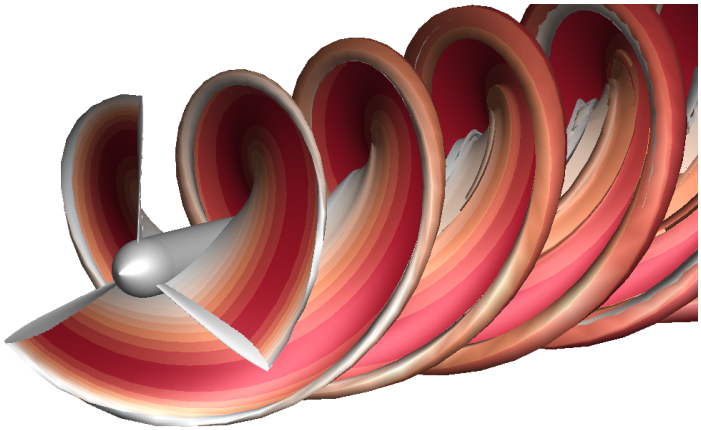

Figure 2.16: Free wake computed by PUMA, colored by circulation.

2.4 Airfoil polars

The BEMT, lifting line, RANS/BET, and actuator-line computations all rely on tabulated airfoil polars. In this work, it was decided to use 2D polars, as opposed to the 2.5D and 3D polars which were presented in section 1.3.1. The main reason for this is that, as seen in section 2.1.1.2, the flow is mostly two dimensional on the blade, so the extra computational cost associated with the use of 2.5D or 3D polars was deemed unjustified. Furthermore, they are significantly less expensive to generate than 2.5D or 3D polars, which is convenient for pre-design studies.

Polars were computed for the airfoils of six different blade sections, which are marked in figure 2.17. The hub line was added for reference as a dashed line on the figure. The polars were obtained by means of 2D steady RANS computations. Fine meshes were used for this purpose, with 300 points on the airfoil surface and a growth rate of 1.05 normal to the surface. The value of y^+ at the airfoil surface is less than 1 for all simulations. For each airfoil, the mesh has a total of 1 million cells. Slices of the mesh used for the computation of the polar of the section located at $r/R = 1$ is shown in figure 2.18. For these computations, the convective term was discretized using an AUSM scheme, and the turbulence model that was used is the same as for the 3D CFD computations presented in section 2.2. The numerical parameters were based on best practices recommended from previous work at ONERA.

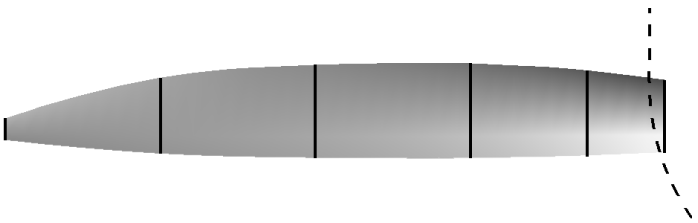

Figure 2.17: Blade sections used for 2D airfoil polar computations.

For each airfoil, computations were carried out for various Mach numbers and incidence angles, ranging respectively between 0.2 and 0.85, and between -8° and 12°. These ranges were chosen sufficiently large to be able to explore off-design points. For some of these points, the flow is partly separated, leading to unsteady phenomenon. In these cases, the lift and drag coefficients were taken as the average of the last iterations. Strictly speaking, it would have been more appropriate

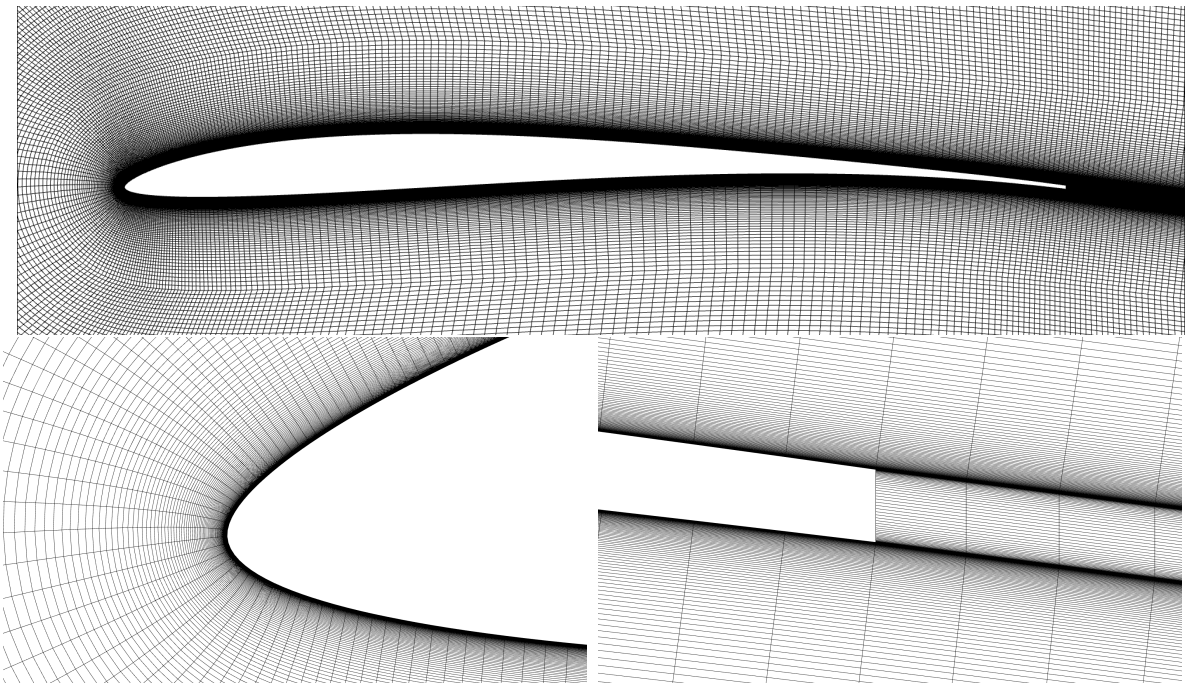

Figure 2.18: Slices of the mesh used for the computation of the polar of the section located at $r/R = 1$.

to use an average value of an unsteady simulation instead, but it was not done in this work as the detached points are rarely used in the body-force computation anyways. For reference, on the design operating point, the angles of attack along the blade vary between 2° and 4°. Each airfoil polar was computed for a constant value of Re/M, which was calculated by considering the local chord of the associated blade section, and the thermodynamic constants at the altitude studied (sea-level in this case).

No correction was applied to the lift and drag coefficients $C_l(M, \alpha)$ and $C_d(M, \alpha)$ that were computed with this method. Empirical corrections exist, in particular to account for the rotation effect that delays stall compared to an isolated 2D airfoil. These corrections will be investigated in future work, and were neglected in this thesis under the condition that the operating points that are explored do not bring the airfoil polars too close to stall.

The lift and drag coefficients as a function of the incidence angles are shown in appendix B for different Mach numbers for the six blade sections considered.

Conclusion

This chapter first presented the HAD-1 propeller, which will be studied throughout the thesis. It is a three-bladed light propeller, which operates in subsonic but compressible flow. At the cruise operating point, the flow is two dimensional on the whole blade. A study of the propeller for different blade pitch angles revealed this is the case for pitch angles between 37° and 51°. The body-force models will therefore be evaluated in this range of pitch angles in chapter 5. An installed configuration was also presented, which consists of a wing placed $0.75R$ behind the rotor.

The finite volume setups were presented in the second section. A full-matched structured mesh of a single blade channel will be used as a reference in chapters 3 and 4. A blade-resolved Chimera mesh will be used as a reference in chapters 5 and 6. For the body-force models, a fully-structured grid is used for the RANS/BET parametric study of chapter 3, otherwise both the RANS/BET and actuator line models use a Chimera mesh.

A lifting-line solver was also presented, and the methodology used to compute the tabulated 2D airfoils polars, on which rely both body-force methods and the lifting line model, was detailed.

Chapter 3

Development of a physically consistent steady body-force model

It was explained in the literature review that many different practices exist when it comes to steady CFD-actuator disk couplings, even within those that model the propeller as source terms. This chapter is dedicated to the development of such a model, called the RANS/BET model. The implementation of the model is first detailed, highlighting its strong point, which is the flexibility it offers when it comes to source term distribution. Comparing different practices from the literature, three studies are conducted related to source term distribution. The object of these studies are the effect of i) the shape of the volume where the source terms are applied, ii) the axial distribution of the forces, and iii) the relative position within this volume of the sampling lines where the local flow parameters are extracted for the BET computation.

The tip-loss corrections are then investigated, first explaining why they are necessary by analyzing a computation with prescribed loads. A focus is made on Glauert's correction as implemented in the literature for axial flow, and a generalization is proposed to extend the implementation to non-axial flow (propeller in incidence or in installed configuration). A simple calibrated correction is also explored, and all corrections are compared and analyzed.

Finally, a study of the effect of the energy source term is proposed. Its necessity is highlighted for the sake of thermodynamic consistency. Two formulations are then analyzed and compared.

Contents

3.1 Detailed implementation of the RANS/BET model

3.1.1 Model overview

The RANS/BET model is a steady coupling between CFD and a volumic actuator disk-like model that relies on the blade element theory to compute the blade loads, similarly to some of the models described in section 1.3, and injects them as volumic source terms in a RANS calculation. An overview of how the model works is presented in this section. The workflow is divided into a number of steps, which are illustrated in figure 3.1.

1. A steady RANS computation is initiated on a mesh that does not include the rotor blades.
2. At the end of each CFD iteration, the velocities from the solution are sampled on n_θ lines evenly distributed in the azimuthal direction. The lines have the shape and length of the blade's quarter chord line (straight in the case of the HAD-1 propeller). Each line is split in n_r elements, each representing a blade section. In this work, $n_\theta = 90$ and $n_r = 50$ were found to be a good compromise between accuracy and computational cost.
3. The blade loads are computed along each of the n_θ lines with the BET and the 2D airfoil polars presented in section 2.4.
4. The loads are converted into source terms in an auxiliary mesh. The shape of this mesh and the way the source terms are distributed in the axial direction are parameters that are chosen by the user.
5. The source terms are injected in the CFD computation by interpolation from the auxiliary grid to the computational mesh. The axial position of the auxiliary grid relative to the computational mesh, and in particular relative to the sampling lines, is also an input parameter.
6. These source terms are accounted for at the next CFD iteration. The previous steps are then repeated until the CFD flow field and BET loads are converged.

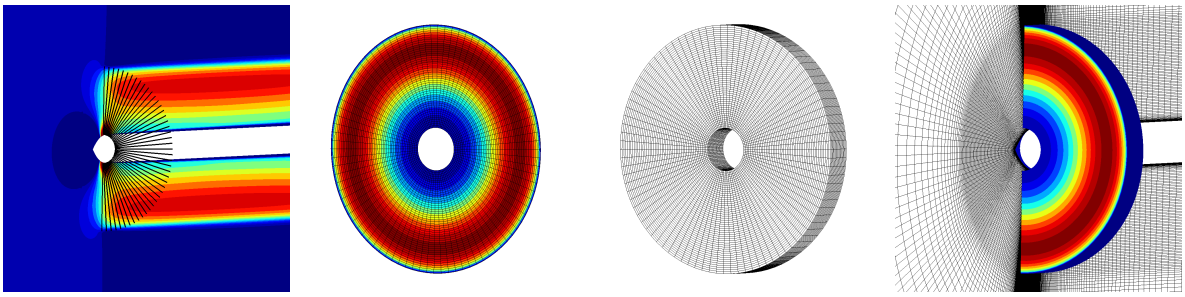

(a) Velocity sampling (b) Disk load from BET (c) Source term volume (d) Source term distribution

Figure 3.1: RANS/BET method recap.

The strength of the model is that it offers a lot of freedom to distribute the source terms in the CFD computations. It is thus appropriate to compare different practices from the literature, which were presented in section 1.3.2. The two following sections give more details into how the blade loads are computed, and how they are transformed into source terms.

3.1.2 Computation of blade loads

In the RANS/BET model, the loads are computed in a very similar approach to what was presented in section 1.3.1. The velocities from the CFD computation are initially expressed in the Cartesian frame $\boldsymbol{v}_{\boldsymbol{xyz}}^{\boldsymbol{CFD}}$, and must first be projected in the local 2D frame used in the BET computation. When the quarter chord line is straight, this frame is simply the local polar frame (e_r, e_θ, e_a). With respect to the blade element theory assumptions, the radial velocity is neglected and the relative velocity is obtained as:

$$\boldsymbol{v}_{\boldsymbol{rel}}(r,\theta) = \left(v_a^{CFD}(r,\theta), v_t^{CFD}(r,\theta) - \Omega r\right). \tag{3.1}$$

From there, the axial and tangential forces exerted on each blade element $\left(f_a(r,\theta), f_t(r,\theta)\right)$ are obtained as in section 1.3.1. They are then projected in the Cartesian frame and scaled as in equation (1.55) to obtain the disk loads $\boldsymbol{f} = (f_x, f_y, f_z)$.

3.1.3 Computation of source terms and distribution

Once the loads are computed, the sampling lines are stacked into a surface (referred to as loading disk), and the loads are interpolated from nodes to cell centers. The loads, in newtons, must then be distributed in the computational mesh as body forces in $N.m^{-3}$ for the momentum equations and in $W.m^{-3}$ for the energy equation. In the RANS/BET method, this is done by using an auxiliary cylindrical grid. This grid has n_r cells in the radial direction, n_θ in the azimuthal direction, and n_a in the axial direction. The radial and tangential distribution of the points are the same as for the sampling lines, but the distribution of the axial points is free and may vary with the radius. This gives the freedom to use pseudo-cylindrical volumes, such as the volume swept by the blades. The effect of the volume shape will be investigated in section 3.2.1.

The n_a cells located at a given r and a given θ can thus be associated with the force $\boldsymbol{f}(r,\theta)$ of the sampling surface element located at this same r and θ. In the RANS/BET model, this force is then distributed in the axial direction among the n_a cells located at the same r and θ, over a total volume $\mathcal{V}_t(r)$. A diagram of the distribution method is represented in figure 3.2. Figure 3.2a shows the loading disk, where $\boldsymbol{f}(r,\theta)$ is shown in red. This force is distributed in the blue volume $\mathcal{V}_t(r)$ from figure 3.2b, which corresponds to the sum of all the cell volumes $\mathcal{V}_c(x,r)$ in the axial direction at a given azimuth and radius:

$$\mathcal{V}_t(r) = \sum_{n_a} \mathcal{V}_c(x,r). \tag{3.2}$$

To obtain a uniform distribution of the source terms over the auxiliary mesh in the axial direction, the force density in each cell must be:

$$\boldsymbol{s_u}(r,\theta) = \frac{\boldsymbol{f}(r,\theta)}{\mathcal{V}_t(r)}. \tag{3.3}$$

A weight function $w(x)$ can also be applied to the sources to change the distribution in the axial direction as long as it is divided by a normalization factor $F_n(r)$. The effect of the weight function will be investigated in section 3.2.2. The final form of the distributed source terms is then:

$$\boldsymbol{s_w}(r,\theta,x) = \frac{w(x)}{F_n(r)}\boldsymbol{s_u}(r,\theta) \quad \text{where} \quad F_n(r) = \frac{\sum_{n_a} w(x)\mathcal{V}_c(x,r)}{\mathcal{V}_t(r)}. \tag{3.4}$$

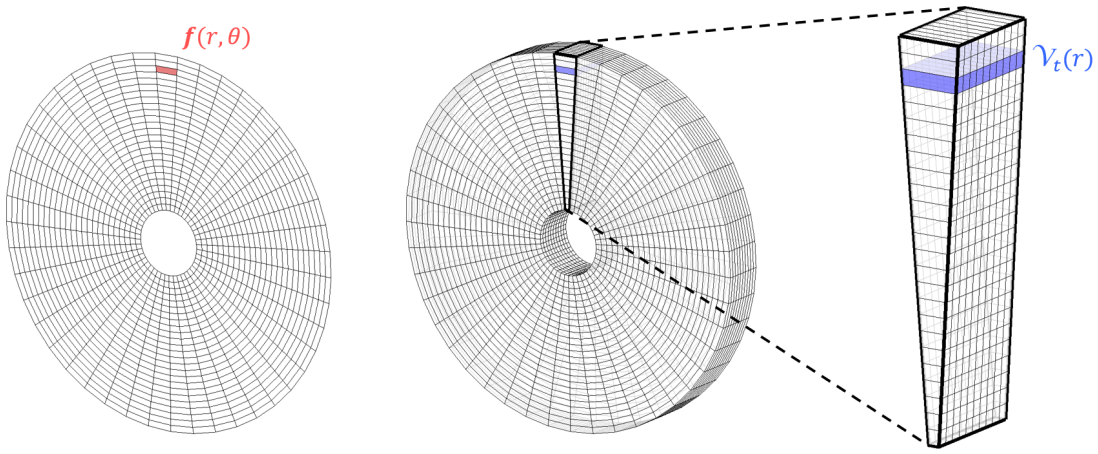

(a) Loading disk (b) Auxiliary grid

Figure 3.2: RANS/BET source term distribution.

The normalization factor $F_n(r)$ was chosen so that:

$$\sum_{n_a} \boldsymbol{s_w}(r,\theta,x)\mathcal{V}_c(r,x) = \boldsymbol{f}(r,\theta). \tag{3.5}$$

The axial position of the auxiliary volume relative to the sampling lines in also free, and will be investigated in section 3.2.3. The source term field $\boldsymbol{s_w}(r,\theta,x)$ is injected into the CFD computation by interpolation from the auxiliary volume to the computational mesh and is accounted for in the right-hand-side of the RANS equations at the next CFD iteration, as in equations (1.56) and (1.57). A focus on the energy source term is made in section 3.4.

3.2 Parametrization for a physically consistent approach

For the RANS/BET method, the previous section explained that several choices have to be made regarding the construction of the loads and their distribution: i) the shape of the volume where the source terms are applied, ii) the position of this volume relative to the sampling lines where the local flow parameters are extracted and iii) the axial distribution of the forces. In this section, several options for these parameters are tested and discussed, and their influence on the resulting loads and flow fields are investigated. General conclusions are then drawn about source term distribution.

All the computations are conducted on the full-matched structured mesh of the infinitely long cylindrical hub presented in section 2.2.3, and the operating point is the one from table 2.2. The RANS/BET model was used as presented in section 3.1, so without a tip-loss correction.

3.2.1 Shape of source term volume

The source term volume can be chosen to have any shape as long as it is coherent with the sampling lines. In this section, three different shapes are compared, which are represented in figure 3.3. The options considered are the volume swept by the blades in a blade-resolved simulation (labeled 'fitted box'), a cylinder that encompasses the volume swept by the blades (labeled 'bounding box'),

and another cylinder that has a length of $1.5 * c_{max}$ (labeled 'extended box'). In the following, the axial length of the body-force volumes are written $l_{BF}(r)$.

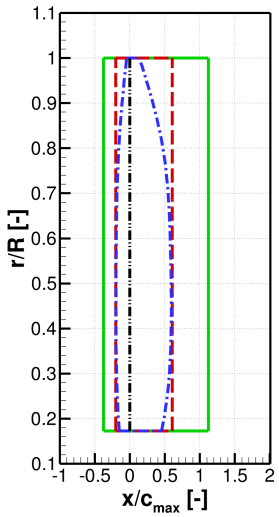

Fitted box (----), Bounding box (— —), Extended box (——), Sampling line (-·-·-)

Figure 3.3: Sections of source term volumes.

For all cases, the sampling lines are placed at x=0, which corresponds to the blade's quarter chord line. The volumes are placed so that their upstream boundaries are $0.25 l_{BF}$ upstream of the sampling lines, as in Figure 3.3. The axial distribution of the source terms replicates the setup proposed by Ortun and relies on the calibrated Weibull density function used in Ref. [62]:

$$w_W = \frac{\gamma_1}{\gamma_2}\left(\frac{x}{\gamma_2}\right)^{\gamma_1 - 1} e^{-\frac{x}{\gamma_2}\gamma_1} \quad \text{with} \quad \gamma_1 = 2 \text{ and } \gamma_2 = 0.3. \tag{3.6}$$

This function mainly distributes the sources at the forefront of the volume, as shown in figure 3.5. The reasons behind this setup are explained in the rest of this section.

A RANS/BET simulation was conducted for each volume shape. The radial distributions of the axial and tangential loads evaluated by the BET are plotted in Figures 3.4a and 3.4b. A flow field analysis downstream of the propeller is also made. Figures 3.4c and 3.4d show the radial profiles of the axial and tangential velocities half a propeller radius downstream of the sampling lines.

In all these figures, the curves for the different volume shapes all overlap one another. An analysis of the flow field further downstream, not shown here, leads to the same observation. The number of cells the source term volume has in the axial direction was also found to have no impact on the results. It can therefore be concluded that the shape of the source term volume has no impact on the results of the model. It should be noted here that: i) this is an important finding as this question is rarely directly addressed in literature on similar methods, ii) and that this conclusion is in fact related to the choice of how the axial distribution is made, as will be demonstrated in the next section. In the rest of the dissertation, for the steady RANS/BET calculations, the source terms are always distributed in a volume shaped as the extended box. This is done to relax the constraint on cell-size for the interpolation of the source terms into the computational mesh.

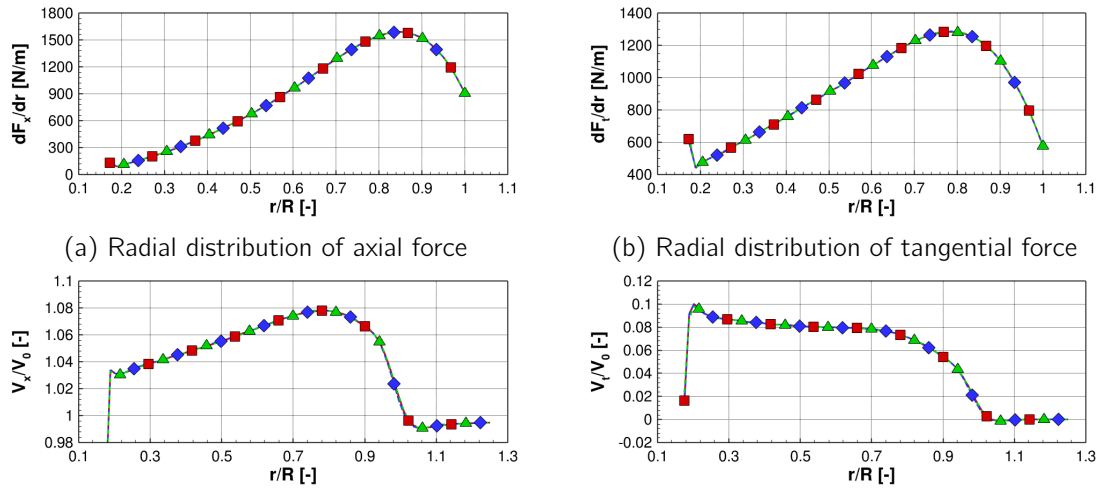

(a) Radial distribution of axial force

(b) Radial distribution of tangential force

(c) Axial velocity field

(d) Tangential velocity field

Fitted box (- - ◆ - -), Bounding box (—■—), Extended box (- ▲ -)

Figure 3.4: Computation results for three shapes of source term volumes.

3.2.2 Axial distribution

A Gaussian projection kernel is commonly used in the literature to directly distribute the source terms into the CFD computational mesh, without resorting to interpolations [89, 95]. However other distribution functions can be used. Actually, thin airfoils operating at subsonic conditions have their aerodynamic center close to the quarter chord. This property can be reproduced in a RANS/BET body-force simulation by using a weight density to unevenly distribute the source terms in the axial direction. For example, a Weibull density function can be used, as done by Ortun [62].

To quantify the influence of the source term distribution on the RANS/BET results, we consider here three axial distribution densities: uniform, Gaussian and Weibull, shown in figure 3.5. For each one, the sampling plane remains fixed at the quarter chord, and three computations are conducted in which the auxiliary source term grid is placed so that 25%, 50% and 75% of the source terms are distributed upstream of the sampling plane.

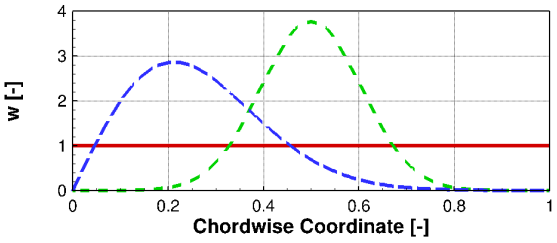

Uniform (——), Gaussian (- - -), Weibull (— —)

Figure 3.5: Density functions used for axial distribution of source terms.

Figures 3.6a and 3.6b show the radial distribution of axial and tangential loads for each computation. Figures 3.6c and 3.6d show the axial and tangential velocities half a propeller radius downstream of the rotation center. For a given percentage of the sources distributed upstream of

the sampling lines, all the tested distribution functions lead to identical blade loads and flow fields. This result clearly shows that the shape of the axial distribution function has no direct impact on the results, which can be interpreted physically. Since no radial forces are applied in the body force volume, a fluid particle travels through the volume at approximately the same radius. The flow being axisymmetric, the acceleration seen by the fluid particle throughout its movement in the body force volume is a constant modulated by the normalized distribution function. As such, the integral of the acceleration over a given streamline is the same regardless of the distribution function. The same observation was made for a computation with an incidence angle of 9°, suggesting that this result can be extended to non axial flow to some extent.

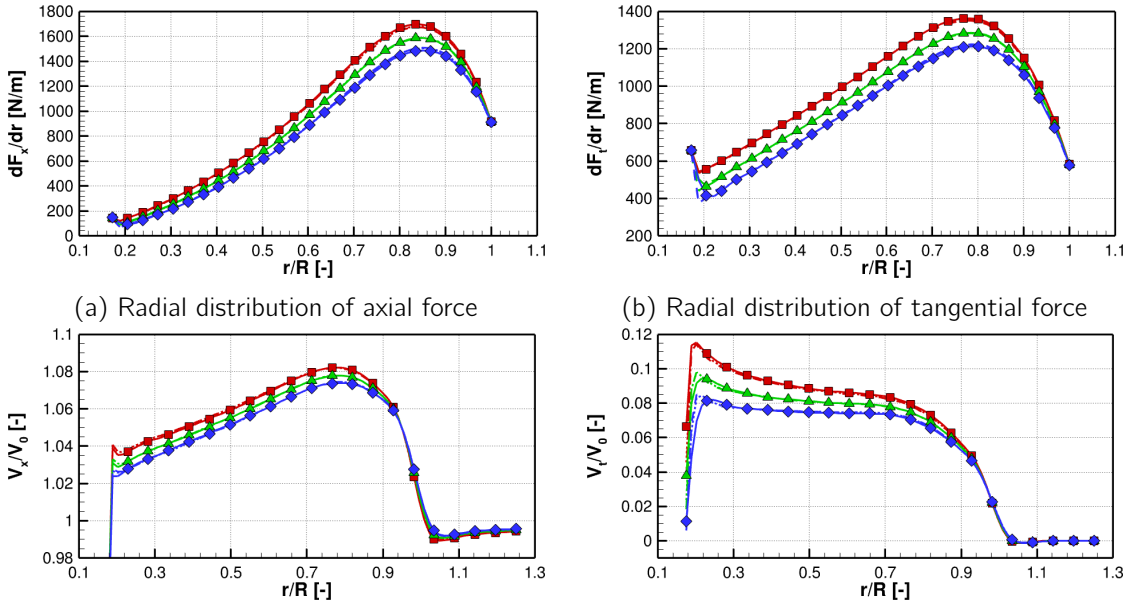

(a) Radial distribution of axial force

(b) Radial distribution of tangential force

(c) Axial velocity field

(d) Tangential velocity field

Uniform 25% (—■—), 50% (—▲—), 75% (—◆—),
Gaussian 25% (- ■ -), 50% (- ▲ -), 75% (- ◆ -),
Weibull 25% (- - ■ - -), 50% (- - ▲ - -), 75% (- - ◆ - -)

Figure 3.6: RANS/BET computation results for different source terms distributions.

The only parameter that has an effect on the results is the quantity of source terms that is distributed upstream of the sampling lines. This parameter is critical because if more sources are placed upstream of the sampling lines, the velocities used for the BET will be higher, resulting in lower angles of attack and lower blade section loadings. Conversely, if less source terms are placed upstream of the sampling lines, the induced velocities will be low and the efforts higher. This system is stable but its convergence point still depends on the location of the auxiliary grid, as shown in figure 3.6.

3.2.3 Position of the source term volume

The two previous sections have shown that the RANS/BET method's key parameter is the quantity of source terms that is distributed upstream of the velocity sampling lines. This comes down to choosing the axial position of the auxiliary source term volume. To correctly select this parameter,

velocities in the wake of the propeller are compared in this section with fundamental BEMT results, which were presented in section 1.2 and are recalled hereafter. Actuator disks model the propeller as a pressure jump that guarantees axial velocity continuity. Theory shows that, under a few assumptions, the induced axial velocity in the wake far downstream is twice that in the disk plane. Glauert also shows that the tangential velocity induced by an actuator disk is discontinuous, its value immediately downstream of the rotor plane being twice the one in the actuator disk plane [28]. When the wake contraction is limited, as it is the case for a lightly loaded propeller such as HAD-1, this tangential velocity is constant in the wake by Kelvin's theorem.

Only the flow field induced by the body forces is relevant for comparison with BEMT. It is obtained by subtracting the velocity field of a RANS computation (accounting for the spinner and hub but without source terms) from a RANS/BET computation (accounting for the spinner, the hub, and source terms). This is done to isolate the contribution of the propeller to the flow field from the distortion of the flow by the spinner and the hub. In the RANS/BET computation of this section, the auxiliary source term volume is placed so that 50% of the source terms are distributed upstream of the velocity sampling lines and the rest downstream, using a Gaussian axial distribution.

Figure 3.7 shows longitudinal slices of axial velocity, tangential velocity, and pressure fields induced by the body forces. The limits of the body-force volume is represented with white lines. The first slice clearly shows the continuity of axial velocity through the body-force region, whereas the other two show a jump in tangential velocity and pressure, as in the BEMT theory. A more in depth analysis, not shown here, revealed that these jumps are very sudden when using axial distribution functions that smear the source terms over a small region (Gaussian or Weibull distributions), and much smoother when using a uniform distribution. However, the axial velocity flow fields were found to be nearly identical, even within the body force volume, regardless of the distribution function. In all cases, the flow fields were found to be identical outside the body force volume, as seen in the previous section.

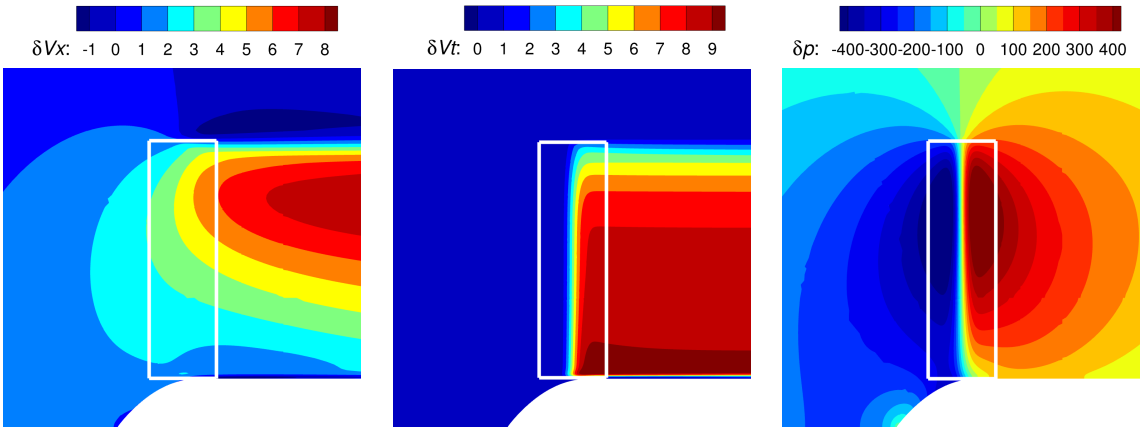

(a) Axial induced velocity field (b) Tangential induced velocity field (c) Induced pressure field

Figure 3.7: Longitudinal slices of fields induced by the body forces.

Figure 3.8 shows the radial variation of the induced axial and tangential velocities for RANS/BET and BEMT computations at different axial locations (labeled 'BF'), where $X = 0$ is

the propeller plane (i.e., the velocity sampling plane in RANS/BET). The theoretical value of the induced flow far downstream is also plotted (labeled 'Froude and Glauert Theory'), which is obtained by multiplying the RANS/BET velocity fields from the propeller plane by 2, as it is the case in the BEMT.

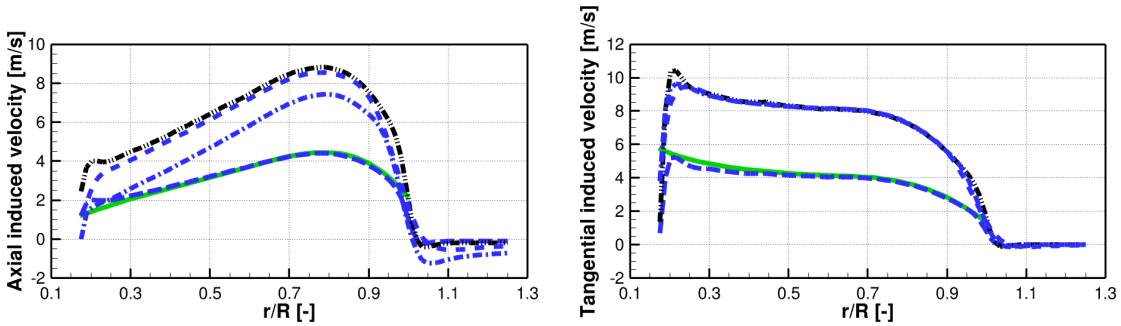

(a) Spanwise axial velocity profiles

(b) Spanwise tangential velocity profiles

BF $X = 0$ **(— —), BF** $X = 0.5 * R_{tip}$ **(----), BF** $X = 3.5 * R_{tip}$ **(- - -),**
Froude and Glauert Theory (-·-·-), BEMT $X = 0$ **(——)**

Figure 3.8: RANS/BET and BEMT induced velocity profiles comparison.

For the induced axial velocity, the radial distributions tend progressively toward the theoretical value predicted by Froude's theory. For the induced tangential velocity, Glauert's theoretical value is reached rapidly behind the propeller. The velocity profile then stays constant downstream because the wake contraction is negligible. Both these observations would evidently not be the same if more or less than 50% of the source terms were distributed upstream the sampling lines, as already shown in figure 3.6. Indeed if less sources are distributed upstream, the induced velocities are lower in the rotor plane and much higher downstream, leading to a velocity ratio much larger than 2. It is the opposite if more than 50% of sources are distributed upstream.

Figure 3.8 also shows that the induced velocities in the rotor plane computed by BEMT are almost identical to those computed by RANS/BET, which further shows that the source terms are correctly distributed in the RANS/BET computation and that the velocities are correctly sampled.

These results therefore show that in order to verify the founding results of the BEMT, the source terms should be equally distributed upstream and downstream of the sampling lines. This is interesting because it is what some authors do without detailed justification. Ortun [62] and Reboul et al. [75] use a calibrated Weibull axial distribution and place the source term volume 25% of its length in front of the sampling plane. By integrating the Weibull function in the axial direction, it can be shown that this setup corresponds to a distribution of 50% of the source terms upstream the sampling lines. Sørensen et al. [95] distribute the source terms using a Gaussian density centered on the sampling lines, which also corresponds to a distribution of 50% of the source terms upstream of the sampling lines. In the rest of the dissertation, half the source terms are distributed upstream of the sampling plane, and half downstream.

3.3 Tip-loss corrections

Different source term distribution methods have been evaluated and an optimal setup has been found. The RANS/BET model needs to be further refined by adding a tip-loss correction. The two following sections explain why a tip-loss correction is necessary, and assess four tip-loss corrections, including two from the literature.

3.3.1 Computation with prescribed loads

In this section, the radial loads are prescribed using the results from the RANS blade-resolved approach instead of being computed using the BET. The objective is to evaluate how accurately the RANS/BET model can predict the velocity fields when the correct radial loads are prescribed. Figure 3.9 shows the azimuthal average of the velocity fields half a radius behind the propeller computed by RANS with a blade-resolved approach, and the velocity fields computed by the RANS/BET model with prescribed loads. The trends of the blade-resolved computation are very well predicted by the RANS/BET model for both the axial and tangential velocity fields. This result further shows that the RANS/BET model does correspond to a time-averaged vision of the blade-resolved computation, because for a periodic steady flow, the azimuthl average of the blade-resolved computation is equivalent to the time average.

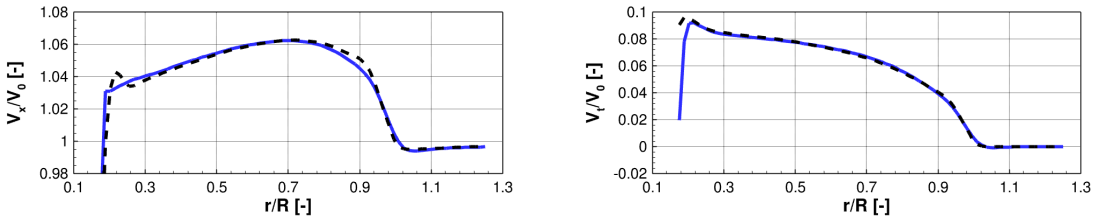

(a) Azimuthal average of axial velocity field (b) Azimuthal average of tangential velocity field

Blade-resolved (- - -), RANS/BET with prescribed loads (——)

Figure 3.9: Velocities from RANS/BET computation with prescribed forces.

At the end of the RANS/BET computation with prescribed loads, the disk loads are recomputed by the BET from the velocity fields of the solution. The objective is now to evaluate if the right loads can be computed by the BET from the correct velocity fields. Figure 3.10 shows the radial distribution of the axial and tangential loads that are prescribed in the body-force computation, and the loads that are recomputed by the BET from the velocity fields of the solution. The results show that the loads are overestimated by the BET computation by up to 40% near the tip of the blades.

This section thus shows that the correct velocity fields are predicted by the body-force computation if the correct radial loads are prescribed. However, the BET greatly overestimates the loads at the blade tip from the correct velocity fields.

There are two reasons for this discrepancy. The first is that no tip-loss correction was used during the BET computation, leading to largely overestimated tip loads as explained in section 1.2.5. The second comes from the absence of 2D polar correction for blade sweep and dihedral angles, but as explained in section 2.4 this effect is believed to be relatively small in this case. The following sections will thus be dedicated to finding effective tip-loss corrections for the RANS/BET model.

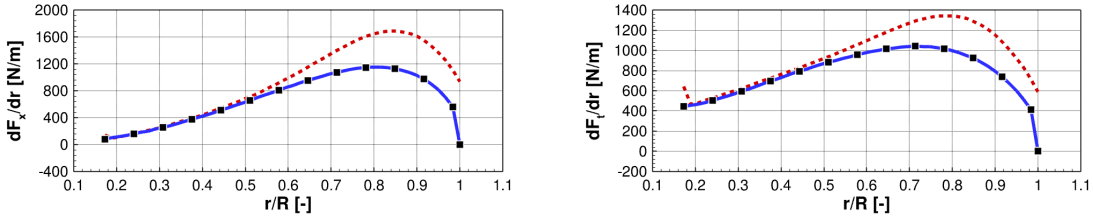

(a) Spanwise thrust

(b) Spanwise tangential loads

Blade-resolved (■), Loads prescribed in body force computation (——), Loads recomputed by BET (- - -)

Figure 3.10: Blade loads from RANS/BET computation with prescribed forces.

3.3.2 The Glauert correction

3.3.2.1 Correction for uniform inflow

The first correction investigated is Glauert's tip correction as implemented by Shen et al. [83]. This correction, initially developed for wind turbines, was presented in section 1.3.3. Figure 3.11 shows the spanwise thrust, torque, and sectional angle of attack obtained from RANS/BET and BEMT computations, with and without the Glauert correction. First, the correction leads to identical results with the BEMT and RANS/BET models. This serves as a validation of Shen et al.'s implementation of Glauert's tip-loss correction for propeller applications. However, the sectional angles of attack reveal some discrepancies. The differences between BEMT and RANS/BET at the blade root are due to the presence of the hub, which accelerates the flow and thus lowers the angles of attack in the RANS/BET computation. Indeed this effect is not included in the BEMT calculation. Discrepancies are also visible at the very tip of the blade for the computations with the correction. The BEMT model predicts a final drop in the angles of attack which is coherent with the consideration of the corrected velocities. However the RANS/BET model computes a rise of the angles of attack which seems non-physical. This could be caused by the division of the sampled velocities by F_G in equation (1.68). Indeed at the tip F_G tends toward 0, leading to numerical issues. This was not addressed by Shen et al. and was solved in this work by using a value R' for R in equation (1.46) that is slightly larger than the actual tip radius of the blade, which could still lead to a divergence of the angle of attack α. However this is only a problem at the very tip of the blade and has a negligible impact on the loads so it was not investigated further.

3.3.2.2 Generalized correction for non-uniform inflow

For cases where the inflow is not uniform, the formulas in equation (1.65) for the induction factors are no longer valid. This issue does not arise in BEMT because it directly solves for the induction factors. However in CFD, the induction factors have to be recomputed from the flow field at each iteration and this step is not straightforward in non-uniform inflow. Indeed, the CFD solution contains the velocities induced by the propeller as well as any other contribution (free flow, incidence component, interaction effects...). In practice the flow induced by the propeller cannot be isolated, making the exact computation of the propeller induction factors impossible.

As a solution, it is proposed here to approximate the velocities sampled in CFD as the sum of the velocity field induced by the propeller $\boldsymbol{v^i}$ and the steady CFD solution $\boldsymbol{v^{p-o}}$ of the configuration

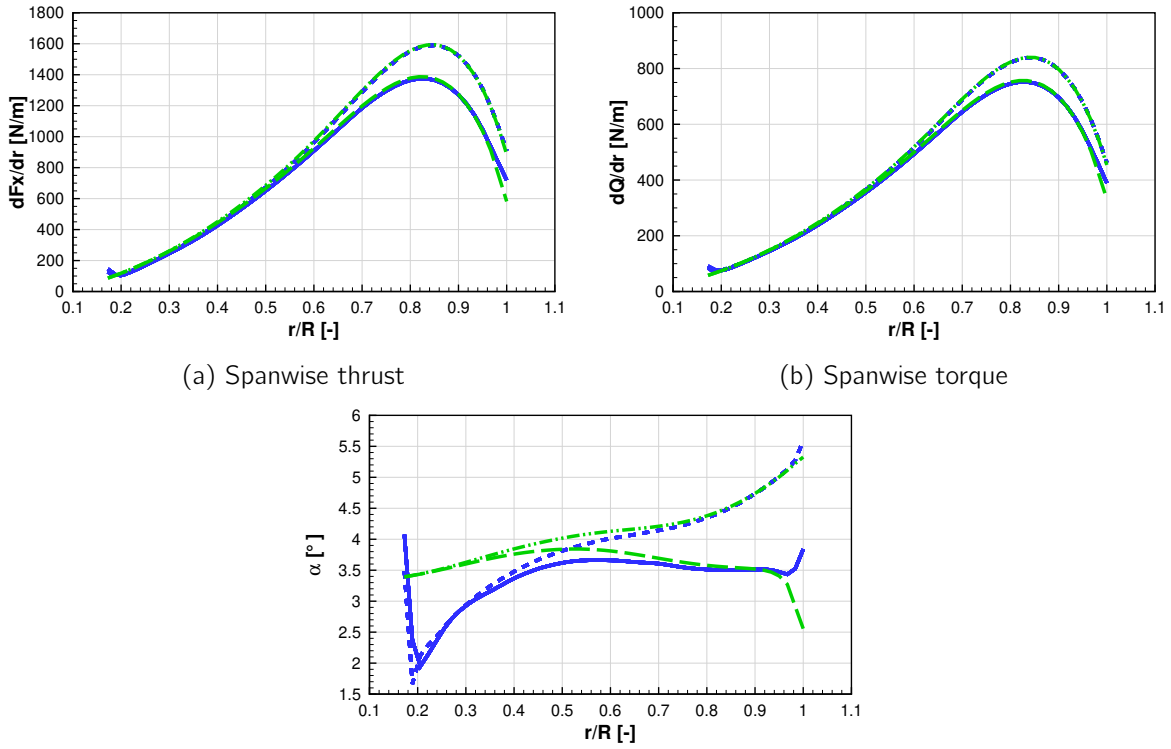

(a) Spanwise thrust

(b) Spanwise torque

(c) Sectional angle of attack

RANS/BET – no correction (- - -), BEMT – no correction (-·-·-), RANS/BET – Glauert correction (——), BEMT – Glauert correction (— —)

Figure 3.11: Comparison of RANS/BET and BEMT results with and without the Glauert correction.

without the propeller, i.e. in power-off configuration. This approximation comes down to neglecting the effect of the propeller slipstream on the other objects for the computation of the tip-loss correction. It is important to note that this approximation is only made to compute the tip correction, the BET computation still remains fully coupled. With this assumption, the velocity field $\boldsymbol{v}^{\boldsymbol{CFD}}$ extracted from CFD can be written as:

$$\begin{cases} v_x^{CFD} = v_x^i + v_x^{p-o} \\ v_t^{CFD} = v_t^i + v_t^{p-o} \end{cases}. \tag{3.7}$$

The induction factors can then be re-written as:

$$\begin{cases} a_x^{CFD} = \dfrac{v_x^{CFD} - v_x^{p-o}}{V_0} \\ a_t^{CFD} = \dfrac{v_t^{CFD} - v_t^{p-o}}{\Omega r} \end{cases}. \tag{3.8}$$

Still using equation (1.68), the corrected velocities become:

$$\begin{cases} v_x^{\text{cor}} = \dfrac{v_x^{CFD} - v_x^{p-o}}{F_G} + v_x^{p-o} \\ v_t^{\text{cor}} = \dfrac{v_t^{CFD} - v_t^{p-o}}{F_G} + v_t^{p-o} \end{cases}. \tag{3.9}$$

For cases where the propeller is isolated under an incidence angle Θ, the power-off field can be further approximated to an analytic field, because the nacelle perturbation is located where $F \approx 1$:

$$\begin{cases} v_x^{p-o} = V_0 \ \cos\Theta \\ v_z^{p-o} = V_0 \ \sin\Theta \end{cases}. \tag{3.10}$$

For cases where $\Theta = 0$, the generalized correction is equivalent to the correction by Shen et al. [83] presented in the previous section.

The need for this correction is quantified in appendix C. This appendix also includes the validation of the correction on two cases: the isolated HAD-1 propeller in incidence and the HAD-1 propeller in installed configuration. In the rest of the dissertation, this generalized formulation is always used when the Glauert tip-loss correction is mentioned.

3.3.3 Calibrated correction

As will be shown in the next section, Glauert's tip-loss correction does not sufficiently reduce the loads at the blade tip to match the blade-resolved computations. This indicates that it does not model the tip vortex with enough accuracy. In this section, a calibrated correction is proposed to further lower the loads at the blade tip. This correction is directly applied to the loads by multiplying C_n and C_t by the factor F_{cal} in equation (1.54). F_{cal} is designed to reduce the difference in spanwise thrust between the RANS/BET simulation with Glauert correction, and the blade-resolved (BR) simulation. This difference is measured by the ratio

$$\tau = \frac{(dF_x/dr)_{BR}}{(dF_x/dr)_{RANS/BET}}. \tag{3.11}$$

By analogy with Shen et al.'s factor F_S [83] presented in section 1.2.5, F_{cal} is computed as

$$F_{cal} = \frac{2}{\pi}\cos^{-1}\left[\exp\left(-g_1\frac{N_b(R-r)}{2r\sin\phi}\right)\right] * \frac{2}{\pi}\cos^{-1}\left[\exp\left(-g_2\frac{N_b(d_r-r)}{2r\sin\phi}\right)\right], \tag{3.12}$$

where g_1, g_2 and d_r are calibration coefficients chosen to best fit the ratio τ over the blade span. τ and F_{cal} are represented in figure 3.12 with the coefficients g_1, g_2 and d_r optimized on HAD-1's operating point. It can be seen that the modeling function proposed for F_{cal} is not perfect, but it does respect the decreasing trend of τ over the span.

Evidently, τ and thus F_{cal} are most likely very case dependent. The idea here is not to derive a universal correction, but rater to propose an effective method that is easy to implement. Indeed, F_{cal} can be computed using the blade loads from a blade-resolved computation and a RANS/BET computation with Glauert's tip correction. Since the RANS/BET and BEMT results were found to be identical, the cost of the calibrated correction can be lowered further to one blade-resolved simulation of an isolated blade in axial inflow, and one BEMT computation.

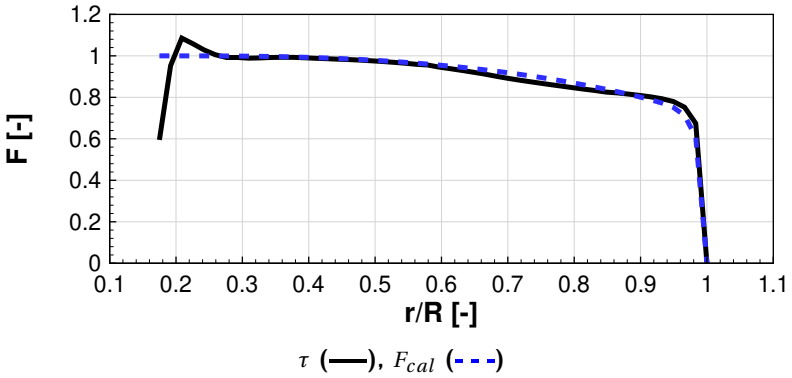

Figure 3.12: Calibration of the tip loads correction.

The calibration is made on a single operating point, and its robustness to changing conditions is essential for the method to be attractive. It will be shown in the following chapters that the correction calibrated on an isolated propeller with a 45° blade pitch angle in axial flow is still very reliable for all cases studied in this dissertation, which include a wide range of blade pitch angles, incidence angles up to 9°, and interaction effects.

3.3.4 Comparison and analysis

In this section, four tip-loss corrections are evaluated and compared:

- Glauert's tip-loss correction, implemented as in section 3.3.2.2.
- Glauert's tip-loss correction with the additional factor F_S of Shen et al. [83], presented at the end of section 1.3.3.
- Glauert's tip-loss correction with the additional calibrated factor F_{cal} from section 3.3.3.
- Calibrated loads correction only. The correction F'_{cal} is computed from the ratio τ' of the spanwise thrust from the blade-resolved simulation and from the RANS/BET simulation without any tip correction. The constants g_1, g_2 and d_r are thus different from the previous correction.

The simulations using these corrections are compared to a RANS/BET computation without a tip-loss correction and to a blade-resolved CFD-RANS computation. All computations are conducted at the operating point from table 2.2. The propeller thrust, power and efficiency computed by each approach are given in table 3.1. The radial distribution of thrust and tangential loads are shown in figure 3.13.

The Glauert correction leads to a good prediction of the efficiency but does not reduce the thrust and power sufficiently. The same observation is made when the Shen et al. correction is added, despite a more accurate prediction at the very tip of the blade. The Glauert + calibrated loads correction gives a good prediction of the propeller thrust, power and efficiency. The spanwise loading is also very close to the blade-resolved results despite a slight overestimation that persists near the tip. The calibrated loads correction alone is rather accurate on spanwise loads but poorly predicts the propeller efficiency. Because this method does not correct the sampled velocities, the lift and drag coefficients interpolated in the 2D airfoil characteristics are necessarily not the correct ones. The correction of the thrust with F'_{cal} brings it down to the right value, but the

Table 3.1: Integrated loads for each tip-loss correction

Modeling method	Thrust [N]	Power [kW]	Efficiency [-]
RANS blade-resolved	1390	164.4	0.863
RANS/BET - no correction	1748 (+25.7%)	199.1 (+21.1%)	0.896 (+3.3pts)
RANS/BET - Glauert	1574 (+13.3%)	184.3 (+12.1%)	0.872 (+0.9pts)
RANS/BET - Glauert + Shen	1514 (+9.0%)	176.8 (+7.5%)	0.874 (+1.1pts)
RANS/BET - Glauert + loads calibration	1426 (+2.6%)	167.3 (+1.8%)	0.870 (+0.7pts)
RANS/BET - loads calibration only	1438 (+3.5%)	162.9 (-0.9%)	0.901 (+3.8pts)

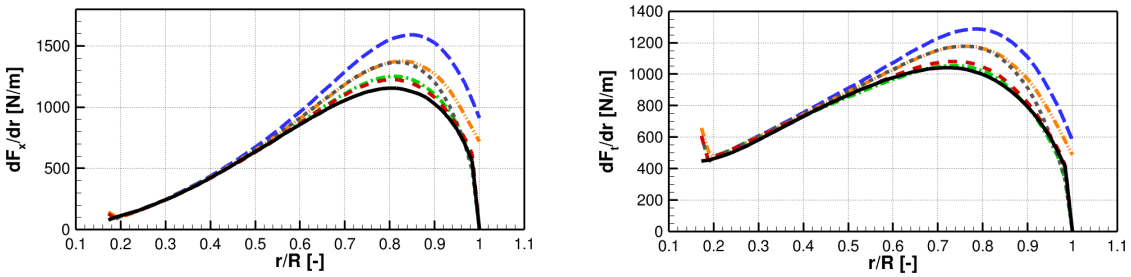

(a) Spanwise thrust

(b) Spanwise tangential loads

RANS/BET - no correction (— —), RANS/BET - Glauert (-·-·-),
RANS/BET - Glauert + Shen (· · · · ·), RANS/BET - Glauert + loads calibration (- - -),
RANS/BET - loads calibration only (-·-·-), RANS blade-resolved (——)

Figure 3.13: Radial distribution of loads for each tip-loss correction.

same factor has no reason to be suited for the torque as well. This observation highlights that, contrary to sampled velocity corrections, the loads correction has an arguable physical significance when applied elsewhere than at the very tip of the blade to model 3D effects. For example, the computation of an effective angle of attack directly from the sampled flow may hit a detached point in the 2D airfoil characteristics, whereas it would have hit an attached point if the sampled velocity had been corrected first, thus leading to a drastically different lift to drag ratio, even if the loads are corrected by F'_{cal} afterwards. This observation is also true for the Glauert + loads calibration correction, even if the correction is satisfying in this case. In order to replicate the flow physics as well as possible, it would be best to use a calibrated correction of sampled velocities and a Shen et al. correction of the loads to account for 3D effects at the very tip of the blades. However, the correction of the sampled velocities changes simultaneously α and v_{rel}, which modifies C_l and C_d by interpolation, thus finally modifying the loads. This deep coupling makes it difficult to calibrate a sampled velocities correction. As a result, the Glauert + loads calibration correction was used in the rest of the thesis and its validity for other propeller operating points with different blade loadings will be investigated in the next chapters.

The wake velocity profiles one radius behind the propeller for each computation are represented in Figure 3.14. They show a direct correlation between loading overshoot and wake velocity overshoot.

It is important to note that the coefficients used for the calibrated tip-loss are specific to a given propeller. In theory, any propeller geometry modification changes the circulation distribution over the blade span and modifies the tip vortex, which in turn should require a new specific tip-loss correction. In practice, a small change in twist or chord distribution that does not modify the tip

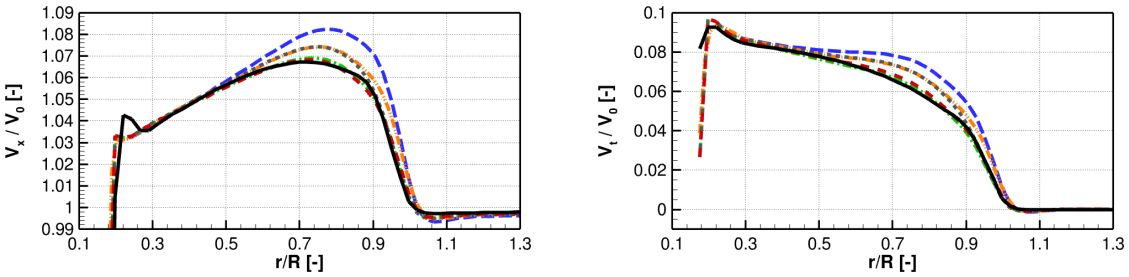

(a) Spanwise axial velocity profiles

(b) Spanwise tangential velocity profiles

RANS/BET - no correction (— —), RANS/BET - Glauert (-·-·-),
RANS/BET - Glauert + Shen (·····), RANS/BET - Glauert + loads calibration (- - -),
RANS/BET - loads calibration only (----), RANS blade-resolved (——)

Figure 3.14: Wake velocity profiles for each tip-loss correction.

vortex structure significantly may not require a new calibration, but this has not been tested in the current work. As a result, this type of correction is not the best suited for a wide parametric exploration for propeller design. It can however be very effective to evaluate the performance of a given propeller on the aircraft on which it is installed when conducting installed simulation.

3.4 Investigation into the energy source term

This section's objective is to give an insight into what the energy source term should be. This includes explaining why it must be accounted for, and how it must be formulated. This question is rarely addressed in depth in the literature for CFD-actuator disk models. The main reason for this is that these types of body-force models are mostly used in the wind turbine sector, and that most often only the incompressible Navier-Stokes equations are solved in their applications, omitting the energy equation.

3.4.1 Necessity of the energy source term

This section is dedicated to proving the necessity of the energy source term in the energy equation. This is done in two manners, first with an analytic approach by analysing the flow equations, and second by validating the conclusions using the RANS/BET model.

First, the conservation of mass and momentum equations are recalled:

$$\frac{\partial \rho}{\partial t} + \nabla \cdot (\rho \boldsymbol{u}) = \frac{d\rho}{dt} + \rho \nabla \cdot \boldsymbol{u} = 0, \tag{3.13}$$

$$\frac{\partial \rho \boldsymbol{u}}{\partial t} + \nabla \cdot (\rho \boldsymbol{u}\boldsymbol{u}) - \nabla \cdot \boldsymbol{\sigma} = \boldsymbol{s_M}, \tag{3.14}$$

where $\boldsymbol{\sigma} = -p\mathbb{I} + \boldsymbol{\tau}$, $\boldsymbol{\tau}$ is the viscous stress tensor, and $\boldsymbol{s_M}$ is the vector of the momentum sources. Using the definition of the material derivative and the conservation of mass from equation (3.13), equation (3.14) leads to

$$\rho \frac{d\boldsymbol{u}}{dt} = \nabla \cdot \boldsymbol{\sigma} + \boldsymbol{s_M}. \tag{3.15}$$

Taking the dot product of $\boldsymbol{u}$ and equation (3.15), a formula for the conservation of the kinetic energy is obtained:

$$\rho \frac{d}{dt}\left(\frac{u^2}{2}\right) = \boldsymbol{u} \cdot (\nabla \cdot \boldsymbol{\sigma}) + \boldsymbol{u} \cdot \boldsymbol{s_M}. \tag{3.16}$$

Note here that the momentum source terms directly lead to an increase of the kinetic energy. By also imposing the conservation of energy without additional source terms in the energy equation, the increase in kinetic energy must be compensated by a decrease of the internal energy, and thus a decrease of the temperature. Furthermore, from the conservation of the total energy equation without a source term, an expression of the entropy S can be obtained. The full demonstration is presented in appendix D, only the final equation is shown here:

$$\rho T \frac{dS}{dt} = -\boldsymbol{u} \cdot \boldsymbol{s_M} + \nabla \cdot (\boldsymbol{\tau} \cdot \boldsymbol{u}) - \boldsymbol{u} \cdot (\nabla \cdot \boldsymbol{\tau}) - \nabla \cdot \boldsymbol{q}. \tag{3.17}$$

In the general case, the flow is in the same direction as the source terms, so $\boldsymbol{u} \cdot \boldsymbol{s_M}$ is positive. This equation thus shows that if no source terms are added in the energy equation, then the momentum source terms have a negative contribution to the variation of entropy, which is obviously non-physical.

Figure 3.15a shows a slice of the temperature field of a RANS/BET computation without source terms in the energy equation. It clearly shows a decrease of temperature in the rotor area, which is maintained in the wake. This is associated to an increase in density, which in particular leads to a decrease of the entropy (figure 3.15b). These effects validate the previous demonstration, and highlight the need for source terms in the energy equation.

It should be noted that the observations made are of small amplitude, less than a degree in the temperature field for instance. Furthermore, as will be shown in section 3.4.4, the presence of the energy source term has no impact on the propeller loads, nor on the velocity fields. It is however important to consider that a non-physical solution cannot be satisfying. Also, the effects shown here are time averaged. For the actuator line model, the temperature and entropy drops are concentrated in the proximity of each blade, which could have more significant consequences than for the steady RANS/BET model. This is investigated in section 4.1.4.

3.4.2 Work done by the body-forces

The conservation of energy equation that accounts for the work done by the body-forces is:

$$\frac{\partial \rho E}{\partial t} + \nabla \cdot \left(\rho E \boldsymbol{u}\right) - \nabla \cdot (\boldsymbol{\sigma} \cdot \boldsymbol{u}) + \nabla \cdot \boldsymbol{q} = \boldsymbol{u} \cdot \boldsymbol{s_M}, \tag{3.18}$$

where the right hand side of the equation corresponds to the work done by the source terms of the momentum equation, $\boldsymbol{s_M}$.
Writing the specific total energy E as the sum of the specific internal energy e and the kinetic energy, we get:

$$\frac{\partial \rho e}{\partial t} + \frac{\partial}{\partial t}\left(\frac{\rho u^2}{2}\right) + \nabla \cdot (\rho e \boldsymbol{u}) + \nabla \cdot \left(\rho \frac{u^2}{2} \boldsymbol{u}\right) + \nabla \cdot \boldsymbol{q} - \nabla \cdot (\boldsymbol{\sigma} \cdot \boldsymbol{u}) = \boldsymbol{u} \cdot \boldsymbol{s_M} \tag{3.19}$$

By developing the partial time derivatives and the divergence operators, reordering the terms, and simplifying, we get:

$$\rho \frac{de}{dt} + \rho \frac{d}{dt}\left(\frac{u^2}{2}\right) + \nabla \cdot \boldsymbol{q} - \nabla \cdot (\boldsymbol{\sigma} \cdot \boldsymbol{u}) = \boldsymbol{u} \cdot \boldsymbol{s_M} \tag{3.20}$$

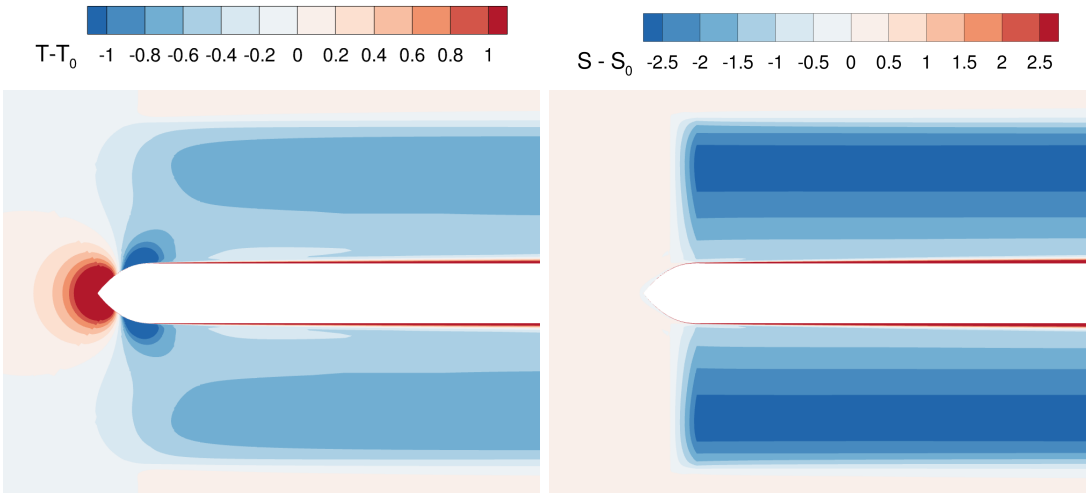

(a) Temperature field (b) Entropy field

Figure 3.15: Slices of a RANS/BET computation without source terms in the energy equation.

Substituting with the conservation of kinetic energy form equation (3.16), we ultimately obtain:

$$\rho \frac{de}{dt} = \nabla \cdot (\boldsymbol{\sigma} \cdot \boldsymbol{u}) - \boldsymbol{u} \cdot (\nabla \cdot \boldsymbol{\sigma}) - \nabla \cdot \boldsymbol{q} \tag{3.21}$$

Note here that the contribution of the momentum source terms through the increase of the kinetic energy cancels out with the energy source term that models the work of the body forces. By accounting for their work in the energy equation, the momentum source terms only contribute to the increase of kinetic energy and have no effect on internal energy.

Now looking at the entropy, the second law of thermodynamics gives the expression:

$$\rho T \frac{dS}{dt} = \rho \frac{de}{dt} - \frac{p}{\rho} \frac{d\rho}{dt} \tag{3.22}$$

It was shown in equations (3.13) and (3.21) that when the work of the momentum source terms are accounted for in the energy equation, then $\frac{de}{dt}$ and $\frac{d\rho}{dt}$ do not depend on the momentum source terms, so they do not contribute to the variation of entropy either.

3.4.3 Viscous losses

In his PhD thesis dedicated to turbomachiery body-force models, Hall [30] argues that some losses should be considered, as the real flow on a blade is not reversible. This is due in particular to the boundary layer that develops on the blade surface, which is not included in the body force computations. He suggests writing the energy source term as the sum of the classical reversible formulation $\boldsymbol{u} \cdot \boldsymbol{s_M}$ and a term responsible for irreversible losses

$$\dot{e} = T \boldsymbol{u} \cdot \nabla S. \tag{3.23}$$

In a short demonstration, invoking in particular the conservation of rothalpy, he argues that

$$\dot{e} = \boldsymbol{s_M} \cdot (\Omega r \boldsymbol{e}_\theta - \boldsymbol{u}), \tag{3.24}$$

which ultimately leads to

$$\boldsymbol{u}\cdot\boldsymbol{s_M}+\dot{e}=(\boldsymbol{s_M}\cdot\boldsymbol{e_\theta})\Omega r. \tag{3.25}$$

His demonstration can be challenged but the physical significance of the result is convincing. Indeed, the power in the engine shaft is $f_\theta\Omega r$, so it makes sense for this power to be fully transferred to the fluid through the energy source term.

In the following, a more thorough demonstration is proposed, which in particular links the losses directly to the drag coefficients of the 2D airfoil polars.

The starting point of the demonstration comes from the fact that the RANS/BET and actuator line models compute the momentum source terms from tabulated 2D airfoil polars, for which the viscous losses are modeled by the drag coefficient. It would therefore be appropriate for theses losses to express themselves as an increase of entropy. For this reason, we propose to subtract the contribution of the drag of the 2D airfoil polars from the energy conservation equation, as a source term (written $s_{E,v}$), to account for the viscous thermodynamic losses, such that the energy equation should be written:

$$\frac{\partial\rho E}{\partial t}+\nabla\cdot\left(\rho E\boldsymbol{u}\right)-\nabla\cdot(\boldsymbol{\sigma}\cdot\boldsymbol{u})+\nabla\cdot\boldsymbol{q}=\boldsymbol{u}\cdot\boldsymbol{s_M}-s_{E,v} \tag{3.26}$$

For the RANS/BET and actuator line models, the momentum source term can be broken down as

$$\boldsymbol{s_M}=\left(s_{x,L}+s_{x,D}\right)\boldsymbol{e_x}+\left(s_{\theta,L}+s_{\theta,D}\right)\boldsymbol{e_\theta}, \tag{3.27}$$

with

$$\begin{cases} s_{x,L}=g\dfrac{1}{2}\rho c d_r v_{rel}^2 C_l\cos\phi \\ s_{x,D}=-g\dfrac{1}{2}\rho c d_r v_{rel}^2 C_d\sin\phi \\ s_{\theta,L}=g\dfrac{1}{2}\rho c d_r v_{rel}^2 C_l\sin\phi \\ s_{\theta,D}=g\dfrac{1}{2}\rho c d_r v_{rel}^2 C_d\cos\phi \end{cases}, \tag{3.28}$$

where $\cos\phi=\dfrac{\Omega r-v_t}{v_{rel}}$, $\sin\phi=\dfrac{v_x}{v_{rel}}$, $\boldsymbol{v_{rel}}=v_x\boldsymbol{e_x}+(v_t-\Omega r)\boldsymbol{e_\theta}$, d_r is the radial length of the blade element, and g is a generic volumic distribution function.

Only the viscous drag component should be included in this new source term. It should thus be expressed as:

$$s_{E,v}=\boldsymbol{v_{rel}}\cdot\left(s_{x,D}\boldsymbol{e_x}+s_{\theta,D}\boldsymbol{e_\theta}\right). \tag{3.29}$$

Note that the velocity used in the dot product to express the work done by the drag force is $\boldsymbol{v_{rel}}$ and not $\boldsymbol{u}$ because the blade loads are computed with the BET in the relative frame.

After simplifications detailed in appendix D, it can be shown that the source term on the right hand side of equation (3.26) can be simplified to

$$\boldsymbol{u}\cdot\boldsymbol{s_M}-s_{E,v}=\left(s_{\theta,L}+s_{\theta,D}\right)\Omega r \tag{3.30}$$

$$=(\boldsymbol{s_M}\cdot\boldsymbol{e_\theta})\,\Omega r. \tag{3.31}$$

This expression is equivalent to the one proposed by Hall, and further shows that the losses are exactly due to the drag of the 2D airfoils.

In a similar manner as presented in appendix D.1, the entropy variation can be expressed in a case where the energy source term is $\boldsymbol{u}\cdot\boldsymbol{s_M} - s_{E,v}$:

$$\rho T\frac{dS}{dt} = -s_{E,v} + \nabla\cdot(\boldsymbol{\tau}\cdot\boldsymbol{u}) - \boldsymbol{u}\cdot(\nabla\cdot\boldsymbol{\tau}) - \nabla\cdot\boldsymbol{q} \tag{3.32}$$

It is shown in appendix D.2 that $s_{E,v}$ is always negative, so the additional source term suggested in this section does in fact lead to an increase of entropy, that is in particular proportional to the drag coefficient of the momentum body force.

3.4.4 Comparison and analysis

This section compares the formulations presented previously ($s_{E,0} = 0$, $s_{E,1} = \boldsymbol{u}\cdot\boldsymbol{s_M}$ and $s_{E,2} = (\boldsymbol{s_M}\cdot\boldsymbol{e_\theta})\Omega r$) on RANS/BET cases. The computational setup is the same as for the previous computations of this chapter (infinite cylindrical hub, constant blade pitch angle at 45°, 3D computation but axisymmetric flow).

Figure 3.16a shows the radial profile of the energy source term field injected in the computation, for each formulation of s_E. The first thing to note is that $s_{E,2}$ is greater than $s_{E,1}$ for all radii. This is consistent with what was shown previously, which explains that this positive difference in energy is converted into entropy. Furthermore, this is not linked to a difference in blade loads, shown in figure 3.16b, because they are identical regardless of the energy source term chosen. This shows in particular that using the correct energy source term in a computation is more about physical and thermodynamic consistency rather than propeller performance, as long as the compressible effects remain small.

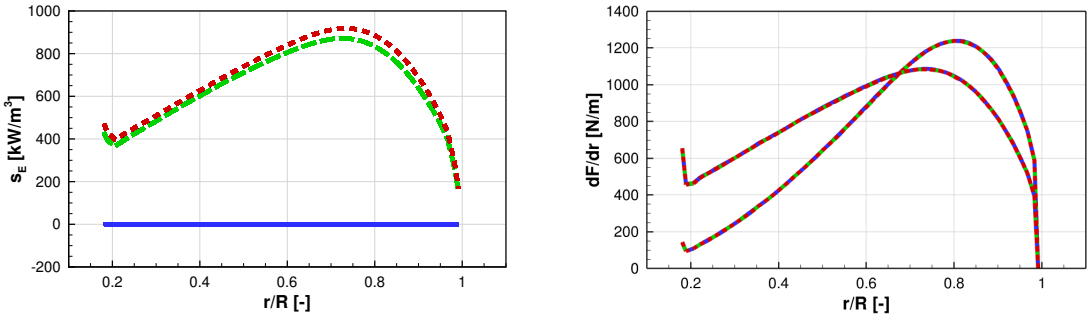

(a) Radial profiles of the energy source terms

(b) Axial and tangential blade loads

$s_{E,0}$ (——), $s_{E,1}$ (– – –), $s_{E,2}$ (- - -)

Figure 3.16: Radial profiles obtained with the different energy source term formulations.

Figure 3.17 shows slices of the stagnation temperature field for each computation, its increase being linked to the work done by the body forces. The field is constant for the computation without energy source terms, as no work is associated to the momentum source terms. The stagnation temperature does rise in the source term volume for the two other computations, but the fields are not identical. This shows that the surplus of energy between $s_{E,2}$ and $s_{E,1}$ is partially converted into work, and not only to entropy. Slices of the entropy fields are presented in figure 3.18. The slice

of the computation with $s_{E,0}$ shows the same field as in figure 3.15b with a magnified color map. The other two slices are consistent with what was explained in the previous sections: $s_{E,1}$ leads to a constant entropy outside of the boundary layer, and $s_{E,2}$ to a slight increase, as predicted by previous demonstrations.

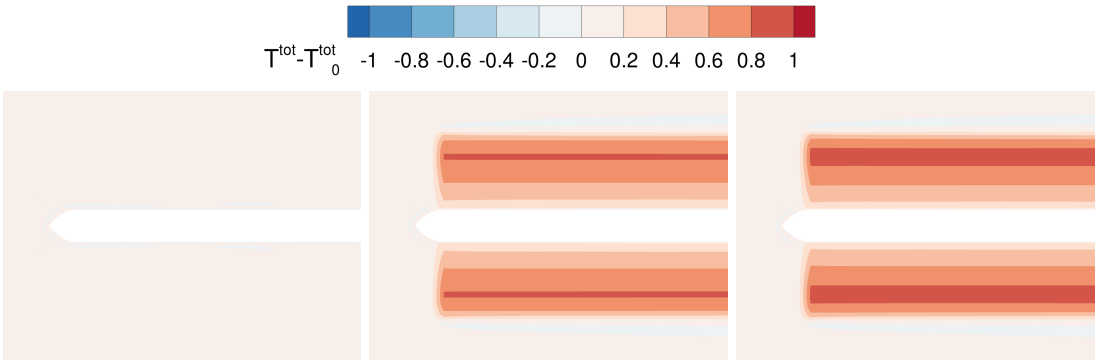

(a) Computation with $s_{E,0}$ (b) Computation with $s_{E,1}$ (c) Computation with $s_{E,2}$

Figure 3.17: Stagnation temperature slices computed by RANS/BET with different energy source terms.

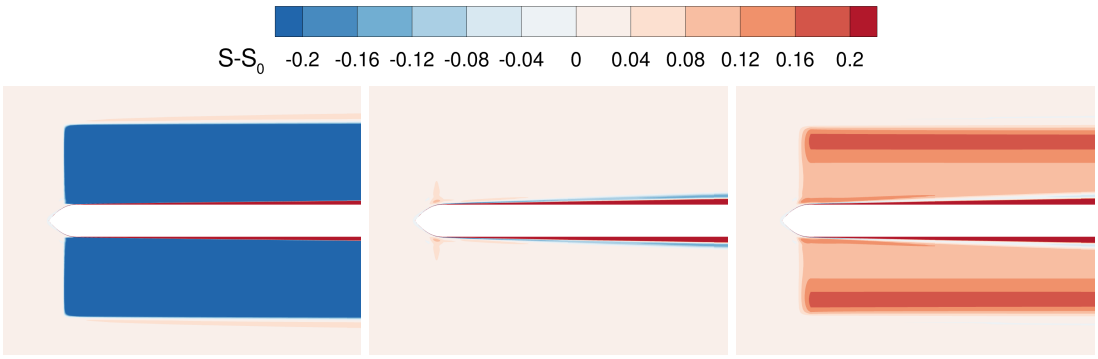

(a) Computation with $s_{E,0}$ (b) Computation with $s_{E,1}$ (c) Computation with $s_{E,2}$

Figure 3.18: Entropy slices computed by RANS/BET with different energy source terms.

Figure 3.19 shows temperature and density radial profiles half a propeller radius behind the rotation center. For $s_{E,0}$, the temperature drop and density rise mentioned in section 3.4.1 are clearly visible. Adding an energy source term solves this problem, but the differences in the profiles between $s_{E,1}$ and $s_{E,2}$ are very small. They become negligible when looking at the axial momentum profiles in figure 3.20a. The impact of the very presence of the energy source term vanishes when inspecting the axial velocity profiles from figure 3.20b. The same thing was observed for the tangential momentum and velocity. This is consistent with the fact that the energy source term has no influence on the propeller loads, as seen in figure 3.16b.

A few things can be conclude from this investigation into the energy source term:

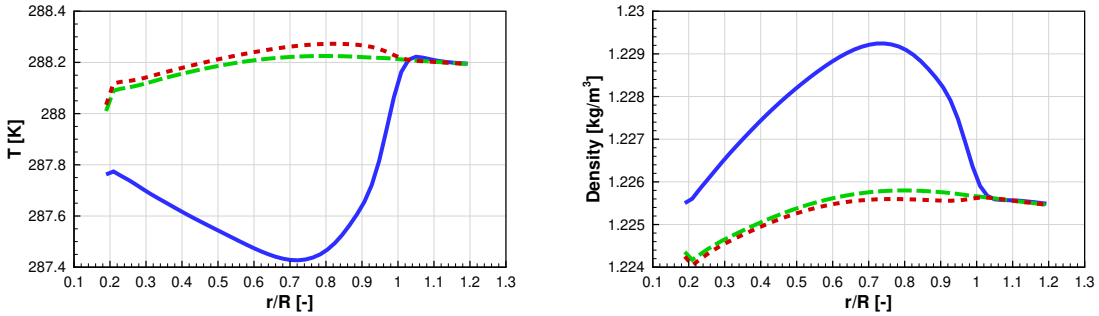

(a) Temperature profile

(b) Density profiles

$s_{E,0}$ (——), $s_{E,1}$ (– –), $s_{E,2}$ (- - -)

Figure 3.19: Radial thermodynamic profiles in the wake half a propeller radius behind the rotation center.

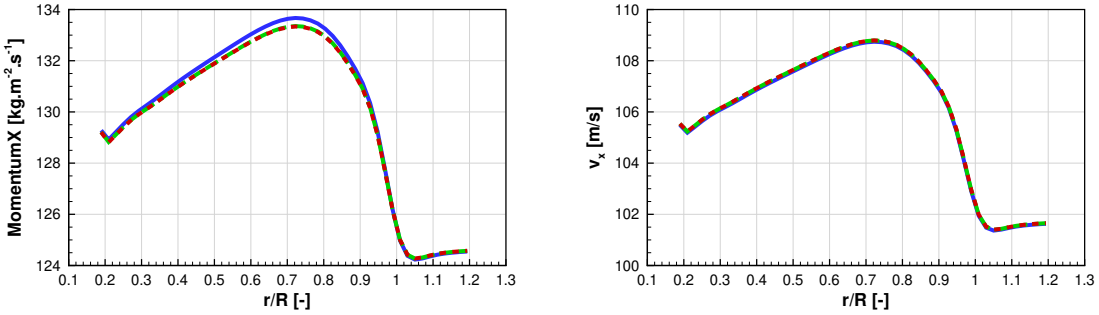

(a) Axial momentum profile

(b) Axial velocity profile

$s_{E,0}$ (——), $s_{E,1}$ (– –), $s_{E,2}$ (- - -)

Figure 3.20: Radial kinematic profiles in the wake half a propeller radius behind the rotation center.

1. Adding a source term in the energy equation does not modify the propeller loads or the velocity fields for the propeller considered. However, its absence leads to decreasing entropy, and modified temperature, density and momentum fields. An energy source term must therefore always be included in computations.

2. The formulation $s_{E,1} = \boldsymbol{u} \cdot \boldsymbol{s_M}$ corresponds to the work done by the momentum body forces $\boldsymbol{s_M}$. It exactly compensates the increase in kinetic energy and does not lead to the creation of entropy.

3. It can be argued that the body forces should model the entropy created in the boundary layer of the real blades. This can be achieved by using a source term slightly greater than $s_{E,1}$.

4. It was shown analytically and using RANS/BET computations that $s_{E,2} = (\boldsymbol{s_M} \cdot \boldsymbol{e_\theta})\Omega r$ accounts for the viscous losses modeled in the computation by the drag from the 2D airfoil polars.

This investigation is continued in the actuator line study in section 4.1.4, where the flow is no longer time-averaged and where the differences between the formulations have more impact locally.

Conclusion

This chapter first detailed how the RANS/BET model works, and how it was implemented. In short, at each iteration, it samples local CFD velocities along radial lines and uses a BET analysis to compute spanwise blade loads from tabulated 2D airfoil polars. The blade loads are then modeled in the CFD computations as source terms. Comparing different parametrizations, three conclusions were drawn related to source term distribution, unifying the different practices from the literature. It was found that:

- the shape of the source term volume has no impact on propeller performance or on the flow field.
- the shape of the distribution function of the source terms in the axial direction has no direct impact on the simulation outside of the body-force volume, the only parameter that matters is the percentage of source terms distributed upstream of the sampling lines.
- 50% of the source terms should be placed upstream of the sampling lines to match fundamental momentum theory results. When the RANS/BET model is setup this way, it closely matches results from the blade element momentum theory computations.

The necessity of tip-loss corrections was explained. A generalized implementation of Glauert's tip-loss correction for non-axial flow was proposed, as well as a calibrated correction of the blade's tip loads. Glauert's correction alone proved to be insufficient to match blade-resolved loads at the tip, so it will be combined with a calibrated loads correction in the rest of the thesis.

The study of the energy source term showed that its absence leads to temperature drops in the wake to compensate the increase of kinetic energy due to the momentum source terms. This also destroys entropy in the propeller area. As a result, an energy source term should always be used in body-force computations. Two formulations of this source terms were compared, analytically and numerically. Both solve the problem of the temperature drops in the wake, and it was found that one is isentropic whereas the other one creates entropy associated to the viscous drag. The study will be continued in section 4.1.4 for the actuator line.

Chapter 4

Development of a robust actuator line model

This chapter focuses on the development and study of the actuator line model. The model is similar to what was presented in the literature review, but with a novel implementation technique for propellers that significantly increases computational efficiency. This implementation is detailed in the first section, along with a follow-up of the previous chapter's study on the energy source term.

A study of the effect of source term distribution using a 2D Gaussian smearing function is conducted, first by analyzing the results of a computation with prescribed loading, and then by quantifying the effect of the smearing parameter on blade loads in fully coupled simulations.

An investigation into velocity sampling is then made, comparing the point and integral sampling techniques used in the literature. The effect of the sampling position relative to the position of the previous source term injection is also studied, as it is an implementation aspect that is rarely mentioned in literature.

Finally, the robustness of the model to mesh variation and time-step variation is evaluated.

Contents

4.1 Actuator line model implementation

The actuator line model developed in this work is essentially based on previous work from the literature review presented in section 1.4, but with slight changes in the implementation to allow fast computations. First, the choices that were made in this work relative to the possibilities offered in the literature are presented. Next, the model implementation, which is a specificity of this work, is explained. Finally, the investigation into the energy source term, initiated in section 3.4 is continued for this unsteady model.

4.1.1 Model overview

As for the RANS/BET model, the workflow of the actuator line model can be divided into a few steps, which are presented hereafter and illustrated in figure 4.1.

1. An unsteady RANS computation is initiated on a mesh that does not include the rotor blades. In this implementation, an overset cylinder, shown in figure 4.1a, is required. This cylinder is used as a support for the actuator lines and contains all the source terms. The reason for this is explained more in depth in section 4.1.2. Each cell in the radial direction is used as an actuator line element.
2. At the end of each CFD iteration, the velocities from the solution are sampled for each element. The model allows sampling at the mesh cell associated to the actuator line element, or integral averaging as presented in section 1.4.4.2. The effect of the sampling method is investigated in section 4.3.1.
3. The blade loads are computed on each actuator line element with the BET and the 2D airfoil polars presented in section 2.4.
4. The actuator lines are rotated by 1°. The reason for doing this step before loads distribution is explained in section 4.3.2.
5. The loads of each actuator line element are distributed using the 2D Gaussian kernel from equation (1.77), which projects the loads around the actuator line element, at a constant radius. Since each cell in the radial direction is used as an actuator line element, this ensures that the loads are smoothly distributed between the hub radius R_h and R, and that no source terms are distributed above the tip of the blades. The Gaussian kernel is isotropic in the curved iso-radius surface, but the Gaussian parameter can vary with the radius (to be linked to the local chord length for instance). The effect of the distribution method is presented in section 4.2.
6. These source terms are accounted for at the next CFD iteration, and the previous steps are repeated.

4.1.2 Implementation

In this work, the implementation of the actuator line model fully relies on an overset cylindrical grid. This mesh is shown in figure 4.1a, and slices are shown in green in figure 2.15. The grid has 360 cells in the azimuthal direction, 35 in the axial direction, and 120 in the radial direction, for a total of 1.5 million cells. The points are evenly distributed in the axial and azimuthal directions, but unevenly in the radial direction: they are closer together in the proximity of the hub, and at $r = R$ to better capture the tip vortices. Because this radial distribution corresponds to the discretization

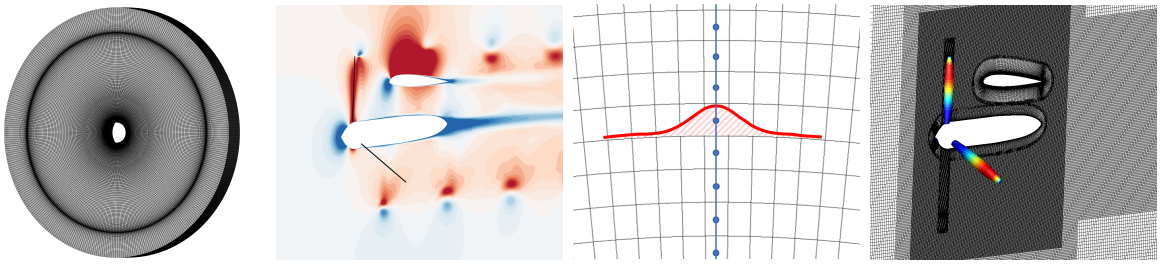

(a) Overset cylinder (b) Velocity sampling colored by axial velocity (c) Loads distribution (d) Iso-surface of g_{2D}, colored by axial load

Figure 4.1: Actuator line method recap.

of the actuator line as well, it is also better to add more points where the loading gradients are the largest, which justifies further the extra refinement at $r = R$. At the very tip of the blade, the dimensions of the cells are $l_\theta = c_{tip}/3 = \bar{c}/7$, $l_r = c_{tip}/20 = \bar{c}/50$ and $l_x = c_{tip}/7 = \bar{c}/18$, where $\bar{c}$ is the average chord length over the whole blade span. The cell length in the azimuthal direction is a little small compared to the best practices presented in section 1.4.2, especially considering the Gaussian parameter ϵ is linked to the local chord length in the following. This is a clear downside of using a cylindrical grid for which the cells expand with the radius. The size of the cells is however only a problem at the tip of the blade, since the local chord length increases downward the blade, and so does l_θ. Regardless, a mesh sensitivity study is presented in section 4.4.1.

As briefly explained in the previous section, the cylindrical grid is the direct support of the actuator lines. There are two reasons for this:

- The first is due to the modeling of the tip vortices. As explained in section 1.4.3, projecting the blade loads using 3D Gaussian functions leads to smeared tip vortices and thus to overestimated blade loads. It is reported in the literature that using 2D projection kernels limits this effect as it avoids smearing the blade loads over the tip of the blade. Using a cylindrical grid is then a convenient way to implement a 2D Gaussian projection.

- The second is due to implementation considerations. When using a 3D Gaussian projection, each actuator line element of each blade creates a source term over the whole computational domain. This is clear when looking at the double sum from equation (1.70). From an implementation standpoint, the computational domain is distributed between different processors. The processor that computes the AL element load must therefore send the load to all other processors so each one can account for the contribution of that element on its zone. This can quickly become very computationally expensive if the actuator line is very refined or if the propeller has many blades. The issue is even more striking if the velocity sampling is done using the integral averaging technique. Indeed in this case, the weighted average of each zone must be communicated to a single processor for it to compute the sum and then the load of the element, and so for every AL element.

  This issue is not addressed in literature, and some implementations probably only focus on the zones that are in close proximity of each AL element, a list of which can be computed in preprocessing, to avoid some MPI communications. Nevertheless, it is generally known in the aeronautics community that the actuator line model does not offer significant gains in

computational cost compared to full blade-resolved computations. However, the method undeniably still offers time gains in mesh creation.

The major upside of using a 2D projection Gaussian kernel and a cylindrical grid is that all actuator line elements become independent of one another. If the cylinder is split between the different processors at constant radii, the integral velocity sampling, the computation of the AL element loads, and the distribution of the source terms, can simply be made with manipulations on arrays and no MPI communications. The co-process time due to the actuator line computations thus become negligible compared to the cost of the CFD iteration. The gains allowed by this implementation are quantified at the end of chapter 6 for the installed configuration.

All things considered, the significant gains compared to blade-resolved computations offered by this implementation are made at the cost of a few downsides:

- The cylindrical Chimera grid induces an additional cost because of the interpolations that must be made at each iteration. This price is however a small one to pay, because since the cylinder does not move (only the position of the source terms rotates), the interpolation coefficients can be computed only once at the beginning of the simulation, which accelerates the interpolations in the rest of the computation.

- The major drawback of this method comes from the dissipation induced by the Chimera interpolations. Since the cells of the cylinder and of the background grid are not of identical size in the interpolation zone, some information is necessarily lost in this area. This is especially true in the region of the tip vortices because the cylindrical grid is especially fine in this zone. In the cases studied in this work, the background mesh was chosen relatively fine to correctly propagate the tip vortices in the wake, but the dissipation can still be significant. It is something to keep in mind when using a similar implementation, and in any case, this is an issue that is unavoidable with any Chimera computation, even for blade-resolved simulations.

4.1.3 Shape of the cylindrical grid

To study interaction effects, the presence of the nacelle is important because it changes the flow field seen by the propeller, and its impact on nearby lifting surfaces, for instance, can be significant. However, in actuator line computations from the literature, the hub is most often not included. The body forces thus create strong root vortices which should not exist when the hub is there. In this work, the nacelle is always included, so the actuator line model must be implemented in a way that does not create root vortices that do not appear in the blade-resolved simulations. This was achieved progressively by bringing the actuator line closer and closer to the hub surface. This short study is presented in this section, which justifies the shape of the cylindrical Chimera grid shown previously in figure 2.15.

Three cylindrical grids are studied, which are shown in figure 4.2. For each simulation, the actuator line goes all the way down to the bottom of the colored meshes. Source terms are injected in the computation starting two cells above the bottom of the mesh, because these two layers are used for interpolation between the cylinder grid and the hub grid in the Chimera approach. The second grid has significantly different cell sizes between the two meshes, especially in the upstream area at the radius of the blade root. Trying to bring the cylindrical grid even lower towards the hub thus leads to Chimera interpolation problems. This is why the shape of the cylinder was changed for Grid 3, which fits the shape of the hub and copies the growth rate of the hub mesh to avoid

differences in cell size. This third mesh stops just above the most refined cell layers of the hub, 20 cells away from the hub surface.

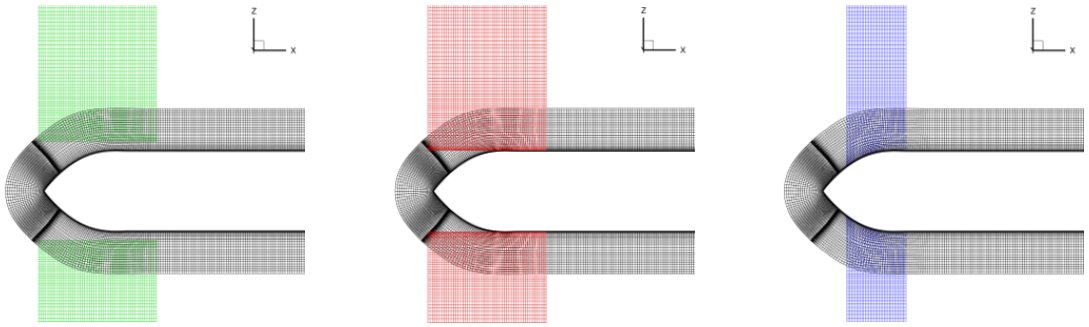

(a) Grid 1 (b) Grid 2 (c) Grid 3

Figure 4.2: Shapes of the Chimera cylinder tested for the actuator line computations.

Axial slices of the tangential velocity fields obtained with each grid, extracted half a propeller radius behind the rotor plane, are shown in figures 4.3a, 4.3b, and 4.3c. The same slice for a blade-resolved simulation is added in figure 4.3d for reference. Grid 3 is the only one that correctly neutralizes the root vortices. The reason for this is that the root vortices originate at the extremities of the actuator lines, but for Grid 3 the hub boundary layer prevents them from developing.

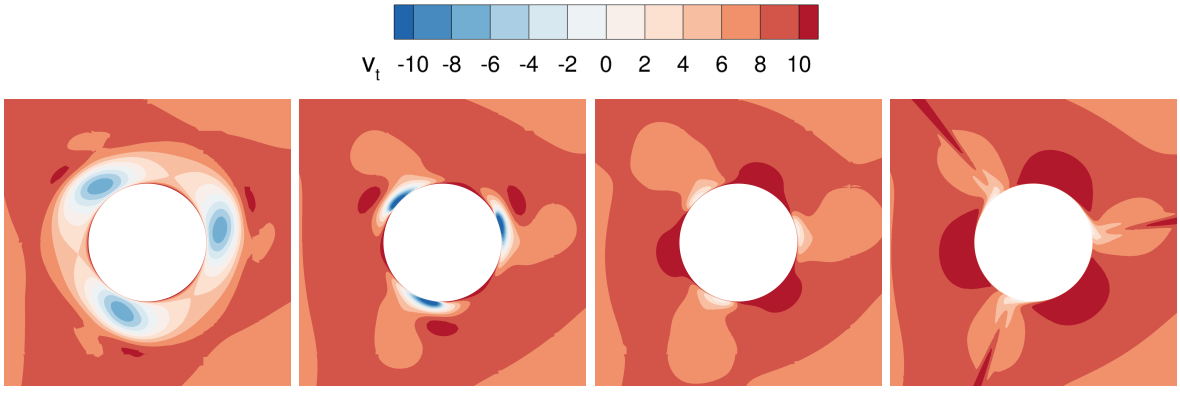

(a) Grid 1 (b) Grid 2 (c) Grid 3 (d) Blade-resolved

Figure 4.3: Slices of tangential velocity fields half a radius behind the rotor plane.

In the flowing, the third cylindrical grid is always used. However this mesh is not a perfect cylinder, so its i index (corresponding to the radial direction) is no longer at a constant radius at the very bottom of the cylinder. Yet because the method implementation relies on arrays manipulations, the 2D Gaussian distribution (and integral sampling), is made at constant i. As a result, near the hub, the sampling and the distribution is not strictly made at iso-radius. In practice, this is assumed to have very little impact on the propeller performance and the velocity fields, as the effect is very localized. This can even be seen as a positive side effect, because the

source term distribution better follows the streamlines, which are dominated by the presence of the spinner in this area.

4.1.4 Effect of the energy source term

This section studies the effect of the source term in the energy equation on actuator line computations. As in section 3.4, three formulations of the source term are compared: $s_{E,0} = 0$, $s_{E,1} = \boldsymbol{s_M} \cdot \boldsymbol{u}$, and $s_{E,2} = (\boldsymbol{s_M} \cdot \boldsymbol{e_\theta})\Omega r$ (where $\boldsymbol{s_M}$ is the source term vector from the momentum equations). A computation was conducted with each expression. Figure 4.4a shows the the radial distribution of the energy source term for each method, before it being multiplied by the Gaussian distribution g_{2D}. Similarly to what was observed for the steady model, $s_{E,2}$ is a little larger than $s_{E,1}$ along the blade. As can be seen in figure 4.4b, all three computations lead to roughly the same blade loads, with slightly greater tip loads for the computation without an energy source term.

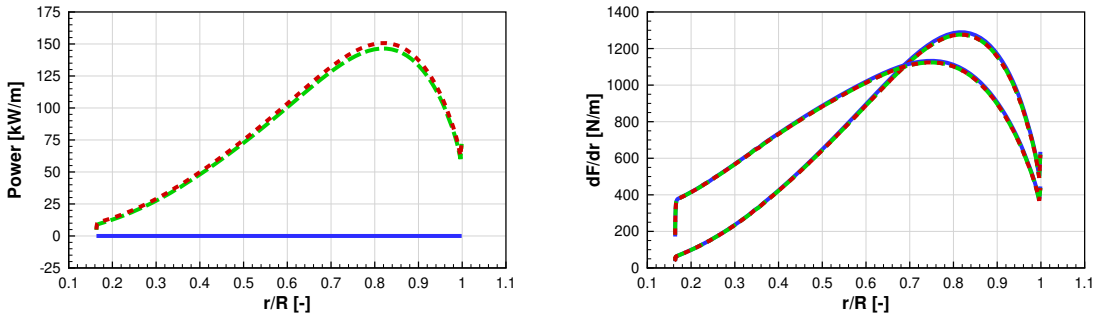

(a) Radial profiles of the energy source terms, before the distribution by g_{2D}

(b) Axial and tangential blade loads

$s_{E,0}$ (——), $s_{E,1}$ (– –), $s_{E,2}$ (- - -)

Figure 4.4: Radial profiles obtained with the different energy source term formulations.

Slices of the temperature fields are shown in figure 4.5 for the three actuator line computations and for a reference blade-resolved computation. For the actuator line computations with $s_{E,1}$ and $s_{E,2}$, as well as for the blade-resolved computations, the temperature only varies close to the blade due to pressure effects. However, the actuator line computation with $s_{E,0}$ is characterized by significant temperature drops (by up to 5°) in the blade wakes. As explained in section 3.4, this is due to a drop in internal energy to allow for the fluid to accelerate in line with the momentum source terms.

This temperature drop is almost fully compensated by a rise of density, because the pressure field, not shown here, is almost identical for all actuator line simulations. This rise in density also leads to a rise in momentum compared to the other actuator line computations, but the velocity fields stay relatively similar, leading to the comparable blade loads from figure 4.4b. This is interesting because if only looking at the blade loads, velocity and pressure fields, it could be concluded that the energy source term can be neglected. This is for instance what was done by Merabet and Laurendeau while studying 2D airfoils [53], which led them to neglect the energy source term in their follow-up work on helicopter modeling with actuator lines [54]. However, neglecting this source term leads to significant physical inconsistencies, such as decreasing entropy, which was already observed for the RANS/BET model. Entropy slices are shown in figure 4.6.

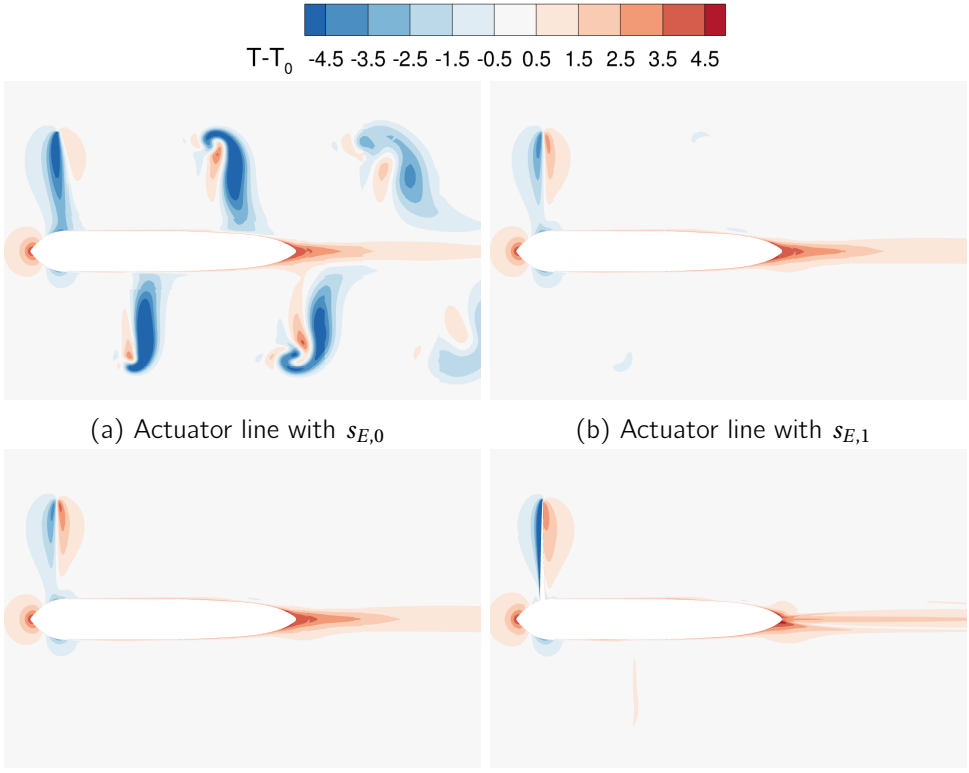

(a) Actuator line with $s_{E,0}$

(b) Actuator line with $s_{E,1}$

(c) Actuator line with $s_{E,2}$

(d) Blade-resolved

Figure 4.5: Temperature slices.

The entropy effects are more visible in the actuator line model than for the steady model because they are concentrated around the blades. Figure 4.6a also shows some oscillations in the flow. The computations with $s_{E,1}$ and $s_{E,2}$, which were very similar for the fields mentioned until now, differentiate themselves slightly when looking at the entropy fields. $s_{E,2}$ creates some entropy, which is of the same order of magnitude as the one created in the blade-resolved computation. This observation is consistent with the demonstration of the previous section which showed that $s_{E,2}$ creates the entropy related to the viscous losses on the blade. As for the simulation with $s_{E,1}$, the actuator lines seem to create no entropy. The slightly negative patches are assumed to be caused by numerical phenomena, most likely due to the Chimera interpolations at the downstream boundary of the overset cylinder.

The conclusions of this section are mostly similar to the ones made for the steady body-force model. Neglecting the energy source term has little effect of pressure and velocity fields, and on blades loads. It however leads to temperature drops in the wake and to the destruction of entropy. $s_{E,1}$ leads to a fully reversible evolution of the fluid, whereas $s_{E,2}$ creates entropy. This section further offers a comparison with a blade-resolved reference, which shows that the entropy created by $s_{E,2}$ is very similar to the entropy field of the blade-resolved simulation. This serves as a validation of the demonstration made in chapter 3, which showed that this formulation modeled the energy losses associated to airfoil drag.

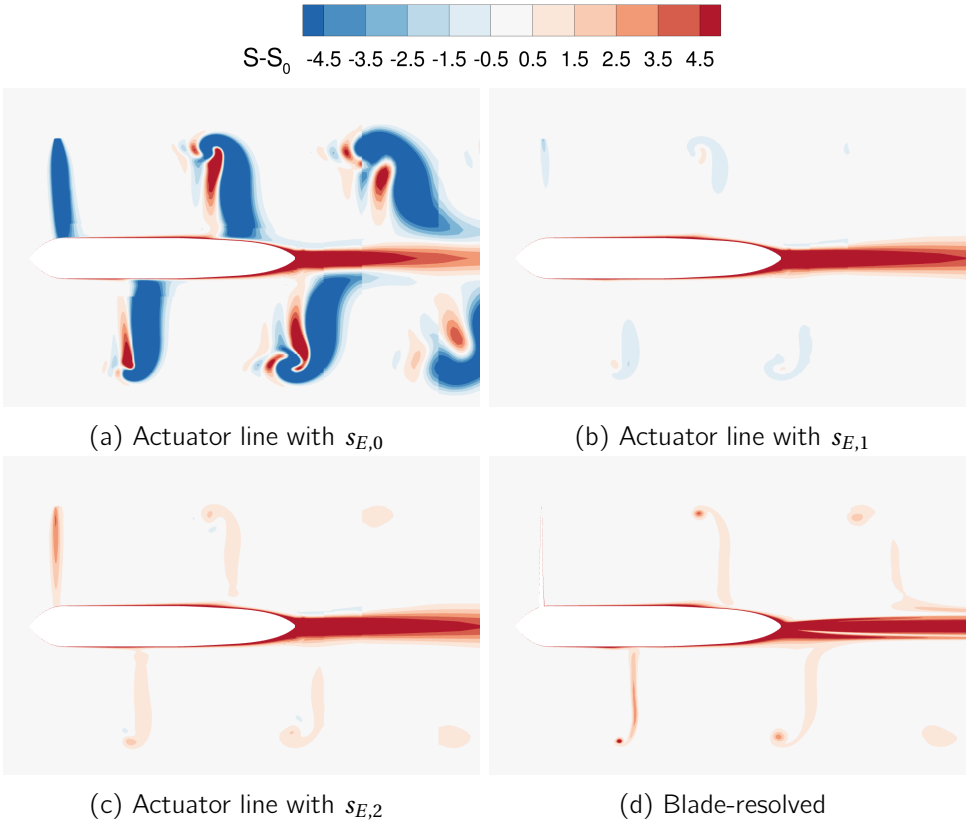

(a) Actuator line with $s_{E,0}$

(b) Actuator line with $s_{E,1}$

(c) Actuator line with $s_{E,2}$

(d) Blade-resolved

Figure 4.6: Entropy slices.

4.2 Source term distribution

4.2.1 Computation with prescribed loading

This section shows results of an actuator line computation in which the blade loads are prescribed from a blade-resolved computation. The objective is twofold: the first is to show what the flow field computed by an actuator line model looks like, and the second is to evaluate the wake precision that can be expected from such a simulation in the ideal case where the injected loads are exactly the ones that are supposed to be obtained. In this section, the prescribed loading was distributed with the 2D Gaussian function g_{2D} from equation (1.77) with a Gaussian parameter ϵ that varies with the local chord length such that $\epsilon = 0.3c$. The actuator line results are compared to results from a blade-resolved simulation used as reference.

4.2.1.1 Wake analysis

Figure 4.7 shows slices of the propeller wake half a radius behind the rotor plane. Axial velocity is represented in figures 4.7a and 4.7b, and tangential velocity in figures 4.7c and 4.7d. The lines from the blade-resolved field have been added over the actuator line slices to ease the comparison. Except in the viscous wake of the blades where the comparison is less straightforward, the actuator line reproduces the blade-resolved fields very well. The trends of both the axial and tangential velocities are well reproduced between the blade wakes and in the hub region. The limits of the

actuator line model can be seen in the viscous blade wakes, and this zone is investigated in the following.

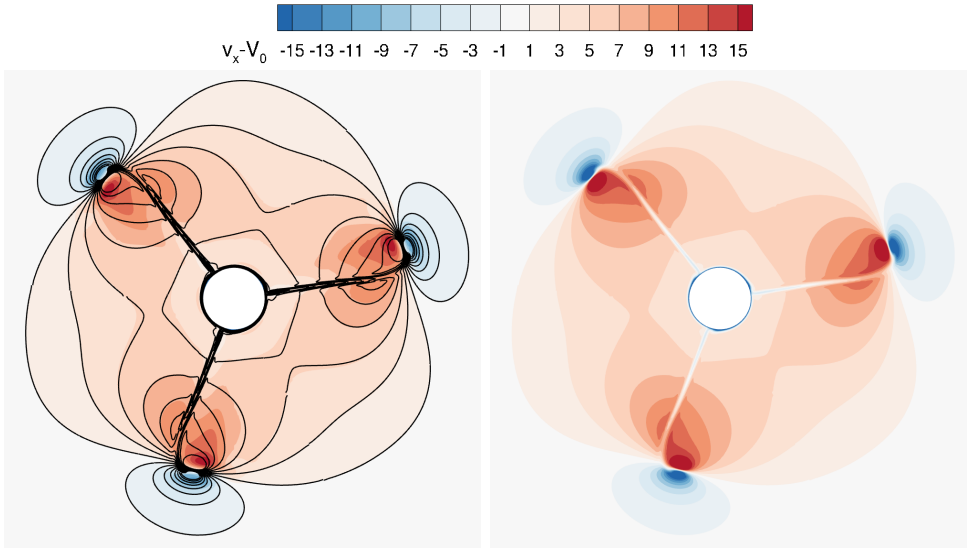

(a) Actuator line – v_x (b) Blade-resolved – v_x

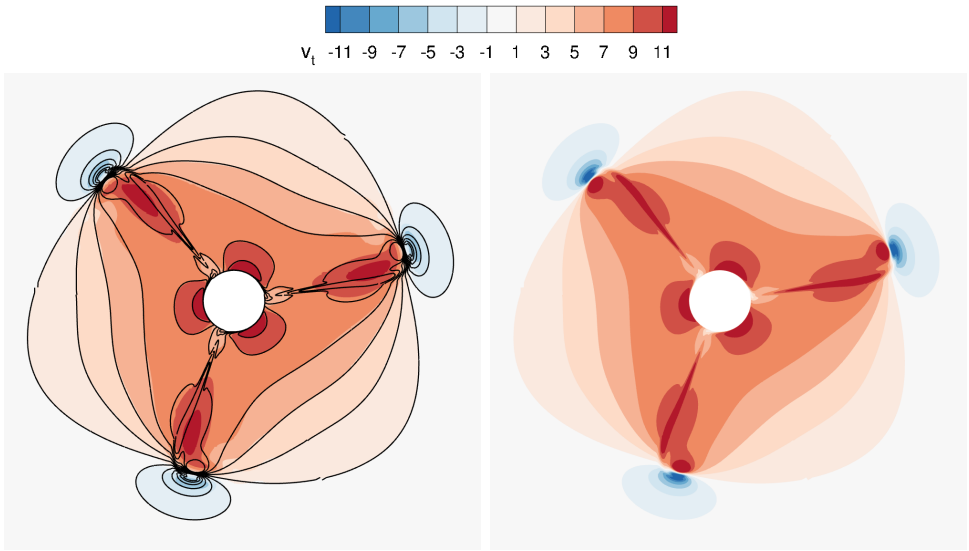

(c) Actuator line – v_t (d) Blade-resolved – v_t

Figure 4.7: Velocity fields slices for actuator line and blade-resolved computations.

Figure 4.8 shows the same slices as the previous figure but focused in the blade wake area. Two important areas are worth commenting:

1. The first area of interest is the whole space in the direct wake of the blade. In the blade-resolved simulation, it is characterized by a viscous wake which can be seen on figure 4.8c as a deficit in axial velocity along a line. In the actuator line computation, the viscous wake does not exist because no blade walls are modeled. However, the actuator line model does include the viscous drag of the 2D airfoil profiles, which is distributed in the computation in the

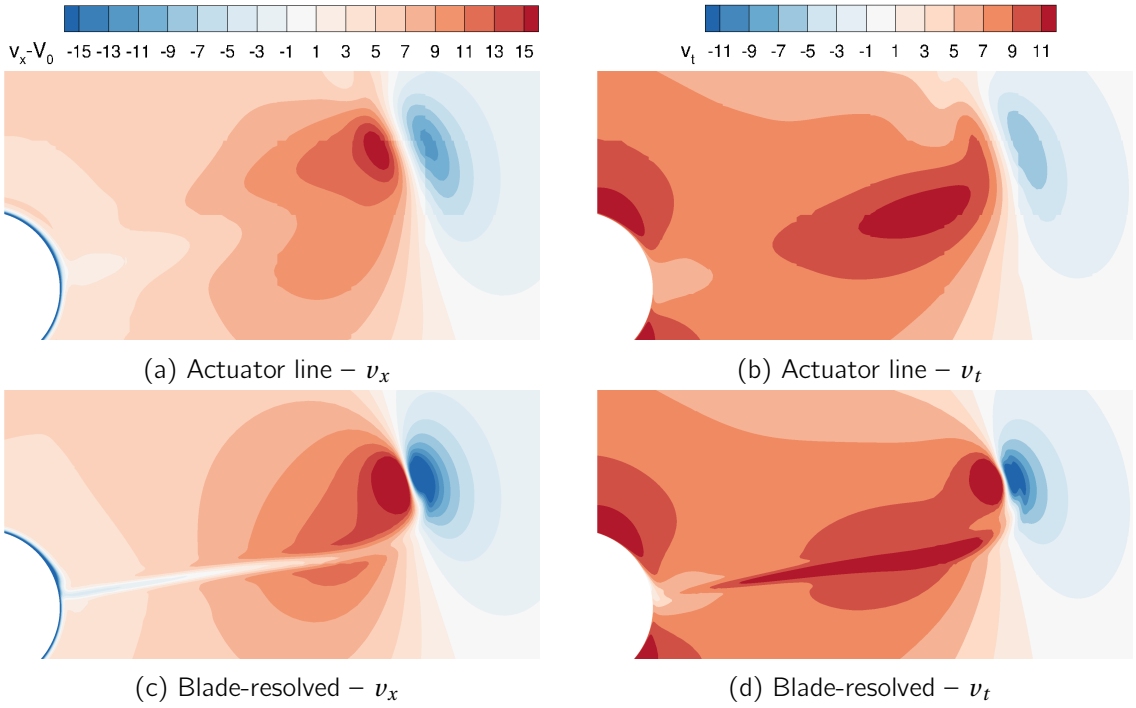

(a) Actuator line – v_x

(b) Actuator line – v_t

(c) Blade-resolved – v_x

(d) Blade-resolved – v_t

Figure 4.8: Velocity fields for actuator line and blade-resolved computations – focus in blade wake.

same ways as the lift, using the Gaussian smearing function. The effect of this drag force is to locally lower the axial component of the fluid, as can be observed in figure 4.8a. When the Gaussian parameter is chosen very small (this can in practice only be done with prescribed loading or else instabilities appear), the drag is concentrated on a line, which manifests itself in the wake with something that replicates the viscous wake very well, splitting the tip vortex as in figure 4.8c.

2. The second is the tip vortex area, on the right of the figures. The slices clearly demonstrate the vortex smearing that results from Gaussian distribution of the body forces. This shows that despite using a 2D Gaussian kernel to avoid distributing source terms above the radius of the blade, and using a smearing parameter close to what is considered in literature as the optimal value of $\epsilon = 0.25c$ (presented in section 1.4.2), the tip vortices are still weaker than in the blade-resolved simulation. Two aspects should however be kept in mind to temper this observation. First, the smeared vortex observed in the actuator line computation could partly be due to numerical dissipation. Indeed, the fully structured mesh from the blade-resolved simulation is very refined in the tip area, whereas the Cartesian background grid of the actuator line computation, although very fine as well, does not allow similarly small cell length, especially in the radial direction, which tends to dissipate the root vortex core. Second, some of the smearing must also come from the Chimera interpolation. This is also a downside of the chosen implementation of the actuator line method, as explained in section 4.1.2. To allow for a better comparison between the actuator line and blade-resolved methods, a comparison was made using a Chimera blade-resolved computation using the setup detailed in section 2.2.2.2 but for the isolated configuration, with the same background mesh as for

the actuator line computations. Unfortunately, the grids were not fine enough for the viscous wake to go through the Chimera interpolation, which creates a bias in the comparison. This is shown on figure 4.9 which shows the dissipation of the viscous wake across the Chimera interpolation, in particular near the tip of the blade. Note that this slice only shows the cells that are solved, the masked and interpolated cells are hidden. Nevertheless, it was found that the actuator line tip vortices are still more diffuse than the ones from the Chimera blade-resolved solution, but not as strikingly as with the full structured mesh. This effect is investigated more in depth in chapter 5.

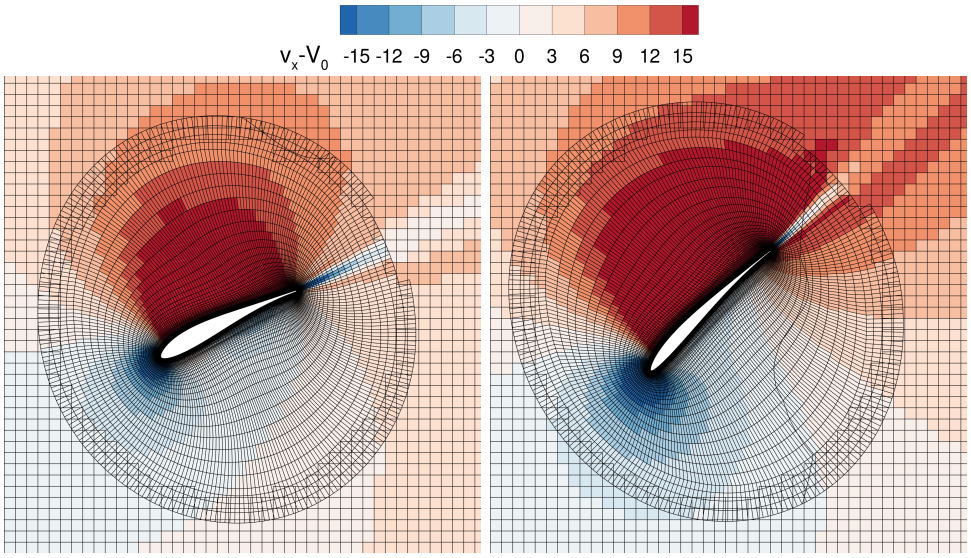

(a) Slice at $r/R = 0.4$ (b) Slice at $r/R = 0.75$

Figure 4.9: Dissipation of the viscous wake of a blade-resolved Chimera computation.

Slices of the tip vortices were made half a radius behind the propeller, the normal of the plane being chosen as the vector going through the pressure minimums. The extraction process is illustrated in figure 4.10. This method is used throughout the rest of the dissertation when studying the tip vortices. It ensures that the slice is made normal to the vortex [18]. A line of this plane is then extracted, which goes through the center of the vortex and perpendicular to the viscous wake direction. Figure 4.11 shows the tangential velocity and pressure fields along this line. It shows that the smearing clearly manifests itself as a weaker velocity field inside the vortex, and a larger viscous core radius. This also results in a smaller pressure drop at the center of the vortex due to the radial equilibrium.

In a fully coupled actuator line computation, the smeared tip vortices create smaller induced velocities at the actuator line location, which lead to stronger loads. These stronger loads then induce tip vortices with a greater circulation. So in practice, when the simulation is fully coupled, the blade loads, and the wake to some extent, are in a way more accurate than what is shown in this section because of slight error compensation.

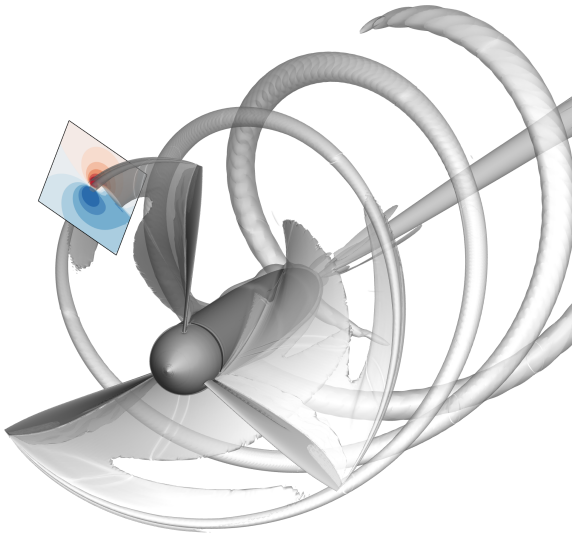

Figure 4.10: Illustration of the vortex extraction procedure, for a blade-resolved computation.

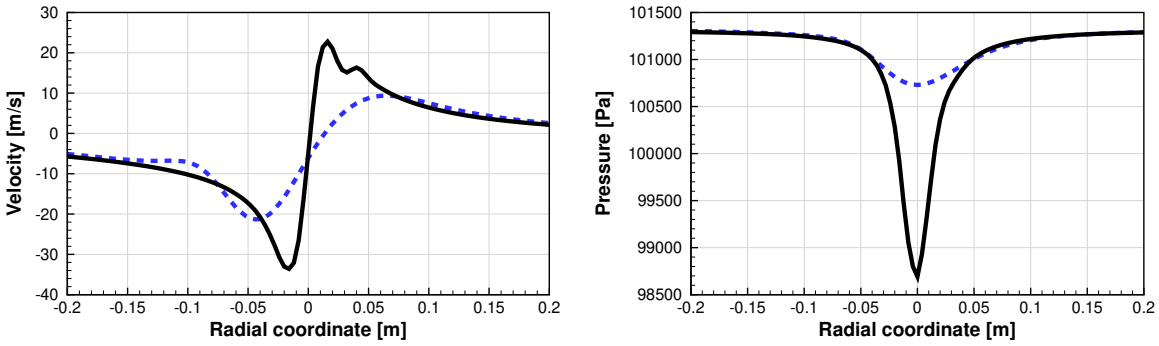

(a) Tangential velocity

(b) Pressure

Figure 4.11: Extractions on a line across the tip vortex, half a radius behind the rotor.

4.2.1.2 Blade element theory computation

In this subsection, the converged flow fields from the actuator line computation with prescribed loadings are used to recompute blade loads using the blade element theory. The velocities are sampled with and integral averaging method using the same function used for the distribution of the source terms (g_{2D} with $\epsilon = 0.3c$). The loads recomputed in this manner, as well as the prescribed loads injected in the computation, are shown in figure 4.12. As expected from the literature review and the previous discussion, the BET analysis overshoots the tip loads because the smeared vortices lead to smaller induced velocities. At the blade root, the blade loads are underestimated. In both cases, it can be expected for the blade loads computed with a fully coupled simulation to be in between the two curves shown here to reach an equilibrium between flow fields

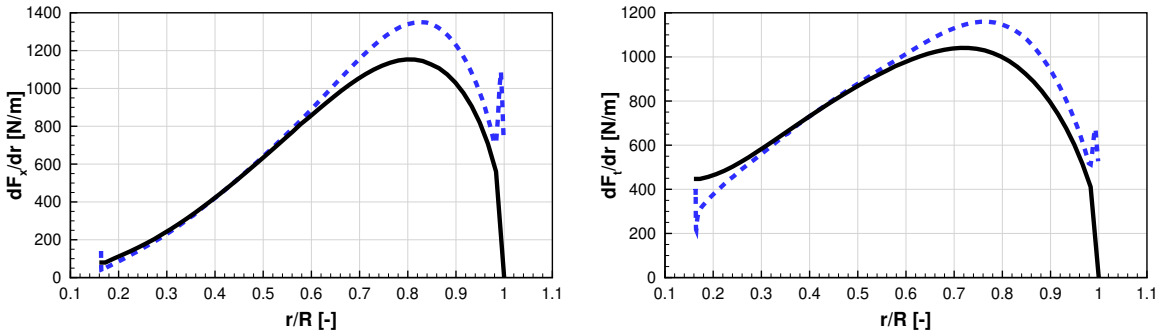

(a) Axial blade loads (b) Tangential blade loads

Blade-resolved reference, used for the prescribed loading (——),
Loading computed from BET analysis at the end of the computation (- - -)

Figure 4.12: Axial and tangential blade loads.

and blade loads, as discussed above for the velocity fields in the vortices. It is also interesting to note the oscillations at the tip of the blade. In a fully coupled simulation, these oscillations would not be stable. The simulation would stabilize with a different loading at the tip, and thus create a solution with a slightly different flow topology. As a result, it makes little sense to spend time trying to optimize the loads distribution function to get the best prediction of the flowfield possible, because the flow topology will necessarily be different at the blade tip when switching to a fully coupled simulation. Because of this, in the rest of the dissertation, the actuator line computations are always fully coupled, including the parametric studies that are conducted in the following subsection.

4.2.2 Effect of the Gaussian parameter

The effect of the Gaussian smearing parameter ϵ is studied in this section. All actuator line computations are fully coupled, meaning that the blade loads are computed at each time step with the BET from the local velocities before being distributed in the CFD computation. The velocity sampling is made with the integral averaging method, weighted by the 2D Gaussian distribution function g_{2D}. The smearing parameter thus has an effect on the velocity sampling and on loads distribution. Four different smearing parameters are studied, one that is constant equal to $\epsilon = 0.4\bar{c}$ (where $\bar{c}$ is the blade's average chord length), and three that vary with the local chord length: $\epsilon = 0.5c$, $\epsilon = 0.4c$, and $\epsilon = 0.3c$. As a reminder, the blade's chord law is shown in figure 2.2. Slices of the g_{2D} field are shown in figure 4.13 for each smearing parameter. It was found that parameters lower than $\epsilon = 0.3c$ lead to strong oscillations in the flow caused by a Gaussian function discretized over too few cells at the tip of the blade.

The blade loads computed with the parameters $\epsilon = 0.4\bar{c}$ and $\epsilon = 0.4c$ are shown in figure 4.14. Despite the source term distribution being relatively different on the whole span, the differences between the two computations are only visible at the tip. In this region, the maximum thrust is slightly shifted toward the tip for the computation with $\epsilon = 0.4\bar{c}$, and the loads are a little more overestimated. This overestimation, caused by lower induced velocities, tends to show that the concentration of the tip vortex is more influenced by the size of ϵ at the blade tip than by its value on the whole blade span. Linking ϵ to the local chord thus seems to be a good idea because it

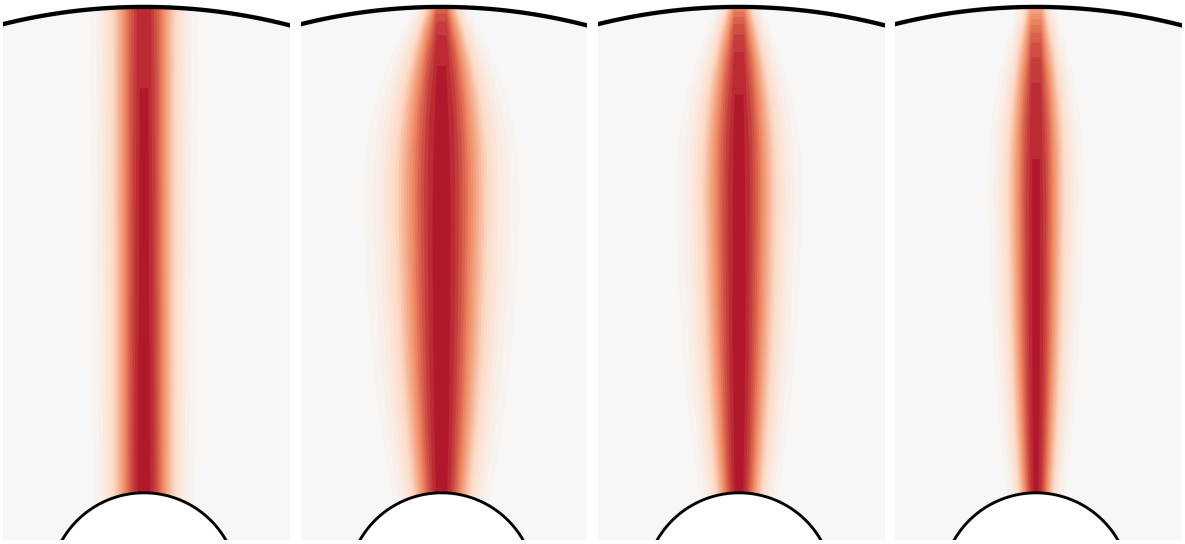

(a) $\epsilon = 0.4\bar{c}$ (b) $\epsilon = 0.5c$ (c) $\epsilon = 0.4c$ (d) $\epsilon = 0.3c$

Figure 4.13: Slices of g_{2D} fields in rotor plane for different Gaussian parameters ϵ.

ensures a reduced smearing at the blade tip. However, it is not clear whether this approach offers any other real benefits. Its effect on the blade wake compared to $\epsilon = 0.4\bar{c}$ does not lead to any striking difference. Nevertheless, reducing the loads at the tip is appreciated and ϵ is always linked to the local chord in the rest of the thesis.

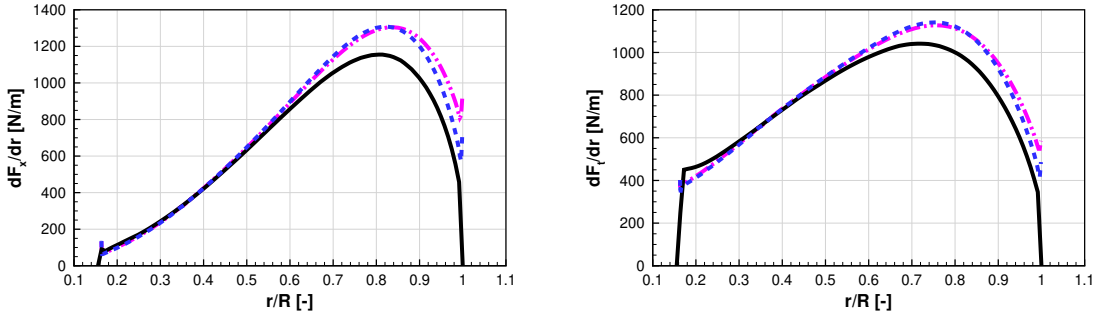

(a) Axial blade loads (b) Tangential blade loads

Blade-resolved (——), Actuator line with $\epsilon = 0.4\bar{c}$ (-·-·-), Actuator line with $\epsilon = 0.4c$ (- - -)

Figure 4.14: Blade loads obtained with different smearing parameters.

Next, the effect of the smearing length is investigated. The blade loads computed with the parameters $\epsilon = 0.5c$, $\epsilon = 0.4c$ and $\epsilon = 0.3c$ are shown in figure 4.15. Again, the differences can only be witnessed at the blade tip. As expected, reducing the smearing length tends to decrease the tip loads. This effect is however relatively small. A reason for this is that the chord length at the tip is very small, so that regardless of the value by which it is multiplied, the loads are approximately

distributed on the same amount of cells. In any case, the slow decrease of the tip loads with ϵ suggests that the blade-resolved loads could never be recovered with a mesh of acceptable size. This is interesting because studies in the literature often show that, at least for wind turbines, the actuator line model is quite sensitive to the choice of ϵ and that the correct loads can be obtained with $\epsilon = 0.25c$. This does not seem to be the case here. Yet, even though the actuator line model as implemented in this work consistently overestimates the tip loads, its relative insensitivity to ϵ is convenient from a design standpoint as it requires no calibration.

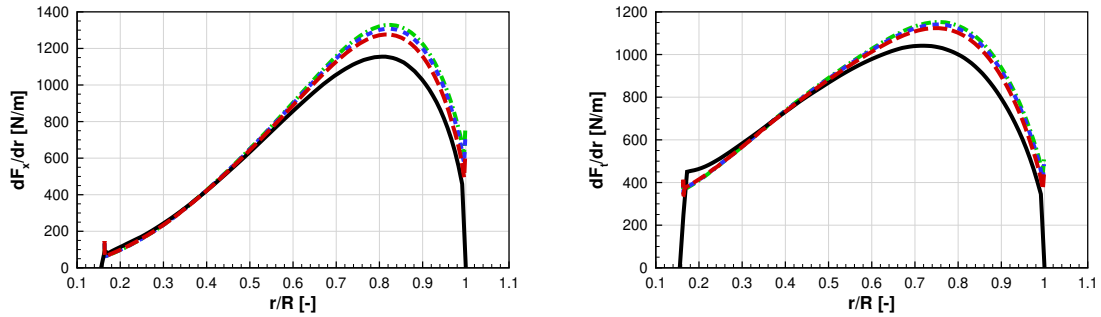

(a) Axial blade loads

(b) Tangential blade loads

Blade-resolved (——), Actuator line with $\epsilon = 0.5c$ (- - -),
Actuator line with $\epsilon = 0.4c$ (- - -), Actuator line with $\epsilon = 0.3c$ (— —)

Figure 4.15: Blade loads obtained with different smearing parameters.

4.3 Velocity sampling

4.3.1 Point and integral sampling

The model's robustness to the smearing parameter is also a positive consequence of the integral sampling method. In this section, two sampling methods are compared: integral averaging and sampling directly on the actuator line points, as done in the original implementation of the models. Two actuator line computations were conducted for each approach, with $\epsilon = 0.4c$ and $\epsilon = 0.3c$. The blade loads are shown in figure 4.16. The first thing to note is that the line sampling method creates instabilities when the smearing parameter is small ($\epsilon = 0.3c$). These instabilities create the load oscillations shown here, but also oscillations in time, from one time step to the other. An attempt was made to stabilize the computation by lowering the time step. The oscillations disappeared almost completely, and the loads stabilized just below the computation with $\epsilon = 0.4c$, thus only marginally reducing the gap with the blade-resolved loads that was identified in the previous section. Second, the simulation using line sampling and $\epsilon = 0.4c$ leads to tip loads that are slightly smaller than with integral sampling and the same smearing parameter. They are actualy much closer to the ones obtained with integral sampling and $\epsilon = 0.3c$. In theory, as explained in section 1.4.4.2 line and integral sampling should lead to the same result for 2D steady incompressible flow, and by neglecting viscosity and drag. The difference observed between the two methods are thus probably linked to the drag component that is included in the actuator line simulations shown here, and to the compressibility that is substantial near the tip. Finally, it appears that the integral sampling is less sensitive to the smearing parameter.

In the rest of the dissertation, the integral sampling method is retained for the robustness it offers, and because line sampling offers no significant improvement on loads prediction.

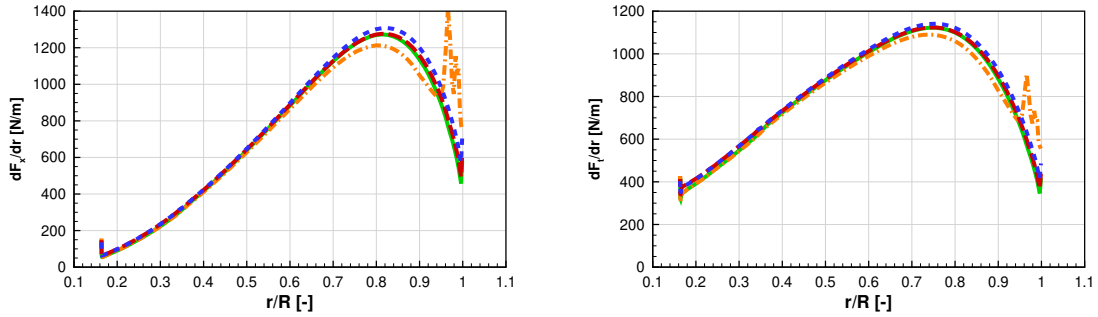

(a) Axial blade loads

(b) Tangential blade loads

Integral sampling with $\epsilon = 0.4c$ (- - -), Integral sampling with $\epsilon = 0.3c$ (— —),
Line sampling with $\epsilon = 0.4c$ (——), Line sampling with $\epsilon = 0.3c$ (-·-·-)

Figure 4.16: Blade loads obtained with different sampling methods and smearing parameters.

4.3.2 Sampling position relative to previous source term injection

This short subsection clarifies a point relative to the velocity sampling that, to the author's knowledge, is never directly mentioned in literature. More specifically, it concerns the position the actuator line should be at to sample the velocities, relative to where the source terms were distributed at the previous iteration and where they are going to be distributed at the end of the current iteration. The issue is summarized in the diagram from figure 4.17.

The most intuitive way to proceed is to rotate the actuator line at the beginning of the coupling iteration. By doing so, the velocities are sampled around the actuator line location, and the loads are then distributed around the same location to be accounted for at the next CFD iteration. This approach is shown in figure 4.17a. This is consistent in the sense that the source term in a cell is computed using the velocity in that same cell. However doing so raises a few issues. First, with this method, the sampling is not made around the bound vortex, so it contributes to the sampled velocity. This should be avoided, as explained in section 1.4.4. Second, the blade loads then strongly depend on the smearing parameter and on the time step. Indeed, depending on these parameters, the sampling will be more or less influenced by the bound vortex created in the previous iteration. Third, this is inconsistent for steady actuator line computations, (for 2D applications or propeller computation in the relative frame for instance), where it makes no sense to sample the velocities in front of the bound vortices instead of in the center.

Another approach, which is more consistent with theory, is to rotate the actuator line after the velocity sampling step (figure 4.17b). This way, the sampling is centered on the bound vortex, which solves the previously described issues. A downside of this approach is that it induces a lag, equal to a time step, for the actuator line to respond to a local and non-axisymetric perturbation (incidence or interaction effect). The time step must then also be chosen with this consideration in mind.

The discrepancy between the two approaches is quantified on blade loads in figure 4.18. The differences are significant, especially at the tip, where the distance between the actuator lines

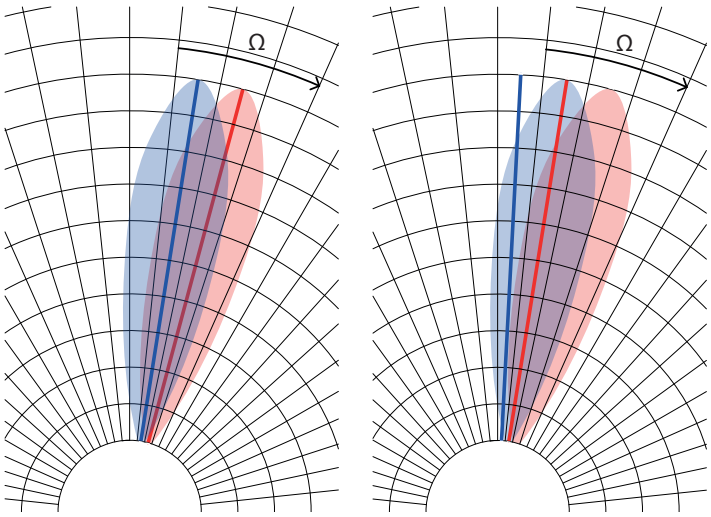

(a) Intuitive approach (b) Consistent approach

Figure 4.17: Clarification of the velocity sampling position relative to source terms injection. The colored surfaces correspond to the area in which are distributed the loads computed from the velocities sampled around the line of the same color. The elements relative to the time t are in blue and $t+\Delta t$ in red.

becomes larger. Another interesting thing to note is that, in this case, the effect of the ϵ parameter is reversed compared to what was seen previously: a smaller value leads to larger loads. This is due to the limited smearing at the tip, which creates small induced velocities at the position of the next actuator line location.

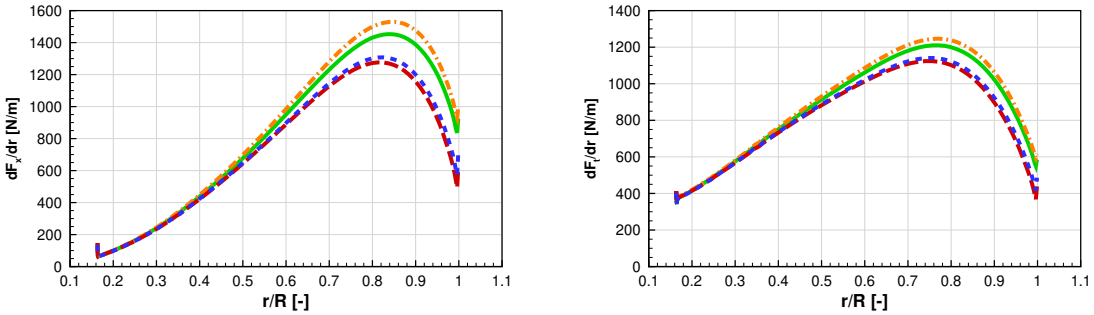

(a) Axial blade loads (b) Tangential blade loads

Consistent approach with $\epsilon = 0.4c$ (- - -), Consistent approach with $\epsilon = 0.3c$ (— —),
Intuitive approach with $\epsilon = 0.4c$ (——), Intuitive approach with $\epsilon = 0.3c$ (-·-·-)

Figure 4.18: Blade loads obtained with the different approaches and smearing parameters.

The differences between the two approaches are reduced with a very small timestep compared to the smearing length. Another way to improve the model is to conduct an actuator line computation at each sub iteration of the temporal timestep. This would avoid the $\Delta\phi$ lag mentioned previously.

However, the CFD solver does not allow the trigger method, used to run coprocess scripts between temporal iterations, to be used for sub-iterations easily. As a result this option was not investigated in this work.

4.4 Solution robustness

The previous sections showed that the actuator line model, as implemented in this work, is very robust to velocity sampling and source term distribution parameters. This section evaluates the model robustness to mesh refinement and to a lower time step.

4.4.1 Mesh sensitivity

This section compares actuator line results for the baseline mesh presented in section 2.2.3 and used for the previous computations, and a finer mesh. In this finer mesh, the length of the background grid cells in the propeller area is divided by two compared to the regular mesh, leading to cells that are 8 times smaller because the grid is Cartesian. The Chimera cylindrical grid is also more refined, with twice the number of cells in the azimuthal and axial directions. The fine mesh has 100 million cells in total, compared to the 40 million cells of the baseline mesh. Its purpose is to validate the results obtained with the baseline mesh, but it is too large to be used in a typical design routine.

The blade loads obtained for the two meshes with a smearing parameter of $\epsilon = 0.3c$ are shown in figure 4.19. The loads are almost identical, both in the axial and tangential direction. This shows that the smearing Gaussians are correctly discretized on the baseline mesh, and that it is fine enough to correctly capture the velocity fields in the propeller plane.

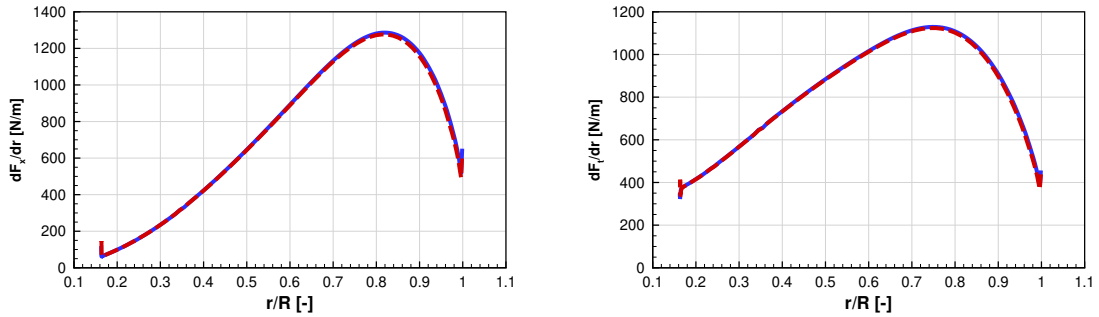

(a) Axial blade loads

(b) Tangential blade loads

Figure 4.19: Blades loads obtained with the different meshes.

A slice in the plane of the tip vortex was made in the wake close to the blade. The velocity and pressure fields, extracted on a slice going through the vortex core, are presented in figure 4.20. The slices show that the velocity fields predicted with each mesh are quite similar in the potential area ($|r| \geq 0.05$). However, differences arise in the viscous core of the vortex. This region is known to strongly depend on the mesh, even for blade-resolved simulations. As a result, the baseline

mesh is deemed fine enough to be converged on the majority of the wake. A similar refinement is thus used in chapters 5 and 6 to study the propeller performance under different conditions.

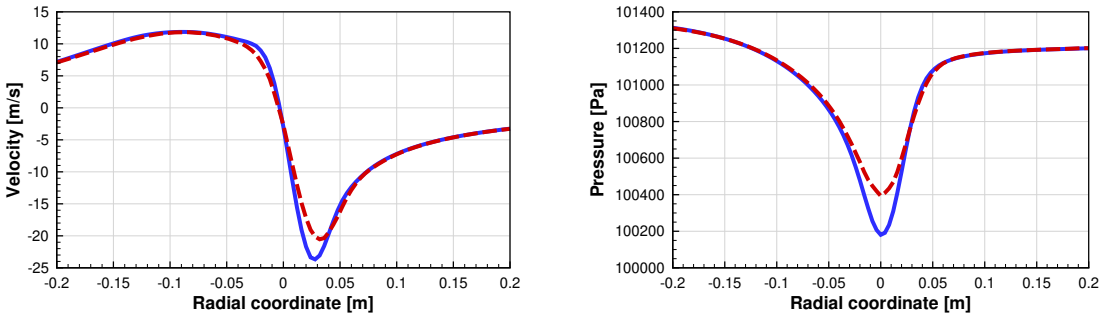

(a) Velocity normal to extraction line

(b) Pressure field

Refined mesh (——), Baseline mesh (– –)

Figure 4.20: Extractions on a line across the tip vortex, a quarter radius behind the rotor.

4.4.2 Time step sensitivity

In all the previous computations, the time step was chosen so that the actuator line rotates $\Delta\phi = 1°$ between each iteration. In the actuator line model, this value needs to be chosen in accordance with the smearing parameter so that there is enough source term overlap from one iteration to the other. Otherwise, oscillations appear in the flow and the computation becomes unstable. For a given parameter, the time step should be small enough to avoid instabilities, but as large as possible to reduce the number of iterations needed to reach convergence. In the present case, with a smearing parameter of $\epsilon = 0.3c$, $\Delta\phi = 1°$ was found to be a good compromise. This however raises the question whether a smaller time step has an effect on the results or not.

Two actuator line computations were conducted, with $\Delta\phi = 1°$ and $\Delta\phi = 0.5°$, to evaluate this effect. The blade loads obtained in both cases are shown in figure 4.21, and they are overall very similar. This shows that increasing $\Delta\phi$ to save on computation time is not necessarily made at the cost of fidelity, as long as the computation stays stable. In the rest of the dissertation, the time step is thus always chosen so that $\Delta\phi = 1°$. As a reference, the unsteady blade-resolved computations were found to need a time step of no more than $0.5°$ to avoid oscillations.

Conclusion

This chapter was dedicated to the development of an actuator line model for propellers. A novel implementation based on a Chimera cylinder was proposed, which enables parallel and vectorized computations of the blade loads and of their distribution, accelerating the simulations significantly compared to classic implementations. The energy source term investigation led to the same observations as for the RANS/BET model, with the additional conclusion that the irreversible formulation leads to an entropy field very similar to the one computed with a blade-resolved approach.

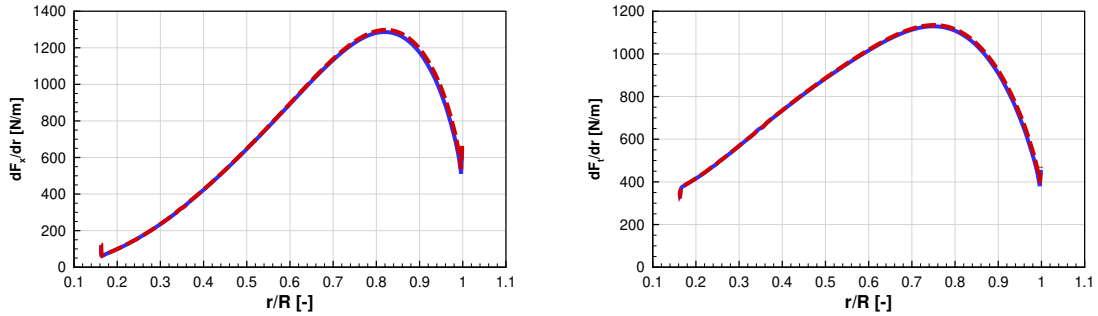

(a) Axial blade loads

(b) Tangential blade loads

$\Delta\phi = 1°$ (——), $\Delta\phi = 0.5°$ (– –)

Figure 4.21: Blade loads obtained with the different time steps.

The source term distribution study closely compared the actuator line wake computed with prescribed loads to the one from a blade-resolved computation, highlighting the smearing induced by the actuator line. Fully coupled simulations showed that the actuator line model, as implemented in this work, is quite robust to the Gaussian smearing parameter of a 2D Gaussian projection. The comparison of the point and integral velocity sampling techniques showed that both lead to the same blade loads, but that oscillations appear when using the point sampling method for small smearing parameters that are stable when using integral sampling. It was also explained that the velocities should be sampled where the source terms were distributed at the previous iteration in order to avoid the influence of the bound vortex. Computations were run with a more refined mesh and a smaller time step, leading to similar blade loads.

The actuator line model developed here is thus very robust to i) the choice of the smearing parameter, ii) the mesh size, and iii) the time-step. It is therefore a very convenient tool for design studies, as the parameters do not have to be meticulously calibrated between each iteration. The model does however consistently lead to an overestimation of the blades' tip loads and to a smeared wake. The consequences of these issues will be addressed in the two following chapters.

Chapter 5

Assessment of the models on an isolated propeller

Now that both body-force models' formulations have been refined and that best practices have been defined, their performance will be evaluated by comparison with blade-resolved Chimera computations for several application cases. In this chapter, the comparison is made for the HAD-1 propeller in isolated configuration. First, the models are studied on the propeller's nominal operation point, in axial flow at a 45° blade pitch angles. For each model, the propeller loads are presented, as well as the average wake and the unsteady wake for the blade-resolved and actuator line computations. Second, propeller performance is compared for each model for different blade pitch angles. Finally, the propeller is studied under incidences of 3°, 6° and 9°. The averaged and unsteady propeller loads are compared, and the average wake at a 9° incidence angle is analyzed.

Contents

5.1 Study on the nominal operating point

This section presents the study of the isolated propeller configuration at the cruise axial operating point from table 2.2. A focus is first made on propeller loads, and then a study of the average and unsteady wake is proposed.

5.1.1 Propeller loads

The integrated loads, obtained for each propeller modeling method, are shown in table 5.1. Before getting into the specifics of the performance of each model, it is important to clarify what is used as a reference to compare the body-force models to. In the two previous chapters, the objective was to understand what aspect of the flow physics each body-force model can and cannot capture. As a result, the chosen reference was the one that best replicates the flow physics, i.e. a CFD computation using the full-matched structured blade-resolved grid presented in section 2.2.2.1. Yet as explained in section 2.2.1.1, in the general case when studying interaction effects, the blades must rotate because the flow is no longer axisymmetric. This can be done using a sliding mesh or a Chimera approach, which in any case downgrades the quality of the solution. This effect is quantified on propeller performance at the top of table 5.1. The Chimera approach overestimates the blade loads by about 1% compared to the full-matched blade-resolved simulation, but only slightly modifies the propulsive efficiency. In the wake, the Chimera approach creates additional diffusion caused by the interpolation. This effect is quantified in section 5.1.3. Because the purpose of the body-force models is to study interaction effects, it makes sense for the reference to be chosen as the most accurate model that would actually be used for a similar purpose. As a result, in this chapter and the next, the blade-resolved simulations used as a reference are always the ones relying on the Chimera approach.

Back to the integrated loads from table 5.1, it is shown that the actuator line model overestimates both thrust and power by around 5%, leading to a good prediction of the efficiency. The same can be said for the lifting-line computation. The RANS/BET model predicts the thrust and power quite accurately thanks to the calibrated tip-loss correction, but the slight offset between the two leads to an overshoot of the efficiency by more than one point.

Table 5.1: Integrated propeller loads for each approach.

	Thrust [N]	Power [kW]	Efficiency [-]
Blade-resolved – Chimera mesh	1406	166.8	0.8605
Blade-resolved – full-matched mesh	1390 (-1.2%)	164.5 (-1.4%)	0.8624 (+0.19pts)
Actuator line	1480 (+5.3%)	175.1 (+5.0%)	0.8629 (+0.23pts)
RANS/BET	1430 (+1.7%)	166.7 (-0.1%)	0.8760 (+1.55pts)
Lifting line	1463 (+4.0%)	174.0 (+4.3%)	0.8581 (-0.24pts)

Figure 5.1 shows the spanwise distribution of axial and tangential loads along the blade for each modeling method. All the methods are very accurate on the lower part of the blade, despite slight differences at the blade root. This is especially true for the lifting-line computation. A reason for this could be that in this simulation the nacelle is only accounted for using a perturbation field and that no retroaction is possible. For the RANS/BET model, the overestimated loads at the root could be caused by an insufficiently fine discretization of the source term volume in this area. On the upper part of the blade, all methods overestimate the maximum loads distribution by at most 5%, but they place the maximum at the correct radius. For the actuator line and

RANS/BET models, reasons for these overshoots were given in chapters 3 and 4. For the lifting-line computations, Falissard and Pantel suggested it could be linked to mutual induction effects in the radial direction due to the large chord variation at the tip of the blade, and were able to decrease the tip loads by stacking the lifting line at the propeller mid-chord instead of the quarter chord [22].

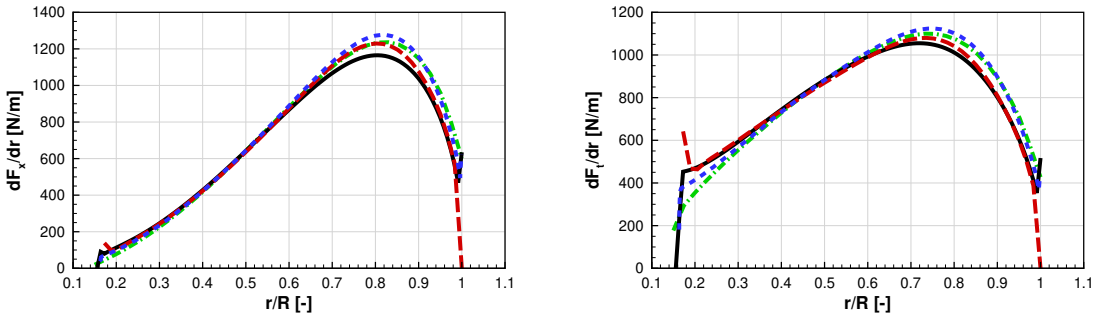

(a) Axial blade loads (b) Tangential blade loads

Blade-resolved – Chimera mesh (——), Actuator line (- - -), RANS/BET (— —), Lifting line (-·-·-)

Figure 5.1: Radial distribution of blade loads.

The angles of attack computed by the BET analysis for the actuator line, RANS/BET and lifting line are shown in figure 5.2. At the root of the blade, this graph is consistent with what was explained for the blade root loads. For the rest of the blade, the actuator line and lifting line simulations lead to very similar angles of attack. This serves as a validation of the actuator line model, because it shows that the correct loads are not obtained by error compensation but because the induced velocities are indeed computed correctly. For the RANS/BET model, the tip correction directly applied on the blade loads creates a discrepancy between the loads computed by the BET and the loads applied in the CFD computation, and thus a discrepancy between the flow field and the local angles of attack. Since the loads are reduced by the loads correction, the induced velocities are smaller and the angles of attack higher. This explains the relatively high angles of attack at the blade tip, even though the blade loads shown in figure 5.1 are not too overestimated in this area.

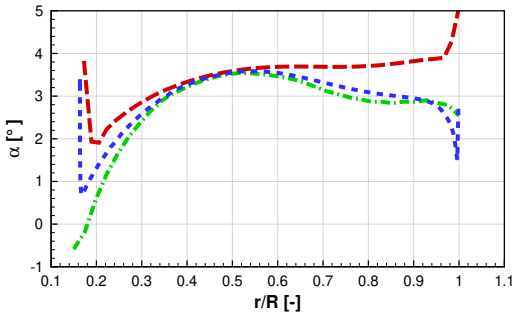

Actuator line (- - -), RANS/BET (— —), Lifting line (-·-·-)

Figure 5.2: Angle of attack distribution along the blade.

5.1.2 Average wake

The azimuthally averaged velocity profiles half a radius behind the propeller are shown in figure 5.3. Both body-force models reproduce the CFD trends very accurately. At almost all radii, the over or underestimations of the velocities are directly linked to the prediction of the blade loads, and so for both the axial and tangential directions. The effect of the smearing on the actuator line computation also seems visible on these figures, where the velocity drop at the tip of the blade is less steep than for the blade-resolved computation.

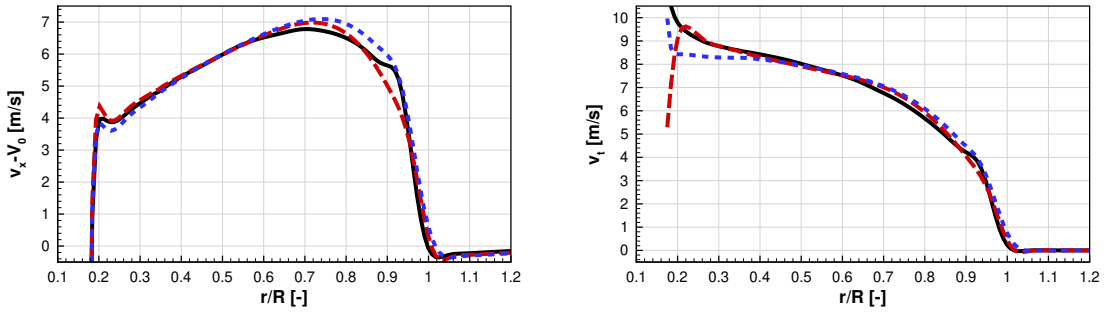

(a) Axial velocity (b) Tangential velocity

Blade-resolved – Chimera mesh (——), Actuator line (- - -), RANS/BET (— —)

Figure 5.3: Azimuthally averaged velocity fields half a radius behind the propeller.

5.1.3 Unsteady wake

This subsection evaluates the accuracy of the wake computed by the actuator line method. It is compared to the wake computed by two blade-resolved approaches: full-matched mesh (BR-FM) and Chimera mesh (BR-C), thus also quantifying the dissipation effect induced by the Chimera approach that was mentioned in section 4.2.1.1 and at the beginning of section 5.1.1.

The axial and tangential velocity fields half a radius behind the propeller are shown in figures 5.4 and 5.5. It was already shown in section 4.2.1.1 that the actuator line model creates a smeared wake compared to the full-matched blade-resolved computation. These figures show that the reference blade-resolved Chimera mesh creates a relatively smeared wake as well, halfway between the full-matched blade-resolved and the actuator line solutions. This is true for the viscous wake that is dissipated in a similar manner as for the actuator line, but also for the tip vortices which seem to be weaker. Farther away from the blade wakes, the three computations lead to very similar flow fields. In particular, at the blade root, the actuator line model seems to replicate the flow physics well thanks to the shape of the overset cylinder studied in section 4.1.3.

To give a more quantitative insight into the ability of each model to predict the propeller wake, the flow field from the slice was extracted on four radial lines at different azimuths. These extraction lines are shown in black in figures 5.4 and 5.5 and are located:

- at 51°, relatively far away from the blade wake
- at 68°, just before the tip vortex
- at 74°, at the center of the tip vortex
- at 83°, along the viscous wake

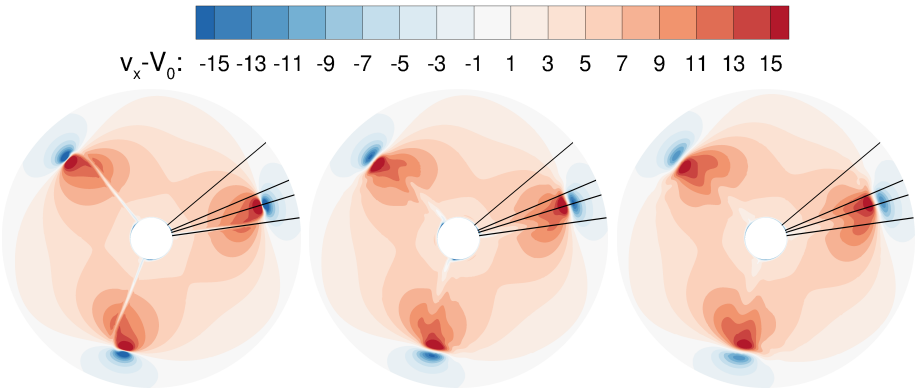

(a) BR-FM (b) BR-C (c) Actuator line

Figure 5.4: Slice of the axial velocity field half a radius behind the propeller. The lines correspond to the extractions made in figure 5.6.

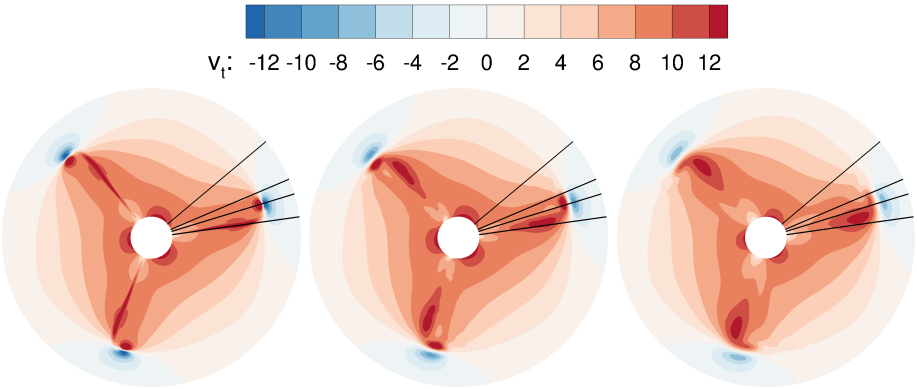

(a) BR-FM (b) BR-C (c) Actuator line

Figure 5.5: Slice of the tangential velocity field half a radius behind the propeller. The lines correspond to the extractions made in figure 5.6.

The axial and tangential velocity fields extracted along these lines are shown in figure 5.6.

Far away from the blade wakes (figures 5.6a and 5.6b), both blade-resolved computations create a similar flow. The flow computed by the actuator line computation is very close, reproducing the exact trends, with localized discrepancies that go up to 0.5 m/s at most. For the extraction line just before the tip vortex (figures 5.6c and 5.6d), there is an increase in velocity for the BR-C and the actuator line computations near the blade tip, but not for the BR-FM computation. The reason for this is that the slice is made outside of the area of influence of the tip vortex for the BR-FM simulation. However, because the tip vortex is smeared for the BR-C and actuator line computations, the tip vortex does have an influence on this extraction line, which creates these velocity spikes. Inside the tip vortex (figures 5.6e and 5.6f), the smearing leads to less intense and less steep velocity variations for the actuator line and BR-C computations than for the BR-FM. For the three previous extraction lines, it is also important to note that the actuator line often slightly overestimates the velocities along the blade, especially at the tip. This is more or less visible on

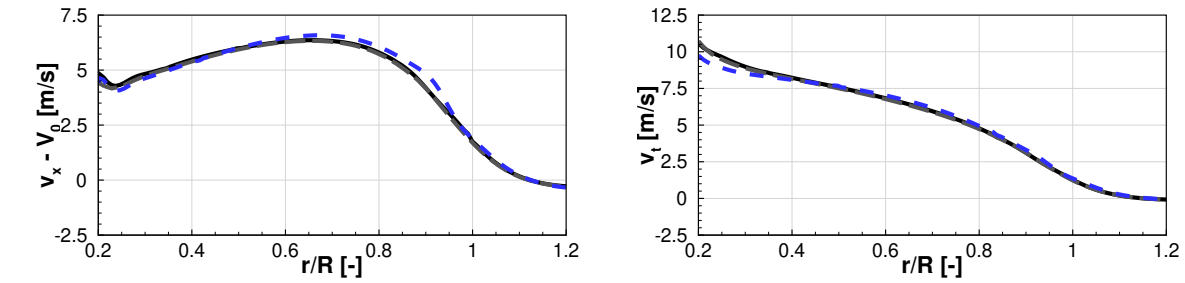

(a) : v_x at 51°, far from blade wake

(b) v_t at 51°, far from blade wake

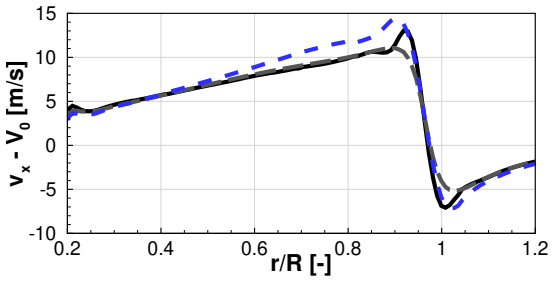

(c) v_x at 68°, before tip vortex

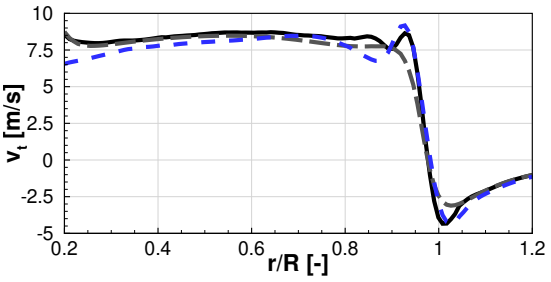

(d) v_t at 68°, before tip vortex

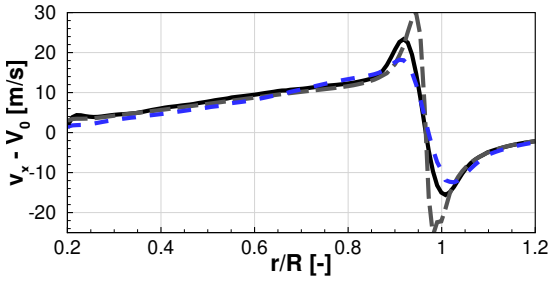

(e) v_x at 74°, center of tip vortex

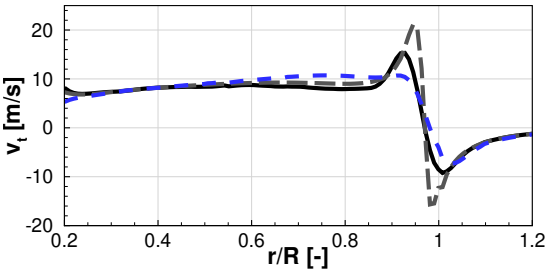

(f) v_t at 74°, center of tip vortex

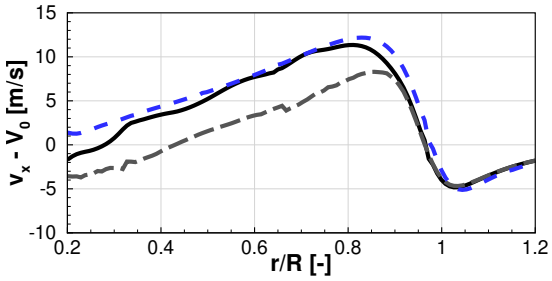

(g) v_x at 83°, viscous wake

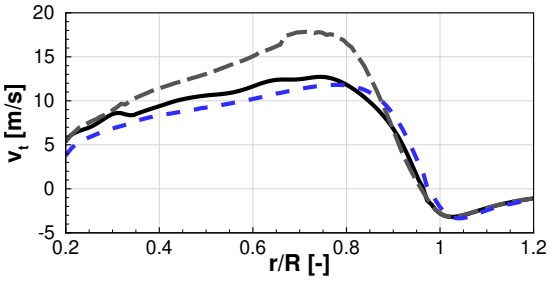

(h) v_t at 83°, viscous wake

Blade-resolved – Chimera mesh (——), Blade-resolved – full-matched mesh (– –), Actuator line (- - -)

Figure 5.6: Velocity profiles extracted half a radius behind the propeller at different azimuth angles.

the graphs depending on the scaling used. This is most likely due to the 5% overestimation of the blade loads at the tip, which must increase induced velocities overall. Inside the blade viscous wake (figures 5.6g and 5.6h), the actuator line and BR-C velocities are very similar. The full-matched mesh from the BR-FM computation allows the conservation of the viscous wake without too much

dissipation, thus concentrating the effect of the drag on just a few cells. This leads in particular to a more significant axial velocity deficit along the span.

Two points should be remembered from this section. The first is that even for a blade-resolved computation, the approach taken (full-matched mesh or Chimera) has a significant impact on the wake, even for a Chimera mesh that is quite fine. Second, considering that the BR-C computation is the most appropriate reference when evaluating actuator line results (for the reasons explained in section 5.1.1), the actuator line model predicts the propeller slipstream with an excellent accuracy, reproducing all blade-resolved trends from blade root to blade tip.

5.2 Propeller characteristic

The previous section showed that the actuator line and RANS/BET models perform very well on the cruise operating point. In this section, the models are used for different pitch angles to evaluate their resilience to a change of operating conditions, where the loads distribution on the blade varies significantly. In particular, this study allows an assessment of the robustness of the RANS/BET model's loads tip-loss correction, which was calibrated for a blade pitch angle of 45°. The study focuses on blade pitch angles from 37° to 49°, to avoid the angles that challenge the BET hypothesis too much, as explained in section 2.1.1.2. As a reminder, the flow around the blades for different pitch angles as well as the propeller performance are thoroughly presented in appendix C using blade-resolved simulations.

The propeller thrust, power, and efficiency as a function of blade pitch angle and thrust are plotted in figure 5.7 for the body-force and BR-C computations. For the actuator line, the thrust and power curves show that the 5% overestimation seen at a 45° pitch angle is about the same for all the pitch angles, leading to a very good prediction of propeller efficiency for all pitch angles as well. This is important because the aim of the actuator line method developed here is to study installation effects, in which the input is often the thrust rather than the blade pitch angle. As a result, if the propeller is trimmed for thrust, the propeller power will also be correct, and so will the tangential loads that induce the swirl. This is less true for the RANS/BET model, which predicts the thrust and power more accurately than the actuator line model for a given pitch angle (differences with the BR-C computations do not go beyond 2%), but is off on the efficiency characteristic by up to 1.5 points.

The blade loads are shown in figure 5.8 for the pitch angles of 37°, 41° and 49°. Apart at 37° where the trends are slightly different because the loads are very low, the body-force models behave similarly as for the 45° pitch angle that was analyzed in the previous section. This shows that the propeller characteristics from figure 5.7 were not obtained by error compensation.

In short, all these figures show that the accuracy of the body-force models for a 45° pitch angle is similar for other pitch angles, even when the propeller is lightly or highly loaded. For the RANS/BET model, this also shows that it is sufficient to calibrate the loads tip-loss correction on a single operating point, because it remains relevant over a wide range of operating points.

5.3 Propeller in incidence

The body-force models were previously evaluated on an isolated propeller under axial inflow. For the RANS/BET model, this leads to an axisymmetric solution, and to a steady solution in the relative frame for the actuator line model. The next step is to assess how both models respond to

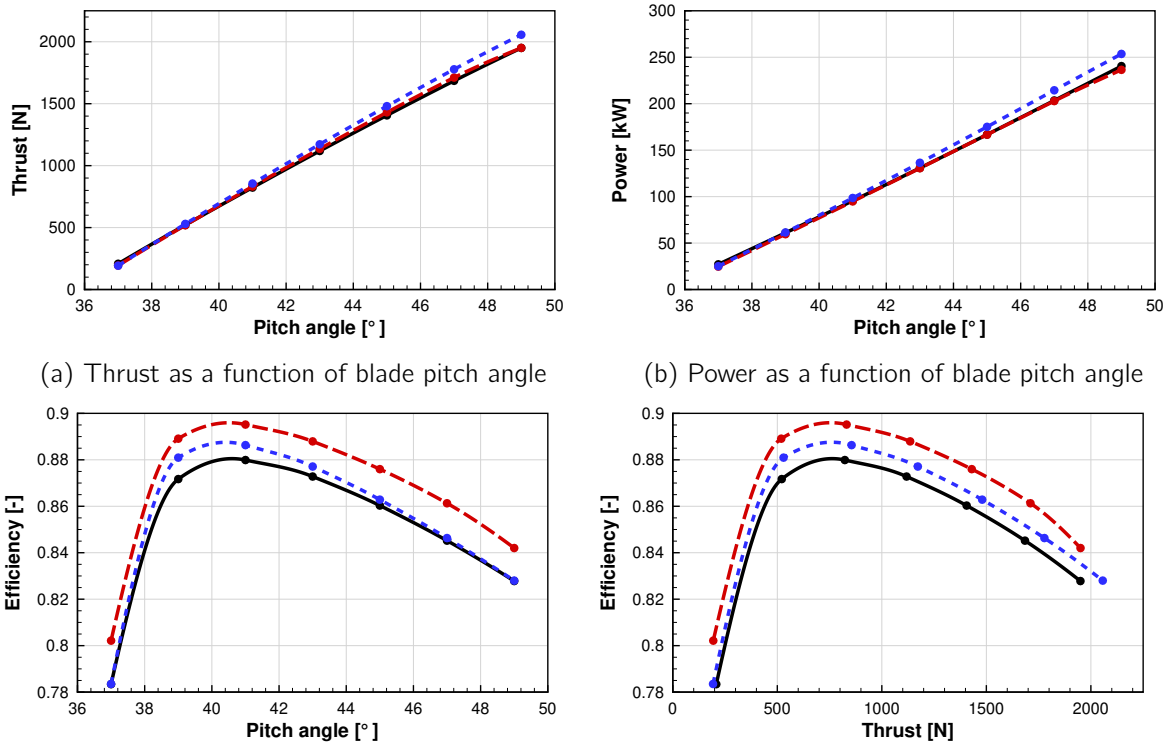

(a) Thrust as a function of blade pitch angle

(b) Power as a function of blade pitch angle

(c) Efficiency as a function of blade pitch angle

(d) Efficiency as a function of thrust

Blade-resolved – Chimera mesh (——), Actuator line (- - -), RANS/BET (— —)

Figure 5.7: Propeller characteristics obtained by blade pitch variation.

a non-uniform inflow. Here, the isolated propeller is put under incidence, creating an azimuthal distortion of the inflow whose intensity scales with the incidence angle.

5.3.1 Propeller loads

5.3.1.1 Average loads

Figure 5.9 shows the propeller thrust, power, 1P load modulus, and 1P phase angle (defined in section 1.1.3) averaged over a full propeller revolution for the studied incidence angles. For the thrust and power, the trends are well predicted by the body-force models, and the observations are very similar to those made in axial flow. The actuator line overpredicts thrust and power by 5% consistently, regardless of the incidence angle. The RANS/BET model overpredicts thrust by 2% and is extremely accurate on power, once again regardless of the incidence angle. The prediction of the 1P effects is also very satisfying. Both body-force models predict the 1P loads magnitude within 1%. The phase of these 1P loads is relatively independent of the incidence angle for all computations, and it is predicted with an error of about 2° for both body-force methods, which is by far low enough to fuel models that conduct structural analyses.

In the rest of this chapter, the results are studied more in depth for an incidence angle of 9° for the sake of brevity. The same analysis was performed on the other incidence angles and the conclusions were found to be similar.

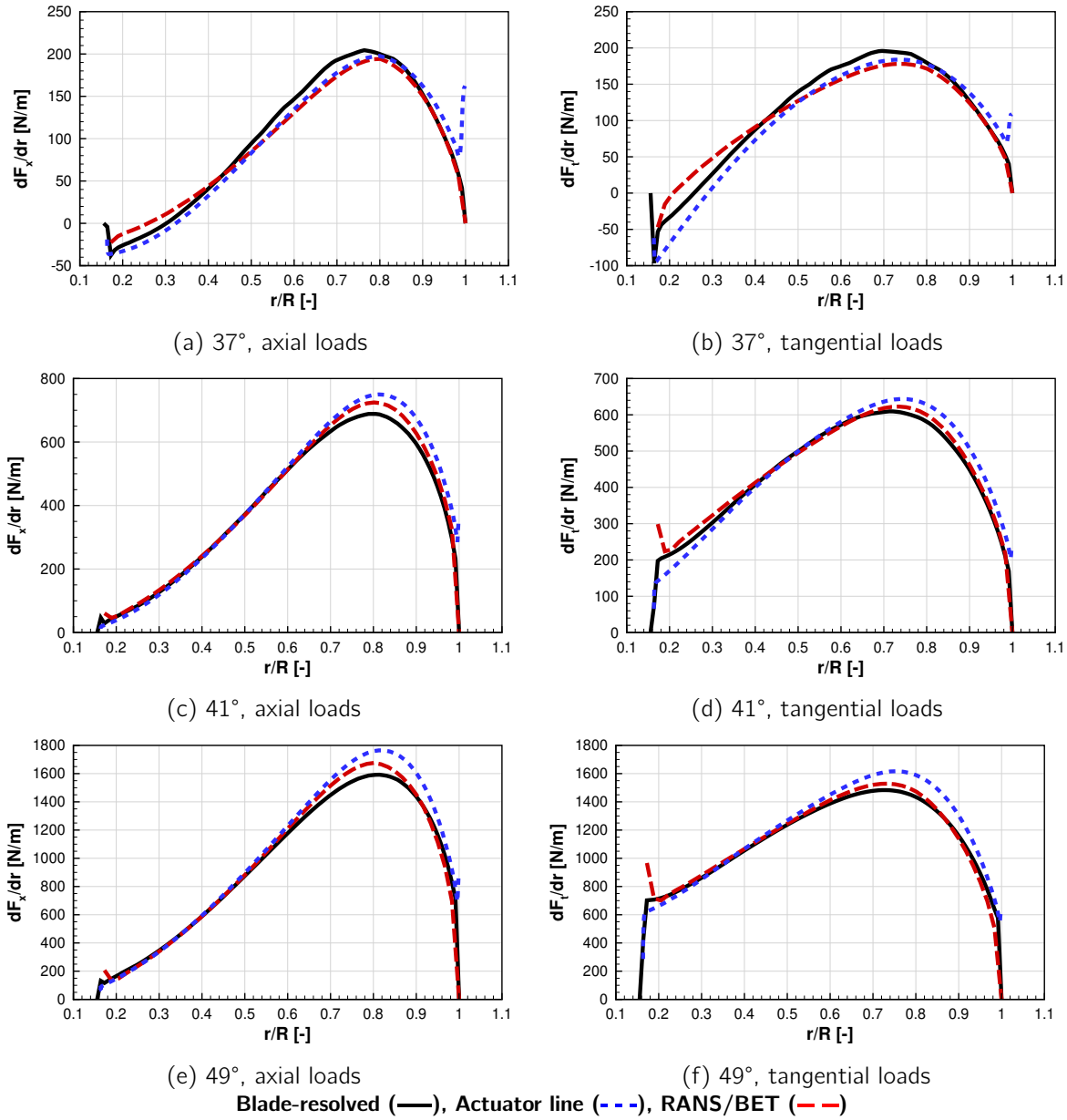

(a) 37°, axial loads

(b) 37°, tangential loads

(c) 41°, axial loads

(d) 41°, tangential loads

(e) 49°, axial loads

(f) 49°, tangential loads

Figure 5.8: Radial distribution of blade loads for different blade pitch angles.

5.3.1.2 Unsteady loads at 9° of incidence

This section focuses on the variation of blade loads over a revolution at a 9° incidence angle. Figure 5.10 shows the azimuthal variation of integrated blade axial and tangential loads over a revolution for the three computations. Both body-force methods reproduce the general blade-resolved trends accurately, including the azimuths at which the maximum and minimum axial and tangential loads are reached. The actuator line loads curves are offset compared to the blade-resolved results by around +5%. The RANS/BET model is overall more accurate but less consistent, by slightly overestimating or underestimating the loads depending on the azimuth.

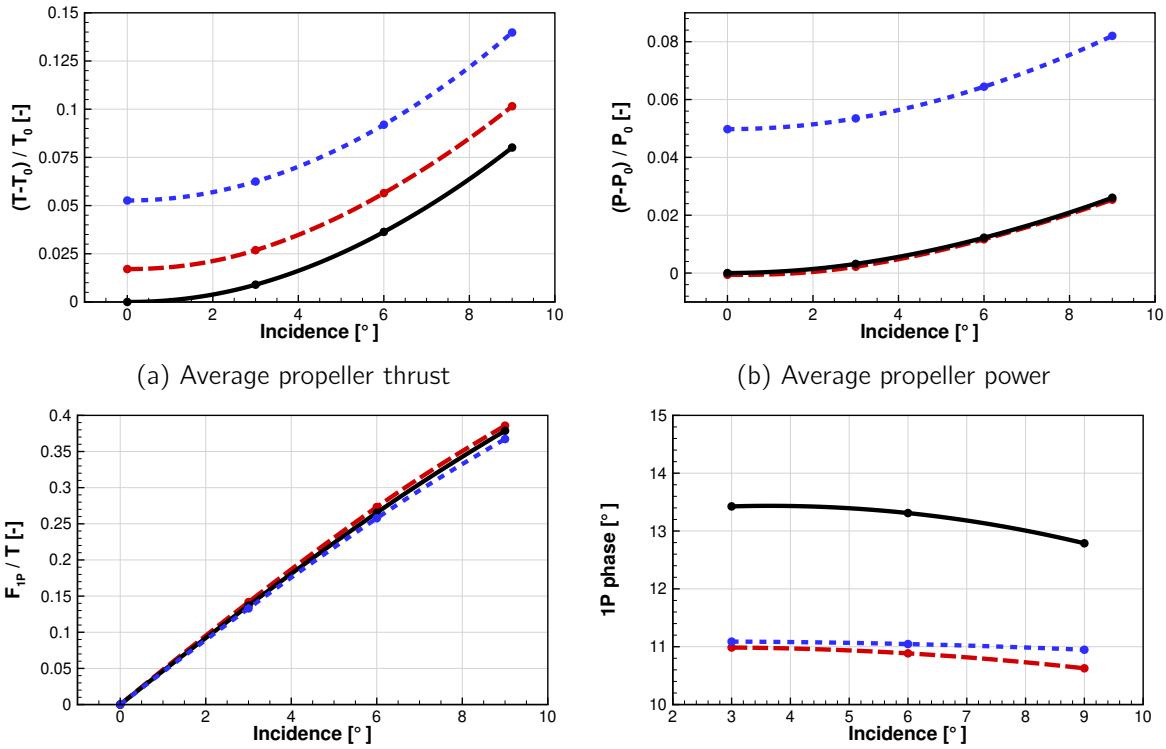

(a) Average propeller thrust

(b) Average propeller power

(c) Average 1P loads normalized by thrust

(d) Average propeller 1P phase

Blade-resolved – Chimera mesh (——), Actuator line (- - -), RANS/BET (— —)

Figure 5.9: Propeller performance averaged over a revolution for different incidence angles.

These curves are compared in the frequency domain in table 5.2. The fast Fourier transform (FFT) results are limited to the first two frequencies, considering the next ones have negligible amplitudes. For both body-force models, the amplitude and phase of the first two modes are very close to those of the blade-resolved reference.

Table 5.2: Amplitude and phase coefficients of single blade loads obtained by Fourier analysis.

Component	Approach	Mode 0	Mode 1		Mode 2	
		A [N]	A [N]	ϕ [°]	A [N]	ϕ [°]
Axial	Blade-resolved	506	358	−102	32	156
	Actuator line	534	372	−100	32	165
	RANS/BET	517	378	−98	32	170
Tangential	Blade-resolved	548	384	−102	16	−169
	Actuator line	566	392	−100	14	−162
	RANS/BET	548	400	−96	12	−142

To correctly predict the wake, the body-force integrated blade loads must be in phase with those computed by the reference blade-resolved method and their amplitudes must be similar, but their spanwise distributions also need to be similar. Figure 5.11 shows the spanwise distribution of

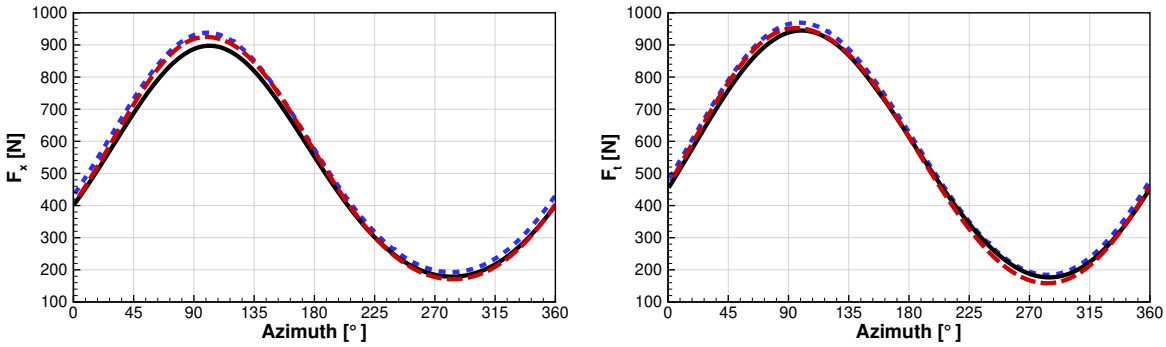

(a) Axial loads (b) Tangential loads

Blade-resolved – Chimera mesh (——), Actuator line (- - -), RANS/BET (— —)

Figure 5.10: Blade integrated loads over a revolution, for a 9° incidence.

axial and tangential loads for the azimuth with the maximum efforts (top curve), the minimum efforts (bottom curve), and the average efforts over all azimuths (middle curve). As shown previously, the azimuths of the max and min efforts are relatively similar for the three modeling methods. The curves are overall quite similar to those found in section 5.1 in axial flow. The curves almost overlap one another on the first part of the blade, and a slight overestimation persists when getting closer to the blade tip. For the actuator line method, this overestimation is always of about 5%. For the RANS/BET method, the tip loads decrease with the integrated blade loads, and eventually the curves go slightly below the blade-resolved results. This shows that, even though the generalized Glauert correction yields satisfying results (see appendix C), the global tip-loss correction could still be further refined, in particular the calibrated loads correction.

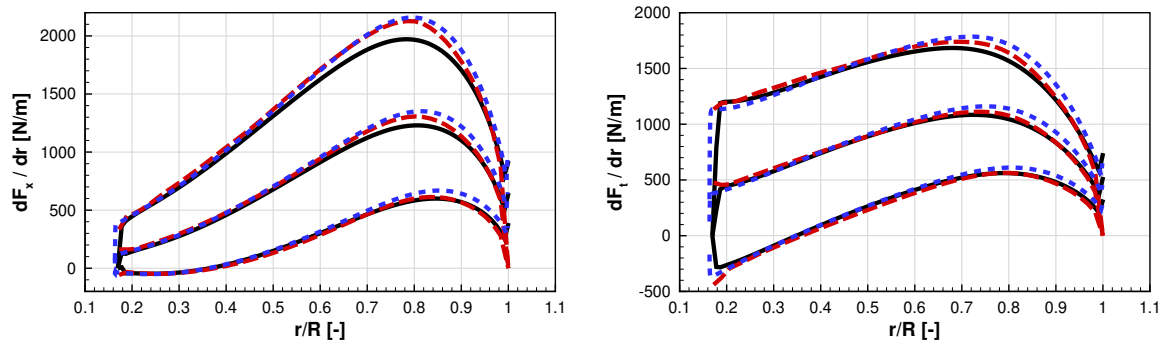

(a) Axial loads (b) Tangential loads

Blade-resolved – Chimera mesh (——), Actuator line (- - -), RANS/BET (— —)

Figure 5.11: Maximum (top), average (middle), and minimum (bottom) spanwise blade loads over a revolution, for a 9° incidence.

5.3.2 Propeller average wake at 9° of incidence

On top of computing the correct blade loads, one of the main objectives of the body-force models is to compute an accurate wake to eventually capture interaction effects. This section studies the average wake at a 9° incidence angle computed by the two body-force models, and compares them to the one from the Chimera blade-resolved computation. An unsteady analysis of the wake was also conducted, but it was deemed that it added little compared to the unsteady analysis of the axial flow from section 5.1.3, and to the study of the average flow which follows. It was thus omitted in this work for the sake of brevity.

Figures 5.12 and 5.13 show slices of the averaged axial and tangential velocity fields half a rotor radius downstream of the propeller. The velocity fields shown are those extracted from the CFD computation minus the free flow components, i.e. the induced velocities. Overall, both body-force models compute a very good prediction of the average wake. The azimuthal variations are very well captured and the perturbations are of the same order of magnitude. The small differences between the models are most visible in two areas.

- The first one is at the radius where the loads are maximum, near the tip. The overestimations of the loads by the actuator line model leads to consistently higher velocities in this area, at all azimuths. This is in particular visible in the axial velocity field. For the RANS/BET model, it can be inferred that the overestimation of the velocities does depend on the azimuth, as for the loads, even though this is hardly visible on figure 5.12.
- The second one is the area near the root. Figure 5.13 shows a pocket where the induced tangential velocity is negative at an azimuth of 90°. This area is very well predicted by the actuator line model, and is to some extent also captured by the RANS/BET model. This zone could correspond to a root vortex, but it is most likely simply a zone where the induced velocities are too small to compensate the vertical acceleration of the flow around the nacelle.

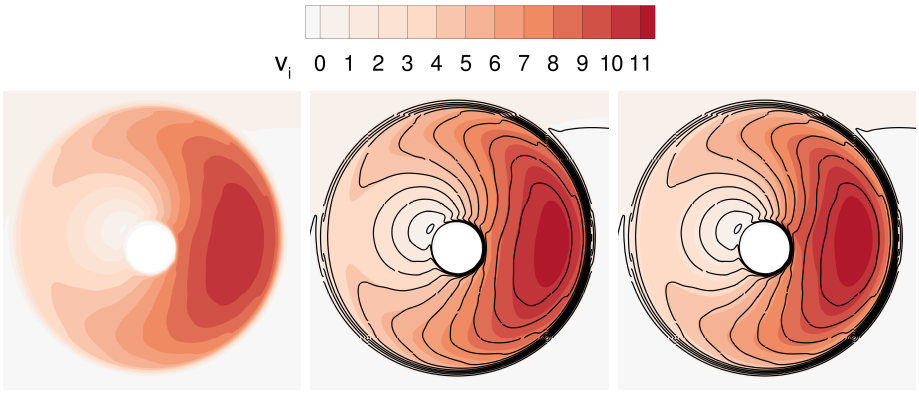

(a) Blade-resolved (b) Actuator line (c) RANS/BET

Figure 5.12: Slices of the averaged axial induced velocity field half a radius behind the propeller, for a 9° incidence.

Four lines are extracted from these slices at 4 azimuths (0°, 90°, 180°, 270°) for a more quantitative approach. Axial and tangential velocities on these lines are shown in figure 5.14. They confirm what was said previously and show that all trends are very accurately predicted by the body-force models.

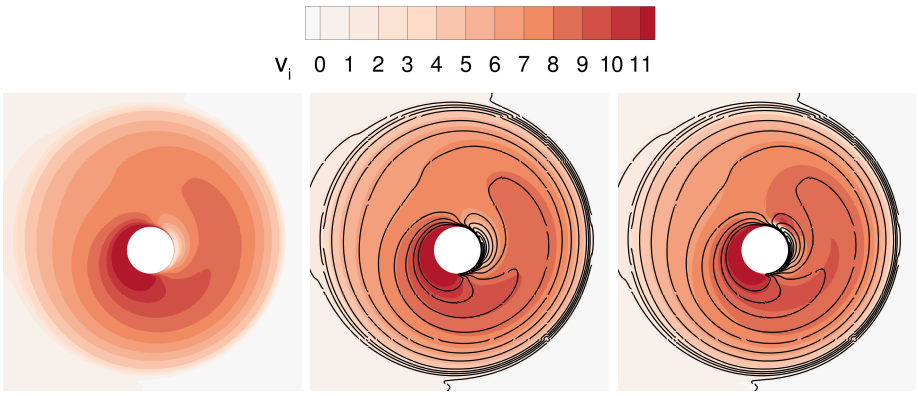

(a) Blade-resolved (b) Actuator line (c) RANS/BET

Figure 5.13: Slices of the averaged tangential induced velocity field half a radius behind the propeller, for a 9° incidence.

Conclusion

This chapter evaluated the ability of the body-force models to predict blade loads and the flowfield for an isolated propeller under different conditions. In axial flow at a 45° pitch angle, the actuator line model overestimated propeller thrust and power by around 5% compared to the blade-resolved simulation, especially at the blade tips. The RANS/BET model is more accurate thanks to the calibrated tip-loss correction, by overestimating thrust by 1.7% and underestimating torque by 0.1%. Again, the discrepancies are stronger at the blade tips. Both body-force models are able to capture the trends of the average wake very accurately, despite slight overshoots due to the overestimated loads. Slices of the unsteady wake were made for the actuator line model and some smearing was definitely visible, but it is not too far from the smearing induced by the Chimera interpolations of the blade-resolved reference.

The body-force models were also tested for blade pitch angles between 37° and 49° to evaluate their ability to predict a wide variety of blade loadings. The relative discrepancies observed at a 45° pitch angles are found to be similar for other pitch angles. This shows in particular that the RANS/BET loads tip-loss correction that was calibrated at 45° does not have to be recalibrated for all pitch angles. The propeller characteristics computed in this manner follow the blade-resolved trends very accurately.

Under incidences of 3°, 6° and 9°, the same observations are made on the propeller performance averaged over a revolution. The in-plane loads magnitude are predicted within 1% and the phase with an error of about 2°. The unsteady loads were analyzed in the frequency domain, and the modes were roughly of the same amplitude and phase as the blade-resolved results. The average wake was also studied, and the corrects trends are predicted by both body-force models at all azimuths.

In short, both the steady RANS/BET model and the unsteady actuator line model are very robust to changes of operating point in isolated configuration. The loads and velocity fields are predicted with all the correct trends and with relative discrepancies that are largely acceptable for such reduced-order methods.

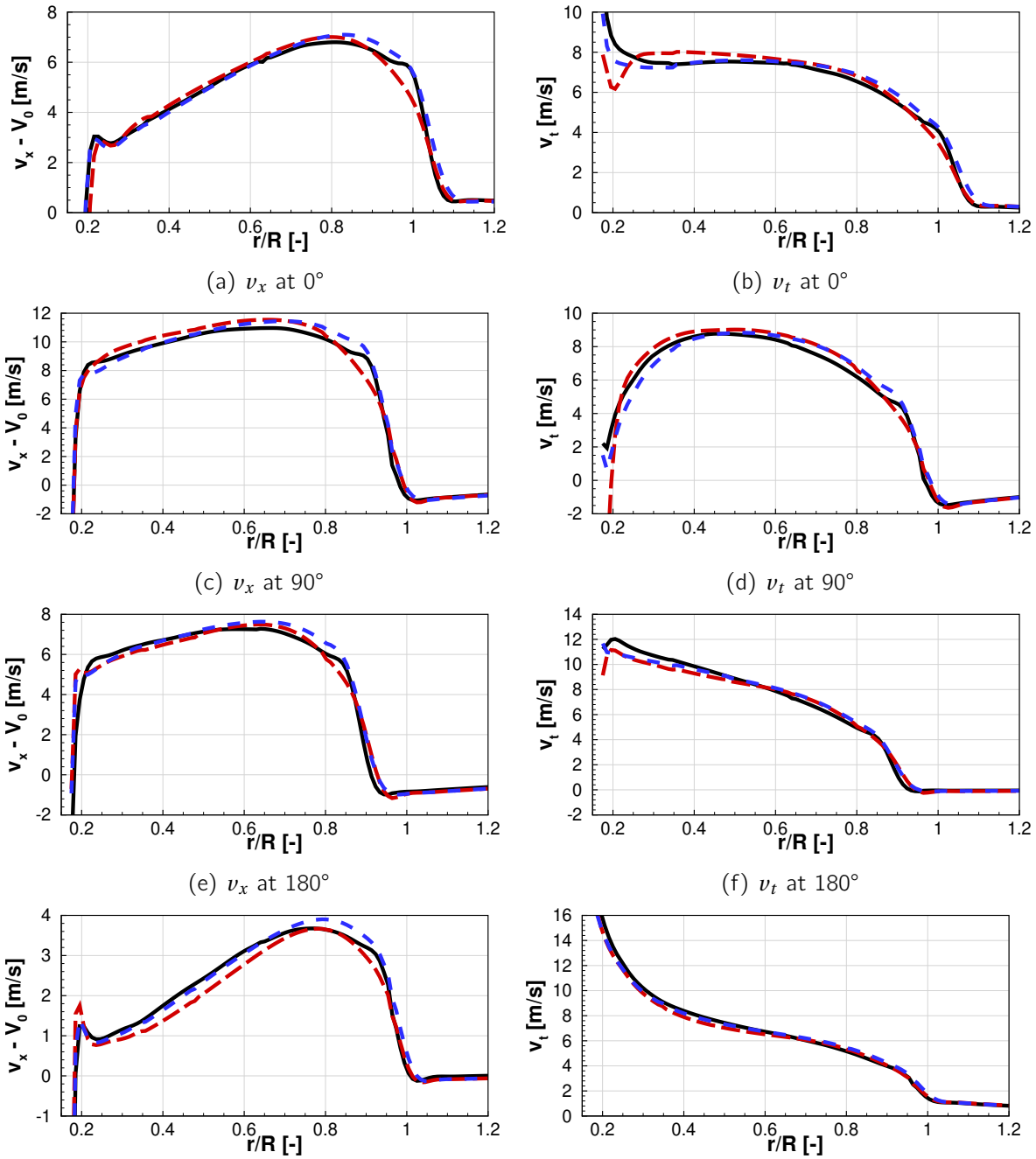

(a) v_x at 0° (b) v_t at 0°

(c) v_x at 90° (d) v_t at 90°

(e) v_x at 180° (f) v_t at 180°

(g) v_x at 270° (h) v_t at 270°

Blade-resolved – Chimera mesh (——), Actuator line (- - -), RANS/BET (— —)

Figure 5.14: Profiles of induced velocities extracted half a radius behind the propeller at different azimuth angles.

Chapter 6

Validation of the models on an installed configuration

This chapter presents the study of the installed configuration, made up of a wing downstream of the HAD-1 propeller. The wing induces an up-wash in the propeller plane, leading to an unsteady blade load over a revolution. Likewise, the tip vortices shed by the propeller periodically hit the wing, inducing unsteady wing loads as well. The objective of this chapter is to evaluate the body-force models in more realistic conditions, similar to what the models could be used for in a pre-design study.

In the first section, the distortion induced by the wing in the propeller plane is estimated with a study of the wing and nacelle configuration without a propeller. In the second section, the propeller loads computed with each approach are compared. This includes both the average loads and the unsteady loads. The wing loads are analyzed in a final section. The average loads are first presented in a three-way comparison between the blade-resolved, RANS/BET, and actuator line computations. The unsteady wing loads are then compared for the blade-resolved and actuator line computations.

Contents

6.1 Installed configuration and power-off flow field

The installed configuration presented in figure 2.1.2 is recalled in the following figures, which show the induced axial velocity field for the power-off, blade-resolved, RANS/BET, and actuator line models.

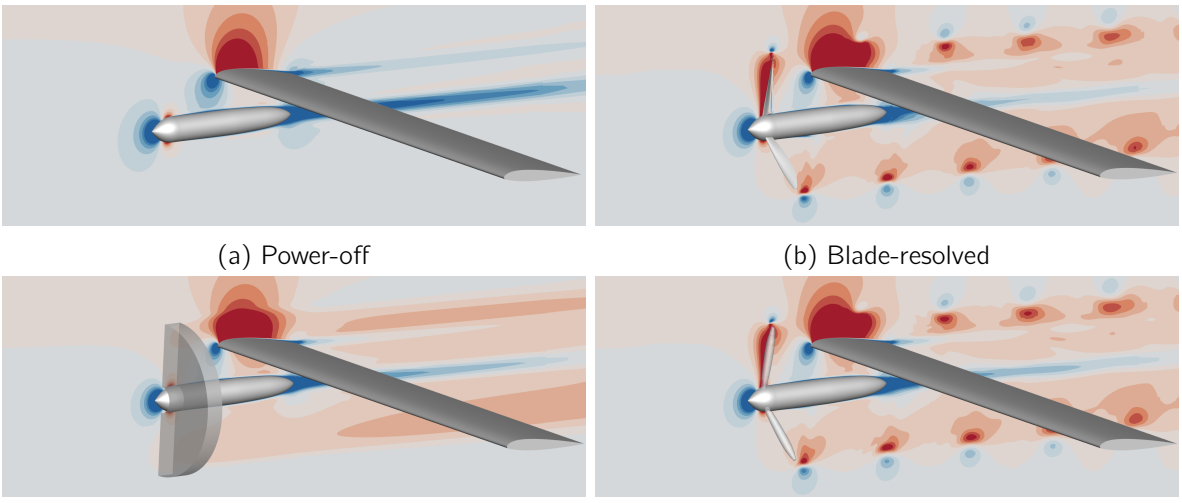

(a) Power-off (b) Blade-resolved

(c) RANS/BET (d) Actuator line

Figure 6.1: Slices of the axial velocity field of the installed configuration, power-off and for the three modeling methods, colored by $v_x - V_0$.

The rest of this section quantifies the distortion induced by the wing in the propeller plane. A good approximation of this field can be obtained with a simulation of the wing and the nacelle without the propeller. Slices of the flow in the propeller plane obtained in this configuration are shown in figure 6.2. Figures 6.2a and 6.2b show the relative axial and tangential distortion, and figure 6.2c shows the local equivalent incidence angle. The propeller disk is shown in black for reference. These figures show that the wing induces an up-wash in the upper half of the propeller disk. The distortion is inhomogeneous and its maximum amplitude is of about 2.5% for the axial and tangential velocities. The local incidence angles do not exceed 4° apart from near the nacelle, so the effect of the wing on the propeller is expected to be less intense that what was seen in chapter 5 for an incidence of 9°.

6.2 Propeller loads

As for the cases where the propeller is under incidence, the distortion in the propeller plane creates unsteady blade loads throughout a rotation. This section first studies the time-averaged propeller loads, and then focuses on the azimuth-dependent blade loads.

6.2.1 Average loads

The time-averaged propeller loads are presented in table 6.1. For the actuator line model, the thrust and power overestimations are of about 5%, which is consistent with the results from the previous chapter. The RANS/BET results are also in line with the results obtained for the isolated

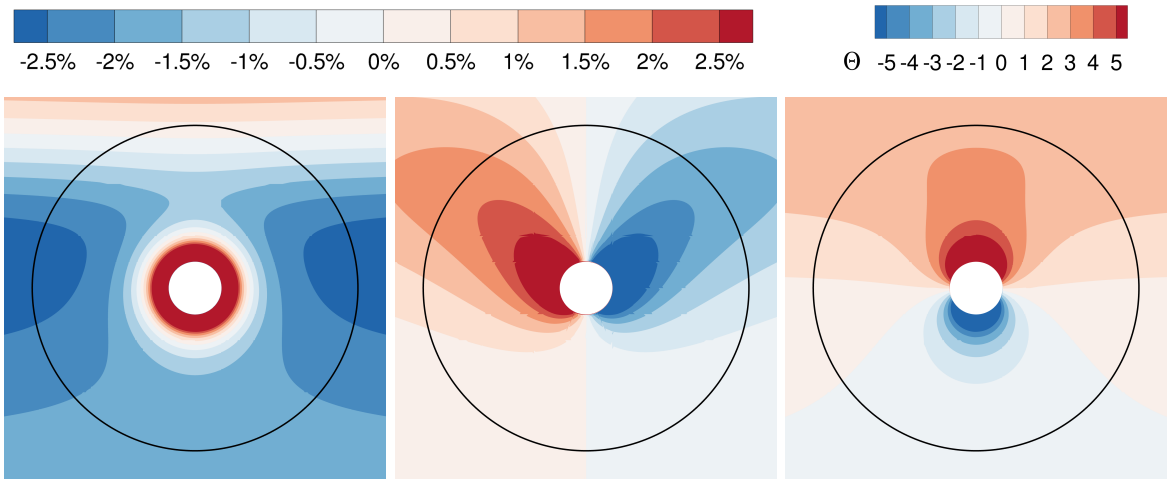

(a) Axial velocity field: $\frac{v_x - v_\infty}{v_\infty}$ (b) Tangential velocity field: $\frac{v_t}{\Omega r}$ (c) Local incidence angle

Figure 6.2: Distortion fields in the propeller plane, from a simulation with wing and nacelle only.

configuration, with a discrepancy of about 2.5% on the thrust and a very accurate prediction of the power. As in the previous chapter for the cases under incidence, the variation of the blade load over a rotation leads to the appearance of 1P loads, displayed in table 6.1 as a modulus and a phase angle. The norm of the in-plane force is very well predicted by both body-force methods (difference of just a few newtons). The models are also accurate on the phase angle, which they compute with an error below 2°.

Table 6.1: Propeller performance averaged over a full rotation

Quantity	Blade-resolved	Actuator line	RANS/BET
Thrust [N]	1492	1562 (+4.7%)	1528 (+2.4%)
Power [kW]	173.5	181.3 (+4.5%)	174.1 (+0.3%)
Efficiency [-]	0.878	0.880 (+0.2pts)	0.896 (+1.8pts)
1P Loads [N]	54	56 (+4.8%)	58 (+7.9%)
1P Phase [°]	14.4	13.4 (-1.0°)	12.7 (-1.7°)

6.2.2 Unsteady loads

Figure 6.3 shows the azimuthal variation of blade axial and tangential loads over a revolution for the three methods. The first thing to note is that the amplitude of the signals is relatively small compared to the 9° incidence case (figure 5.10). This is consistent with the weaker distortion field that was shown in section 6.1. The objective of this chapter is thus to evaluate the ability of the body-force models to respond to an inhomogeneous perturbation rather than a strong one as in chapter 5. This inhomogeneous aspect is visible on the curves by their irregularities, as opposed to the sinusoidal signal from figure 5.10 in incidence.

Despite these irregularities, the blade-resolved trends are very accurately reproduced by both body-force models, including the azimuths at which the maximum and minimum loads are obtained. The actuator line curves are offset compared to the blade-resolved results by around +5%. The

RANS/BET model is less consistent, by overshooting and undershooting the loads depending on the azimuth. Furthermore, the discrepancy between axial and tangential loads predictions is particularly visible in this configuration.

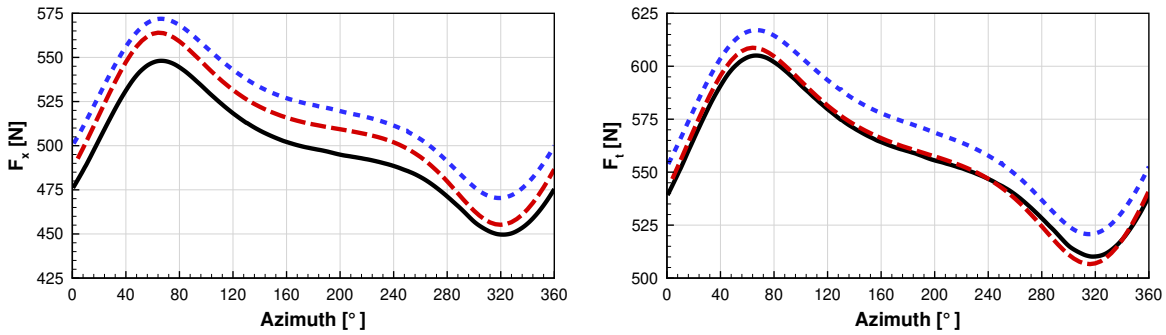

(a) Axial loads

(b) Tangential loads

Blade-resolved (——), Actuator line (- - -), RANS/BET (– –)

Figure 6.3: Blade loads over a revolution.

These curves are compared in the frequency domain in table 6.2. Contrary to the case in incidence where the signal was mostly modeled by the first mode, here three modes are relevant to describe the curves. All modes are well predicted by both body-force methods. The discrepancies between actuator line and blade-resolved results mostly come from the signal's average value, whereas for the RANS/BET model they come from the slight amplitude differences. The phase of each mode is accurately predicted by both methods.

Table 6.2: Amplitude and phase coefficients of single blade loads obtained by Fourier analysis.

Component	Approach	Mode 0	Mode 1		Mode 2		Mode 3	
		A [N]	A [N]	ϕ [°]	A [N]	ϕ [°]	A [N]	ϕ [°]
Axial	Blade-resolved	497	35	−103	20	−122	4	−138
	Actuator line	521	37	−103	20	−116	4	−130
	RANS/BET	510	38	−101	22	−110	5	−118
Tangential	Blade-resolved	557	36	−103	18	−117	4	−128
	Actuator line	570	37	−102	17	−112	3	−120
	RANS/BET	558	39	−99	19	−104	4	−109

The disk distributions of the axial and tangential blade loads are shown in figure 6.4. Figures 6.4a and 6.4d show the blade loads for the blade-resolved (BR) computation. Figures 6.4b and 6.4e show the difference between actuator line (AL) and blade-resolved loads. The difference is only significant near the tip of the blade, and is greater at the azimuths where the blade is the most loaded. This is consistent with the 5% overshoot that was seen in figure 6.3. Figures 6.4c and 6.4f show the difference between RANS/BET and blade-resolved loads. For the axial loads, the observation is similar to that of the actuator line but with a smaller amplitude. The sharp

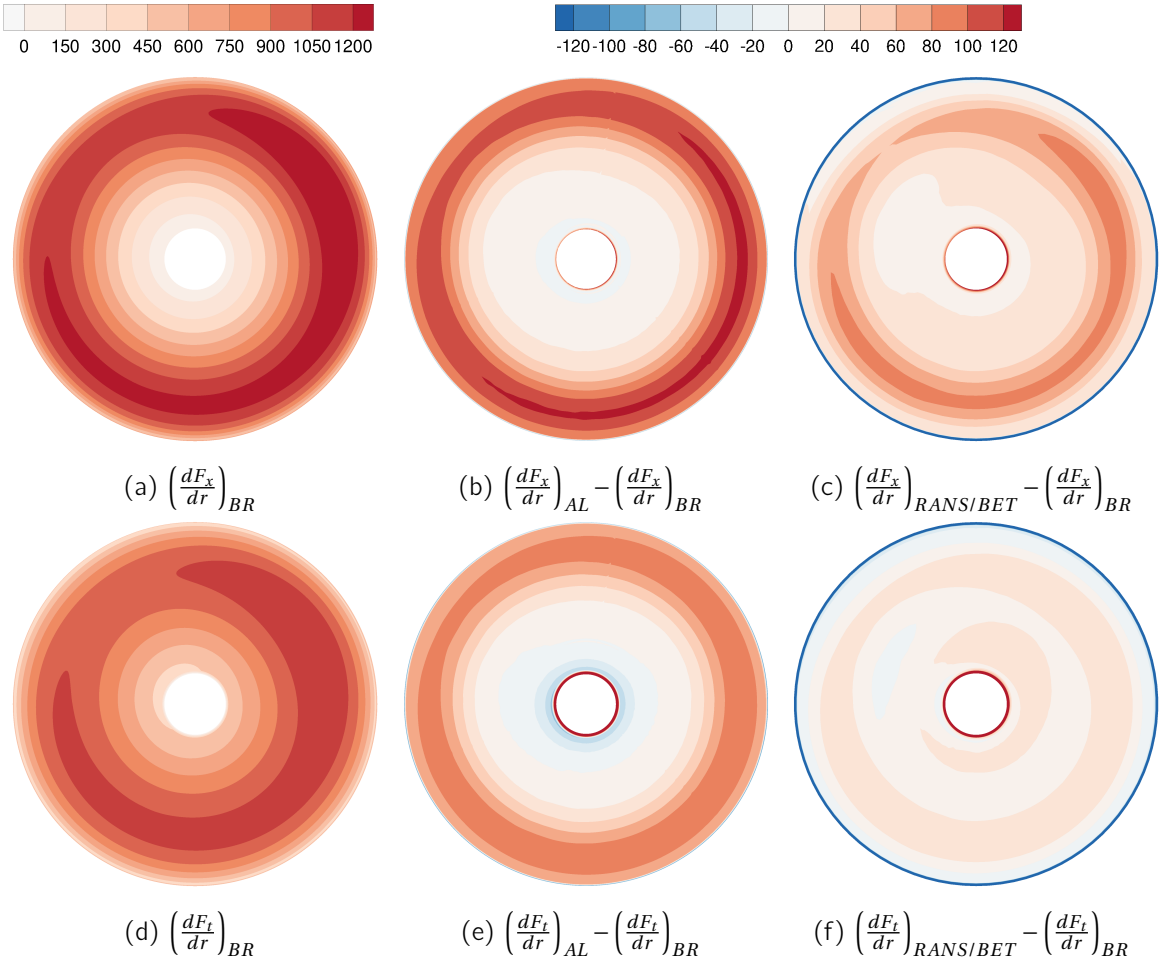

(a) $\left(\frac{dF_x}{dr}\right)_{BR}$ (b) $\left(\frac{dF_x}{dr}\right)_{AL} - \left(\frac{dF_x}{dr}\right)_{BR}$ (c) $\left(\frac{dF_x}{dr}\right)_{RANS/BET} - \left(\frac{dF_x}{dr}\right)_{BR}$

(d) $\left(\frac{dF_t}{dr}\right)_{BR}$ (e) $\left(\frac{dF_t}{dr}\right)_{AL} - \left(\frac{dF_t}{dr}\right)_{BR}$ (f) $\left(\frac{dF_t}{dr}\right)_{RANS/BET} - \left(\frac{dF_t}{dr}\right)_{BR}$

Figure 6.4: Disk axial and tangential loads (in N/m) for each method.

decrease of the loads at the very tip is in particular well predicted thanks to the calibrated tip-loss correction. For the tangential loads, the difference is very small for all radii at all azimuths.

6.3 Wing loads

This section studies the effect of the propeller on the wing, which is of first importance when trying to evaluate aircraft performance as a whole. First the average wing loads are compared for the three modeling methods, and then the unsteady loads for the blade-resolved and actuator line computations.

6.3.1 Average loads

Table 6.3 shows the average wing lift and drag coefficients for the blade section located between $y = -2R$ and $y = 2R$ (y being the wing spanwise direction). This area of interest, shown in figures 2.6 and 2.7, corresponds to the zone that is mostly affected by the propeller slipstream. The integrated lift coefficient suggests that the wing is overall only lightly disturbed by the propeller, however the

reason for this is that the propeller increases the lift on one side of the wing and decreases it on the other, leading to an average close to the prop-off value. In average, the slipstream increases the wing drag at all spanwise positions, leading to a 14% increase of the drag, which is significant and more representative of the effect of the propeller on the wing. In any case, both body-force models are able to provide an accurate prediction of the average integrated wing loads.

Table 6.3: Wing loads averaged over a full rotation

Quantity	Prop off	Blade-resolved	Actuator line	RANS/BET
C_L	0.5040	0.5060	0.5064	0.5069
C_D	0.01380	0.01571	0.01571	0.01567

The sectional average lift and drag distributions along the wing are plotted in figure 6.5. Because of its direction of rotation, the propeller wake creates an up-wash on one side of the wing and a down-wash on the other, thus explaining the general shape of the lift curves. For both the lift and the drag, the body-force models are able to predict all blade-resolved trends with an excellent accuracy. The slight amplitude overshoots by the actuator line model are most likely caused by the overestimated blade loads.

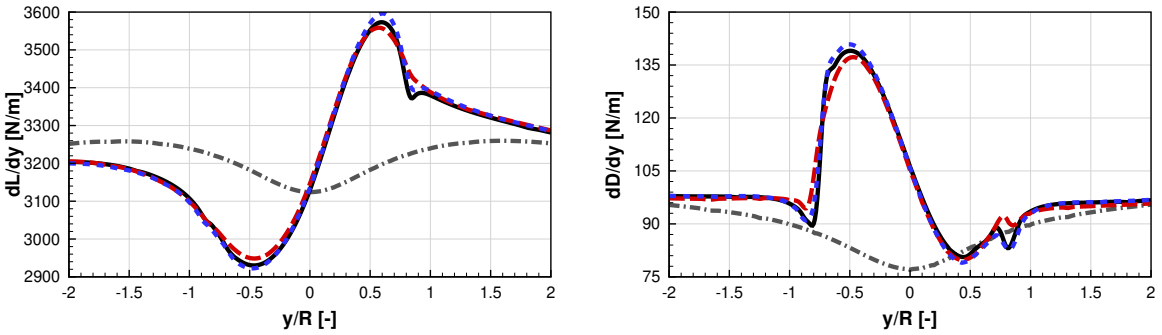

(a) Lift (b) Drag

Prop-off (- - -), Blade-resolved (——), Actuator line (- - -), RANS/BET (— —)

Figure 6.5: Spanwise distribution of the average wing loads.

The wing's average pressure coefficients (C_p) were extracted on the spanwise locations where the lift is maximum ($y/R = 0.6$) and minimum ($y/R = -0.5$). These C_p profiles are shown in figures 6.6 and 6.7 for both body-force methods, the blade-resolved computation, and the computation without the propeller. First, these figures show the discrepancy with the power-off computation, which represents the average effect of the propeller on the wing. It is most noticeable at the leading edge, both on the pressure and suction sides, which is consistent with a change of the section's angle of attack due to the average velocities induced by the propeller. Second, the C_p profiles computed by the two body-force simulations are extremely close to the blade-resolved reference. In both figures, the slight differences are consistent with the results shown in figure 6.5 (slight overestimation of the maximum lift by the actuator line model, and slight overestimation of the minimum lift by the RANS/BET model).

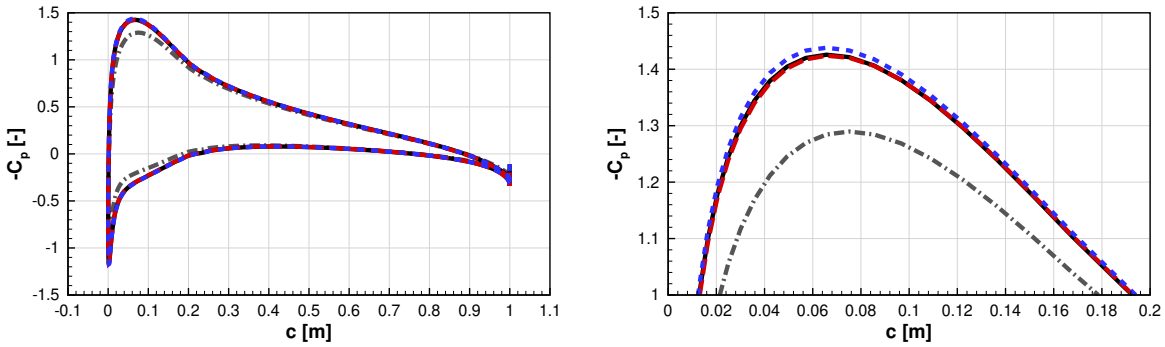

(a) Slice of the wing section (b) Zoom at the leading edge of the suction side

Prop-off (----), Blade-resolved (——), Actuator line (- - -), RANS/BET (— —)

Figure 6.6: Average pressure coefficient profile of the wing at the spanwise location where the lift is maximum ($y/R = 0.6$).

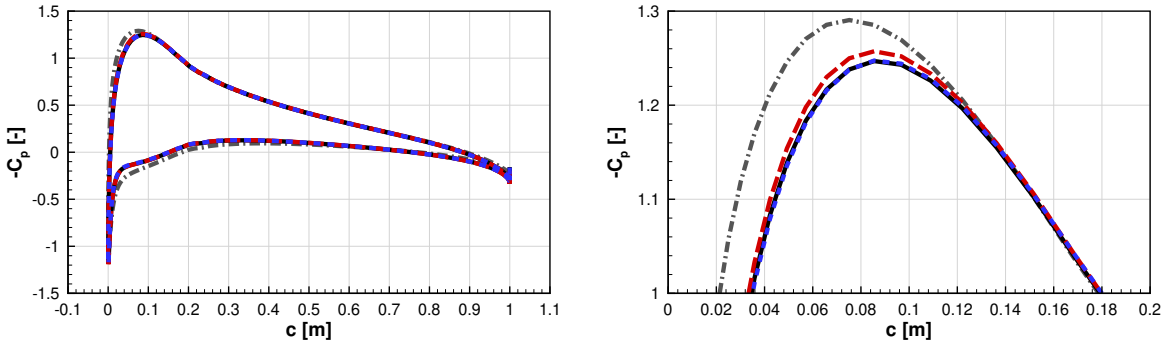

(a) Slice of the wing section (b) Zoom at the leading edge of the suction side

Prop-off (----), Blade-resolved (——), Actuator line (- - -), RANS/BET (— —)

Figure 6.7: Average pressure coefficient profile of the wing at the spanwise location where the lift is minimum ($y/R = -0.5$).

6.3.2 Unsteady loads

This section studies the time-dependent wing loads, and thus only focuses on blade-resolved and actuator line computations. The unsteady wing loads are strongly affected by the propeller blades' tip vortices that periodically hit the wing. Figure 6.8 shows Q-criterion iso-surfaces for a time step where a blade tip vortex hits the wing leading edge, for the blade-resolved and actuator line computations. Two important observations can be made from this figure. The first is that the vortex-systems for the two methods seem very similar. In particular, the helical vortices hit the wing leading edge at the same time-step in both simulations. Second, the viscous wake, which corresponds to the sheet shed from the blade surface in the blade-resolved simulation, hardly reaches the wing surface as a thin sheet. There are two reasons for this: (i) at the top of the blade, the thin viscous wake does not make it through the Chimera interpolation due to cell sizes that are too large in the background grid (as was shown in figure 4.8), and (ii) the Cartesian background grid is in any case not suited to maintain the viscous wake without dissipation. As a

result, the viscous wake only has a small impact on wing loads in the blade-resolved simulations. This brings the blade-resolved results even closer to the actuator line results in the following.

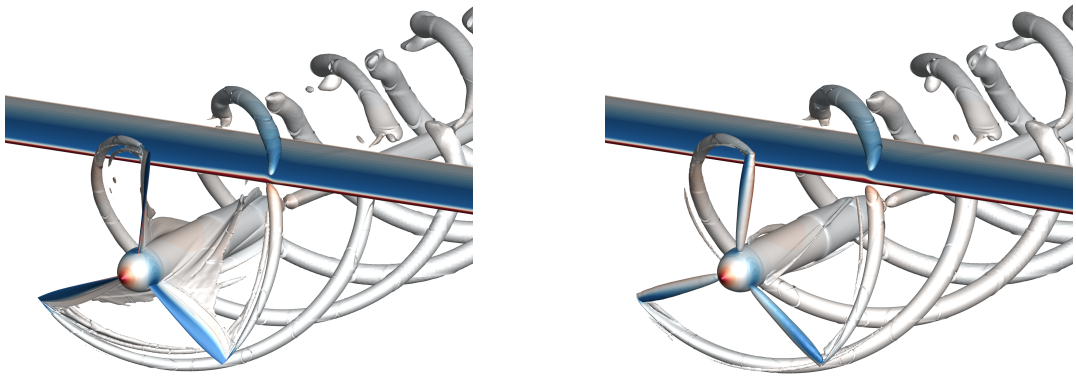

Figure 6.8: Iso-surface of the Q-citerion for the blade-resolved (left) and actuator line (right) computations, colored by pressure.

Figure 6.9 shows the time-varying lift and drag, integrated on the area of the wing behind the propeller (between $y = -2R$ and $y = 2R$), as a function of a reference blade position, as defined in section 1.1.3. The loads are 120°-periodic so the study only focus on a third of a revolution. The curves for the two modeling methods are in phase and the trends are similar. The actuator line amplitude is however slightly higher due to the overestimated blade loads.

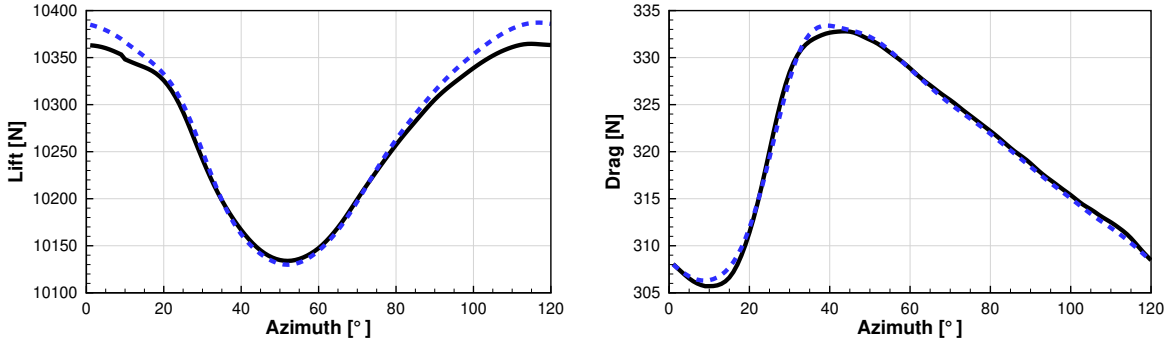

(a) Lift (b) Drag

Blade-resolved (——), Actuator line (- - -)

Figure 6.9: Time varying wing loads as a function of blade azimuth.

These unsteady evolutions are compared in the frequency domain in table 6.4, where the amplitude and phase coefficients of the first three modes are presented. The phase angles are very similar, but the amplitudes differ slightly for the lift (up to 10% for the amplitude of the first mode). The amplitudes are however almost identical for the drag. This suggests that the tip vortices, which have different structures between the two computations because of the smearing of the actuator line, do not modify the angles of attack of the wing sections in quite the same

manner. This could also be linked to the overestimation of the blade loads by the actuator line model, which also modifies the structure of the tip vortices.

Table 6.4: Amplitude and phase coefficients of wing loads obtained by Fourier analysis.

Component	Approach	Mode 0	Mode 1		Mode 2		Mode 3	
		A [N]	A [N]	ϕ [°]	A [N]	ϕ [°]	A [N]	ϕ [°]
Lift	Blade-resolved	10266	115	19	21	−111	5	160
	Actuator line	10273	127	19	21	−109	4	150
Drag	Blade-resolved	320	12	−165	5	123	2	61
	Actuator line	320	12	−163	4	123	2	53

Figures 6.10 and 6.11 show instantaneous spanwise wing loads, focusing on the instants where the propeller wake has the most impact. Figure 6.10 shows the wing lift at timesteps for which the lift is the highest and the lowest. Figure 6.11 shows the wing drag at timesteps for which the drag is the highest and the lowest. All graphs show that the actuator line model is able to capture the correct time-accurate trends with an excellent precision, even though the wing loading profiles can vary significantly in time, especially for the drag.

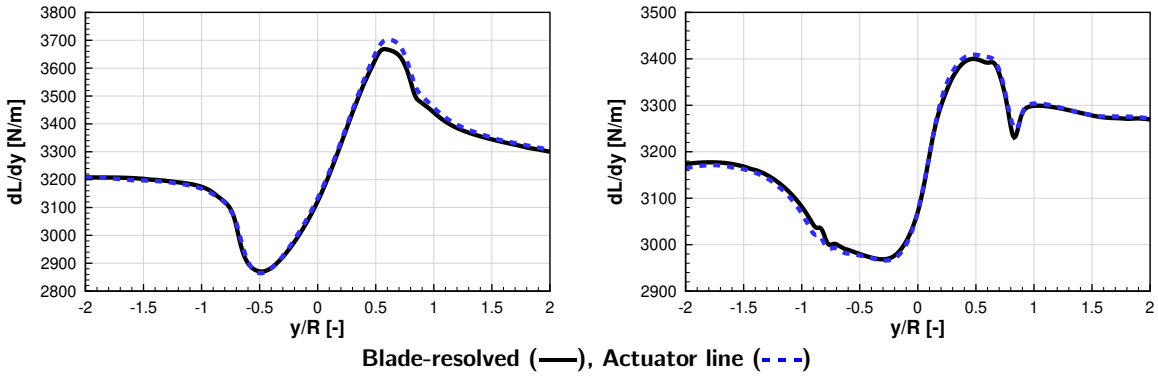

Figure 6.10: Instantaneous wing spanwise lift distribution at time steps where integrated lift is maximum (left) and minimum (right).

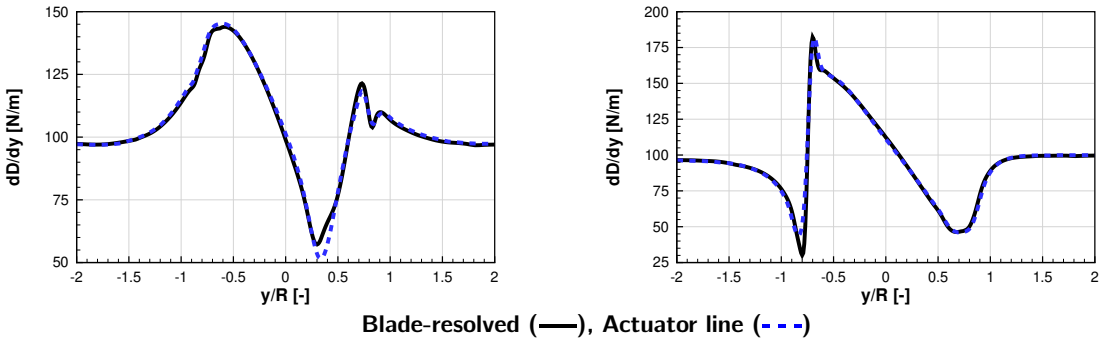

Figure 6.11: Instantaneous wing spanwise drag distribution at time steps where integrated drag is maximum (left) and minimum (right).

Figure 6.12 shows the C_p profiles of the most highly loaded wing section at the time step where the wing lift is maximum (corresponding to the lift peak in figure 6.10). The unsteady pressure distribution is computed by the actuator line with the same accuracy as for the average pressure distribution.

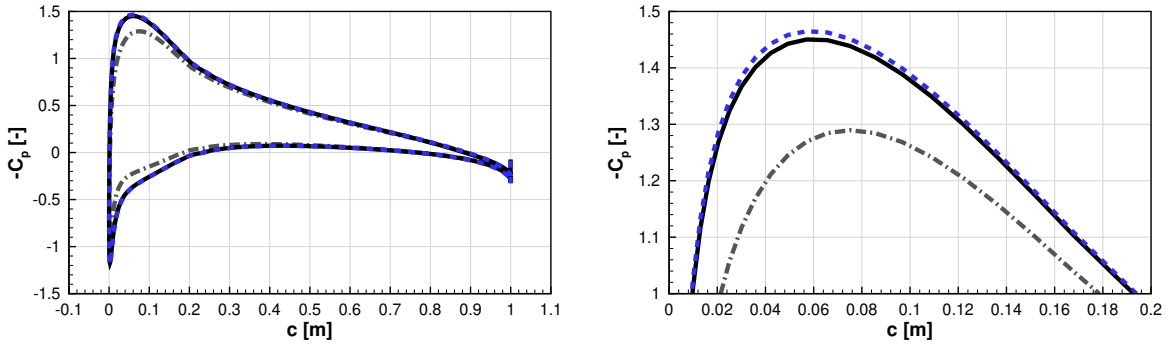

(a) Slice of the wing section (b) Zoom at the leading edge of the suction side

Prop-off (----), Blade-resolved (——), Actuator line (- - -)

Figure 6.12: Instantaneous pressure coefficient profile of the wing at the spanwise location where the lift is maximum ($y/R = 0.6$), at the time step where the wing loads are the highest.

6.4 Computational cost of each method

The initial objective of body-force modeling is to reduce the computational cost of aerodynamic analyses. It is therefore only natural to come back to this question in this last chapter, where both steady and unsteady body-force methods are used in a test case that is representative of a typical final application of the models. The CFD-actuator disk models enable conducting steady instead of unsteady simulations, so the gain is intuitively significant. However as mentioned previously, it is generally known in the aeronautics community that the actuator line model does not offer a significant reduction of computational cost compared to the blade-resolved computations.

Yet the gain induced by these reduced-order methods are rarely quantified in the literature. One of the few examples of such a study is Stokkermans' PhD thesis [88]. He modeled a four-bladed wing tip-mounted propeller with an actuator-line model and a steady CFD-actuator disk model that also relies on source terms. In his work, the propeller loads were prescribed from a blade-resolved computation, resulting in a one-way coupling and cutting the cost of the velocity sampling and the BET analysis compared to the models developed in this thesis. Stokkermans found that in these conditions, the actuator line model resulted in a 17% reduction in computational cost compared to a blade-resolved reference. An 85% reduction was observed for his steady body-force model.

A thorough comparison of the computational cost of each method developed here is not straightforward. Depending on the modeling method used, the mesh is distributed between a different number of processors, the boundaries between the zones are not necessarily similar, and this can for instance have a more or less significant impact on the time needed for the Chimera interpolations. The method proposed here is to compare the total CPU time, i.e. the total time taken for the computation multiplied by the number of processors on which the computation was distributed. This approach gives a gross estimate of the relative cost of each method, which is

satisfying enough from an engineering standpoint. The computation of 9 propeller rotations from a uniform field took 45 000 CPU hours for the blade-resolved approach, and only 22 000 for the actuator line computation, which is equivalent to a very significant reduction of computational cost of around 50%. Two points are worth mentioning. The first is that this is substantially more important that the gains computed by Stokkermans in his work using prescribed blade loads. This must be thanks to the implementation method used in this work, which, as explained in chapter 4, replaces loops and MPI communications with arrays manipulations. The second is that the cost of the blade-resolved computations climbs rapidly with the number of blades, because it adds more cells to the mesh, but mostly because more Chimera interpolations need to be made at each iteration. However because the cost of the one co-process iteration of the actuator line as implemented in this thesis is negligible compared to the cost of the CFD iteration, adding more blades would not lead to any significant extra cost. The reduction of the computational cost enabled by the actuator line model is thus expected to increase with the number of blades.

In this work, the RANS/BET model was found to need 16 000 CPU hours (64% reduction compared to blade-resolved) to reach convergence of the residuals. Because this computation is steady, it is difficult to compare it rigorously to the other computations. For instance, the simulation could have been stopped earlier when the wing loads are converged. This criteria definitely depends on a team's practices, and may in part explain the less important reduction than in Stokkerman's work. Also, the RANS/BET model is based on interpolations, which are expensive because they require MPI communications. An alternate implementation, more similar to what is done for the actuator line, could be developed to cut computational costs further. In any case, the relative reduction cost is also expected to rise with the number of blades for the same reason as for the actuator line model.

Another important aspect should be mentioned. A method's efficiency should be analyzed as a whole and not only focused on the computational cost of the CFD simulation. For the blade-resolved computations, the body-fitted blade meshes are sometimes difficult to make. Furthermore, a new mesh has to be made every time the propeller's blade pitch angle changes, which is inefficient when trimming to match a target thrust. This problem does not arise for body-force computations, where the blade pitch angle can simply be modified during the computation with no intervention on the mesh. However, the body-force models require the computation of the 2D airfoil polars. Yet all things considered, this is relatively inexpensive compared to full blade-resolved computations. It is one of the main advantages of using 2D polars instead of 3D polars, as explained in chapter 1.

Conclusion

This chapter evaluated both body-force models in installed configuration. The wing induces a light non-uniform distortion in the propeller plane, with local incidence angles of less than 5°. These loads are overpredicted by the actuator line by 5% for all azimuths. The RANS/BET model is more accurate but less consistent from one azimuth to the other. For both models, the spanwise loads are very accurate on the majority of the blade, the discrepancies appear at the blade tips.

The time-averaged spanwise distribution of the wing loads are very similar for all three computations, the body-force models being able to reproduce all blade-resolved trends. The distribution of the pressure coefficients at the most and least loaded spanwise locations are extremely similar as well. The same goes for the actuator line, which is able to reproduce the time-accurate wing loadings with great accuracy, despite significant variations of the shape of the wing loadings throughout a blade rotation.

Finally, the computational costs of each modeling approach were compared for the simulation of the installed configuration. For this three-bladed propeller, the actuator line model is 2 times less expensive than the blade-resolved computation (significantly more than in the literature thanks to the novel implementation proposed in this work), and the RANS/BET model by about 2.8 times. These reductions were analyzed, and it was noted that the advantage of using body-force methods would grow with number of propeller blades. The gain offered by the body-force models goes beyond theses numbers when analyzing the cost of each method as a whole, including the time needed to construct the meshes for example.

Conclusions and perspectives

Conclusions

This thesis was dedicated to the development and validation of steady and unsteady fully coupled body-force models for propeller aerodynamics modeling. The objective of these models is to capture interaction effects and to offer significant gains in computational resources compared to full blade-resolved CFD so that they are attractive for powered aircraft pre-design studies.

Both steady and unsteady models, respectively called RANS/BET and actuator line, are based on methods found in the literature, which were detailed in chapter 1. They rely on a blade element theory approach to compute the blade loads, using local CFD velocities. For both models, a thorough review of the existing methods for velocity sampling and source term distribution was presented. It was shown in particular that no real consensus exists when it comes to the steady model. For the actuator line models, it was explained that the smearing parameter used to distribute the loads in the proximity of the actuator lines should be meticulously chosen to ensure model stability and accuracy, and that it has a first order effect on the results. It was also shown that this parameter needs to be chosen in accordance with local cell length and with the time step. In the literature, these models are mostly used in the wind turbine sector. Few applications exist in the propeller field, and most use prescribed loadings or 3D polars.

The three-bladed propeller studied in this work, the ONERA HAD-1 propeller, presented in chapter 2, was chosen because it satisfies most of the blade element theory assumptions at its cruise design point. It is thus a good test case to validate the newly developed body-force models. It operates in subsonic but compressible flow, and the flow is two dimensional on the whole blade. A study of the propeller characteristic showed that this is the case in particular for blade pitch angles between 37° and 49°, angle range that was studied with the body-force models. The CFD setup, which relies on a finite volume solver, was also presented in this chapter, from numerical parameters to computational meshes.

Chapter 3 detailed the implementation of the steady RANS/BET model, based on a full coupling between the blade element theory and CFD. Three conclusions were drawn related to source term distribution, unifying the different practices from the literature. It was found that:

- the shape of the source term volume has no impact on the blade loads nor on the flow field
- the shape of the distribution function of the source terms in the axial direction has no direct impact on the simulation outside of the body-force volume, the only parameter that matters is the percentage of source terms distributed upstream of the sampling lines.
- 50% of the source terms should be placed upstream of the sampling lines to match fundamental momentum theory results. When the RANS/BET model is setup this way, it closely matches results from blade element momentum theory computations.

The necessity of tip-loss corrections was then explained. A generalized implementation of Glauert's tip-loss correction for non-axial flow was proposed, as well as a calibrated correction of the blade's tip loads. An in-depth study of the source term in the energy equation was also conducted, which lacked in literature. It was found that its absence leads to internal energy drops in the wake to compensate the increase of kinetic energy due to the momentum source terms, and that it destroys entropy in the propeller area. An energy source term should therefore always be used in body-force computations. Two formulations of this source terms were compared. Both solve the problem of the internal energy drops in the wake, and it was found that one is isentropic whereas the other one creates entropy by accounting for the airfoil drag losses.

The development of an actuator line model adapted to propeller applications was presented in chapter 4. A novel implementation based on a Chimera cylinder was proposed, which enables parallel and vectorized computations of the blade loads and of their distribution, accelerating the simulations significantly compared to classic implementations. A source term distribution study closely compared the actuator line wake computed with prescribed loads to the one from a blade-resolved computation, highlighting the smearing induced by the actuator line. Fully coupled simulations showed that the actuator line model, as implemented in this work, is quite robust to the Gaussian smearing parameter of a 2D Gaussian projection. The comparison of the point and integral velocity sampling techniques showed that both lead to the same blade loads, but that oscillations appear when using the point sampling method for small smearing parameters that are stable when using integral sampling. A model sensitivity study showed that the actuator line model implemented in this thesis is robust to mesh refinement and time-step variations.

The results of both body-force models were compared to reference blade-resolved Chimera computations in isolated configuration in chapter 5. On the cruise operating point at a blade pitch angle of 45°, the actuator line model overestimates propeller thrust and power by around 5% compared to the blade-resolved simulation, especially at the blade tips. The RANS/BET model is more accurate thanks to the calibrated tip-loss correction, by overestimating thrust by 1.7% and underestimating torque by 0.1%. Again, the discrepancies are stronger at the blade tips. Both body-force models are able to capture the trends of the average wake very accurately, despite slight overshoots due the overestimated loads. Slices of the unsteady wake were made for the actuator line model and some smearing is definitely visible, but it is not too far from the smearing induced by the Chimera interpolations of the blade-resolved reference. The body-force models were also tested for blade pitch angles between 37° and 49° to evaluate their ability to predict a wide variety of blade loadings. Conclusions were overall similar to those at a 45° pitch angle, both the RANS/BET and actuator line models being able to predict the trends of the propeller performance. This shows in particular that the RANS/BET loads tip-loss correction that was calibrated at 45° does not have to be recalibrated for all pitch angles. The models were also evaluated under incidences of 3°, 6° and 9°, and were in general as accurate as in axial flow. The propeller in-plane loads were in particular very well predicted.

The final chapter was dedicated to evaluating both body-force models in an installed configuration, composed of a wing placed downstream of the propeller. The wing induces a light non-uniform distortion in the propeller plane, with local incidence angles of less than 5°. The propeller loads are overpredicted by the actuator line by 5% for all azimuths. The RANS/BET model is more accurate but less consistent from one azimuth to the other. For both models, the spanwise loads are very accurate on the majority of the blade, the discrepancies appear at the blade tips. The average spanwise distributions of the wing loads are very similar for all three computations, the body-force models being able to reproduce all blade-resolved trends. The distribution of the pressure coefficients at the most and least loaded spanwise locations on the wing are extremely

similar as well. The same goes for the actuator line, which is able to reproduce the time-accurate wing loadings with great accuracy, despite significant variations of the distribution of the wing loadings throughout a blade rotation. Finally, the computational costs of each modeling approach were compared for the simulation of the installed configuration. For this three-bladed propeller, the actuator line model is 2 times less expensive than the blade-resolved computation (significantly more than in the literature thanks to the novel implementation proposed in this work), and the RANS/BET model by about 2.8 times. These reductions were analyzed, and it was noted that the advantage of using body-force methods would grow with number of propeller blades. The gain offered by the body-force models goes beyond theses numbers when analyzing the cost of each method as a whole, including the time needed to construct the meshes for example.

Putting the study into perspective, a more general conclusion can be made by looping back to the specifications of the ideal tool to study interaction effects for pre-design studies, which was made in the introduction. The models developed and validated in this thesis can now be evaluated using the five aforementioned criteria.

1. *The model should account for the coupled effect of the propellers on the airframe and the retro-action of the airframe on the propellers.*

   This was clearly demonstrated in chapter 6, in which propeller loads and wing loads were found to be in excellent agreement with blade-resolved results, when looking at both time-averaged and time-accurate results.

3. *The model should simplify confidentiality issues between aircraft and engine manufacturers.*

   The fact that body-force models do not rely on the full blade geometry is definitely a huge upside compared to the typical blade-resolved simulations. The RANS/BET and actuator line models developed in this work rely on 2D airfoil polars, but these could for instance be supplied to the aircraft manufacturer by the engine manufacturer without disclosing the blade's airfoils. Both body-force models however strongly depend on the blade's chord and twist laws, which can be sensitive material to share between companies.

5. *The model should be fast enough to allow quick design loops for pre-design studies.*

   The gains obtained when using the body-force models instead of a blade-resolved Chimera approach were briefly mentioned in the installed configuration study at the end of chapter 6. They were found to be very significant in the cases studied here, and expected to be even higher for propellers with more blades, but a more in depth study should be conducted to provide a more general answer. Apart from the computational cost, it should be noted that the body-force methods offer significant time gains compared to blade-resolved computations when creating the mesh. In particular, when the propeller pitch angle is trimmed for thrust, a new mesh must be generated for the blade resolved method and not for the body-force approaches.

Items 2 and 4 were not investigated in this work and will therefore be addressed in the perspectives.

Perspectives

In the end, the work conducted in this thesis lays the foundation of two body-force models capable of predicting aerodynamic interaction effects, which were developed and validated in conditions

that are optimal when using 2D airfoil polars to compute the blade loads: subsonic flow, little interactions between blades, 2D flow on the blade... However the propellers that are currently of interest for the industry are much faster and much more loaded (from the propellers of the Airbus A400M to the CFM Rise open fan engine). This challenges the assumptions of the blade element theory and the new flow conditions could strongly impact the quality of the results from both body-forces methods. An effort of generalization must therefore most likely be made for highly loaded propellers.

Generalization for highly loaded propellers

First, the geometries of highly loaded propellers differ significantly from the HAD-1 propeller studied in this thesis. They have more blades, such that the use of isolated 2D airfoil polars becomes less appropriate. Furthermore the high solidity reduces the cross-section in the propeller area, thus accelerating the fluid to maintain a constant mass flow rate. A correction for this effect exists for body-force models in the field of turbomachinery [41], but it has yet to be adapted to the models studied in this work.

Second, highly loaded propellers operate at different conditions than HAD-1, with higher freeflow velocities and rotation speeds. This creates significant compressibility effects, so the body-force models should be able to predict the correct propeller thermodynamics. In this work, an overview of the impact of the energy source term was presented and basic guidelines were given. An evaluation of these guidelines on a more loaded propeller remains to be made. The higher loads also lead to more frequent flow separation on the blade. For instance, highly loaded propellers often feature a leading edge vortex in take-off conditions. This links back to the fourth criteria mentioned in the introduction: *The model should be able to explore off-design points*. This implies the correct prediction of flow separation, which for a rotating blade can most likely only be achieved with an appropriate correction of the 2D airfoil polars for rotational effects, which was not investigated in this thesis. Also, even if the flow separation is correctly predicted on the blade loads, it should be correctly transferred on the flow field as well. The capacity of the actuator line model to create vortices from an interpolation in a separated part of a 2D airfoil polar remains to be seen.

Multidisciplinary studies

The main advantage of fast methods is that they can be coupled for multidisciplinary studies in an affordable time, which is particularly welcome for aircraft pre-design. This led to the second criteria of the introduction: *The model should be easily compatible with aeroelasticity and aeroacoustic studies*. The fact that the body-force models rely on the blade element theory is convenient for both disciplines. For aeroelsaticity, it means for instance that the quarter-chord line can be easily curved and twisted due to structural computations, and this curvature can be accounted for at each computation of the body-forces. For aeroacoustics, the 2D tabulated airfoils can also include the pressure coefficients on each airfoil, which enables the reconstruction of a pressure field on the blade at each iteration, as done by Reboul et al. for the RANS/BET model [75]. The technique has yet to be applied to the actuator line, as well as any other aeroacoustic analysis of the unsteady wake.

Appendix A

Characterization of the HAD-1 propeller

The objective of this appendix is to illustrate the different flow regimes at which the HAD-1 propeller can operate. This is done at the flow condition from table 2.2 for different blade pitch angles. The propeller characteristic from figure 2.5 showed that the propeller is in breaking regime bellow 37° and in stalled regime above 51°. The following study focuses on 5 blade pitch angles: 33° (breaking), 37° (low thrust), 45° (design point), 51° (high thrust) and 55°(stalled).

Figure A.1 shows the axial load, tangential load, and circulation distribution on the blade for these 5 pitch angles. The circulation along the blade was obtained by integrating the velocity along a contour for different radii. The method was found to be independent of the chosen contour for attached flow, but it is not expected to be the case for stalled areas where the method becomes less reliable. These graphs show that the flow is separated on the majority of the blade for the pitch angle of 55°.

Figures A.2 and A.3 show the blade surface for each pitch angle; figure A.2 shows the suction side and figure A.3 the pressure side. The surfaces are colored by pressure and frictions lines are traced over them. The figures shows the clear separation at 55°. At 33°, the pressure and suction sides are inverted because of angles of attack that are too low. The flow is also separated on the upper side of the blade. For the 37°, 45° and 51° pitch angles, the flow is fully attached except for a root vortex that appears as the blade is more loaded. Apart from that, the flow is mostly two dimensional, even though the friction lines on the suction side start to bend near the tip when the blade is highly loaded.

Figures A.4, A.5 and A.6 show slices of the flow at r/R values of 0.4, 0.75 and 0.95. They locally illustrate with more details the observations made previously.

An iso-surface of the Q-criterion is shown in figure A.7 for each pitch angle. Slices of the axial and tangential velocity fields half a radius behind the propeller are shown in figures A.8 and A.9.

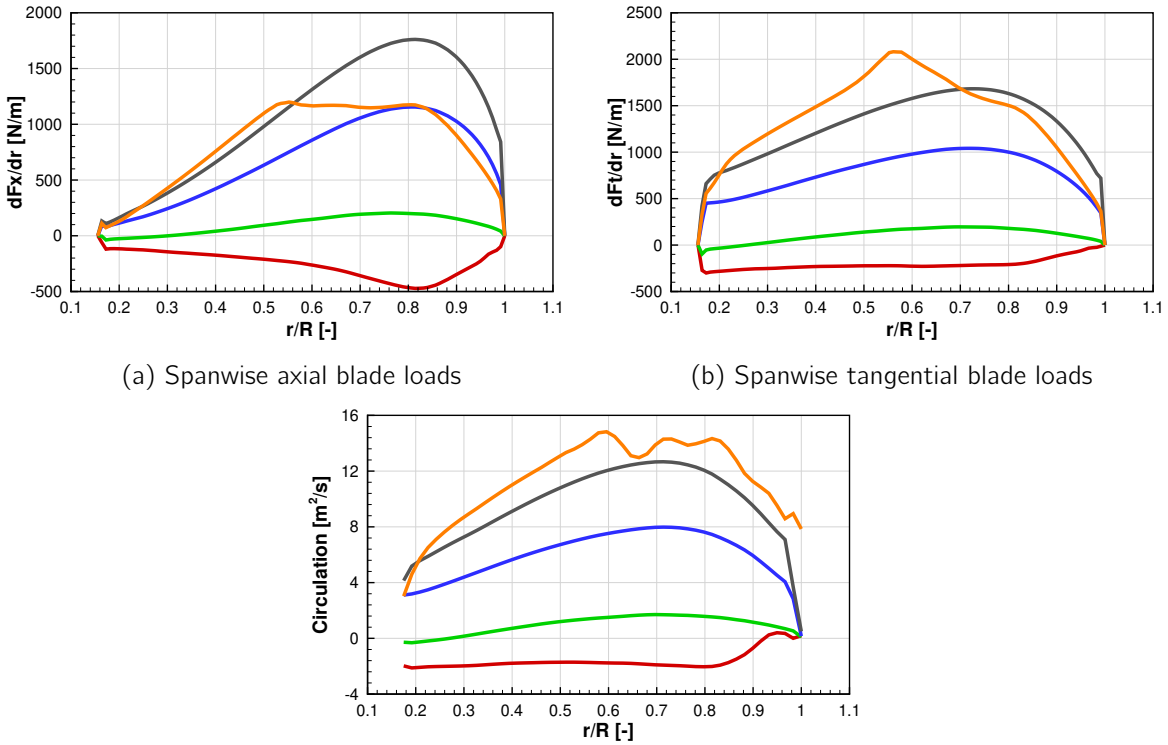

(a) Spanwise axial blade loads

(b) Spanwise tangential blade loads

(c) Spanwise blade circulation

33° (—), 37° (—), 45° (—), 51° (—), 55° (—)

Figure A.1: Spanwise distribution of blade loads for different pitch angles.

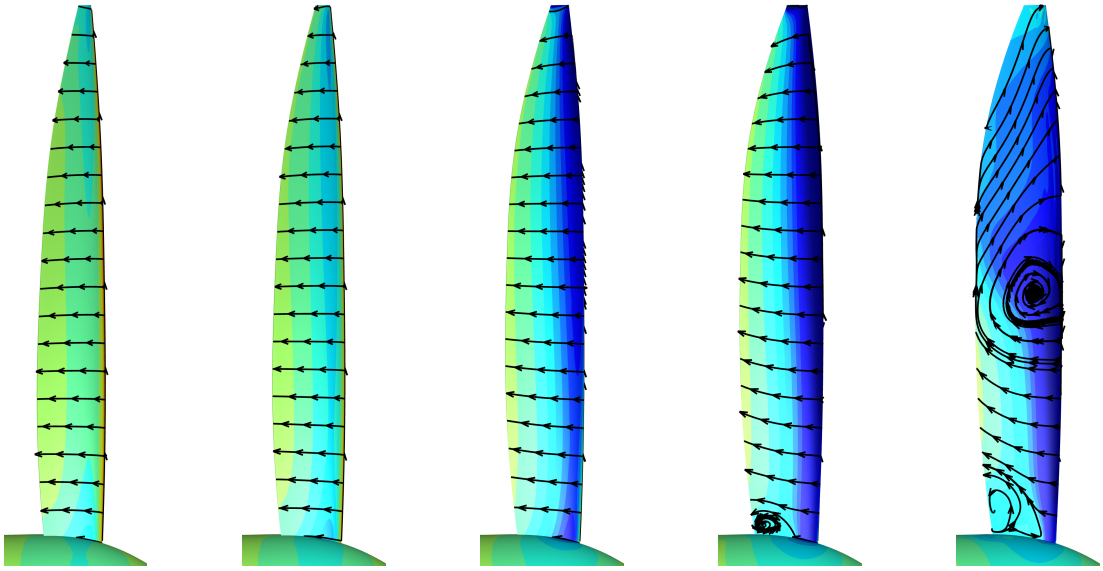

(a) 33° (b) 37° (c) 45° (d) 51° (e) 55°

Figure A.2: Blade suction side for different pitch angles.

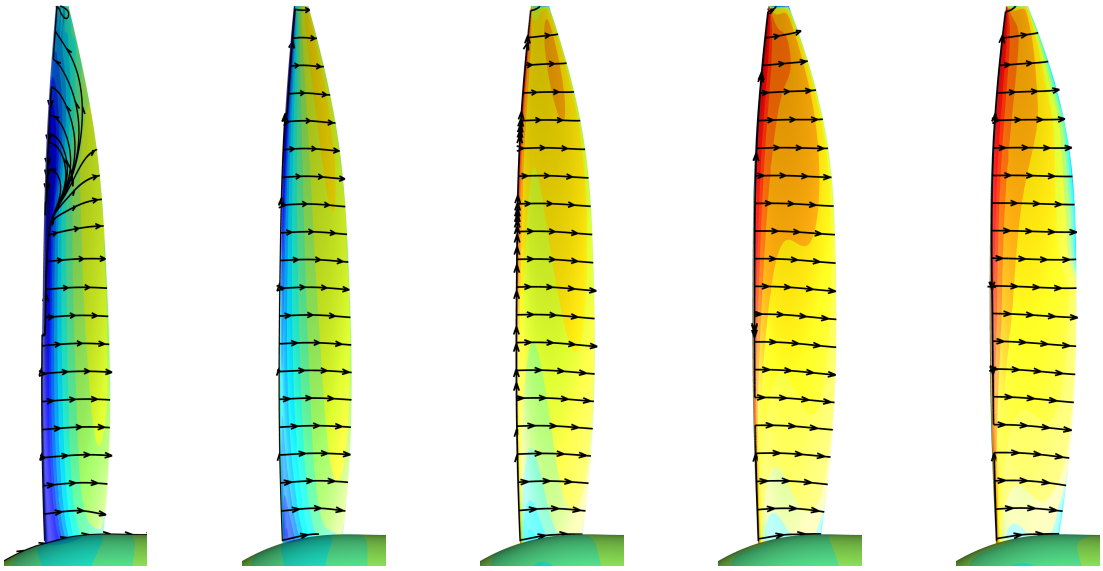

(a) 33° (b) 37° (c) 45° (d) 51° (e) 55°

Figure A.3: Blade pressure side for different pitch angles.

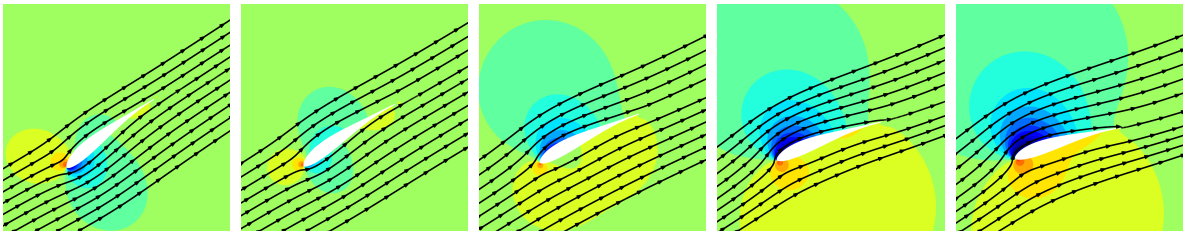

(a) 33° (b) 37° (c) 45° (d) 51° (e) 55°

Figure A.4: Blade sections at $r/R = 0.4$ for different blade pitch angles.

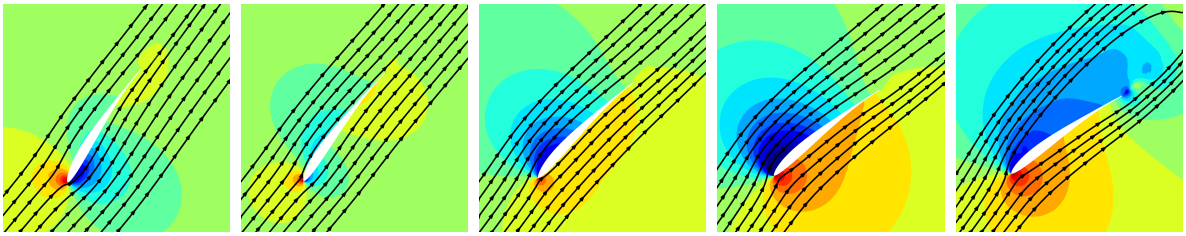

(a) 33° (b) 37° (c) 45° (d) 51° (e) 55°

Figure A.5: Blade sections at $r/R = 0.75$ for different blade pitch angles.

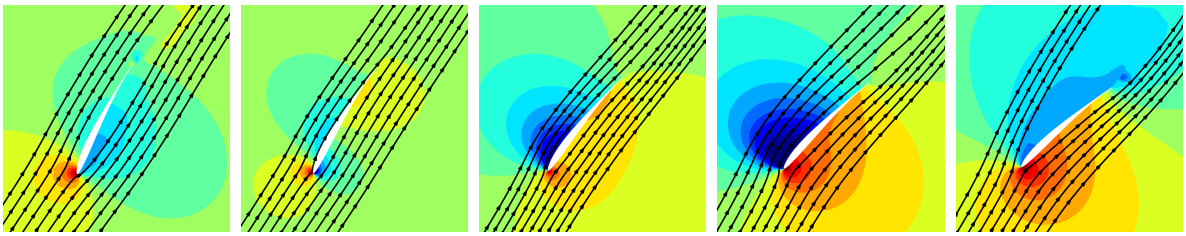

(a) 33° (b) 37° (c) 45° (d) 51° (e) 55°

Figure A.6: Blade sections at $r/R = 0.95$ for different blade pitch angles.

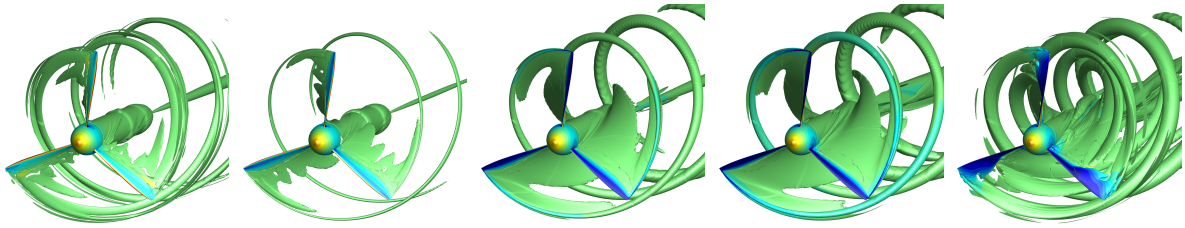

(a) 33° (b) 37° (c) 45° (d) 51° (e) 55°

Figure A.7: Iso-surfaces of the Q-criterion of 10000 for different blade pitch angles.

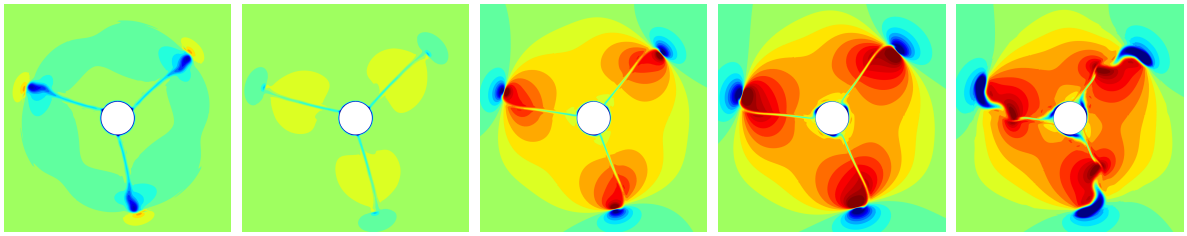

(a) 33° (b) 37° (c) 45° (d) 51° (e) 55°

Figure A.8: Slices of the axial velocity field half a radius behind the propeller.

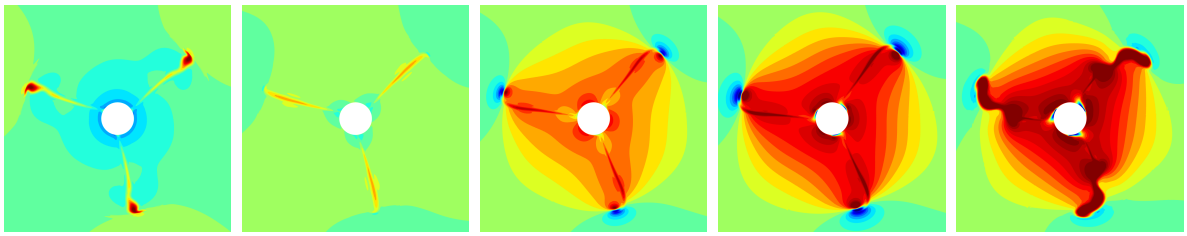

(a) 33° (b) 37° (c) 45° (d) 51° (e) 55°

Figure A.9: Slices of the tangential velocity field half a radius behind the propeller.

Appendix B

2D airfoil polars of 6 blade sections of the HAD-1 propeller

This appendix shows the 2D airfoil polars of the HAD-1 propeller, which were presented in section 2.4. The reader is referred to this section for more details on the computational setup. The following only shows the lift and drag coefficients as a function of the incidence angles, and so for different Mach numbers for the six blade sections considered.

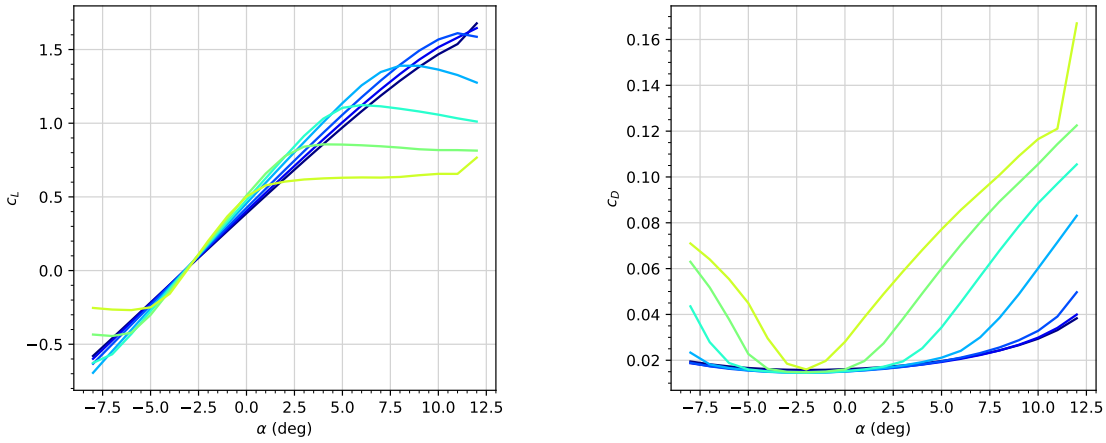

M=0.2, Re=354000 (—), M=0.3, Re=531000 (—), M=0.4, Re=708000 (—), M=0.5, Re=885000 (—), M=0.55, Re=973500 (—), M=0.6, Re=1.062e6 (—), M=0.65, Re=1.1505e6 (—),

Figure B.1: Polar of blade airfoil located at $r/R = 0.15$.

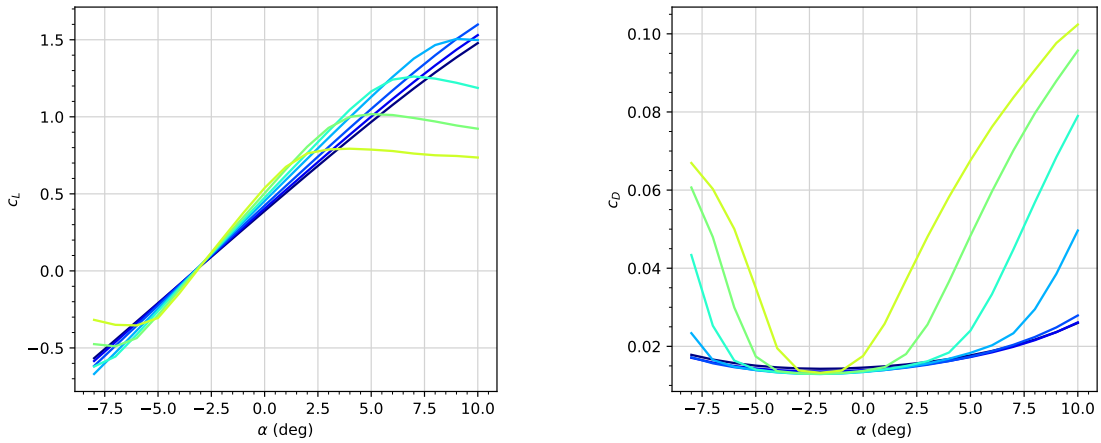

M=0.2, Re=428000 (——), M=0.3, Re=642000 (——), M=0.4, Re=856000 (——), M=0.5, Re=1.07e6 (——), M=0.55, Re=1.177e6 (——), M=0.6, Re=1.284e6 (——), M=0.65, Re=1.391e6 (——),

Figure B.2: Polar of blade airfoil located at $r/R = 0.25$.

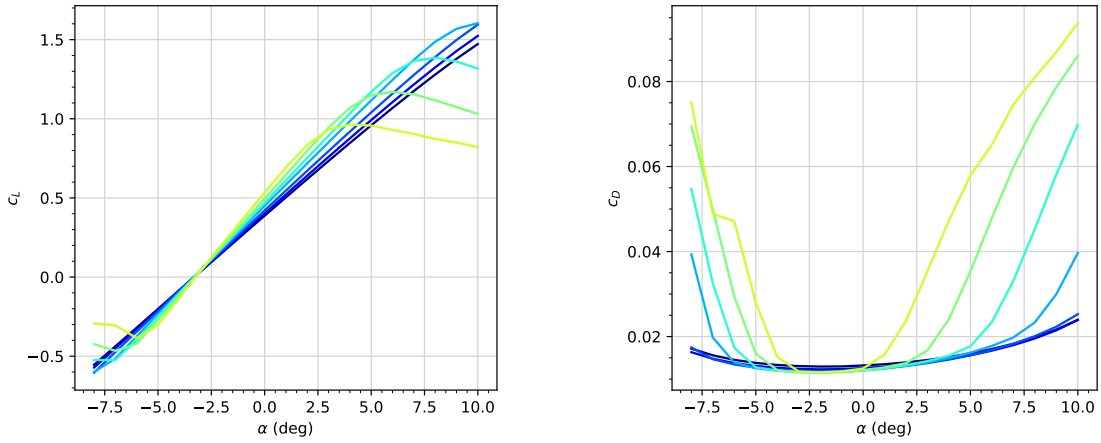

M=0.2, Re=512000 (——), M=0.3, Re=768000 (——), M=0.4, Re=1.024e6 (——), M=0.5, Re=1.28e6 (——), M=0.55, Re=1.408e6 (——), M=0.6, Re=1.536e6 (——), M=0.65, Re=1.664e6 (——),

Figure B.3: Polar of blade airfoil located at $r/R = 0.4$.

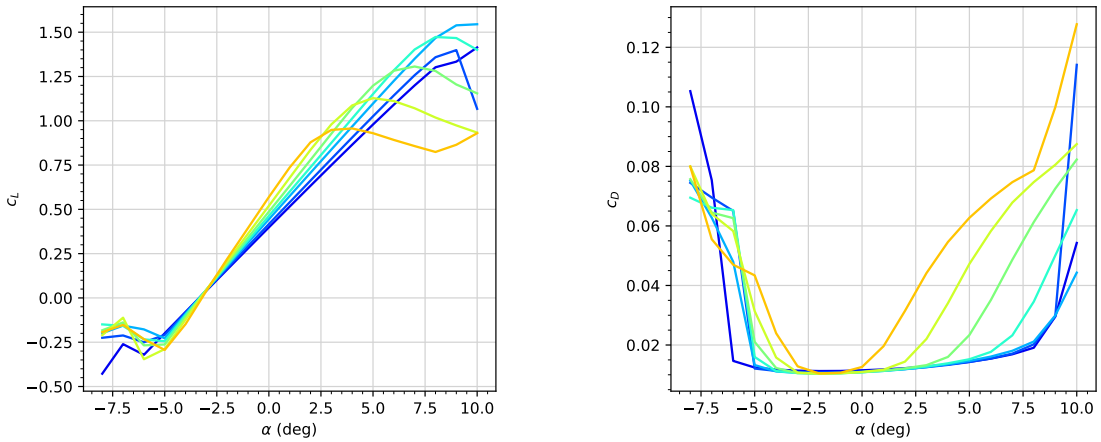

M=0.3, Re=852000 (—), M=0.4, Re=1.136e6 (—), M=0.5, Re=1.42e6 (—), M=0.55, Re=1.562e6 (—), M=0.6, Re=1.704e6 (—), M=0.65, Re=1.846e6 (—), M=0.7, Re=1.988e6 (—),

Figure B.4: Polar of blade airfoil located at $r/R = 0.6$.

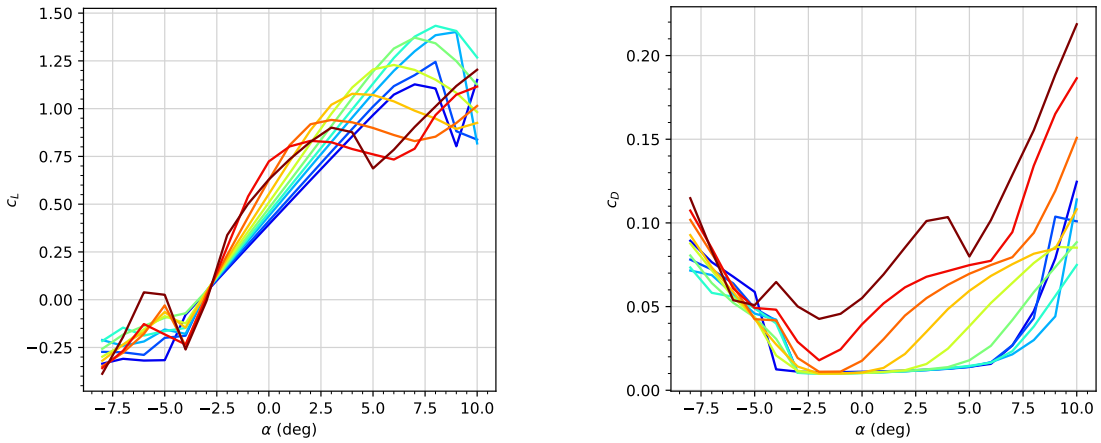

M=0.3, Re=798000 (—), M=0.4, Re=1.064e6 (—), M=0.5, Re=1.33e6 (—), M=0.55, Re=1.463e6 (—), M=0.6, Re=1.596e6 (—), M=0.65, Re=1.729e6 (—), M=0.7, Re=1.862e6 (—), M=0.75, Re=1.995e6 (—), M=0.8, Re=2.128e6 (—), M=0.85, Re=2.261e6 (—),

Figure B.5: Polar of blade airfoil located at $r/R = 0.8$.

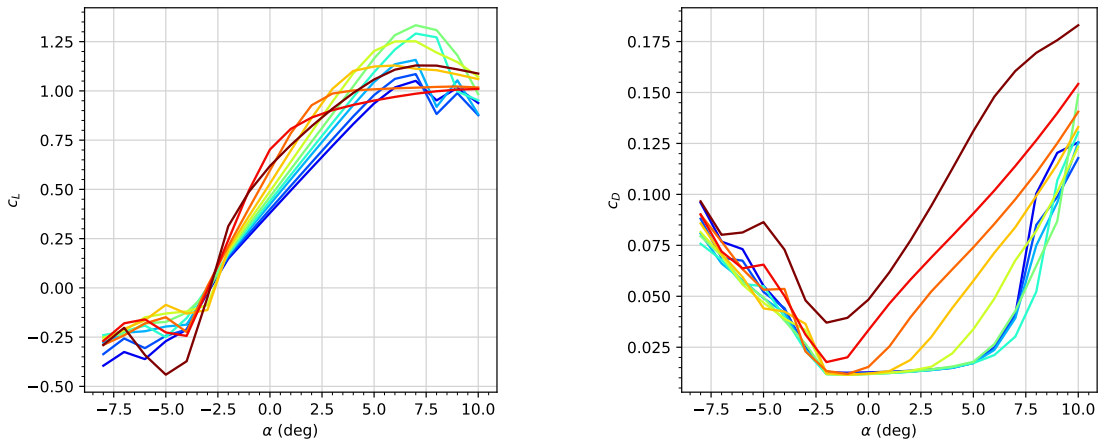

M=0.3, Re=258000 (—), M=0.4, Re=344000 (—), M=0.5, Re=430000 (—), M=0.55, Re=473000 (—), M=0.6, Re=516000 (—), M=0.65, Re=559000 (—), M=0.7, Re=602000 (—), M=0.75, Re=645000 (—), M=0.8, Re=688000 (—), M=0.85, Re=731000 (—),

Figure B.6: Polar of blade airfoil located at $r/R = 1$.

Appendix C

Validation of the generalized Glauert correction

It was explained in section 3.3.2 that the implementation of Glauert's tip-loss correction proposed by Shen et al. [83] should be adapted for non-uniform inflow. A generalized workflow was proposed in section 3.3.2.2 for propellers under incidence or in installed configuration. This appendix is dedicated to quantifying the need for the generalized formulation, and to validate the correction on two cases: the isolated HAD-1 propeller in incidence and the HAD-1 propeller in installed configuration.

C.1 Analytical comparison of the two formulations

This section is dedicated to the analytic comparison of the two formulations, to understand the effect of neglecting the non-uniform inflow while accounting for the tip-correction. By subtracting equations (1.68) and (3.9) to estimate the difference in corrected velocities between the two approaches, one gets:

$$\begin{cases} \Delta v_x^{cor} = \left(\frac{1}{F_G} - 1\right)\left(v_x^{p-o} - V_0\right) \\ \Delta v_t^{cor} = \left(\frac{1}{F_G} - 1\right) v_t^{p-o} \end{cases} \tag{C.1}$$

Three observations can be made from these equations:

- Δ is directly proportional to the power-off field, so the greater the perturbation, the greater the importance of using the generalized correction.
- The factor $\left(\frac{1}{F_G} - 1\right)$ is almost 0 near the hub, so it is unnecessary to account for the hub in the power-off field.
- The factor $\left(\frac{1}{F_G} - 1\right)$ tends to infinity near the tip, so the effect of the power-off field is amplified at the tip when the generalized correction is not used.

In the following, the results for 3 approaches are compared: a blade-resolved computation used as reference, and two RANS/BET computations, one with the correction for uniform flow and one with the generalized correction for non-uniform flow. Two cases are studied, the isolated configuration in incidence and the installed configuration.

C.2 Validation on an isolated propeller in incidence

For the isolated propeller in incidence ($\Theta = 9°$), the RANS/BET model only computes the time-averaged flow field, so in the following, the blade-resolved results are also time averaged to allow a comparison. Table C.1 shows the integrated propeller loads for each computation. Both RANS/BET computations overestimate the thrust and power by around the same margin, regardless of the correction used. However, the axial correction fails to predict the in-plane (1P) loads correctly, whereas the generalized correction significantly improves the results. This hints that the variation of the loads with the azimuths may be incorrect and that the thrust and power may be accurately predicted by error compensation.

Table C.1: Comparison of averaged propeller loads computed by blade-resolved and RANS/BET approaches

	Blade-Resolved	RANS/BET Axial Correction	RANS/BET Generalized Correction
Thrust [N]	1458	1563 (+7.2%)	1558 (+6.9%)
Power [kW]	167.9	170.2 (+1.4%)	171.6 (+2.2%)
1P Loads [N]	567	720 (+27.1%)	598 (+5.5%)
1P Phase [°]	10.5	9.3 (-1.2)	9.8 (-0.7)

The variation of blade thrust and power with the azimuth are plotted on Figure C.1, an azimuth of 0° corresponding to the Z axis and the positive direction is chosen to be the same as the propeller rotation. The plots show that both RANS/BET signals are in phase with the blade-resolved reference. However, whereas the generalized correction only slightly overestimates the thrust at some azimuths, the axial correction overestimates the amplitude of the signal significantly (+31%). The same thing is observed for the power curve. This is coherent with what was explained in section C.1. At an azimuth of 90°, the blade fully advances against the incidence component so Δv_t^{cor} is highly negative, thus increasing the angle of attack compared to the simulation with the generalized correction and leading to overestimated loads. Conversely, at an azimuth of 270°, the blade fully advances with the incidence component so Δv_t^{cor} is highly positive, thus decreasing the angle of attack compared to the simulation with the generalized correction and leading to underestimated loads.

Figures C.2 and C.3 show the axial and tangential disk loads from the RANS/BET simulations, from which were subtracted the disk loads from the blade-resolved simulation. The first observation to be made is that for the RANS/BET simulation with axial correction, the overestimations around 90° and underestimations around 270° mentioned previously are mainly caused by tip loads, as explained in section C.1. Second, the RANS/BET simulation with the generalized correction leads to a much better prediction of the disk loads. Both axial and tangential loads are still slightly overestimated compared to the blade-resolved results, but this effect is almost constant on the whole disk. This shows that this generalized tip correction accurately accounts for the incidence effects.

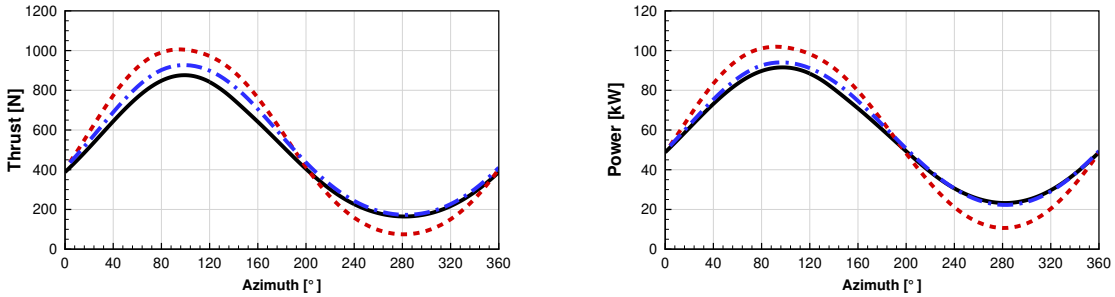

Blade-resolved (——), RANS/BET – Axial Correction (- - -), RANS/BET – Generalized Correction (-·-·-)

Figure C.1: Blade thrust and power over a revolution.

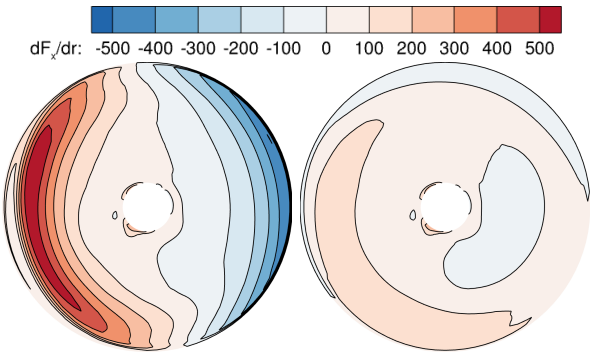

(a) Axial correction (b) Generalized correction

Figure C.2: Blade axial loads in N/m. Difference between RANS/BET and blade-resolved.

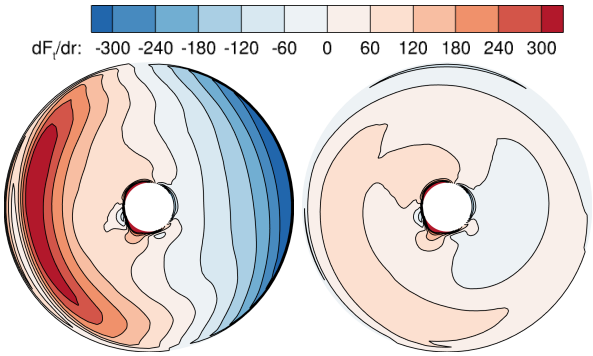

(a) Axial correction (b) Generalized correction

Figure C.3: Blade tangential loads in N/m. Difference between RANS/BET and blade-resolved.

C.3 Validation on a propeller in installed configuration

This section is dedicated to the study of the installed configuration. For this case there is no incidence, but the wing creates an up-wash in the propeller plane, leading to a non-zero perturbation field. Figure C.4 shows the normalized power-off field in the propeller plane which was extracted from a steady simulation of the hub and wing only. The disk was blanked where F_G is greater than 0.95 (ie. in the vicinity of the hub) because the velocity field has a negligible effect on the tip correction in this area, and the hub radius is shown in grey for reference. Contrary to the previous case, this power-off field is not constant: it is strongest on the upper part of the propeller disk, and particularly at +55° and -55°. Furthermore in this configuration, the power-off field is relatively weak compared to the freeflow and to the rotation velocity ($\pm 2.5\%$ at most). Nevertheless, the following results show that it is still necessary to use the generalized correction in such a case. This power-off field was used at each BET computation in equation (3.9).

The integrated averaged loads are shown in table C.2. The thrust and power are again overestimated for both corrections, but the computation with the generalized correction is overall more precise. For the 1P loads, the observations are the same as for the isolated configuration.

Figure C.5 shows the variation of blade thrust and power with the azimuth. The signal is not as sinusoidal as for the incidence case due to the more irregular perturbation field. For all

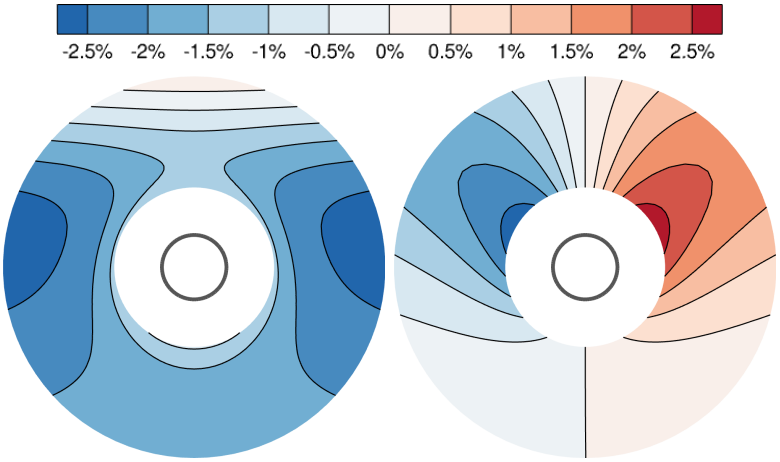

(a) Axial velocity field: $\frac{v_x^{p-o} - V_0}{V_0}$ (b) Tangential velocity field: $\frac{v_t^{p-o}}{\Omega r}$

Figure C.4: Normalized power-off fields in propeller plane for installed case.

Table C.2: Comparison of averaged propeller loads computed by blade-resolved and RANS/BET approaches

	Blade-Resolved	RANS/BET Axial Correction	RANS/BET Generalized Correction
Thrust [N]	1492	1561 (+4.6%)	1528 (+2.4%)
Power [kW]	173.5	176.3 (+1.6%)	174.1 (+0.3%)
1P Loads [N]	53.5	73.7 (+37.7%)	57.7 (+7.9%)
1P Phase [°]	14.4	13.2 (-1.2)	12.7 (-1.7)

computations, the load peaks are still located around where the power-off field is the strongest. As seen previously, the RANS/BET model with the axial correction still largely overestimates the maximum and minimum loads, even though the power-off field is in this case much weaker than in section C.2. This is mainly due to the $\left(\frac{1}{F_G} - 1\right)$ factor in equation (C.1). The RANS/BET model with the generalized correction gives a much more accurate and consistent prediction of thrust for different azimuths, and the power prediction is almost perfect. This shows that even in slightly non-axisymmetric cases, the generalized correction should be used.

Figures C.6 and C.7 show the RANS/BET disk loads with the same manipulation as for figures C.2 and C.3. As seen previously, the load differences between the blade-resolved and the RANS/BET with axial correction results are located mainly at the tip. Again, the general correction gives a more consistent load overestimation at the tip, almost evenly spread out over all azimuths.

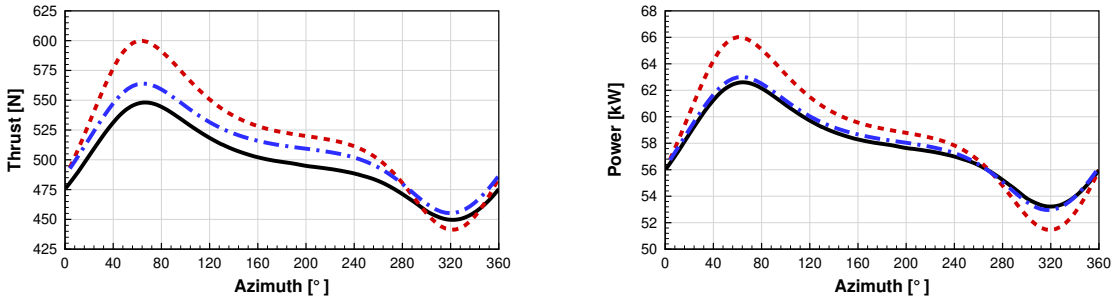

Blade-resolved (——), RANS/BET – Axial Correction (- - -), RANS/BET – Generalized Correction (-·-·-)

Figure C.5: Blade thrust and power over a revolution.

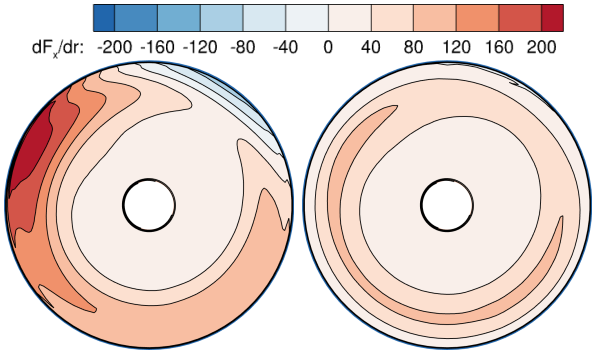

(a) Axial correction (b) Generalized correction

Figure C.6: Blade axial loads in N/m. Difference between RANS/BET and blade-resolved.

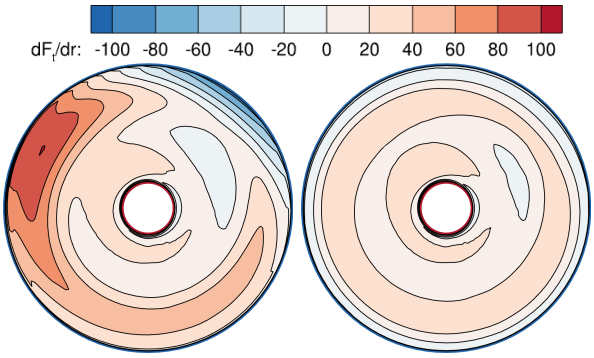

(a) Axial correction (b) Generalized correction

Figure C.7: Blade tangential loads in N/m. Difference between RANS/BET and blade-resolved.

Appendix D

Equations related to the energy source term

D.1 Necessity of the energy source term

First, the conservation of mass and momentum equations are recalled:

$$\frac{\partial \rho}{\partial t} + \nabla \cdot (\rho \boldsymbol{u}) = \frac{d\rho}{dt} + \rho \nabla \cdot \boldsymbol{u} = 0, \tag{D.1}$$

$$\frac{\partial \rho \boldsymbol{u}}{\partial t} + \nabla \cdot (\rho \boldsymbol{u}\boldsymbol{u}) - \nabla \cdot \boldsymbol{\sigma} = \boldsymbol{s_M}, \tag{D.2}$$

where $\boldsymbol{\sigma} = -p\mathbb{I} + \boldsymbol{\tau}$, $\boldsymbol{\tau}$ is the viscous tensor, and $\boldsymbol{s_M}$ is the vector of the momentum sources.
Using the definition of the material derivative and the conservation of mass from equation (D.1), equation (D.2) leads to

$$\rho \frac{d\boldsymbol{u}}{dt} = \nabla \cdot \boldsymbol{\sigma} + \boldsymbol{s_M}. \tag{D.3}$$

Taking the dot product of $\boldsymbol{u}$ and equation (D.3), a formula for the conservation of the kinetic energy is obtained:

$$\rho \frac{d}{dt}\left(\frac{u^2}{2}\right) = \boldsymbol{u} \cdot (\nabla \cdot \boldsymbol{\sigma}) + \boldsymbol{u} \cdot \boldsymbol{s_M}. \tag{D.4}$$

Note here that the momentum source terms directly lead to an increase of the kinetic energy. By also imposing the conservation of energy without additional source terms in the energy equation, the increase in kinetic energy must be compensated by a decrease of the internal energy, and thus a decrease of the temperature.
The conservation of specific total energy E, without an energy source term, yields:

$$\frac{\partial \rho E}{\partial t} + \nabla \cdot \left(\rho E \boldsymbol{u}\right) = \nabla \cdot (\boldsymbol{\sigma} \cdot \boldsymbol{u}) - \nabla \cdot \boldsymbol{q}. \tag{D.5}$$

Writing the specific total energy E as the sum of the specific internal energy e and the kinetic energy, we get:

$$\frac{\partial \rho e}{\partial t} + \frac{\partial}{\partial t}\left(\frac{\rho u^2}{2}\right) + \nabla \cdot (\rho e \boldsymbol{u}) + \nabla \cdot \left(\rho \frac{u^2}{2} \boldsymbol{u}\right) + \nabla \cdot \boldsymbol{q} - \nabla \cdot (\boldsymbol{\sigma} \cdot \boldsymbol{u}) = 0. \tag{D.6}$$

By developing the partial time derivatives and the divergence operators, and reordering the terms, we get:

$$\rho \overbrace{\left(\frac{\partial e}{\partial t} + \boldsymbol{u} \cdot \nabla e\right)}^{\frac{de}{dt}} + e \overbrace{\left(\frac{\partial \rho}{\partial t} + \boldsymbol{u} \cdot \nabla \rho + \rho \nabla \cdot \boldsymbol{u}\right)}^{0} + \rho \overbrace{\left(\frac{\partial}{\partial t}\left(\frac{u^2}{2}\right) + \boldsymbol{u} \cdot \nabla\left(\frac{u^2}{2}\right)\right)}^{\frac{d}{dt}\left(\frac{u^2}{2}\right)} + \frac{u^2}{2} \overbrace{\left(\frac{\partial \rho}{\partial t} + \boldsymbol{u} \cdot \nabla \rho + \rho \nabla \cdot \boldsymbol{u}\right)}^{0} - \nabla \cdot (\boldsymbol{\sigma} \cdot \boldsymbol{u}) + \nabla \cdot \boldsymbol{q} = 0. \tag{D.7}$$

Which leads after simplification to:

$$\rho \frac{de}{dt} + \rho \frac{d}{dt}\left(\frac{u^2}{2}\right) + \nabla \cdot \boldsymbol{q} - \nabla \cdot (\boldsymbol{\sigma} \cdot \boldsymbol{u}) = 0. \tag{D.8}$$

Substituting with equation (D.4), we ultimately obtain:

$$\rho \frac{de}{dt} = -\boldsymbol{u} \cdot \boldsymbol{s_M} + \nabla \cdot (\boldsymbol{\sigma} \cdot \boldsymbol{u}) - \boldsymbol{u} \cdot (\nabla \cdot \boldsymbol{\sigma}) - \nabla \cdot \boldsymbol{q}. \tag{D.9}$$

The second law of thermodynamics gives an expression for entropy S:

$$\rho T \frac{dS}{dt} = \rho \frac{de}{dt} - \frac{p}{\rho} \frac{d\rho}{dt} \tag{D.10}$$

Using equations (D.1) and (D.9), we get:

$$\rho T \frac{dS}{dt} = -\boldsymbol{u} \cdot \boldsymbol{s_M} + \nabla \cdot (\boldsymbol{\sigma} \cdot \boldsymbol{u}) - \boldsymbol{u} \cdot (\nabla \cdot \boldsymbol{\sigma}) - \nabla \cdot \boldsymbol{q} + p \nabla \cdot \boldsymbol{u} \tag{D.11}$$

Rewriting $\boldsymbol{\sigma}$ as $-p\mathbb{I} + \boldsymbol{\tau}$ and developing the $\nabla \cdot (p\boldsymbol{u})$ term that appears, the equation simplifies to:

$$\rho T \frac{dS}{dt} = -\boldsymbol{u} \cdot \boldsymbol{s_M} + \nabla \cdot (\boldsymbol{\tau} \cdot \boldsymbol{u}) - \boldsymbol{u} \cdot (\nabla \cdot \boldsymbol{\tau}) - \nabla \cdot \boldsymbol{q} \tag{D.12}$$

This equation shows that the momentum source terms have a negative contribution to the variation of entropy, which is obviously non-physical.

D.2 Viscous losses

The starting point of the demonstration comes from the fact that the RANS/BET and actuator line models compute the momentum source terms from tabulated 2D airfoil polars, for which the viscous losses are modeled by the drag coefficient. It would therefore be appropriate for theses losses to express themselves as an increase of entropy. For this reason, we propose to subtract

the contribution of the drag of the 2D airfoil polars from the energy conservation equation, as a source term (written $s_{E,v}$), to account for the viscous thermodynamic losses, such that the energy equation should be written:

$$\frac{\partial \rho E}{\partial t} + \nabla \cdot \left(\rho E \boldsymbol{u}\right) - \nabla \cdot (\boldsymbol{\sigma} \cdot \boldsymbol{u}) + \nabla \cdot \boldsymbol{q} = \boldsymbol{u} \cdot \boldsymbol{s_M} - s_{E,v} \tag{D.13}$$

For the RANS/BET and actuator line models, the momentum source term can be broken down as

$$\boldsymbol{s_M} = \left(s_{x,L} + s_{x,D}\right) \boldsymbol{e_x} + \left(s_{\theta,L} + s_{\theta,D}\right) \boldsymbol{e_\theta}, \tag{D.14}$$

with

$$\begin{cases} s_{x,L} = g \dfrac{1}{2} \rho c d_r v_{rel}^2 C_l \cos\phi \\ s_{x,D} = -g \dfrac{1}{2} \rho c d_r v_{rel}^2 C_d \sin\phi \\ s_{\theta,L} = g \dfrac{1}{2} \rho c d_r v_{rel}^2 C_l \sin\phi \\ s_{\theta,D} = g \dfrac{1}{2} \rho c d_r v_{rel}^2 C_d \cos\phi \end{cases}, \tag{D.15}$$

where $\cos\phi = \dfrac{\Omega r - v_t}{v_{rel}}$, $\sin\phi = \dfrac{v_x}{v_{rel}}$, $\boldsymbol{v_{rel}} = v_x \boldsymbol{e_x} + (v_t - \Omega r) \boldsymbol{e_\theta}$, d_r is the radial length of the blade element, and g is a generic volumic distribution function.

Only the viscous drag component should be included in this new source term. It should thus be expressed as:

$$s_{E,v} = \boldsymbol{v_{rel}} \cdot \left(s_{x,D} \boldsymbol{e_x} + s_{\theta,D} \boldsymbol{e_\theta}\right). \tag{D.16}$$

Note that the velocity used in the dot product to express the work done by the drag force is $\boldsymbol{v_{rel}}$ and not $\boldsymbol{u}$ because the blade loads are computed with the BET in the relative frame.

$$s_{E,v} = \boldsymbol{v_{rel}} \cdot \left(s_{x,D} \boldsymbol{e_x} + s_{\theta,D} \boldsymbol{e_\theta}\right) \tag{D.17}$$

$$= \left[v_x \boldsymbol{e_x} + (v_t - \Omega r) \boldsymbol{e_\theta}\right] \cdot \left(s_{x,D} \boldsymbol{e_x} + s_{\theta,D} \boldsymbol{e_\theta}\right) \tag{D.18}$$

$$= \left[v_x s_{x,D} + (v_t - \Omega r) s_{\theta,D}\right] \tag{D.19}$$

$$\boldsymbol{u} \cdot \boldsymbol{s_M} = \left[v_x \boldsymbol{e_x} + v_t \boldsymbol{e_\theta}\right] \cdot \left[\left(s_{x,L} + s_{x,D}\right) \boldsymbol{e_x} + \left(s_{\theta,L} + s_{\theta,D}\right) \boldsymbol{e_\theta}\right] \tag{D.20}$$

$$= \left[v_x s_{x,L} + v_x s_{x,D} + v_t s_{\theta,L} + v_t s_{\theta,D}\right] \tag{D.21}$$

$$\boldsymbol{u} \cdot \boldsymbol{s_M} - s_{E,v} = \left[v_x s_{x,L} + v_t s_{\theta,L}\right] + \Omega r s_{\theta,D} \tag{D.22}$$

$$v_x s_{x,L} + v_t s_{\theta,L} = g \frac{1}{2} \rho c d_r v_{rel} C_l \left[v_x (\Omega r - v_t) + v_t v_x\right] \tag{D.23}$$

$$= g \frac{1}{2} \rho c d_r v_{rel} C_l \left[v_x \Omega r\right] \tag{D.24}$$

$$= \Omega r s_{\theta,L} \tag{D.25}$$

$$\boldsymbol{u}\cdot\boldsymbol{s_M} - s_{E,v} = \left(s_{\theta,L} + s_{\theta,D}\right)\Omega r \tag{D.26}$$

$$= \left(\boldsymbol{s_M}\cdot\boldsymbol{e_\theta}\right)\Omega r \tag{D.27}$$

This expression is equivalent to the one proposed by Hall, and further shows that the losses are exactly due to the drag of the 2D airfoils. In a similar manner as presented in appendix D.1, the entropy variation can be expressed in a case where the energy source term is $\boldsymbol{u}\cdot\boldsymbol{s_M} - s_{E,v}$:

$$\rho T\frac{dS}{dt} = -s_{E,v} + \nabla\cdot(\boldsymbol{\tau}\cdot\boldsymbol{u}) - \boldsymbol{u}\cdot(\nabla\cdot\boldsymbol{\tau}) - \nabla\cdot\boldsymbol{q} \tag{D.28}$$

It will now be shown that $s_{E,v}$ is always negative. From equations (D.19) and (D.15), we get:

$$s_{E,v} = g\left[-v_x\frac{1}{2}\rho c d_r v_{rel}^2 C_d\frac{v_x}{v_{rel}} + (v_t - \Omega r)\frac{1}{2}\rho c d_r v_{rel}^2 C_d\frac{\Omega r - v_t}{v_{rel}}\right] \tag{D.29}$$

$$= -g\frac{1}{2}\rho c d_r v_{rel} C_d\left[v_x^2 + (\Omega r - v_t)^2\right] \tag{D.30}$$

Because $s_{E,v}$ is always negative, the additional source term suggested in this section does in fact lead to an increase of entropy, which is in particular proportional to the drag coefficient of the momentum body force.

Bibliography

[1] C. Adkins and R. Liebeck, *Design of optimum propellers*, Journal of Propulsion and Power, 10 (1983).

[2] N. Ben Nasr, F. Falissard, J. Decours, R. Gaveriaux, Y. Delrieux, S. Canard-Caruana, M. Laban, H. Brouwer, M. Albreicht, C. Scholz, C. Diette, and D. Chartrain, *Propeller Analysis Using Low & High Fidelity Aero-acoustic Methods*, in 35th AIAA Applied Aerodynamics Conference, AIAA AVIATION Forum, American Institute of Aeronautics and Astronautics, June 2017.

[3] A. Betz, *Schraubenpropeller mit geringstem Energieverlust. Mit einem Zusatz von l. Prandtl*, in Nachrichten von der Gesellschaft der Wissenschaften zu Göttingen, weidmannsche buchhandlung ed., 1919, pp. 193–217.

[4] F. Blondel, R. Boisard, M. Milekovic, G. Ferrer, C. Lienard, and D. Teixeira, *Validation and comparison of aerodynamic modelling approaches for wind turbines*, Journal of Physics: Conference Series, (2016).

[5] R. Boisard, *Numerical Analysis of Rotor/Propeller Aerodynamic Interactions on a High-Speed Compound Helicopter*, Journal of the American Helicopter Society, 67 (2022), pp. 1–15.

[6] N. K. Borer, M. D. Moore, and A. Turnbull, *Tradespace Exploration of Distributed Propulsors for Advanced On-Demand Mobility Concepts*, in 14th AIAA Aviation Technology, Integration, and Operations Conference, AIAA AVIATION Forum, American Institute of Aeronautics and Astronautics, June 2014.

[7] E. Branlard, *Tip-Losses with Focus on Prandlt's Tip Loss Factor*, in Wind Turbine Aerodynamics and Vorticity-Based Methods: Fundamentals and Recent Applications, Springer International Publishing, 2017, pp. 227–245.

[8] M. Bühler, P. Weihing, L. Klein, T. Lutz, and E. Krämer, *Actuator Line Method Simulations for the Analysis of Wind Turbine Wakes Acting on Helicopters*, Journal of Physics: Conference Series, 1037 (2018).

[9] L. Cambier, S. Heib, and S. Plot, *The Onera elsA CFD software: input from research and feedback from industry*, Mechanics & Industry, 14 (2013), pp. 159–174.

[10] D.-G. Caprace, P. Chatelain, and G. Winckelmans, *Lifting Line with Various Mollifications: Theory and Application to an Elliptical Wing*, AIAA Journal, 57 (2019), pp. 17–28.

[11] M. J. Churchfield, S. J. Schreck, L. A. Martinez, C. Meneveau, and P. R. Spalart, *An Advanced Actuator Line Method for Wind Energy Applications and Beyond*, in 35th Wind Energy Symposium, American Institute of Aeronautics and Astronautics, 2017.

[12] M. Cormier, P. Weihing, and T. Lutz, *Evaluation of the Effects of Actuator Line Force Smearing on Wind Turbines Near-Wake Development*, Journal of Physics: Conference Series, 1934 (2021).

[13] R. Courant, K. Friedrichs, and H. Lewy, *Über die partiellen Differenzengleichungen der mathematischen Physik*, Mathematische Annalen, 100 (1928), pp. 32–74.

[14] K. O. Dağ, *Combined pseudo-spectral / actuator line model for wind turbine applications*, PhD thesis, Technical University of Denmark, 2017.

[15] K. O. Dağ and J. N. Sørensen, *A new tip correction for actuator line computations*, Wind Energy, 23 (2020), pp. 148–160.

[16] O. De Vries, *Fluid Dynamic Aspects of Wind Energy Conversion*, tech. rep., AGARD, July 1979.

[17] K. A. Deere, J. K. Viken, S. Viken, M. B. Carter, M. Wiese, and N. Farr, *Computational Analysis of a Wing Designed for the X-57 Distributed Electric Propulsion Aircraft*, in 35th AIAA Applied Aerodynamics Conference, American Institute of Aeronautics and Astronautics, Denver, Colorado, 2017.

[18] G. Delattre and F. Falissard, *Influence of Torque Ratio on Counter-Rotating Open-Rotor Interaction Noise*, AIAA Journal, 53 (2015), pp. 2726–2738.

[19] S. Delbecq, J. Fontane, N. Gourdain, H. Mugnier, T. Planès, and F. Simatos, *Référentiel ISAE-SUPAERO Aviation et climat*.
Sept. 2021.

[20] C. Dosne, *Development and implementation of adjoint formulation of explicit body-force models for aero-propulsive optimizations*, PhD Thesis, Institut Polytechnique de Paris, 2024.

[21] S. Drzewiecki, *Méthode pour la détermination des éléments mécaniques des propulseurs hélicoïdaux*, vol. 3 of Bulletin de l'Association Technique Maritime, 1892, pp. 11–31.

[22] F. Falissard and H. Pantel, *On the Use of Lifting Line Approaches for Propellers with Large Chord Variations*, AIAA Journal, 62 (2024), pp. 2377–2380.

[23] I. Fejtek and L. Roberts, *Navier-Stokes computation of wing/rotor interaction for a tilt rotor in hover*, AIAA Journal, 30 (1992), pp. 2595–2603.

[24] J. R. Forsythe, E. Lynch, S. Polsky, and P. Spalart, *Coupled Flight Simulator and CFD Calculations of Ship Airwake using Kestrel*, in 53rd AIAA Aerospace Sciences Meeting, AIAA SciTech Forum, American Institute of Aeronautics and Astronautics, Jan. 2015.

[25] R. Froude, *On the part played in propulsion by differences of fluid pressure*, vol. 30 of Transactions of the Institution of Naval Architects, 1889, pp. 390–405.

[26] W. Froude, *On the Elementary Relation Between Pitch, Slip, and Propulsive Efficiency*, vol. 19 of Transactions of the Institution of Naval Architects, 1878, pp. 47–57.

[27] C. W. Gear, *The Numerical Integration of Ordinary Differential Equations*, Mathematics of Computation, 21 (1967), pp. 146–156.

[28] H. Glauert, *Airplane Propellers*, in Aerodynamic Theory, W. F. Durand, ed., vol. IV, Springer, Berlin, Heidelberg, 1935, pp. 169–360.

[29] J. Guo and J. Hu, *A three-dimensional computational model for inlet distortion in fan and compressor*, Proceedings of the Institution of Mechanical Engineers, Part A: Journal of Power and Energy, 232 (2018), pp. 144–156.

[30] D. K. Hall, *Analysis of civil aircraft propulsors with boundary layer ingestion*, PhD Thesis, Massachusetts Institute of Technology, 2015.

[31] D. K. Hall, E. M. Greitzer, and C. S. Tan, *Analysis of Fan Stage Conceptual Design Attributes for Boundary Layer Ingestion*, Journal of Turbomachinery, 139 (2017).

[32] IATA, *Resolution on the industry's commitment to reach net zero carbon emissions by 2050*, Oct. 2021.

[33] S. Ivanell, J. N. Sørensen, R. Mikkelsen, and D. Henningson, *Analysis of numerically generated wake structures*, Wind Energy, 12 (2009), pp. 63–80.

[34] A. Jameson, W. Schmidt, and E. Turkel, *Numerical Solution of the Euler Equations by Finite Volume Methods Using Runge-Kutta Time Stepping Schemes*, AIAA Paper, (1981).

[35] P. K. Jha, M. J. Churchfield, P. J. Moriarty, and S. Schmitz, *Guidelines for Volume Force Distributions Within Actuator Line Modeling of Wind Turbines on Large-Eddy Simulation-Type Grids*, Journal of Solar Energy Engineering, 136 (2014).

[36] P. K. Jha and S. Schmitz, *Actuator curve embedding – an advanced actuator line model*, Journal of Fluid Mechanics, 834 (2018).

[37] J. Johansen and N. N. Sørensen, *Aerofoil characteristics from 3D CFD rotor computations*, Wind Energy, 7 (2004), pp. 283–294.

[38] T. Kiffer, G. Dufour, R. Gojon, W. Thollet, and L. López de Vega, *Extension and validation of the Body Force Method to a propeller blade*, in AIAA AVIATION 2023 Forum, AIAA AVIATION Forum, American Institute of Aeronautics and Astronautics, June 2023.

[39] V. G. Kleine, A. Hanifi, and D. S. Henningson, *Non-iterative vortex-based smearing correction for the actuator line method*, Journal of Fluid Mechanics, 961 (2023).

[40] J. C. Kok, *Resolving the Dependence on Freestream Values for the k- Turbulence Model*, AIAA Journal, 38 (2000), pp. 1292–1295.

[41] A. P. Kottapalli, *Development of a body force model for centrifugal compressors*, PhD Thesis, Massachusetts Institute of Technology, 2013.

[42] H. Lamb, *Hydrodynamics*, Cambridge University Press, 1932.

[43] F. Le Chuiton, *Actuator disc modelling for helicopter rotors*, Aerospace Science and Technology, 8 (2004), pp. 285–297.

[44] D. S. Lee, D. W. Fahey, A. Skowron, M. R. Allen, U. Burkhardt, Q. Chen, S. J. Doherty, S. Freeman, P. M. Forster, J. Fuglestvedt, A. Gettelman, R. R. De León, L. L. Lim, M. T. Lund, R. J. Millar, B. Owen, J. E. Penner, G. Pitari, M. J. Prather, R. Sausen, and L. J. Wilcox, *The contribution of global aviation to anthropogenic climate forcing for 2000 to 2018*, Atmospheric Environment, 244 (2021).

[45] E. Lynch, E. Hayden, and S. Polsky, *Confidence and Credibility Studies of an Actuator Line Model for Tiltrotor Dynamic Interface Simulations*, in AIAA AVIATION 2021 FORUM, AIAA AVIATION Forum, American Institute of Aeronautics and Astronautics, July 2021.

[46] F. E. Marble, *Three-Dimensional Flow in Turbomachines*, in Aerodynamics of Turbines and Compressors, vol. 1, Princeton University Press, 1964, pp. 83–166.

[47] L. Martinelli and A. Jameson, *Validation of a multigrid method for the Reynolds averaged equations*, in 26th Aerospace Sciences Meeting, American Institute of Aeronautics and Astronautics, 1988.

[48] L. Martinez, S. Leonardi, M. Churchfield, and P. Moriarty, *A Comparison of Actuator Disk and Actuator Line Wind Turbine Models and Best Practices for Their Use*, in 50th AIAA Aerospace Sciences Meeting including the New Horizons Forum and Aerospace Exposition, American Institute of Aeronautics and Astronautics, 2012.

[49] L. A. Martinez-Tossas, M. J. Churchfield, and S. Leonardi, *Large eddy simulations of the flow past wind turbines: actuator line and disk modeling*, Wind Energy, 18 (2015), pp. 1047–1060.

[50] L. A. Martínez-Tossas, M. J. Churchfield, and C. Meneveau, *Optimal smoothing length scale for actuator line models of wind turbine blades based on Gaussian body force distribution*, Wind Energy, 20 (2017), pp. 1083–1096.

[51] L. A. Martínez-Tossas and C. Meneveau, *Filtered lifting line theory and application to the actuator line model*, Journal of Fluid Mechanics, 863 (2019), pp. 269–292.

[52] F. R. Menter, *Two-equation eddy-viscosity turbulence models for engineering applications*, AIAA Journal, 32 (1994), pp. 1598–1605.

[53] R. Merabet and E. Laurendeau, *Parametric Study on the Velocity Sampling Techniques for the Actuator Line Method in 2D*, in AIAA Scitech 2019 Forum, American Institute of Aeronautics and Astronautics, 2019.

[54] R. Merabet and E. Laurendeau, *Hovering Helicopter Rotors Modeling Using the Actuator Line Method*, Journal of Aircraft, 59 (2022), pp. 774–787.

[55] A. Meyer Forsting, G. Pirrung, and N. Ramos García, *A vortex-based tip/smearing correction for the actuator line*, Wind Energy Science, 4 (2019), pp. 369–383.

[56] A. R. M. Meyer Forsting, G. R. Pirrung, and N. Ramos-García, *The wake of an actuator line with a vortex-based tip/smearing correction in uniform and turbulent inflow*, Journal of Physics: Conference Series, 1256 (2019).

[57] R. Mikkelsen, J. N. Sørensen, and W. Z. Shen, *Modelling and analysis of the flow field around a coned rotor*, Wind Energy, 4 (2001), pp. 121–135.

[58] R. F. Mikkelsen, *Actuator Disc Methods Applied to Wind Turbines*, PhD thesis, Technical University of Denmark, 2003.

[59] A. Mittal, K. Sreenivas, L. K. Taylor, and L. Hereth, *Improvements to the Actuator Line Modeling for Wind Turbines*, in 33rd Wind Energy Symposium, American Institute of Aeronautics and Astronautics, 2015.

[60] F. Moens and P. Gardarein, *Numerical simulation of the propeller/wing interactions for transport aircraft*, in 19th AIAA Applied Aerodynamics Conference, American Institute of Aeronautics and Astronautics, 2001.

[61] M. Mudry, *La théorie générale des nappes et filaments tourbillonaires et ses applications à l'aérodynamique instationnaire*, PhD Thesis, Université Pierre et Marie Curie - Paris VI, 1982.

[62] B. Ortun, *A coupled RANS/lifting-line analysis for modelling the aerodynamics of distributed propulsion*, San Francisco, CA, 2018, AHS Technical Conference on Aeromechanics Design for Transformative Vertical Flight.

[63] C. W. Oseen, *Über Wirbelbewegung in einer reibenden Flüssigkeit*, vol. 7 of Arkiv för matematik, astronomi och fysik, 1911.

[64] R. Pacciani, M. Marconcini, and A. Arnone, *A CFD-Based Throughflow Method with Three-Dimensional Flow Features Modelling*, International Journal of Turbomachinery, Propulsion and Power, 2 (2017), p. 11.

[65] H. Pantel, F. Falissard, and G. Dufour, *Assessment of a RANS/BET Body Force Method for Propeller Modeling*, in AIAA AVIATION 2023 Forum, San Diego, United States of America, June 2023, American Institute of Aeronautics and Astronautics.

[66] H. Pantel, F. Falissard, and G. Dufour, *Assessment of Reynolds-Averaged Navier–Stokes/Blade Element Theory Body Force Method for Propeller Modeling*, AIAA Journal, 62 (2024), pp. 758–775.

[67] H. Pantel, F. Falissard, and G. Dufour, *Simulation of an Installed Propeller by means of Steady and Unsteady Body-Force Modeling*, in ICAS 2024: 34th Congress of the International Council of the Aeronautical Sciences, Florence, Italy, Sept. 2024.

[68] L. Prandtl, *Applications of Modern Hydrodynamics to Aeronautics*, Tech. Rep. NACA-TR-116, Jan. 1923.

[69] S. Péron and C. Benoit, *Automatic off-body overset adaptive Cartesian mesh method based on an octree approach*, Journal of Computational Physics, 232 (2013), pp. 153–173.

[70] A. Raichle, S. Melber-Wilkending, and J. Himisch, *A New Actuator Disk Model for the TAU Code and Application to a Sailplaine with a Folding Engine*, in New Results in Numerical and Experimental Fluid Mechanics VI, Berlin, Heidelberg, 2008, Springer, pp. 52–61.

[71] R. G. Rajagopalan and C. K. Lim, *Laminar Flow Analysis of a Rotor in Hover*, Journal of the American Helicopter Society, 36 (1991), pp. 12–23.

[72] R. G. Rajagopalan and S. R. Mathur, *Three Dimensional Analysis of a Rotor in Forward Flight*, Journal of the American Helicopter Society, 38 (1993), pp. 14–25.

[73] S. Ramdin, *Prandtl tip loss factor assessed*, PhD thesis, Delft University of Technology, 2017.

[74] W. Rankine, *On the Mechanical Principles of the Action of Propellers*, in Transactions of the Institution of Naval Architects, vol. 6, London, 1865, pp. 13–34.

[75] G. Reboul, D. Lewis, M. Balmaseda, J. Bailly, F. Falissard, F. Guntzer, and C. Lienard, *Multi-fidelity Aeroacoustic Prediction of an eVTOL Rotor*, in Vertical Flight Society's 79th Annual Forum and Technology Display, West Palm Beach, FL, May 2023.

[76] Safran, *Safran et l'ONERA lancent les essais en soufflerie du futur Open Fan*, Jan. 2024. https://www.safran-group.com/fr/espace-presse/safran-onera-lancent-essais-soufflerie-du-futur-open-fan-2024-01-19.

[77] J. A. Schetz and S. Favin, *Numerical Solution for the Near Wake of a Body with Propeller*, Journal of Hydronautics, 11 (1977), pp. 136–141.

[78] J. A. Schetz and S. Favin, *Numerical solution of a body-propeller combination flow including swirl and comparisons with data*, Journal of Hydronautics, 13 (1979), pp. 46–51.

[79] M. Schollenberger, M. F. Beckers, and T. Lutz, *Validation of ACD and ACL propeller simulation using blade element method based on airfoil characteristics*, in High Performance Computing in Science and Engineering '21, Cham, 2023, Springer International Publishing, pp. 367–380.

[80] M. Schollenberger and T. Lutz, *Comparison of Different Methods for the Extraction of Airfoil Characteristics of Propeller Blades as Input for Propeller Models in CFD*, in New Results in Numerical and Experimental Fluid Mechanics XIII, Cham, 2021, Springer International Publishing, pp. 24–34.

[81] W. Z. Shen, M. O. L. Hansen, and J. N. Sørensen, *Determination of the angle of attack on rotor blades*, Wind Energy, 12 (2009), pp. 91–98.

[82] W. Z. Shen, R. Mikkelsen, J. N. Sørensen, and C. Bak, *Tip Loss Corrections for Wind Turbine Computations*, Wind Energy, 8 (2005), pp. 457–475.

[83] W. Z. Shen, J. N. Sørensen, and R. Mikkelsen, *Tip Loss Correction for Actuator/Navier–Stokes Computations*, Journal of Solar Energy Engineering, 127 (2005), pp. 209–213.

[84] M. Shives and C. Crawford, *Mesh and load distribution requirements for actuator line CFD simulations*, Wind Energy, 16 (2013), pp. 1183–1196.

[85] J.-F. Simon, *Contribution to Throughflow Modelling for Axial Flow Turbomachines*, PhD Thesis, Université de Liège, 2007.

[86] H. Snel and T. Holten, *Review of recent aerodynamic research on wind turbines with relevance to rotorcraft*, AGARD Report CP 552, 7 (1995), pp. 1–11.

[87] R. Stevens, L. A. Martínez-Tossas, and C. Meneveau, *Comparison of wind farm large eddy simulations using actuator disk and actuator line models with wind tunnel experiments*, Renewable Energy, 116 (2018), pp. 470–478.

[88] T. C. A. Stokkermans, *Aerodynamics of Propellers in Interaction Dominated Flowfields: An Application to Novel Aerospace Vehicles*, PhD thesis, Delft University of Technology, 2020.

[89] T. C. A. Stokkermans, N. van Arnhem, T. Sinnige, and L. L. M. Veldhuis, *Validation and Comparison of RANS Propeller Modeling Methods for Tip-Mounted Applications*, AIAA Journal, 57 (2019), pp. 566–580.

[90] J. N. Sørensen, *General Momentum Theory for Horizontal Axis Wind Turbines*, Springer, 2016.

[91] J. N. Sørensen and C. W. Kock, *A model for unsteady rotor aerodynamics*, Journal of Wind Engineering and Industrial Aerodynamics, 58 (1995), pp. 259–275.

[92] J. N. Sørensen and R. Mikkelsen, *A critical view on the momentum theory*, in Torque 2012, Oldenburg, 2012.

[93] J. N. Sørensen and A. Myken, *Unsteady actuator disc model for horizontal axis wind turbines*, Journal of Wind Engineering and Industrial Aerodynamics, 39 (1992), pp. 139–149.

[94] J. N. Sørensen and W. Z. Shen, *Numerical Modeling of Wind Turbine Wakes*, Journal of Fluids Engineering, 124 (2002), pp. 393–399.

[95] J. N. Sørensen, W. Z. Shen, and X. Munduate, *Analysis of wake states by a full-field actuator disc model*, Wind Energy, 1 (1998), pp. 73–88.

[96] W. Thollet, *Modélisations simplifiées de turbomachines pour l'analyse par la simulation des installations motrices complexes d'avions*, PhD Thesis, Toulouse, ISAE-SUPAERO, July 2017.

[97] W. Thollet, G. Dufour, X. Carbonneau, and F. Blanc, *Body-force modeling for aerodynamic analysis of air intake – fan interactions*, International Journal of Numerical Methods for Heat & Fluid Flow, 26 (2016), pp. 2048–2065.

[98] N. Troldborg, *Actuator Line Modeling of Wind Turbine Wakes*, PhD thesis, Technical University of Denmark, 2009.

[99] N. Troldborg, J. N. Sorensen, and R. Mikkelsen, *Numerical simulations of wake characteristics of a wind turbine in uniform inflow*, Wind Energy, 13 (2010), pp. 86–99.

[100] J. Valentin and L. Bernardos, *Validation of a New Solver Based on the Vortex Particle Method for Wings, Propellers and Rotors*, in European Rotorcraft Forum 49, Germany, Sept. 2023.

[101] P. Weihing, C. Schulz, T. Lutz, and E. Krämer, *Comparison of the Actuator Line Model with Fully Resolved Simulations in Complex Environmental Conditions*, Journal of Physics: Conference Series, 854 (2017).

[102] D. Whitfield and A. Jameson, *Three-dimensional Euler equation simulation of propeller-wing interaction in transonic flow*, in 21st Aerospace Sciences Meeting, American Institute of Aeronautics and Astronautics, 1983.

[103] R. E. Wilson and P. B. S. Lissaman, *Applied Aerodynamics of Wind Power Machines*, NTIS, 1974.

[104] N. Yu, S. Samant, and P. Rubbert, *Flow prediction for propfan configurations using Euler equations*, in 17th Fluid Dynamics, Plasma Dynamics, and Lasers Conference, American Institute of Aeronautics and Astronautics, 1984.

[105] W. Zhong, W. Z. Shen, T. Wang, and Y. Li, *A tip loss correction model for wind turbine aerodynamic performance prediction*, Renewable Energy, 147 (2020), pp. 223–238.

[106] W. Zhong, T. G. Wang, W. J. Zhu, and W. Z. Shen, *Evaluation of Tip Loss Corrections to AD/NS Simulations of Wind Turbine Aerodynamic Performance*, Applied Sciences, 9 (2019).

[107] L. A. J. Zori and R. G. Rajagopalan, *Navier-Stokes Calculations of Rotor-Airframe Interaction in Forward Flight*, Journal of the American Helicopter Society, 40 (1995), pp. 57–67.